Karlsruher Institut für Technologie

ELECTRONIC AND PHOTONIC EXCITATIONS IN GRAPHENE NANOSTRUCTURES AND HYBRID SYSTEMS

Zur Erlangung des akademischen Grades eines
DOKTORS DER NATURWISSENSCHAFTEN (Dr. rer. nat.)

von der KIT-Fakultät für Physik
des Karlsruher Instituts für Technologie (KIT)
angenommene

DISSERTATION

von

M. Sc. Marvin Martin Müller

am Institut für Theoretische Festkörperphysik

Tag der mündlichen Prüfung:	08. Juli 2022
Referent:	Prof. Dr. Carsten Rockstuhl
Korreferent:	Prof. Dr. Ralph Krupke

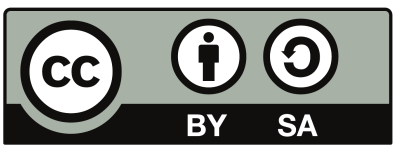

Abstract

Plasmonic modes of photonic nanoantennas offer unprecedented electric field enhancement and confinement and have versatile applications in nanotechnology. For many years, the noble metals have been the workhorses in nanoplasmonics. More recently, low-dimensional materials experienced a surge of popularity as plasmonic materials.

In particular, the unique band structure of two-dimensional *graphene* opens the opportunity to tune its modes even after the fabrication by electronic gating or optical pumping. Moreover, we discuss the one-dimensional polyene and polyacetylene molecules, described within the *Su-Schrieffer-Heeger* (SSH) model, in this work to gain more conceptual insights into the nature of optical modes in nanoantennas.

Nanoantennas modify their local photonic environment and impact, therefore, the optical properties of nearby *quantum emitters*, *e.g.*, their spontaneous emission rates or *Rabi* oscillations. To model the optical properties of hybrid systems consisting of nanoantennas and emitters, the state-of-the-art simulation technique is density functional theory. However, this approach is computationally expensive and cannot be applied to structures of relevant sizes. To overcome this limitation, we rely on a much cheaper time-domain *tight binding* (TB) framework that we develop further to encounter the quantum optical phenomena in an emitter and its chemical interaction with the antenna.

In this thesis, we discuss two issues that arise when a *classical* description for plasmons in nanoantennas is no longer applicable and a *quantum* description is necessary instead. The first issue concerns the TB description of hybrid systems, which consist of a nanoantenna and an adsorbed atom (adatom) acting as an emitter. The commonly used *Purcell* formalism to model such systems neglects electronic tunneling between the adatom and the nanoantenna. Our simulations show that opening this interaction channel modifies the optics of the system. Both, the coupling *strength* and *position* of the adatom are essential. We find two qualitatively different interaction regimes when the adatom is coupled to an *edge* or *bulk* atom of the nanoantenna. Conversely, also the phenomena linked to the adatom are modified. In particular, we observe quenching of the spontaneous emission rate and a decrease of the *Rabi* frequency of transitions in the hybrid system.

The second issue concerns the question what a plasmon in nanoscale systems really is. We outline that literature offers different concepts of what is a plasmonic response. Most of them rely in their definition on the induced charge distribution of a mode or the number of involved single-particle transitions. Our contribution to the field, the *energy-based plasmonicity index* (EPI), assesses the nature of a mode based on energy-space coherence dynamics of the system's density operator. It is introduced, validated, and applied to the SSH chains and to graphene nanoantennas. We find that it is in line with the energy space-based *Coulomb* scaling approach, but not with real space-based approaches such as the generalized plasmonicity index. Hence, the EPI complements existing classification methods and helps to shed light on previously unattended aspects of plasmonicity.

Zusammenfassung in deutscher Sprache

Plasmonische Resonanzen in photonischen Nanoantennen erlauben eine beispiellose Verstärkung und örtliche Konzentrierung elektrischer Felder und finden vielseitige Anwendungen in der Nanotechnologie. Viele Jahre waren die Edelmetalle die Treiber der Nanoplasmonik. In letzter Zeit erfreuen sich aber vor allem niedrigdimensionale Werkstoffe zunehmender Beliebtheit als plasmonische Materialien.

Vor allem die einzigartige Bandstruktur von zweidimensionalem *Graphen* bietet die Möglichkeit, Resonanzen auch nach der Herstellung der Struktur durch elektrisches Dotieren oder optisches Pumpen spektral zu verschieben. Neben Graphen diskutieren wir in dieser Arbeit im Rahmen des *Su-Schrieffer-Heeger*-Modells (SSH) zudem eindimensionale Polyen- und Polyacetylen-Moleküle, um konzeptionelle Einblicke in die Wesensart optischer Moden in Nanoantennen zu erlangen.

Nanoantennen verändern allein durch ihre Präsenz die lokale photonische Umgebung und beeinflussen die optischen Eigenschaften von Quantenemittern in der Nähe, z. B. deren spontane Emissionsraten oder *Rabi*-Oszillationen. Zur Modellierung der optischen Eigenschaften hybrider Systeme, die aus Nanoantennen und Emittern bestehen, ist die führende Simulationsmethode die Dichtefunktionaltheorie. Sie ist jedoch sehr rechenintensiv und kann nicht auf Strukturen relevanter Größe angewandt werden. Um diese Beschränkung zu überwinden, entwickeln wir eine *tight-binding*-Methode (TB) im Zeitbereich, die die quantenoptischen Phänomene im Emitter und seine chemische Wechselwirkung mit der Nanoantenne beschreiben kann.

In dieser Arbeit diskutieren wir zwei Probleme, die auftreten, wenn eine klassische Beschreibung für die oben beschriebenen Systeme nicht mehr anwendbar ist und stattdessen eine quantenmechanische Beschreibung erforderlich wird. Das erste Problem betrifft die TB-Simulationsmethodik hybrider Systeme, die aus einer Nanoantenne und einem adsorbierten Atom (Adatom) bestehen, das als Emitter fungiert. Der üblicherweise verwendete *Purcell*-Formalismus zur Modellierung solcher Systeme vernachlässigt allerdings elektronisches Tunneln zwischen der Nanoantenne und dem Adatom. Unsere Simulationen zeigen, dass sich unter Berücksichtigung dieses Wechselwirkungskanals die optischen Eigenschaften des Systems maßgeblich verändern. Sowohl die Wechselwirkungsstärke zwischen Adatom und Nanoantenne, als auch deren relative Position sind hierfür entscheidend. Wir finden zwei qualitativ verschiedene Wechselwirkungs-Regime, wenn das Adatom am Rand oder an den Mittelteil der Nanoantenne gekoppelt wird. Umgekehrt ändern sich auch die dem Adatom zugehörigen Phänomene. Insbesondere beobachten wir eine Reduzierung sowohl der spontanen Emissionsrate, als auch der *Rabi*-Frequenz optischer Übergänge im hybriden Gesamtsystem.

Die zweite Problematik behandelt die Frage, *was* ein Plasmon in Nanosystemen wirklich ist. Wir zeigen auf, dass es in der Literatur verschiedene Konzepte für plasmonische Resonanzen gibt. Die meisten stützen sich bei ihrer Definition auf die induzierte

Ladungsverteilung der Resonanz oder auf die Anzahl der beteiligten Ein - Teilchen - Übergänge. Unser Beitrag zu dieser wissenschaftlichen Diskussion, der *energy-based plasmonicity index (EPI)*, klassifiziert eine Resonanz anhand der Zeitentwicklung der Kohärenzen im Dichteoperator des Systems, ausgewertet im Energie-Raum. Der EPI wird hier eingeführt, validiert und auf SSH-Ketten und Graphen-Nanoantennen angewandt. Wir stellen fest, dass der EPI Klassifikationsergebnisse liefert, die mit jenen der *Coulomb*-Skalierungs-Methode übereinstimmen. Der *generalized plasmonicity index*, welcher auf Auswertungen im Ortsraum basiert, liefert allerdings keine deckungsgleichen Resultate. Der EPI ergänzt daher die bestehenden Klassifizierungsmethoden und hilft, bisher wenig beachtete Aspekte plasmonischer Resonanzen in den Mittelpunkt zu rücken.

Contents

List of Publications and Conference Contributions

Published peer-reviewed scientific publications related to this thesis

1. M. Kosik, M. M. Müller, M. Pelc, G. W. Bryant, A. Ayuela, C. Rockstuhl, and K. Słowik "Revising quantum optical phenomena in adatoms coupled to graphene nanoantennas", *Nanophotonics* **11**, 3281-3298 (2022)

2. M. M. Müller, N. Perdana, C. Rockstuhl, and C. Holzer, "Modeling and measuring plasmonic excitations in hollow spherical gold nanoparticles", *The Journal of Chemical Physics* **156**, 094103 (2022)

3. M. M. Müller, M. Kosik, M. Pelc, G. W. Bryant, A. Ayuela, C. Rockstuhl, and K. Słowik "From single-particle-like to interaction-meditated plasmonic resonances in graphene nanoantennas", *The Journal of Applied Physics* **129**, 093103 (2021)

4. M. M. Müller, M. Kosik, M. Pelc, G. W. Bryant, A. Ayuela, C. Rockstuhl, and K. Słowik "Modification of the optical properties of molecular chains upon coupling to adatoms", *Physical Review B* **104**, 235414 (2021)

5. M. M. Müller, M. Kosik, M. Pelc, G. W. Bryant, A. Ayuela, C. Rockstuhl, and K. Słowik "Energy-based plasmonicity index to characterize optical resonances in nanostructures", *The Journal of Physical Chemistry C* **124**, 24331 (2020)

Published peer-reviewed scientific publications based on the master thesis

6. M. M. Müller, B. Maier, C. Rockstuhl, and M. Hochbruck, "Analytical and numerical analysis of linear and nonlinear properties of an rf-SQUID based metasurface", *Physical Review B* **99**, 075401 (2019)

Submitted scientific publications

7. G. Ptitcyn, A. G. Lamprianidis, T. Karamanos, V. S. Asadchy, R. Alaee, M. M. Müller, M. Albooyeh, M. S. Mirmoosa, S. Fan, S. A. Tretyakov, and C. Rockstuhl, "Floquet-Mie Theory for Time-Varying Dispersive Spheres", *under review in Laser & Photonics Reviews* (2022)

Conference contributions

1. M. M. Müller, J. Oppermann, J. Straubel, K. Słowik, and C. Rockstuhl, "A novel second quantization scheme for open and dissipative nanophotonics", oral presentation at *Quantum Nanophotonics*; Benasque, Spain, March 2019

2. M. M. Müller, B. Maier, C. Rockstuhl, and M. Hochbruck, "Interaction of an rf-SQUID metasurface with electromagnetic waves", oral presentation at *OPTO*; Toruń, Poland, July 2019

3. M. M. Müller, M. Kosik, K. Słowik, and C. Rockstuhl, "Nonlinear effects in hybrid graphene nanoantenna quantum emitter systems", oral presentation at *Graphene and Co Annual Meeting 2019*; Bad Herrenalb, Germany, October 2019

4. M. M. Müller, M. Kosik, M. Pelc, A. Ayuela, C. Rockstuhl, and K. Słowik, "Co-existence of tunable plasmons and excitons in graphene nanoantennas", poster at *Nanolight*; Benasque, Spain, March 2020

5. M. M. Müller, M. Kosik, M. Pelc, G. W. Bryant, A. Ayuela, C. Rockstuhl, and K. Słowik, "Energy-based plasmonicity index (EPI) for nanooptical resonances", poster at *Quantum Nanophotonics (online)*; Benasque, Spain, March 2021

6. M. M. Müller, M. Kosik, M. Pelc, G. W. Bryant, A. Ayuela, C. Rockstuhl, and K. Słowik, "Sharpening the definition of nano-plasmons: The energy-based plasmonicity index (EPI)", poster at *Quantum Optics X*; Toruń, Poland, September 2021

7. M. M. Müller, M. Kosik, M. Pelc, G. W. Bryant, A. Ayuela, C. Rockstuhl, and K. Słowik, "Tuning the Optical Response of Molecular Chains with Adatoms", poster at *Nanolight*; Benasque, Spain, March 2022

1 | Introduction

Plasmonic modes in classical systems hosting free charge carriers are characterized by the collective oscillation of this charge carrier cloud across the entire system. Despite the fact that nanoplasmonics is a rather young scientific discipline, many of its achievements already found their way into applications, and numerous technological devices contain nanoplasmonic components [1–3]. Among scientific applications, we find plasmonic metamaterials [4, 5], plasmonic single photon sources [6, 7], plasmonic photodetectors [8–12], and sensing tools [13–15], as well as many more other functional devices harnessing plasmonic effects [16–22]. Even in cancer therapy, plasmonic nanoparticles aid to direct electromagnetic energy to regions of the human body where malignant tissue is to be combated [23–25]. Through recent progresses concerning available simulation techniques for nanoscale systems and their fabrication processes, plasmonics experienced a boost even deeper into the nanoscale [20, 26–31].

For decades, the noble metals such as gold or silver have been the most attractive materials for plasmonic applications. In 2004, Novoselov and Geim first succeeded in fabricating thin graphitic films [32] after it has long been believed that such thin two-dimensional (2D) crystals cannot exist [33, 34]. Shortly afterwards, this achievement earned them the Nobel prize in 2010 "for groundbreaking experiments regarding the two-dimensional material graphene" [35]. The subsequent developments in the fabrication of so-called *Van der Waals* heterostructures in general [36] and nanostructured graphene in particular [37, 38] made it possible to harness their extraordinary optical properties, and graphene conquered the field of nanoplasmonics as well. In that process, plasmonic effects in these novel materials were investigated thoroughly both experimentally [39–42] and theoretically [22, 43–48]. The reason for the emerging paramount interest in graphene plasmons were, on the one hand, their much longer lifetimes and higher spatial confinement as compared to the ones in noble metals [49, 50]. On the other hand, electrical gating or optical pumping enables to manipulate the conductivity of graphene and, hence, its absorption even after the sample with a given size and geometry has been fabricated. This renders it a perfect candidate for applications in *tunable* nanoplasmonics [22, 42, 49, 51]. For example, adding already one electron to a graphene nanoantenna can switch additional infrared modes on and off [45].

For nanoantennas with a size below $10\,\mathrm{nm}$, it is necessary to describe its optical response within a quantum mechanical approach rather than by employing classical homogeneous material parameters in the realm of electrodynamics [44, 45, 52, 53]. The method of choice for the theoretical description of the electronic properties of extended 2D graphene is the *tight binding* (TB) model [54]. Fortunately, also *finite* graphene nanoantennas are well-described by this computationally relatively cheap numerical technique such that we do not need to apply more costly *ab initio* approaches like density functional theory (DFT). Direct comparisons between TB and DFT have turned out to yield surprisingly consistent results. Therefore, the huge overhead in computational cost of DFT can-

not be justified in the case of graphene nanostructures [55–58]. The *Su-Schrieffer-Heeger* (SSH) model constitutes an application of the TB approach to one-dimensional systems. It is capable of modeling the electronic, optical, and transport properties of linear carbon molecules, and was extensively studied within the past four decades [59–71]. Although it offers interesting topological characteristics as well [59, 64, 72–75], we concentrate on the conceptual insights that it provides into the formation of resonances in this thesis. In particular, the polyene and polyacetylene chains treated within the SSH model can be viewed as very simple model examples for metallic and insulating molecular species, respectively [76–78, A1, A2]. Based on the above-mentioned TB approach, Thongrattanasiri *et al.* [44] presented a computational framework for nanoplasmonics in 2012 to obtain the optical properties of graphene nanoantennas within a random-phase approximation frequency-domain model, and continued to further develop the approach [45, 79–81]. Shortly afterwards, a *time-domain* extension to also capture nonlinear effects was introduced by Cox and García de Abajo in 2014 [47]. In this thesis, we will rely on the latter approach.

As the TB method is conceptually rather easy to access, it is further developed in this thesis to describe also more complex hybrid systems that consist of a plasmonic nanoantenna coupled to a quantum emitter. Such systems are traditionally treated within the *Purcell*, approach [82] describing the *optical* interaction of a photonic structure coupled to a nearby quantum emitter, *e.g.*, an atom, molecule [83–85], artificially constructed quantum dot [86–89], or an optically active impurity in a solid such as a nitrogen-vacancy-center in diamond [90–93]. The decay of the excited quantum emitter is accompanied by the release of a photon with a certain decay rate. This decay rate, or also its *Rabi* oscillation frequency, may be controlled by the photonic structures nearby, for example by the presence of plasmonic nanocavities [94, 95], photonic crystals [96, 97] – or by plasmonic nanoantennas [98, 99] like graphene nanostructures. The above interaction mechanism is purely optical in nature and does not consider a possible charge transfer from the emitter to the photonic structure and vice versa. However, for the formation of the optical modes of plasmonic dimer antennas, it has been shown that charge transfer between the two constituents of the dimer plays a crucial role [100–109]. But so far, the electronic tunneling between the quantum emitter and the plasmonic antenna has been neglected. To bridge this gap – in the truest sense of the word – we present a simulation framework that takes into account simultaneously the optical and the electronic coupling channels. Within the TB approach utilized in this thesis, it is conceptually straight-forward to include charge transfer from the antenna to the emitter itself, which occurs for separations in the order of a few Ångströms or at most nanometers. In literature, we find approaches to couple adsorbed atoms (*adatoms*) to extended 2D graphene [110–113]. Here, we concentrate on the treatment of coupling adatoms to *finite* graphene structures. We predominantly aim to identify which system parameters modify the structure's optical response the most, if altered.

But it is not just in the interaction to an adatom where quantum effects necessarily need to be considered. Already when miniaturizing a plasmonic antenna, finite-size quantum effects become apparent and deserve a proper treatment. In particular, the continuous energy bands of an infinite solid discretize and transform into discrete energy levels characteristic for molecules. However, not only the states themselves, but also the optical excitation mechanisms undergo a discretization process at the same time. In quantum mechanical systems, we can distinguish between a single-particle-like and plasmonic mode. The former consists of a single electron that jumps from an initial state $|i\rangle$ with energy E_i to a final state $|f\rangle$ with energy E_f upon absorbing a photon with energy $\hbar\omega = E_f - E_i$. The latter emerges in a more complex collective dynamics involving also *Coulomb* inter-

action between potentially a whole set of involved electrons. However, the passage is rather fluent.

Accordingly, as fluent is the concept of plasmons in nanoscale systems in literature. There is already a huge body of literature on the issue of how to define plasmonic response in the quantum realm. However, we do not see any convincing definition of a plasmon in nanoscale systems that would be universally valid. Among previous approaches are quantitative measures as well as computational procedures to decide on the nature of an optical mode in the absorption spectrum. Most of them rely on the induced charge distribution of the mode in real space [114, 115], on the number of single-particle transitions that make up the mode in a single-particle picture [116, 117], or on combinations thereof [118–120]. Also, there is a computationally expensive *Coulomb* energy-based approach that requires a whole set of simulations with gradually increasing electron-electron interaction strengths [121, 122]. Moreover, Townsend and Bryant observed in DFT simulations that the electron dynamics in energy space exhibits either of two qualitatively different behaviors – oscillatory *sloshing* or monotonous *inversion* characteristics [123–125]. Yet, literature misses a handy, easy-to-interpret index that quantifies these energy-space characteristics. To that end, it is at the heart of this work to establish the *energy-based plasmonicity index* (EPI) [A1, A3, A4]. It allows to assess if a mode is plasmonic in the sense of Townsend and Bryant, *i.e.*, that its existence cannot be explained by the non-interacting energy landscape of the structure but only if one takes into account electron-electron interaction as well. To that end, we capitalize on the conceptually simple SSH chains with known electronic nature, and on the possibility to engineer the absorption cross-section of graphene nanoantennas by a suitable doping. With this turning knob, molecular structures that simultaneously support single-particle-like modes and plasmonic ones can be readily created and studied in detail.

Structure of the Thesis

This thesis is divided into nine chapters. After introducing the reader to the topics and problems to be solved in the first chapter, the second chapter recalls the basic theory of electrodynamics in general and the field of nanoplasmonics in particular.

The third chapter addresses the basic physical properties of graphene in the context of optics. We start with the atomic and crystalline structure of extended two-dimensional graphene and shortly review classical graphene plasmonics. Then, we proceed in determining its unique electronic and optical properties within a quantum mechanical tight binding approach.

In the fourth chapter, we introduce a tight binding-based framework to determine the electronic structure of *finite* carbon-based molecules. Before we shortly discuss graphene nanoantennas, we investigate in particular the *Su-Schrieffer-Heeger* chains as prototypical examples of metallic, insulating, and topologically insulating molecular species.

The fifth chapter establishes a time-domain simulation framework based on the previously introduced tight binding model. It is capable of describing the nonlinear electronic dynamics in the nanostructures both in real space and in energy space. From that, induced dipole moments, state population dynamics, and absorption cross-sections can be obtained, for instance.

The sixth chapter deals with an extension of the tight binding approach to hybrid systems that comprise a nanoantenna and an adsorbed foreign impurity atom, acting as a quantum emitter, and treated as a two-level system. We analyze in detail how the electronic and optical properties of the *Su-Schrieffer-Heeger* chains and the two-level system

are modified upon coupling them, and which system parameters are crucial to engineer these modifications.

The seventh chapter reviews different approaches in literature to characterize optical modes in nanostructures. In particular, they aim to tell apart modes that intrinsically belong to *single-particle-like* transitions from those that are *plasmonic* in nature.

In the eighths chapter, we present the energy-based plasmonicity index, our own contribution to the field, to quantify how plasmonic a resonance is in a nanostructure. Contrary to most of the approaches presented in Ch. 7, it relies on the energy-space electron dynamics in the system.

The thesis concludes with the ninth chapter, in which we briefly summarize our findings and provide an outlook for future research to be done along similar lines.

2 | Plasmonics in Nanostructures

2.1 Introduction

When light with a suitable frequency interacts with a finite-sized metallic nanoparticle – a gold sphere for instance –, mobile conduction band electrons in the nanoparticle may be coherently excited. Driven by the external electric field $\mathbf{E}_{\mathrm{ext}}$, the electron cloud performs a collective oscillation stretched across the entire particle relative to the static ionic cores of the host material's atoms. This charge separation effectively induces a dipole moment, which generates an electric field $\mathbf{E}_{\mathrm{ind}}$. The induced electric field is characterized by typical features in the near-, intermediate, and far-field of an electric dipole. The strength of the induced dipole can be driven into resonance by a suitable combination of shape and material making up the nanoparticle, as well as by the choice of the incident field. The quasiparticles that are associated with the quantized hybrid excitations of such charge density oscillations and photons are called *localized surface plasmon polaritons* and introduced in Sec. 2.7.[1]

Plasmonic excitations in nanoparticles confine electromagnetic energy into subwavelength volumes. Close to the edges or tips of the underlying plasmonic particle's geometry, the electric fields of the incident laser beam may easily be enhanced by orders of magnitude [21, 26, 126, 127]. Thus, the nanostructure acts as an *antenna* that produces an induced electric near field that can surpass the external excitation field by far. By this means, physical processes that are sensitive to this total electric field $\mathbf{E}_{\mathrm{total}} = \mathbf{E}_{\mathrm{ext}} + \mathbf{E}_{\mathrm{ind}}$ in their environment can be engineered. But also the opposite direction is viable. The electric field of a photon that is released when an excited quantum emitter decays in the close vicinity of the antenna can be picked up by the antenna and converted into far field radiation, for instance. Hence, plasmonic nanoparticle antennas are perfect objects to convey electromagnetic energy from the macroscopic to the nanoscopic world, and vice versa.

Metallic nanoparticles and plasmonic metasurfaces built from them have been the workhorses for fundamental advances in plasmonics and functional devices in subwavelength optics within the last decades [16–22]. Especially with the recent emergence of cutting-edge fabrication procedures for nanostructures and the advent of accurate simulation frameworks for molecular structures, the field of plasmonics experienced a boost into the nanoscale [20, 26–31]. Substantial advances both on the experimental and on the theoretical side paved the way for a golden age of plasmonics on the nanoscale and subwavelength optics in general. Prime examples of successful applications of plasmonic nanoparticles can be found in plasmon-assisted frequency conversion such as higher har-

[1] Besides the *localized* surface plasmon polaritons that have been described above, there exist also *propagating* surface plasmon polaritons. However, in this thesis, we are not concerned with propagating plasmons that travel along the interface of a dielectric and a metal, for instance. Therefore, we do not specifically introduce their phyiscal concept.

monic generation [128–130], in plasmonic sensing [13–15], and in photothermal medicine such as cancer therapy [23–25]. Also plasmon-based functional devices like plasmonic metamaterials [4, 5], single photon sources [6, 7], and plasmonic photodetectors [8–12] show the broad scope of utility of nanoplasmonics in applied sciences. Besides metallic nanoparticles, further basic building blocks of nanooptical functional devices are single quantum emitters such as artificial quantum dots [86–89] and small molecules [83–85], or optically active impurities in solids (nitrogen-vacancy-centers in diamond for example) [90–93]. This work specifically aims at understanding and characterizing plasmonic modes in small carbon-based optically active molecules.

In this chapter, we aim to introduce the basic principles of classical electrodynamics and the interaction of electromagnetic fields with matter in the context of nanoplasmonics as far as we need them for the purpose of this thesis. We begin with *Maxwell*'s equations in Sec. 2.2 before we move on to the wave equations of propagating waves in Sec. 2.3. To get hands on the description of plasmonic materials in nanophotonics and their emission characteristics, we introduce the *Drude* model of metals in Sec. 2.4 and the emission properties of accelerated charges in Sec. 2.5. Finally, in Sec. 2.6, we introduce the nonlinear optical mechanism of second harmonic generation, and close this chapter with the introduction of localized surface plasmon polaritons in Sec. 2.7.

2.2 Classical Electrodynamics: *Maxwell*'s Equations

Maxwell's equations are four coupled partial differential equations that describe the fundamental fields in the classical electrodynamic theory of light.

Maxwell's Equations in Time Domain

In time domain and space, *Maxwell*'s equations can be written as [131]

$$\nabla \times \mathbf{E}(\mathbf{r},t) = -\frac{\partial \mathbf{B}(\mathbf{r},t)}{\partial t}, \tag{2.1a}$$

$$\nabla \times \mathbf{H}(\mathbf{r},t) = \frac{\partial \mathbf{D}(\mathbf{r},t)}{\partial t} + \mathbf{j}_{\mathrm{tot}}(\mathbf{r},t), \tag{2.1b}$$

$$\nabla \cdot \mathbf{D}(\mathbf{r},t) = \rho_{\mathrm{ext}}(\mathbf{r},t), \tag{2.1c}$$

$$\nabla \cdot \mathbf{B}(\mathbf{r},t) = 0. \tag{2.1d}$$

Here, $\mathbf{E}(\mathbf{r},t)$ denotes the electric field, $\mathbf{H}(\mathbf{r},t)$ the magnetizing field, $\mathbf{D}(\mathbf{r},t)$ is the electric displacement, and $\mathbf{B}(\mathbf{r},t)$ the magnetic field. Moreover, the external electric charge density $\rho_{\mathrm{ext}}(\mathbf{r},t)$ and the total current density $\mathbf{j}_{\mathrm{tot}}(\mathbf{r},t)$ constitute the sources of electric and magnetic fields, respectively. Introducing the polarization $\mathbf{P}(\mathbf{r},t)$ and magnetization $\mathbf{M}(\mathbf{r},t)$, that describe the electric and magnetic response of media to electromagnetic fields, we may relate the electric displacement and the electric field as well as the magnetic field and the magnetizing field by the *constitutive relations*

$$\mathbf{D}(\mathbf{r},t) = \varepsilon_0 \mathbf{E}(\mathbf{r},t) + \mathbf{P}(\mathbf{r},t), \tag{2.2a}$$

$$\mathbf{B}(\mathbf{r},t) = \mu_0 \mathbf{H}(\mathbf{r},t) + \mathbf{M}(\mathbf{r},t). \tag{2.2b}$$

The constants ε_0 and μ_0 are the permittivity and permeability of free space, respectively, obeying $\varepsilon_0 \mu_0 c_0^2 = 1$ with the speed of light in free space c_0. Throughout this thesis, and in the field of optics in general, we assume the absence of external free charge carriers,

$\rho_{\text{ext}}(\mathbf{r},t) = 0$. Moreover, we may assume that all media under consideration are *non-magnetic*, $\mathbf{M}(\mathbf{r},t) = 0$, and, therefore, the magnetizing field and the magnetic field are proportional, which allows us to omit one of the two.

The polarization field $\mathbf{P}(\mathbf{r},t)$, on the contrary, is one of the two crucial auxiliary fields in optics to encounter material properties. It quantifies the response of charge carriers that are bound to the ionic atomic cores of a medium to a stimulating external electric field, $\mathbf{P} = f_P\{\mathbf{E}\}$, typically in dielectrics. In principle, the operation f_P can be of rather complicated form

$$\mathbf{P}(\mathbf{r},t) = \int_{\mathbb{R}^3} \mathrm{d}^3\mathbf{r}' \int_{-\infty}^{t} \mathrm{d}t'\, R_p(\mathbf{r},\mathbf{r}',t,t')\mathbf{E}(\mathbf{r}',t'), \tag{2.3}$$

with a potentially nonlocal and dispersive response kernel tensor $R(\mathbf{r},\mathbf{r}',t,t')$ that characterizes the medium under consideration.

Unbound charge carriers like mobile electrons, as we find them in metals, contribute to the conduction and can be driven by the electric field as well. They are described by the conduction current density $\mathbf{j}_{\text{cond}} = f_j\{\mathbf{E}\}$, which is part of the total current density $\mathbf{j}_{\text{tot}}(\mathbf{r},t) = \mathbf{j}_{\text{cond}}(\mathbf{r},t) + \mathbf{j}_{\text{ext}}(\mathbf{r},t)$ in Eq. (2.1b). External current densities $\mathbf{j}_{\text{ext}}(\mathbf{r},t)$ are assumed to vanish in the field of optics, such that $\mathbf{j}_{\text{tot}}(\mathbf{r},t) = \mathbf{j}_{\text{cond}}(\mathbf{r},t)$. Similar to the polarization field, the conduction current density is related to the electric field *via* an operation f_j of a conduction response kernel R_j and the electric field in a supposedly rather complicated way. To be able to continue further analytically, we consider *homogeneous* materials. Then, the response kernels are of the form $R_{p,j}(\mathbf{r},\mathbf{r}',t,t') = R_{p,j}(\mathbf{r}-\mathbf{r}',t-t')$ and the operations $f_{p,j}$ constitute *convolutions*. Under *Fourier* transformations, convolutions transform to simple products and, therefore, material properties are discussed in frequency domain below.

Maxwell's Equations in Frequency Domain

Unless explicitly stated otherwise in later chapters, it is assumed in this work that the dependencies between the material response and the evoking electromagnetic fields are *linear*, such that the individual frequency components of the fields do not interact with each other. Then, the fields can be expanded into a *Fourier* series

$$\mathbf{E}(\mathbf{r},t) = \int \mathrm{d}\omega\, \tilde{\mathbf{E}}(\mathbf{r},\omega)\mathrm{e}^{-\mathrm{i}\omega t} \quad \text{and} \quad \tilde{\mathbf{E}}(\mathbf{r},\omega) = \frac{1}{2\pi}\int \mathrm{d}t\, \mathbf{E}(\mathbf{r},t)\mathrm{e}^{\mathrm{i}\omega t}, \tag{2.4}$$

and accordingly for all other fields. The set of equations (2.1a)-(2.1d) in the field of linear optics then transforms to

$$\nabla \times \tilde{\mathbf{E}}(\mathbf{r},\omega) = \mathrm{i}\omega\mu_0\tilde{\mathbf{H}}(\mathbf{r},\omega), \tag{2.5a}$$
$$\nabla \times \tilde{\mathbf{H}}(\mathbf{r},\omega) = -\mathrm{i}\omega\tilde{\mathbf{D}}(\mathbf{r},\omega) + \tilde{\mathbf{j}}_{\text{cond}}(\mathbf{r},\omega), \tag{2.5b}$$
$$\nabla \cdot \tilde{\mathbf{D}}(\mathbf{r},\omega) = 0, \tag{2.5c}$$
$$\nabla \cdot \tilde{\mathbf{H}}(\mathbf{r},\omega) = 0, \tag{2.5d}$$

where the magnetic field $\tilde{\mathbf{B}}(\mathbf{r},\omega) = \mu_0\tilde{\mathbf{H}}(\mathbf{r},\omega)$ has been eliminated. The discussion in this introduction shall be limited to *local* materials, which is a good approximation for most natural materials at optical frequencies. However, when going down to the nanometer scale, nonlocal effects become important also in the field of plasmonics for small metallic particles [132, 133] and molecules like graphene nanoantennas [44] that this thesis deals

with mostly. Therefore, the quantum mechanical approach introduced in Ch. 5 accounts for the finite size of the simulated structures. The material response in frequency domain is described as

$$\tilde{\mathbf{D}}(\mathbf{r},\omega) = \varepsilon_0\varepsilon(\mathbf{r},\omega)\tilde{\mathbf{E}}(\mathbf{r},\omega), \tag{2.6a}$$

$$\tilde{\mathbf{j}}_{\mathrm{cond}}(\mathbf{r},\omega) = \sigma(\mathbf{r},\omega)\tilde{\mathbf{E}}(\mathbf{r},\omega), \tag{2.6b}$$

where $\varepsilon(\mathbf{r},\omega)$ and $\sigma(\mathbf{r},\omega)$ are the dielectric function and the conductivity, describing the response of bound and unbound electronic charge carriers in the host medium, respectively.

2.3 The Wave Equations

For electromagnetic waves propagating in a homogeneous medium, we can formulate the wave equations. With the additional assumption that the electric field is free of divergence, $\nabla \cdot \mathbf{E}(\mathbf{r},t) = 0$ and $\nabla \cdot \tilde{\mathbf{E}}(\mathbf{r},\omega) = 0$, the identity $\nabla \times \nabla \times = -\nabla^2$ holds for both fields, $\mathbf{E}(\mathbf{r},t)$ and $\tilde{\mathbf{E}}(\mathbf{r},\omega)$. Moreover, we continue to restrict ourselves to the field of optics, where the magnetization field of the media under consideration and all external sources vanish.

Time Domain

In time domain, we obtain the wave equation by applying the curl operator to Eq. (2.1a), replace the magnetizing field through Eq. (2.1b), and the displacement field through Eq. (2.2a). We arrive at

$$\begin{aligned} \nabla \times \nabla \times \mathbf{E}(\mathbf{r},t) &= -\mu_0 \frac{\partial}{\partial t}\left(\frac{\partial}{\partial t}(\varepsilon_0\mathbf{E}(\mathbf{r},t) + \mathbf{P}(\mathbf{r},t)) + \mathbf{j}_{\mathrm{cond}}(\mathbf{r},t)\right), \\ \left(\nabla^2 - \frac{1}{c_0^2}\frac{\partial^2}{\partial t^2}\right)\mathbf{E}(\mathbf{r},t) &= \mu_0 \frac{\partial^2 \bar{\mathbf{P}}(\mathbf{r},t)}{\partial t^2}, \end{aligned} \tag{2.7}$$

where we introduced a generalized polarization $\bar{\mathbf{P}}(\mathbf{r},t)$ through

$$\bar{\mathbf{P}}(\mathbf{r},t) = \mathbf{P}(\mathbf{r},t) + \int_{-\infty}^{t} \mathbf{j}_{\mathrm{cond}}(\mathbf{r},t')\mathrm{d}t'. \tag{2.8}$$

It combines the response of both bound and unbound charges in the medium in a single quantity. Interesting to note here is that Eq. (2.7) exhibits a source term on the right hand side. It refers to the possibility that electric fields can be introduced into the system which stem from the material response characterized through the generalized polarization $\bar{\mathbf{P}}(\mathbf{r},t)$. In particular, this happens in *nonlinear* media and is discussed below in Sec. 2.6.

Frequency Domain

To obtain the wave equation in frequency domain, we begin similarly to the approach in the time domain. We apply the curl operator to Eq. (2.5a), eliminate therein the magnetizing field through Eq. (2.5b), the displacement field through Eq. (2.6a), and the conduction current density through Eq. (2.6b). Thus, the wave equation in frequency domain for an electric field that propagates through a homogeneous medium reads

$$\begin{aligned} \nabla \times \nabla \times \tilde{\mathbf{E}}(\mathbf{r},\omega) &= \mathrm{i}\omega\mu_0\left(-\mathrm{i}\omega\varepsilon_0\varepsilon(\omega)\tilde{\mathbf{E}}(\mathbf{r},\omega) + \sigma(\omega)\tilde{\mathbf{E}}(\mathbf{r},\omega)\right), \\ \left(\nabla^2 + \frac{\omega^2}{c_0^2}\bar{\varepsilon}(\omega)\right)\tilde{\mathbf{E}}(\mathbf{r},\omega) &= 0, \end{aligned} \tag{2.9}$$

where the generalized dielectric function

$$\bar{\varepsilon}(\omega) = \varepsilon(\omega) + \frac{\mathrm{i}}{\omega\varepsilon_0}\sigma(\omega) \tag{2.10}$$

has been defined, combining again the response of bound and unbound charges in the medium. Please note that working in frequency domain already implies *linearity*, such that Eq. (2.9) does not exhibit any source terms.

Finding the exact form of $\bar{\varepsilon}(\omega)$ is as complicated as it is crucial to determine the optical response of materials. The solution to this important problem cannot be found within *Maxwell*'s theory of electromagnetic fields, but we rather need to harness condensed matter theory. Theoretically, the polarization and the currents induced by an electric field must be found by solving a complex many-body problem taking into account all mutual forces that act between the involved electrons and nuclei. In practice, phenomenological approaches have proven to be surprisingly accurate in describing the main features that are observed in optical experiments. In the next section, a rather simple method to model plasmonic materials will be presented.

2.4 The *Drude* Model of Metals

A simple yet powerful phenomenological approach to model the optical properties of metals constitutes the *Drude* model of the free electron gas. It may be applied to a whole class of materials that host electronic charge carriers, which are *not bound* to their ionic cores and can move relatively freely inside a 3D bulk material or a 2D conductive sheet, as in the case of graphene. The dynamics of a single particle in such a free electron cloud is governed by the equation of motion

$$\frac{\partial^2}{\partial t^2}\mathbf{x}(\mathbf{r},t) + \gamma\frac{\partial}{\partial t}\mathbf{x}(\mathbf{r},t) = -\frac{e}{m_e}\mathbf{E}(\mathbf{r},t), \tag{2.11}$$

where $\mathbf{x}$ is the displacement of the electron with respect to its host atom, e and m_e are the electronic charge and its effective mass, respectively, and γ is a phenomenological damping parameter. It embraces all effects that lead to energy loss, like electron-electron collisions or phonon-creation processes, for instance. The equation of motion is the differential equation of a driven harmonic oscillator without restoring force; with the electric field on the right hand side of Eq. (2.11) as the driving force. Assuming a time-harmonic excitation at frequency ω and substituting the displacement according to the definition of the current density of an electron gas with density n, $\mathbf{j}(\mathbf{r},t) = -ne\dot{\mathbf{x}}(\mathbf{r},t)$, we obtain

$$\tilde{\mathbf{j}}(\mathbf{r},\omega) = \frac{ne^2}{m_e}\frac{1}{\gamma - \mathrm{i}\omega}\tilde{\mathbf{E}}(\mathbf{r},\omega) = \sigma_{\mathrm{Dr}}(\omega)\tilde{\mathbf{E}}(\mathbf{r},\omega). \tag{2.12}$$

We can identify the *Drude* conductivity in Eq. (2.12) and also define the generalized dielectric function of the *Drude* model based on Eq. (2.10)

$$\sigma_{\mathrm{Dr}}(\omega) = \frac{\mathrm{i}\varepsilon_0\omega_p^2}{\omega + \mathrm{i}\gamma}, \qquad \bar{\varepsilon}_{\mathrm{Dr}}(\omega) = \varepsilon(\omega) - \frac{\omega_p^2}{\omega^2 + \mathrm{i}\gamma\omega}, \tag{2.13}$$

where the plasma frequency

$$\omega_p = \sqrt{\frac{ne^2}{m\varepsilon_0}} \tag{2.14}$$

is a function of the electron density n in the system only. In the lossless case ($\gamma = 0$), the conductivity is purely imaginary and the dielectric function purely real. Whereas the real part of the generalized dielectric function quantifies dispersion in the medium, the imaginary part refers to absorption.

2.5 Emission Spectra of Accelerated Charges

Charged particles that are accelerated in an external electric field, in turn, radiate electromagnetic energy, known as *bremsstrahlung*. The radiated power emitted by N_p accelerated particles with masses m_i and charges q_i can be determined with the *Larmor* formula [131]

$$P(t) = \frac{1}{6\pi\varepsilon_0 c_0^3} \sum_{i=1}^{N_p} q_i |\ddot{\mathbf{r}}_i(t)|^2, \tag{2.15}$$

where $\ddot{\mathbf{r}}_i$ is the acceleration of the i-th particle. One can naively generalize this equation to time-varying currents $\mathbf{j}(\mathbf{r},t)$ that are formed by accelerated continuous charge densities $\rho(\mathbf{r},t)$ with $\mathbf{j}(\mathbf{r},t) = \dot{\mathbf{r}}\rho(\mathbf{r},t)$. The dipole moments that are associated with these charge densities can be determined with $\mathbf{p}(\mathbf{r},t) = \int_V \mathrm{d}^3\mathbf{r}'\rho(\mathbf{r}',t)\,(\mathbf{r}-\mathbf{r}')$, where $V \in \mathbb{R}^3$ is a small volume far away from the observation point $\mathbf{r}$, into which the charge density is confined. With that, we can rewrite Eq. (2.15) for our needs and, subsequently, move to *Fourier* domain to obtain the emission intensity [134]

$$I(\omega) = \frac{1}{6\pi^2\varepsilon_0 c_0^3} \left| \int \mathrm{d}t\, \ddot{\mathbf{p}}(t) \mathrm{e}^{\mathrm{i}\omega t} \right|^2 = \frac{\omega^4}{6\pi^2\varepsilon_0 c_0^3} |\tilde{\mathbf{p}}(\omega)|^2. \tag{2.16}$$

The last equality in the above equation holds only for time-harmonic dipole moments. However, also if this is not the case, the emission spectrum is still proportional to the square of the *Fourier* components of the dipole moment, $I(\omega) \propto |\tilde{\mathbf{p}}(\omega)|^2$. The latter has been exploited in the context of higher-harmonic generation in a hybrid system comprised of a metallic spherical nanoparticle and a quantum emitter in Ref. [135] before. Thus, to investigate nonlinear effects such as higher harmonic generation in Ch. 5, we will rely on Eq. (2.16).

2.6 Nonlinear Optics

It was believed for a very long time that the interaction of light with matter and light propagation through media according to Eq. (2.9), for instance, are *linear* processes. In other words, this means that the material parameters that relate the electric field amplitude $\mathbf{E}$ and the material response such as the generalized polarization field $\bar{\mathbf{P}}$ in Eq. (2.8) do not depend on the input power. Not until the 1960s, when the first lasers were operated, this belief had to be revised, and higher harmonics were observed in an optical experiment [136]. The consequences of this discovery were groundbreaking: The optical properties of media depend in general on the light input intensity. Also, the frequency of a light pulse that passes through a medium may in general be altered by the interaction with the medium. And most excitingly, in a nonlinear medium, photons can interact with each other and, consequently, light can be used to manipulate light. In this thesis, *frequency conversion processes* for strong laser fields will be observed when interacting with carbon nanostructures. Thus, we shortly introduce their theory here.

For illustration purposes, to exclusively concentrate on the effect of (non)linearity, we consider a homogeneous, isotropic, and *nondispersive* medium here. For **linear** media, we then have $\bar{\mathbf{P}}(\mathbf{r},t) = \varepsilon_0\eta^{(1)}\mathbf{E}(\mathbf{r},t)$ with a constant of proportionality $\eta^{(1)}$. In that case, Eq. (2.7) simplifies to

$$\left(\nabla^2 - \frac{1+\eta^{(1)}}{c_0^2}\frac{\partial^2}{\partial t^2}\right)\mathbf{E}(\mathbf{r},t) = 0, \tag{2.17}$$

and, consequently, the source term on the right hand side of Eq. (2.7) vanishes. Hence, the additional assumption of linearity allows to apply the principles of linear optics, such as the linear superposition of solutions of *Maxwell*'s equations, the conservation of the frequency of light when it passes through a medium, the inability of photons to interact with each other, and many more.

In **nonlinear** media, on the other hand, the ith component of the generalized polarization field with $i \in \{x, y, z\}$ is obtained through [137]

$$\begin{aligned}\bar{P}_i(\mathbf{r},t) &= \varepsilon_0 \eta^{(1)} E_i(\mathbf{r},t) + \bar{P}_i^{\mathrm{NL}}(\mathbf{r},t) \\ &= \varepsilon_0 \eta^{(1)} E_i(\mathbf{r},t) + \eta^{(2)} E_i^2(\mathbf{r},t) + \eta^{(3)} E_i^3(\mathbf{r},t) + ...\end{aligned} \tag{2.18}$$

Here, $\bar{P}^{\mathrm{NL}}(\mathbf{r},t)$ denotes the nonlinear part of the generalized polarization field, and the parameters $\eta^{(2)}$ and $\eta^{(3)}$ quantify the strength of second-order and third-order nonlinear optical effects, respectively. In homogeneous, isotropic, nondispersive, and nonlinear media, the wave equation in time domain, Eq. (2.7), for an arbitrary component $i \in \{x, y, z\}$ of the electric field $\mathbf{E}(\mathbf{r},t)$ becomes

$$\left(\nabla^2 - \frac{1+\eta^{(1)}}{c_0^2}\frac{\partial^2}{\partial t^2}\right) E_i(\mathbf{r},t) = \mu_0 \frac{\partial^2}{\partial t^2}\left(\eta^{(2)} E_i^2(\mathbf{r},t) + \eta^{(3)} E_i^3(\mathbf{r},t) + ...\right), \tag{2.19}$$

where the right hand side contains only nonlinear terms in $\mathbf{E}(\mathbf{r},t)$. These terms may be perceived as radiating sources, being evoked by the electric field itself through its interaction with the nonlinear medium.

In our discussion on nonlinear effects in Ch. 5, we will investigate molecular species of various symmetries. It turns out that the symmetry of a system is crucial in determining which nonlinear effects can occur. In centrosymmetric systems, for instance, the function $\bar{\mathbf{P}}(\mathbf{E})$ must be *odd*, such that $\bar{\mathbf{P}} \to -\bar{\mathbf{P}}$ if we flip the direction of the incident electric field, $\mathbf{E} \to -\mathbf{E}$. This is only possible for $\eta^{(2)} = 0$, such that in systems with inversion symmetry, the lowest-order nonlinear effect is of third order.

Second Harmonic Generation

As an example of a nonlinear optical effect, we want to discuss second harmonic generation (SHG) in more detail here, which is a second-order effect. We, therefore, have a look at the term proportional to $\eta^{(2)}$ in Eq. (2.19) and neglect all other nonlinear terms,

$$\begin{aligned}\bar{P}_i^{\mathrm{NL}}(\mathbf{r},t) = \eta^{(2)} E_i^2(\mathbf{r},t) &= \eta^{(2)}\left[\mathrm{Re}\left(\int \mathrm{d}\omega\, \tilde{E}_i(\mathbf{r},\omega)\mathrm{e}^{-\mathrm{i}\omega t}\right)\right]^2 \\ &= \frac{\eta^{(2)}}{4}\int \mathrm{d}\omega \int \mathrm{d}\tilde{\omega}\left(\tilde{E}_i(\mathbf{r},\omega)\mathrm{e}^{-\mathrm{i}\omega t} + \tilde{E}_i^*(\mathbf{r},\omega)\mathrm{e}^{\mathrm{i}\omega t}\right)\left(\tilde{E}_i(\mathbf{r},\tilde{\omega})\mathrm{e}^{-\mathrm{i}\tilde{\omega} t} + \tilde{E}_i^*(\mathbf{r},\tilde{\omega})\mathrm{e}^{\mathrm{i}\tilde{\omega} t}\right) \\ &= \frac{\eta^{(2)}}{2}\,\mathrm{Re}\int \mathrm{d}\omega \int \mathrm{d}\tilde{\omega}\left(\tilde{E}_i(\mathbf{r},\omega)\tilde{E}_i(\mathbf{r},\tilde{\omega})\mathrm{e}^{-\mathrm{i}(\omega+\tilde{\omega})t} + \tilde{E}_i^*(\mathbf{r},\omega)\tilde{E}_i(\mathbf{r},\tilde{\omega})\mathrm{e}^{\mathrm{i}(\omega-\tilde{\omega})t}\right).\end{aligned} \tag{2.20}$$

Having a look at the radiated field component at frequency 2ω, that is associated with the field in Eq. (2.20) with $\omega = \tilde{\omega}$, from Eq. (2.19), we obtain

$$\mu_0 \eta^{(2)} \frac{\partial^2}{\partial t^2} E_i^2(\mathbf{r},t)\bigg|_{2\omega} \quad \longrightarrow \quad 2\mu_0 \omega^2 \eta^{(2)} \tilde{E}_i^2(\mathbf{r},\omega)\mathrm{e}^{-2\mathrm{i}\omega t}. \tag{2.21}$$

Thus, the nonlinear properties of the material, $\eta^{(2)} \neq 0$, leads to the emergence of an electric field oscillating with the second harmonic of the incident laser field frequency.

As outlined in Sec. 2.5, the emission intensity is proportional to the squared absolute value of the *Fourier* component of the dipole moment (or polarization field), such that $I_{\text{emission}}(2\omega) \propto \omega^4 \left(\eta^{(2)}\right)^2 |\tilde{\mathbf{E}}(\mathbf{r},\omega)|^4$, whereas the intensity of the incident laser is proportional to $|\tilde{E}_i(\omega)|^2$. Therefore, in the SHG process, the emission intensity is proportional to the square of both the nonlinear parameter $\eta^{(2)}$ and the input intensity,

$$I_{\text{emission}}(2\omega) \propto \left(\eta^{(2)} I_{\text{incident}}(\omega)\right)^2. \tag{2.22}$$

Similar considerations can explain the generation of even higher harmonics, when $\eta^{(n)} \neq 0$ with $I_{\text{emission}}(n\omega) \propto \left(\eta^{(n)} I_{\text{incident}}(\omega)\right)^n$.

2.7 Localized Surface Plasmon Polaritons

Chapters 7 and 8 of this thesis extensively discuss the nature and the characteristics of plasmonic modes in small molecular nanostructures. In particular, it is at the heart of this work to assess which properties of classical plasmons are conveyed into the quantum world and which ones arise as purely quantum mechanical features. In Ch. 5, we present a numerical framework to determine plasmonic modes in molecular nanostructures based on a *quantum mechanical* simulation method. To get familiar with the basic concepts of plasmons, we review the *classical* theory in this section.

Classical localized surface plasmon polaritons (SPPs) constitute modes of small metallic particles that are coupled to an incident electric field and surrounded by a dielectric medium. Other than propagating plasmons, SPPs can be excited by plane wave irradiation without any further sophisticated momentum matching considerations. The below deliberations follow the comprehensive text books of Maier [17] and Jackson [131].

To investigate the main characteristic features of SPPs, we consider the simplest system that supports SPPs, a homogeneous gold sphere with radius R and dielectric function $\varepsilon_{\text{gold}}(\omega)$, determined with the *Drude* model, for instance. It is located at $\mathbf{r} = \mathbf{r}_0$ and embedded into a dielectric of constant permittivity ε_c (for example vacuum with $\varepsilon_c = 1$) inside an electric field $\mathbf{E}_0(\mathbf{r},t) = \mathbf{E}_0(\mathbf{r}_0,t) = E_0\hat{\mathbf{e}}_z \mathrm{e}^{-\mathrm{i}\omega t}$, where $\hat{\mathbf{e}}_z$ is the unit vector in z-direction. It is legitimate to assume here that at any point in time, the external electric field is constant across the sphere, if $R << \lambda_0$, where λ_0 is the wavelength of the electric field in the surrounding dielectric. This assumption is the so-called *quasistatic approximation* and practically means that the discussion here is limited to nanoparticles with characteristic sizes below $\sim 100\,\text{nm}$.

Due to the high symmetry of the configuration, the corresponding *electrostatic* problem can be solved easily, and from that one can deduce the *dynamical* problem for the dipole SPP resonance. The electrostatic potential Φ that solves this configuration with $\mathbf{E} = -\nabla\Phi$ outside the sphere is found [17, 131] to be

$$\Phi(\mathbf{r}) = -E_0\mathbf{r}\cdot\hat{\mathbf{e}}_z + \frac{1}{4\pi\varepsilon_0\varepsilon_c}\frac{\mathbf{p}\cdot(\mathbf{r}-\mathbf{r}_0)}{|\mathbf{r}-\mathbf{r}_0|^3}, \tag{2.23}$$

which is the potential of the externally applied field and that of a dipole $\mathbf{p}$ at position $\mathbf{r}_0$ with dipole moment

$$\mathbf{p}(\omega) = 4\pi\varepsilon_0\varepsilon_c R^3 E_0\hat{\mathbf{e}}_z \frac{\varepsilon_{\text{gold}}(\omega)-\varepsilon_c}{\varepsilon_{\text{gold}}(\omega)+2\varepsilon_c}. \tag{2.24}$$

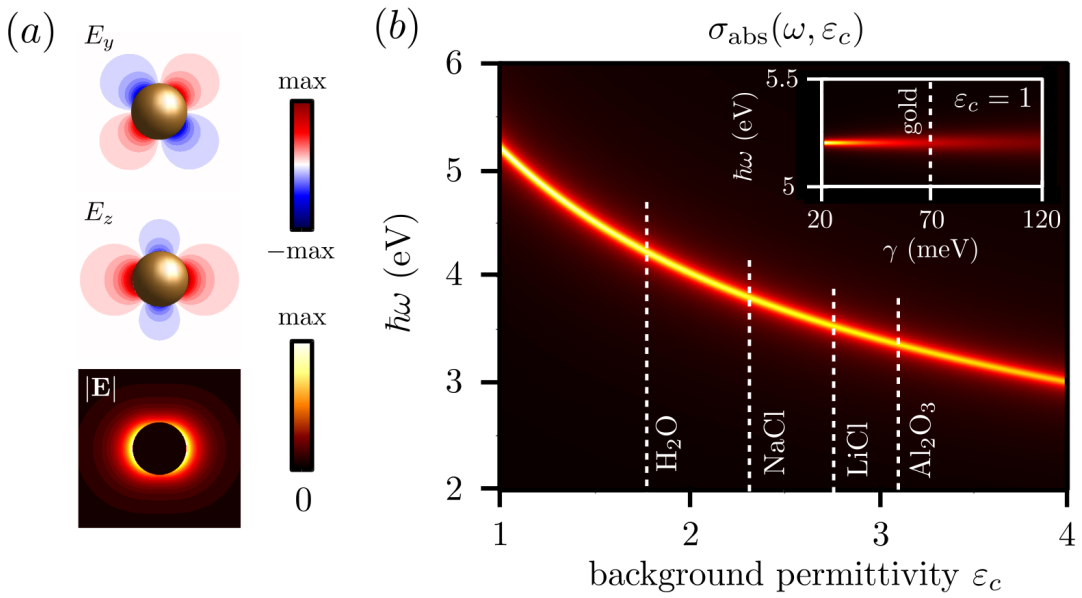

Figure 2.1: (a) Electric field components E_y, E_z, and the absolute value $\mathbf{E}$ of a polarized gold nanosphere in the symmetry plane $x = 0$, as described in the text. **(b)** Dipolar localized surface plasmon mode in the absorption cross section of a gold nanosphere as a function of the permittivity of the surrounding medium. The dielectric function of the sphere is found based on the *Drude* model in Eq. (2.13) with $\hbar\omega_p = 9\,\mathrm{eV}$ and $\hbar\gamma = 70\,\mathrm{meV}$ [138]. The inset shows the plasmon broadening as the damping rate γ is increased. Also, some technologically relevant solvents are mentioned along with their permittivity for yellow light [139].

The associated field-independent quantity is the polarizability of the sphere,

$$\alpha(\omega) = 4\pi R^3 \frac{\varepsilon_{\mathrm{gold}}(\omega) - \varepsilon_c}{\varepsilon_{\mathrm{gold}}(\omega) + 2\varepsilon_c}, \tag{2.25}$$

whose resonance is hit when the absolute value of the complex denominator $|\varepsilon_{\mathrm{gold}}(\omega) + 2\varepsilon_c|$ is minimal. For either negligibly small loss ($\gamma << \omega$) or spectrally almost constant loss in the system ($\partial \mathrm{Im}\,\varepsilon_{\mathrm{gold}}(\omega)/\partial\omega \approx 0$), the imaginary part of $\varepsilon_{\mathrm{gold}}(\omega)$ can be omitted in minimizing the denominator of Eq. (2.25), and we are left with the famous *Fröhlich* resonance condition for the dipolar plasmon,

$$\mathrm{Re}\,\varepsilon(\omega) + 2\varepsilon_c = 0. \tag{2.26}$$

If we further assume air as the surrounding medium ($\varepsilon_c = 1$) and the *Drude* model dielectric function of Eq. (2.13), we obtain the resonance condition for the dipole plasmon in a spherical metallic nanoparticle at the frequency $\omega_{\mathrm{SPP}} = \omega_p/\sqrt{3}$, where ω_p is the plasma frequency of the *Drude* model. An important finding here is that the resonance frequency ω_{SPP} of the localized SPP is *independent* of the size of the sphere.

Figure 2.1a shows the electric field profiles of the components E_y and E_z, and the absolute value of the electric field in the symmetry plane $x = 0$, where $E_x = 0$ for symmetry reasons. At resonance, the total field $\mathbf{E}$ can surpass the externally applied field $\mathbf{E}_0$ by far. In Fig. 2.1b, we show the absorption cross section

$$\sigma_{\mathrm{abs}}(\omega) = \frac{\omega}{\varepsilon_0 c_0} \mathrm{Im}\,\alpha(\omega) \tag{2.27}$$

of the dipolar plasmonic mode of the gold sphere as a function of the permittivity of the surrounding medium. We determine the dielectric function of the sphere based on the *Drude* model in Eq. (2.13) in air, with $\hbar\omega_p = 9\,\mathrm{eV}$ and $\hbar\gamma = 70\,\mathrm{meV}$ [138]. The dipolar plasmon considerably red-shifts as the background permittivity is increased. This can be harnessed in plasmonic sensing devices, where the nanoparticles are used to monitor small changes in the permittivity of the surrounding solvent, for instance. Some values for the permittivity of most common solvents for yellow incident light [139] are indicated by vertical white dashed lines. The inset of Fig. 2.1b shows the plasmon broadening as the *Drude* damping rate γ in Eq. (2.13) is increased. Whereas the spectral position of the resonance remains stable, it becomes weaker and simultaneously its width increases considerably.

In this chapter, we have introduced the basic principles of classical electromagnetic theory and presented the optical mechanisms that will be relevant for the remainder of this thesis. The next chapter is dedicated to the outstanding electronic and optical properties of the unique material, that dominates the discussion in this thesis – graphene.

3 | Electronic and Optical Properties of Graphene

In this thesis, we deal with extensions of the tight binding (TB) model to describe the optical properties of hybrid systems. These hybrid systems comprise carbon-based molecular antennas coupled to a two-level quantum emitter. Among the structures to which the TB model can be applied, the most prominent representative is certainly *graphene*. We devote this chapter to introduce the exceptional properties of this unique material. We present its atomic configuration, geometry, and its electronic and optical features. The chapter is mostly based on comprehensive review articles by Neto *et al.* [140], Allen [141], and Novoselov [35], as well as on text books by Gonçalves [50, 142] and Güçlü *et al.* [143].

3.1 Introduction

The belief that one-atom thick 2D crystals cannot exist in nature due to thermodynamical reasons has long persisted in the scientific community [33, 34, 144]. Nonetheless, Novoselov and Geim managed to fabricate extremely thin graphitic films in 2004 by mechanical exfoliation and characterized them [32]. In 2010, they were awarded the Nobel prize "for groundbreaking experiments regarding the two-dimensional material graphene" [35].

Nowadays, various methods have been identified to fabricate graphene, also for large-scale production. Among them are mechanical exfoliation techniques [145, 146], epitaxial growth approaches [147] on transition metals [148–151], on silicon carbide [152–154], and on hexagonal boron nitride [155, 156]. Laser-induced graphene films can be patterned from polymer films with a CO_2 infrared laser [157], it can be produced *via* chemical vapor deposition [158–162], slicing carbon nanotubes [163], or hydrothermal self-assembly [164]. Yet, it still remains a challenge to fabricate pure graphene of high quality, especially for application purposes outside the academic research environment [165, 166], leading to commercial poor quality graphene production all over the world [167]. In addition to pure graphene, however, there is also growing interest in more complex layered structures of various 2D materials, so-called *Van der Waals* heterostructures, for which graphene can serve as a basic building block [36, 168].

The reasons for the paramount interest in graphene and the active research in its production are versatile. It attracted a lot of attention not least because it was predicted to host electrons with linear dispersion. They obey the relativistic *Dirac* equation rather than the non-relativistic *Schrödinger* equation and, therefore, behave like massless particles in a hexagonal lattice [35, 169]. Consequently, graphene may serve as a miniaturized lab to realize effects like the *Klein* paradox *gedankenexperiment* and chiral tunneling [170], which are usually found in *relativistic* physics. As another consequence of its unique band

structure, doped defect-free graphene offers an ultra-high charge carrier mobility of up to $15000\,\mathrm{cm}^2/\mathrm{Vs}$ and, consequently, a very low resistivity down to $0.7\,\mathrm{k}\Omega$ [171–173]. Even for a vanishing net charge carrier concentration, a finite conductivity of $4e^2/\hbar$ is observed in ungated graphene [172, 174]. Upon electrostatic gating or optical pumping, the conductivity can be increased by orders of magnitude. In that way, graphene's electronic and optical properties can be tuned over a broad parameter range even after the fabrication of the respective graphene structure with fixed geometry and size. The latter property makes it a very promising candidate for applications in tunable plasmonics and strong light-matter interaction [22, 42, 49, 51].

Graphene's mechanical and optical properties are no less impressive. Its *Young*'s modulus was theoretically predicted [175, 176] and also measured [177, 178] to be close to $1000\,\mathrm{GPa}$. Therefore, it is lighter than aluminum but as stiff as diamond. Furthermore, it is so impermeable that not even a single helium atom can penetrate a defect-free graphene monolayer [179–181]. But the latter property is not only restricted to matter, but also holds for light. Undoped extended graphene absorbs 2.3% of incident white light, although it is only one atomic layer thick [182]. Interestingly enough, this number can be related to the fine structure constant $\alpha = e^2/\hbar c_0$ with the speed of light c_0 and the electron charge e, which is usually a fingerprint of relativistic quantum electrodynamics rather than material science.

Gated graphene supports low-loss plasmons in the mid-infrared with much longer lifetimes and much higher spatial confinement than those supported by noble metals [49, 50]. Additionally, the possibilities to tune the plasmon resonance frequency over a broad range of the infrared spectrum fairly easily, and to get access to nonlinear optical response, are even more beneficial features of graphene's unique band structure. Increasing the level of doping even further or reducing the size of finite nanostructured graphene pushes the frequency of the plasmons even into the visible. This, altogether, makes graphene a very promising candidate for future applications in optical sensing, ultrafast electro-optical modulation, graphene-based 2D lasers, and many more fields of research [42].

3.2 Atomic and Geometrical Structure

Since graphene consists exclusively of a single atomic type, its geometrical structure and many of its intriguing electronic properties may directly be deduced from the underlying chemical element and its chemical bonding behavior. Therefore, it is natural to discuss the basic atomic and chemical properties of the *carbon* atom first.

Being the sixth element in the periodic table, a carbon atom hosts six electrons, two of which populate the $1s$ orbital which is closely bound to the ionic core of the atom, see Fig. 3.1a. These two electrons are chemically completely inert, *i.e.* they do not participate in chemical bonding at all. Also, they are not relevant for the electronic properties of carbon allotropes in general and are, therefore, neglected in the following discussion. As illustrated in the same figure, the four remaining valence electrons populate the energetically higher lying $2s$ and $2p$ orbitals in the second shell. Intuitively, one would expect the ground state electronic configuration to be $[1s^2 2s^2 2p^2]$, as depicted in Fig. 3.1a. However, as illustrated in Fig. 3.1b, in the 2D arrangement it is energetically more favorable to form hybridized sp^2 orbitals, which are linear combinations of the $2s$ orbital and two of the three $2p$ orbitals (say, the $2p_x$ and $2p_y$ orbitals). As a consequence, when being arranged in a 2D configuration, the orbitals of the second shell with $n = 2$ undergo a transition from $[sp_x p_y p_z]$ to $[sp^2 p_z]$, as illustrated in Fig. 3.1b. Other hybridization con-

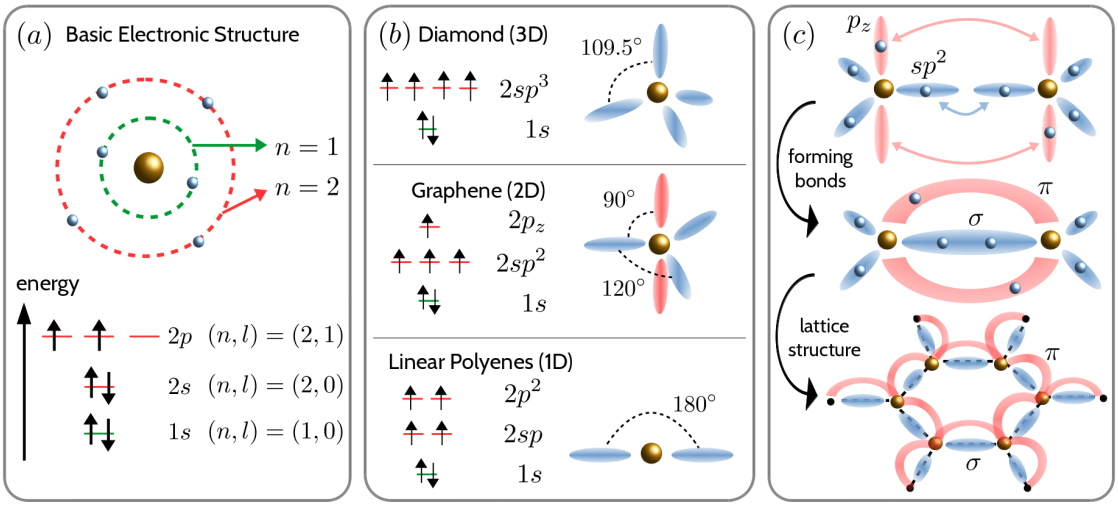

Figure 3.1: (a) Electronic ground state configuration of an isolated carbon atom. The inner shell with quantum number $n = 1$ and the s shell of the outer orbit with angular momentum $l = 0$ host two electrons each, whereas the outer $n = 2$ shell with angular momentum $l = 1$ is populated by the two remaining electrons. **(b)** Hybridization of orbitals in different carbon allotropes: in 3D diamond, four sp^3 orbitals of equal energy form. In the structure of interest for this thesis, 2D graphene, we find three sp^2 orbitals and one p_z orbital. In 1D linear organic carbon-based molecular chains, we observe two sp-hybridized states and two p^2 states. **(c)** Illustration of two close-by carbon atoms at the top, whose p_z orbitals and sp^2 orbitals form π-bonds and σ-bonds, respectively. The strong in-plane σ-bonds that require three direct atomic neighbors are responsible for the hexagonal honeycomb structure of the graphene lattice at the bottom.

figurations in carbon allotropes are the sp^3-hybridization in diamond and the sp and p^2 hybridized orbitals in linear polyenes.

The sp^2 orbitals of neighboring carbon atoms in graphene form strong covalent σ-bonds that lie in the plane of the graphene sheet and are responsible for its hexagonal honeycomb structure, see Fig. 3.1c. The σ-electrons are bound too strongly inside these orbitals to undergo electronic transitions upon infrared or optical excitation and, therefore, remain inert in the context of plasmonics as well. The remaining electron in the p_z orbital, however, is only weakly bound to the host carbon atom and, thus, highly mobile. Mediated through π-bonds that are formed by p_z orbitals of neighboring carbon atoms, it can move to adjacent atomic sites and, in the process, contribute to electronic conduction.

Direct Lattice

Graphene is a one-atom thick 2D sheet of carbon atoms hexagonally arranged in a honeycomb lattice. Its underlying *Bravais* lattice is of triangular shape with basis vectors

$$\mathbf{a_1} = \frac{d_c}{2}\begin{pmatrix} 3 \\ \sqrt{3} \end{pmatrix} \quad \text{and} \quad \mathbf{a_2} = \frac{d_c}{2}\begin{pmatrix} 3 \\ -\sqrt{3} \end{pmatrix}, \tag{3.1}$$

where d_c is the distance between two neighboring carbon atoms. The primitive unit cell spanned by the two basis vectors, as well as the hexagonal *Wigner-Seitz* cell (WSC) of the triangular lattice are shown in shaded green in Fig. 3.2. Each unit cell contains two carbon atoms at $\mathbf{p}_A = d_c\hat{\mathbf{e}}_x$ and $\mathbf{p}_B = 2d_c\hat{\mathbf{e}}_x$, such that the set of all carbon atoms in the matrix can be separated into two disjunct sets of atoms belonging to different sublattices, denoted by A and B, respectively. The subset of atoms of type $A(B)$ can be found at position $\{m\mathbf{a_1} + n\mathbf{a_2} + \mathbf{p}_{A(B)}\}$ for $m, n \in \mathbb{Z}$. The direct lattice vectors connecting pairs of nearest neighbors are (see Fig. 3.2)

$$\boldsymbol{\delta_1} = d_c\hat{\mathbf{e}}_x, \quad \boldsymbol{\delta_2} = \frac{d_c}{2}\begin{pmatrix}-1\\ \sqrt{3}\end{pmatrix}, \quad \boldsymbol{\delta_3} = \frac{d_c}{2}\begin{pmatrix}-1\\ -\sqrt{3}\end{pmatrix}. \tag{3.2}$$

Please note that all three nearest-neighbor atoms of a carbon atom in sublattice A belong to sublattice B, and vice versa. In the following, we are mostly concerned with *finite* samples of graphene constructed by cutting the uderlying graphene lattice in two qualitatively different ways[1]:

1. When cutting along the horizontal axis in Fig. 3.2, we obtain an *armchair* (ac) edge. Characteristic for finite graphene nanoantennas with ac edges and N atoms is the presence of a relatively large energy gap $E_g \propto 1/\sqrt{N}$ between its HOMO and LUMO states [143, 183–185]. The numbers of atoms in sublattice A and B are equal. In structures with ac edges, the HOMO-LUMO gap ensures that adding single electrons potentially increases the *Fermi* energy of the structure significantly. Consequently, they constitute suitable platforms for tunable plasmonic applications.
2. When cutting along the vertical axis in Fig. 3.2, we obtain a *zigzag* (zz) edge. Characteristic for nanoantennas with zz edges is the appearance of potentially a large number of near-zero energy electronic states, that are localized close to the edges of the nanoantenna. In zz edged structures, the numbers of atoms in sublattices A and B differ, and the difference renders how many of these edge states exist in the spectrum. In the charge-neutral undoped configuration, this degenerate shell at zero energy is half filled with electrons. As it requires a large number of additional doping electrons to get off this degenerate shell and change the *Fermi* energy, zz-edged structures are not suitable in *tunable* optics applications in the near-infrared or even visible range. However, they find application in terahertz spectroscopy within the shell, and in magneto-optics due to their spin-polarized ground state [186, 187].

Reciprocal Lattice

The basis vectors $\mathbf{b_1}$ and $\mathbf{b_2}$ of the reciprocal lattice are defined through $\mathbf{a_i} \cdot \mathbf{b_j} = 2\pi\delta_{ij}$ for $i, j \in \{1, 2\}$. Consequently, we find

$$\mathbf{b_1} = \frac{2\pi}{3d_c}\begin{pmatrix}1\\ \sqrt{3}\end{pmatrix} \quad \text{and} \quad \mathbf{b_2} = \frac{2\pi}{3d_c}\begin{pmatrix}1\\ -\sqrt{3}\end{pmatrix}, \tag{3.3}$$

such that it is apparent that also the reciprocal lattice is triangular. Thus, the first *Brillouin* zone (1BZ), which is the *Wigner-Seitz* cell of the reciprocal lattice, is also a hexagon. Figure 3.4a shows the reciprocal lattice of graphene with the 1BZ (shaded green) and the Γ-point, as well as the M-, K-, and K'-points.

[1]The presence of exclusively one edge type in a structure implies that its edges form angles of $\pi/3$ or $2\pi/3$. This is realized in hexagonal and triangular nanoantennas, for instance.

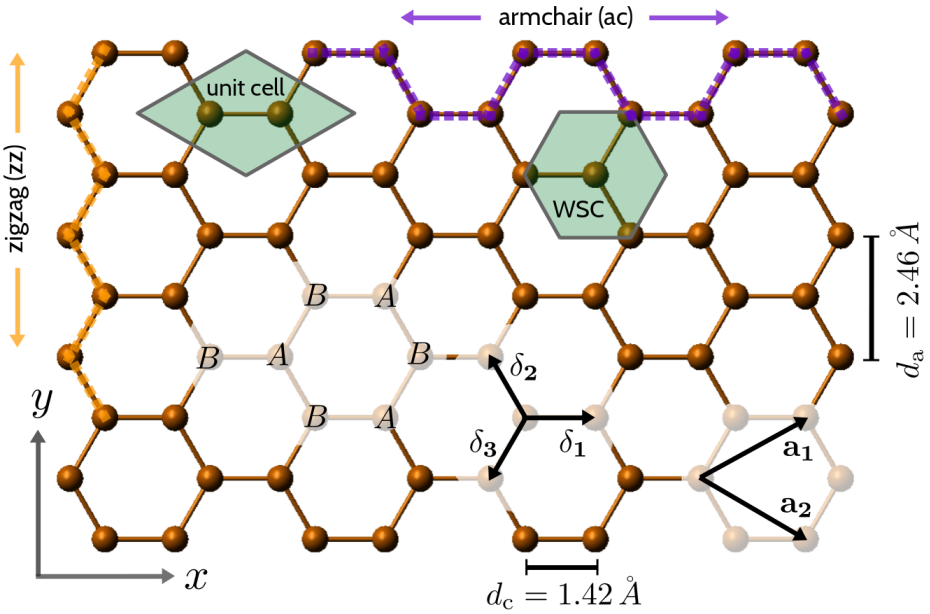

Figure 3.2: Geometric structure of the 2D graphene honeycomb lattice. The lattice vectors of the underlying triangular *Bravais* lattice are denoted as $\mathbf{a_1}$ and $\mathbf{a_2}$, the distance of two carbon atoms is $d_c = 1.42\,\text{Å}$, whereas the lattice constant is $d_a = 2.46\,\text{Å}$. The green shaded regions depict the unit cell constructed directly from $\mathbf{a_1}$ and $\mathbf{a_2}$ and the *Wigner-Seitz* cell (WSC), both containing two carbon atoms. The $\boldsymbol{\delta_i}$ are vectors connecting neighboring carbon atoms in different sublattices of type A and B. Graphene can be cut into finite flakes along two qualitatively different directions, producing either zigzag (zz, orange) or armchair (ac, purple) edges.

3.3 Classical Graphene Plasmonics

Right after the discovery of large-scale production schemes for graphene by mechanical exfoliation [32], its surface conductivity has been calculated within the *Kubo* formalism [188]. One can separate the contributions of *intraband* and *interband* electronic transitions to the surface conductivity $\sigma(\omega) = \sigma_{\text{intra}}(\omega) + \sigma_{\text{inter}}(\omega)$. In the low-temperature limit $\hbar\omega \gg k_{\text{B}}T$, where k_{B} is *Boltzmann*'s constant and T the temperature, one obtains [188, 189]

$$\sigma_{\text{intra}}(\omega) = \frac{\mathrm{i}e^2 E_F}{\pi\hbar^2(\omega + \mathrm{i}\gamma)}, \tag{3.4a}$$

$$\sigma_{\text{inter}}(\omega) = \frac{e^2}{4\hbar}\left(\Theta(\hbar\omega - 2E_F) + \frac{\mathrm{i}}{\pi}\ln\left|\frac{2E_F - \hbar\omega}{2E_F + \hbar\omega}\right|\right). \tag{3.4b}$$

Here, E_F denotes the *Fermi* energy

$$E_{\text{F}} = \hbar v_{\text{F}}\sqrt{\pi n} \tag{3.5}$$

with the *Fermi* velocity in graphene $v_{\text{F}} \approx 10^6\,\text{m/s}$ and the charge carrier density n of the graphene sample. The rate γ is an intrinsic damping parameter, and Θ is the *Heaviside* step function. In the low-energy limit ($\hbar\omega \ll 2E_F$), it is safe to neglect the interband contribution to the optical response of graphene. By comparing the intraband contribution in Eq. (3.4a) and Eq. (2.13), we realize that graphene may be optically modeled as a

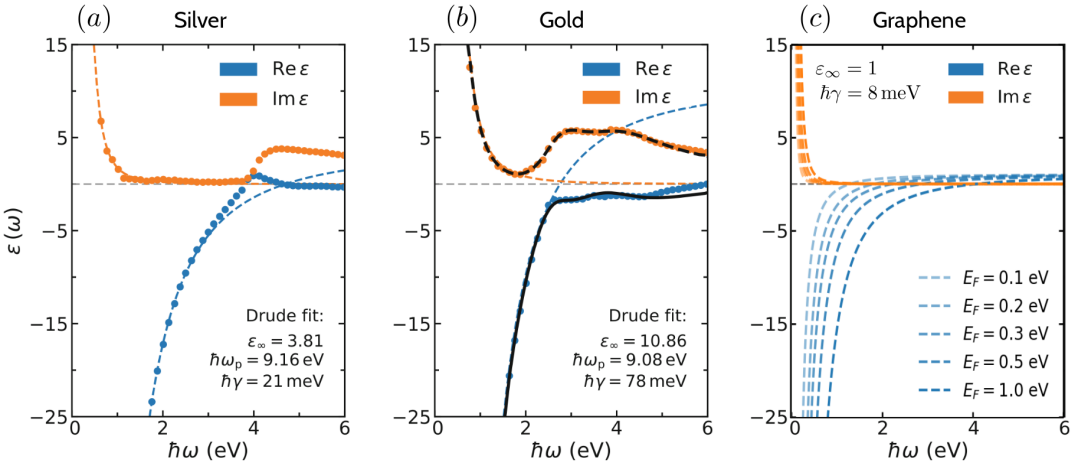

Figure 3.3: Dielectric function $\varepsilon(\omega)$ of the noble metals **(a)** silver and **(b)** gold. Blue and orange circles represent experimentally measured real and imaginary parts, respectively [191]. Colored dashed lines correspond to extended *Drude* model fits according to $\varepsilon(\omega) = \varepsilon_\infty - \omega_\mathrm{p}^2/(\omega^2 + \mathrm{i}\gamma\omega)$ with the parameters given in the bottom right of the figures. The black lines in the gold panel are found with a *Drude*-based analytical model that also accounts for interband transitions [192]. *Adapted with permission from Ref. [142]. Copyright © 2020 Springer.* **(c)** Dielectric function of extended graphene for different *Fermi* energies in vacuum ($\varepsilon_\infty = 1$), as obtained from Eq. (3.4a). A damping parameter of $\hbar\gamma = 8\,\mathrm{meV}$ is assumed [47, 48, 50, 80, 142].

metal in that case. Direct comparison yields the dielectric function

$$\varepsilon(\omega) = 1 + \frac{\mathrm{i}\sigma_\mathrm{intra}(\omega)}{\varepsilon_0 \omega d_\mathrm{g}} \tag{3.6}$$

and the plasma frequency

$$\omega_p = \frac{e}{\hbar}\sqrt{\frac{E_F}{\varepsilon_0 \pi d_\mathrm{g}}}, \tag{3.7}$$

where $d_\mathrm{g} = 0.35\,\mathrm{nm}$ is the thickness of the graphene sheet, quantified by the phenomenological extent of its out-of-plane carbon p_z orbitals[2]. Note, that it follows from Eqs. (3.5) and (3.7), that the plasma frequency in graphene scales with the charge carrier density as $\omega_p \sim \sqrt[4]{n}$, unlike in the 2D electron gas with quadratic dispersion, where $\omega_p \sim \sqrt{n}$ holds [190] – another fingerprint of 2D massless Dirac electrons.

Figure 3.3 shows the dielectric function of the commonly used plasmonic materials; (a) of silver and (b) of gold. The blue and orange filled circles represent experimentally determined real and imaginary parts of the dielectric functions, respectively [191]. The colored dashed lines correspond to *Drude* model fits according to $\varepsilon(\omega) = \varepsilon_\infty - \omega_\mathrm{p}^2/(\omega^2 + \mathrm{i}\gamma\omega)$ with the parameters given in the bottom right of the panels. The black solid (dashed) line in (b) shows the real (imaginary) part of the dielectric function found with a *Drude*-based analytical model that additionally takes into account interband transitions [192]. In Fig. 3.3c,

[2]Please note, that the 2D surface conductivity of graphene in Eq. (3.4a) has units A/V, whereas the volume conductivity of the general *Drude* model in Eq. (2.13) has units A/Vm. To compensate for this, the graphene thickness d_g appears in Eq. (3.7) to convert the surface conductivity into a volume conductivity.

the *Drude* model dielectric function of graphene for intraband contributions is depicted for several experimentally feasible values of the *Fermi* energy E_F. In comparison, we note that the imaginary part of the dielectric function is almost insensitive to the *Fermi* energy, but smaller as compared to the noble metals in the infrared and the optical regime, pointing out the low-loss nature of optical excitations in graphene. On the contrary, the real part of the dielectric function can be shifted considerably as a function of the *Fermi* energy. Therefore, the plasma frequency can be modified by changing the *Fermi* energy over a broad range. This paves the way for tunable and low-loss plasmonic devices made from graphene.

3.4 Tight Binding Model

Plasmonic resonances in metallic nanoparticles can be described surprisingly accurately by classical models considering a homogeneous material description characterized by a dielectric function. An extensively applied example thereof is the macroscopic *Drude* model for metals [193–195] that we applied to 2D graphene in the previous section. It has been shown, that graphene nanoantennas may be well-described within these approaches when the characteristic length of the antenna is above $10\,\mathrm{nm}$ [44, 45]. However, when the size of the particles falls below a critical threshold, finite size effects need to be taken into account to properly describe their optical response [52, 53].

Atomistic approaches that respect the quantum mechanical nature of matter to obtain the electronic energy levels and eigenstates on the nanoscale are multifarious. Common methods of choice, which are not treated within this thesis in detail, are – roughly ordered by ascending degree of complexity – the jellium model [196], quantum fluid dynamics [197–199], the configuration interaction method [200, 201], the *Bethe-Salpeter* approach [202–204], and density functional theory (DFT) [45, 114, 118, 121–125, 205–212].

This thesis is mainly concerned with a further quantum mechanical method, the tight binding (TB) model, first applied to graphitic structures by Wallace in 1947 [54]. Being computationally much less expensive and conceptually rather simple, it has proven to provide surprisingly accurate results if compared to DFT calculations especially in the case of carbon-based structures like graphene nanoantennas [55–58].

To describe the electronic structure of graphene and its optical interactions with light, we employ the nearest-neighbor TB model. The TB model constitutes a simple yet powerful approach to capture the electronic dynamics of the p_z electrons in graphene, which mainly determine its electronic properties. The model's name originates from the assumption that an electron in the p_z orbital of atom l is *tightly bound* to this atom, as the corresponding orbital itself is strongly localized in the vicinity of the atom at position $\mathbf{r}_l$. However, mediated by a small but existing overlap of p_z orbitals of neighboring atoms l and l', electrons may tunnel to the adjacent atomic site with a probability quantified by a value $t_{ll'}$ derived from a hopping integral. The value of this hopping integral is the only free parameter in the framework and cannot be determined within the TB approach itself. For that reason, the TB model is not an *ab initio* approach in quantum chemistry, unlike DFT, for example. The latter does not require such external parameters as an input but only the atomic structure of the molecule to be computed. Whereas DFT provides more exact results for small molecules in general, the TB approach can be generalized to much larger molecules with still accurate results at comparatively low additional computational cost. Thus, the simulation of graphene antennas with hundreds or thousands of atoms is viable within the TB approach. Moreover, additional atoms that are not necessarily

carbon, or defects in the matrix can be easily integrated into the framework because it is conceptually easy to access and readily extensible, as outlined below in Sec. 6.2.

The Hamiltonian of an infinitely extended graphene sheet in the nearest-neighbor TB approximation reads

$$H_{\mathrm{TB}} = -t \sum_{n=0}^{\infty} \sum_{m=1}^{3} \left(|\psi^A_{\mathbf{R}_n}\rangle\langle\psi^B_{\mathbf{R}_n+\boldsymbol{\delta}_m}| + |\psi^B_{\mathbf{R}_n+\boldsymbol{\delta}_m}\rangle\langle\psi^A_{\mathbf{R}_n}| \right), \tag{3.8}$$

where $|\psi^A_{\mathbf{R}_n}\rangle$ represents the p_z orbital of a carbon atom of type A at position $\mathbf{R}_n$ in the n-th unit cell and the $\boldsymbol{\delta}_m$ have been introduced in Eq. (3.2). The periodicity of the lattice allows to expand the localized p_z orbitals into Bloch states in *Fourier* space labeled by $\mathbf{k}$ according to[3]

$$|\psi^A_{\mathbf{R}_n}\rangle = \frac{1}{\sqrt{N}} \sum_{\mathbf{k}} \mathrm{e}^{-\mathrm{i}\mathbf{k}\cdot\mathbf{R}_n} |\psi^A_{\mathbf{k}}\rangle. \tag{3.9}$$

Here, we conceptually introduce a normalization constant $N \to \infty$ which denotes the number of unit cells taken into account in the sum over n in Eq. (3.8), leading to the orthonormalization condition $\sum_{n=0}^{N-1} \mathrm{e}^{\mathrm{i}(\mathbf{k}-\mathbf{k}')\cdot\mathbf{R}_n} = N\delta_{\mathbf{k}\mathbf{k}'}$. Consequently, the Hamiltonian in *Fourier* space reads

$$H_{\mathrm{TB}} = -t \sum_{\mathbf{k}\in 1\mathrm{BZ}} \left(\sum_{m=1}^{3} \mathrm{e}^{\mathrm{i}\mathbf{k}\cdot\boldsymbol{\delta}_m} |\psi^A_{\mathbf{k}}\rangle\langle\psi^B_{\mathbf{k}}| + \sum_{m=1}^{3} \mathrm{e}^{-\mathrm{i}\mathbf{k}\cdot\boldsymbol{\delta}_m} |\psi^B_{\mathbf{k}}\rangle\langle\psi^A_{\mathbf{k}}| \right). \tag{3.10}$$

Introducing

$$\Psi_{\mathbf{k}} = \begin{pmatrix} |\psi^A_{\mathbf{k}}\rangle \\ |\psi^B_{\mathbf{k}}\rangle \end{pmatrix}, \quad H_{\mathbf{k}} = -t \begin{pmatrix} 0 & f_{\mathbf{k}} \\ f^*_{\mathbf{k}} & 0 \end{pmatrix}, \quad f_{\mathbf{k}} = \sum_{m=1}^{3} \mathrm{e}^{\mathrm{i}\mathbf{k}\cdot\boldsymbol{\delta}_m}, \tag{3.11}$$

the *Fourier* space Hamiltonian in Eq. (3.10) can be written in a simplified form,

$$H_{\mathrm{TB}} = \sum_{\mathbf{k}\in 1\mathrm{BZ}} \Psi^\dagger_{\mathbf{k}} H_{\mathbf{k}} \Psi_{\mathbf{k}}. \tag{3.12}$$

From that, we may directly conclude that the spectrum of graphene obtained in the nearest-neighbor TB approximation has the form

$$\begin{aligned} E(\mathbf{k},\pm) &= \pm t|f_{\mathbf{k}}| \\ &= \pm t \sqrt{3 + 2\cos\left(\sqrt{3}k_y d_c\right) + 4\cos\left(\frac{3}{2}k_x d_c\right)\cos\left(\frac{\sqrt{3}}{2}k_y d_c\right)}, \end{aligned} \tag{3.13}$$

where $+$ and $-$ refer to the conduction and valence band above and below $E = 0$, respectively. From the dispersion relation Eq. (3.13), many of the electronic and optical properties of graphene can be deduced. Therefore, the next section is dedicated to analyze the spectrum in more detail.

[3] In finite graphene structures, which lack discrete translational invariance, this expansion is no longer valid. Thus, in the next sections we will continue to work in real space and start from Eq. (3.8) to characterize finite graphene nanoantennas.

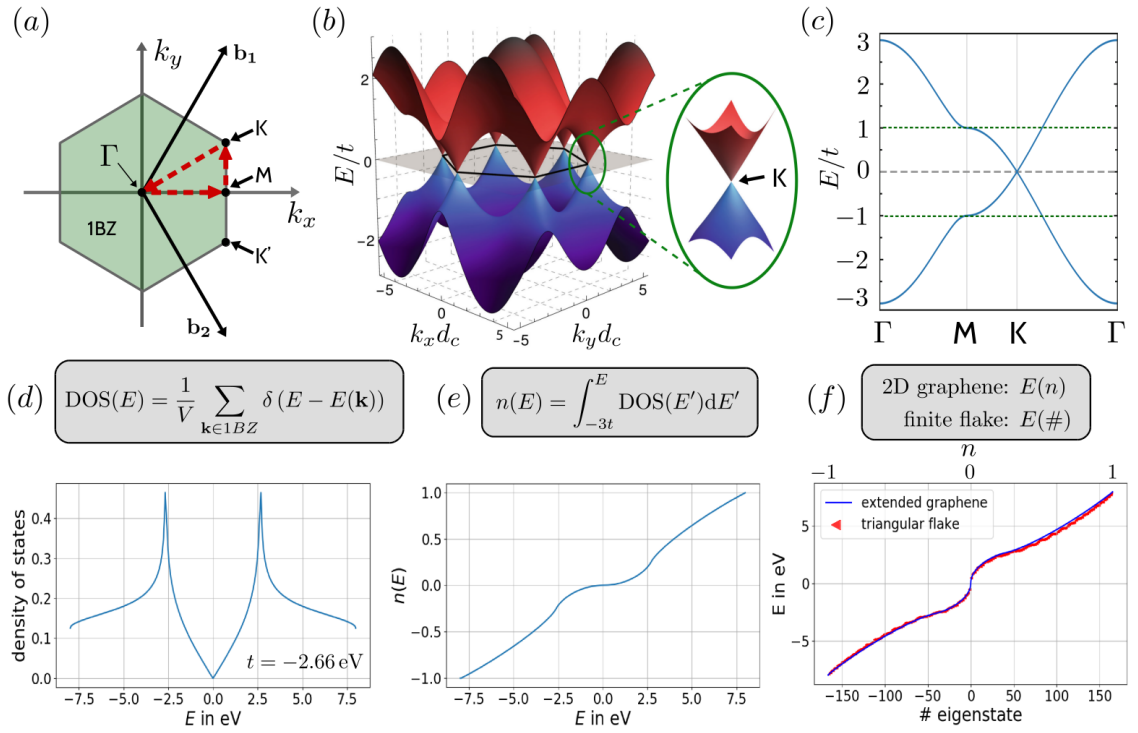

Figure 3.4: (a) First *Brillouin* zone (1BZ) of graphene with the basis vectors $\mathbf{b}_1$ and $\mathbf{b}_2$ of the reciprocal lattice and the characteristic Γ-, K-, M-, and K'-points. **(b)** Dispersion $E(\mathbf{k}, \pm)$ of 2D graphene within the nearest-neighbor TB approximation, see Eq. (3.13). The valence (conduction) band is colored in blue (red). *Adapted with permission from Ref. [142]. Copyright © 2020 Springer.* **(c)** Line plot of the dispersion along the ΓMKΓ-path highlighted in red in (a). **(d)** Density of states of graphene for $t = 2.66\,\mathrm{eV}$. The vertical axis is scaled, s.t. $\int_{-3t}^{3t}\mathrm{DOS}(E)\mathrm{d}E = 2$. **(e)** Charge carrier density $n(E)$ as a function of the *Fermi* energy. **(f)** *Fermi* energy $E(n)$ as a function of charge carrier density (blue line, top axis). Discrete energy level diagram of the finite 330-atomic armchair graphene triangle with side length $4.1\,\mathrm{nm}$ (red markers, bottom axis).

Spectrum of 2D Graphene

Figure 3.4b shows the spectrum of infinitely extended graphene in reciprocal space. Its unit cell exhibits a hexagonal shape (see also Fig. 3.4a) and it consists of two connected bands above and below $E = 0$. At the Γ-point, $\mathbf{k}_\Gamma = \mathbf{0}$, the conduction and valence bands attain their maximum and minimum value of $E = \pm 3t$, respectively. On the other hand, for

$$\mathbf{k}_\mathrm{K} = \frac{2\pi}{3\sqrt{3}d_c}\begin{pmatrix}\sqrt{3}\\ 1\end{pmatrix} \quad \text{and} \quad \mathbf{k}_{\mathrm{K}'} = \frac{2\pi}{3\sqrt{3}d_c}\begin{pmatrix}\sqrt{3}\\ -1\end{pmatrix}, \tag{3.14}$$

the two bands meet at the so-called K- and K'-points, respectively, which mark two particular points at the boundary of the first *Brillouin* zone where $E(\mathbf{k}, \pm) = 0$. The inset in Fig. 3.4b shows the conical shape of the linear dispersion at the K- and K'-point. Moreover, at the M-point, $\mathbf{k}_M = 2\pi/3d_c(1, 0)$, right between the K- and K'-points, we obtain $E(\mathbf{k}, \pm) = \pm t$ and $\nabla_\mathbf{k} E(\mathbf{k}, \pm) = 0$. In Fig. 3.4c, we depict the dispersion along the ΓMKΓ path, highlighted in red in Fig. 3.4a. The green dashed lines correspond to $E = \pm t$.

As we will mainly concern finite graphene nanoantennas below that break the translational symmetry of graphene in all directions, we condense the information contained in the dispersion to a higher stage of aggregation. Therefore, we compute the $\mathbf{k}$-independent density of states (DOS) of graphene [54, 213],

$$\mathrm{DOS}(E) = \frac{1}{V_{1\mathrm{BZ}}} \sum_{\mathbf{k}\in 1\mathrm{BZ}} \delta\left(E - E(\mathbf{k})\right), \tag{3.15}$$

where $V_{1\mathrm{BZ}}$ is the volume of the first *Brillouin* zone in graphene and, derived from that, the charge density n as a function of the energy E of the highest occupied state in the system,

$$n(E) = \int_{-3t}^{E} \mathrm{DOS}(E')\,\mathrm{d}E'. \tag{3.16}$$

Figure 3.4d shows the DOS of graphene in the range between $-3t$ and $3t$ for $t = 2.66\,\mathrm{eV}$. Two interesting features should be discussed here. First, we observe two so-called *van Hove* singularities of high densities of states at $|E| = |t|$. These are the signatures of the vanishing derivatives of the dispersion at the M-points, $\nabla_{\mathbf{k}} E(\mathbf{k}, \pm)|_M = 0$. Second, the density of states at the K- and K'-points vanishes and approaches zero linearly. This is the origin of the unique low-energy electronic properties of graphene, where electrons are treated as massless particles and obey an adjusted relativistic *Dirac* equation rather than the non-relativistic *Schrödinger* equation [169].

Figure 3.4e shows the charge carrier density $n(E)$ as a function of the *Fermi* energy of a graphene structure. For instance, if the *Fermi* energy is $E = 0$, the charge carrier density vanishes as well, *i.e.* the graphene structure is neutral. If $n = -1$, the valence band is completely empty, $n = 1$ corresponds to the completely occupied conduction band. Conversely, the inverse of the quantity, $E(n)$, (see Fig. 3.4f) reveals that a slight change in the charge carrier density leads to substantial modulations of the *Fermi* energy in graphene, especially close to the charge neutral point $n = 0$. Note that here the derivative $\partial E/\partial n|_{n=0}$ diverges, which renders graphene a perfect platform for tunable nanophotonics.

The latter property of 2D graphene directly translates to finite graphene derivates as well, such as graphene nanoribbons, carbon nanotubes, and graphene quantum dots [143] as nanoantennas. To highlight this, we show the single-particle energies of a 330-atomic triangular graphene nanoantenna with side length $4.1\,\mathrm{nm}$ and armchair edges in Fig. 3.4f (red triangular markers, bottom axis). The discrete energy level diagram of the nanostructured graphene follows the line of 2D graphene exactly. Thus, particularly in these finite molecular systems, doping with single electrons substantially modifies their *Fermi* energy and, therefore, their optical properties as well. Before we discuss the optics and plasmonics of these finite graphene nanoantennas in our quantum mechanical TB framework in Ch. 5, we first introduce the electronic properties of finite TB structures in general in Ch. 4.

4 | Electronic Structure of Planar Carbon Molecules

4.1 Introduction

Fully quantum-mechanical approaches, which consistently solve the many-body *Schrödinger* equation for all particles in the system, are computationally extremely expensive. The *Hilbert* space of a system consisting of N distinguishable particles with d degrees of freedom has dimension d^N. Let us exemplarily consider a triangular graphene nanoantenna with $N = 270$ carbon atoms in TB description, which is discussed in more detail in Ch. 8. If we were only interested in the spin degree of freedom of its $N_e = 270\,\pi$-electrons, the dimension of the associated *Hilbert* space 2^{270} already exceeds the number of particles in the visible universe ($\approx 10^{80} \approx 2^{266}$). It is needless to state that this conceptually comparatively simple problem is practically completely intractable.

Therefore, suitable approximations are needed to simulate the dynamics in quantum-mechanical systems efficiently. However, state-of-the-art molecular simulation techniques such as density functional theory, for instance, suffer from high computational costs and are limited to systems with a comparatively small number of atoms. Finite graphene structures that act as nanoantennas comprise of a few hundreds of atoms usually and already pose a challenge for these frameworks. Thus, further simplifications are needed to describe such rather large systems. In practice, this is often done by reducing the number of dynamic particles in the system. To be precise, in the TB framework applied in this work, we do not only freeze the atomic cores, but also five of the six electrons in the carbon atoms. In consequence, only one π-electron per atom is allowed to move around in the molecule being subject to an effective potential that is determined by the remaining frozen particles. This allows to treat molecules with thousands of atoms within a reasonable amount of time and on a reasonable computing infrastructure.

In the previous chapter, we have outlined how the atomic structure and geometry of its lattice determine the fundamental electronic and optical properties of extended 2D graphene. In this chapter, we extend the TB framework to *finite* graphene structures and generalize the applicability of the TB model to carbon-based molecules. In particular, we first study molecular chains described within the TB-based *Su-Schrieffer-Heeger* (SSH) model as prototypical examples of metallic and insulating species. Moreover, an insulating chain that hosts topologically protected edge states will be discussed within this model as well. We then apply the model to finite graphene structures of different shapes and edge types that can act as optical nanoantennas.

4.2 Tight Binding Model for Planar Carbon Molecules

Equation (3.8) expressed the TB Hamiltonian of extended 2D graphene. For an arbitrary planar carbon-based structure consisting of N atoms, it can be generalized in the nearest-neighbor π-electron approximation to

$$H_{\mathrm{TB}} = \sum_{l=1}^{N} \epsilon_l |l\rangle\langle l| + \sum_{\langle l,l'\rangle, l<l'} t_{ll'} \left(|l\rangle\langle l'| + |l'\rangle\langle l| \right), \tag{4.1}$$

where l labels the atoms in the structure situated at $\mathbf{r}_l = (x_l, y_l)$. Moreover, $|l\rangle$ represents the p_z orbital localized around atom l, ϵ_l denotes the on-site energy for an electron occupying state $|l\rangle$, and $\langle l, l'\rangle$ is the pair of nearest-neighbor carbon atoms l and l', where the restriction $l < l'$ avoids double counting of atomic bonds. The hopping parameters $t_{ll'}$ quantify how strongly the adjacent orbitals $|l\rangle$ and $|l'\rangle$ overlap and, therefore, how likely it is for an electron to hop from the atomic site l to site l'.

In the following, we assume that all carbon atoms in the below-investigated structures can be treated equally. In particular, edge effects are assumed not to distort the orbitals localized around atoms at the edges of the structure. This is motivated by the intrinsic assumption that edge atoms are hydrogen-passivated and, therefore, the carbon-carbon hopping rates of edge bonds are equal to bulk bond hopping rates. Indeed, it has been shown that the modifications of hopping rates in 2D structures due to variations of the carbon-carbon bond lengths, for instance, are minor [214, 215]. To maintain consistency throughout this work, we assume $t_{ll'} =: t$ with $t = 2.66\,\mathrm{eV}$ [56, 216] in all carbon structures under investigation below, reminiscent of the hopping rate for extended graphene. Moreover, all on-site energies are assumed to be equal. As they only lead to a constant shift of all energies, we choose $\epsilon_l = 0$ for convenience. Equation (4.1) consequently simplifies to

$$\boxed{H_{\mathrm{TB}} = t \sum_{\langle l,l'\rangle, l<l'} \left(|l\rangle\langle l'| + |l'\rangle\langle l| \right),} \tag{4.2}$$

which is the starting point for all below-investigated molecular structures. Upon diagonalization of the Hamiltonian in Eq. (4.2), we obtain N energy eigenstates which we denote by $|j\rangle$ with $1 \leq j \leq N$, satisfying the eigenvalue equation

$$H_{\mathrm{TB}}|j\rangle = E_j|j\rangle, \tag{4.3}$$

with the corresponding eigenenergies E_j. Each spin-degenerate state $|j\rangle$ can host two electrons of opposite spin. Throughout the whole thesis, magnetic effects are not considered and, therefore, apart from respecting the *Pauli* exclusion principle, we treat electrons of opposite spin equally.

Real-Space Expansion Coefficients

After diagonalization of H_{TB}, we can, in turn, expand the energy eigenstates in the real-space basis $\{|l\rangle\}$ of carbon p_z orbitals with real-valued expansion coefficients a_{jl} according to

$$|j\rangle = \sum_{l=1}^{N} a_{jl}|l\rangle. \tag{4.4}$$

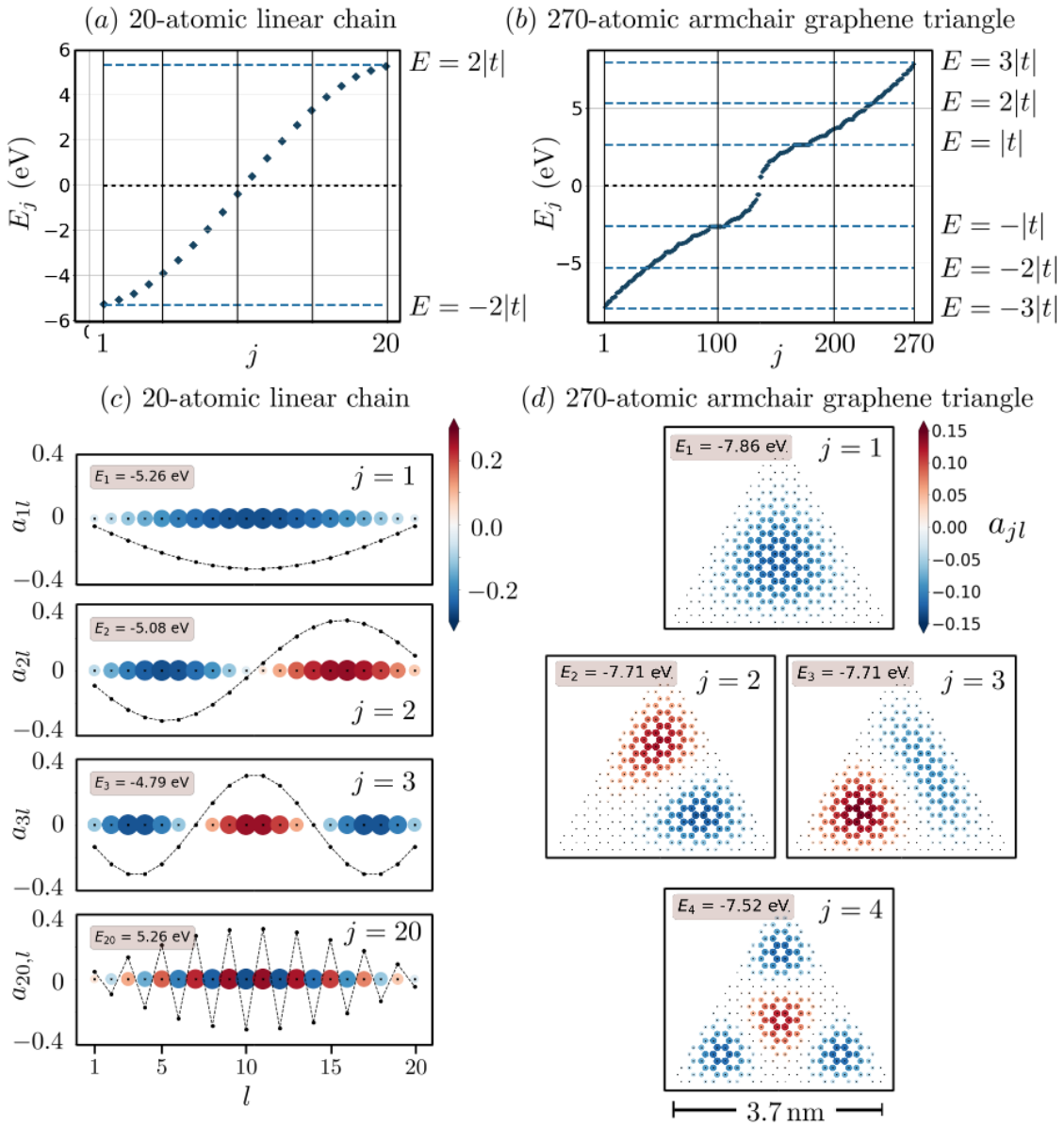

Figure 4.1: Single-particle TB *Jabłonski* diagrams of **(a)** the 20-atomic linear carbon chain and **(b)** the 270-atomic armchair graphene triangle. Real-space expansion coefficients a_{jl} introduced in Eq. (4.4) for selected eigenstates $|j\rangle$ of **(c)** the 20-atomic linear carbon chain and **(d)** the 270-atomic armchair graphene triangle. The areas of the colored circles is proportional to $|a_{jl}|^2$.

As the energy eigenstates and the atomic site orbitals form an orthonormal and complete basis set, the expansion coefficients a_{jl} obey

$$\sum_{j=1}^{N} a_{jl} a_{jl'} = \delta_{ll'} \qquad \text{and} \qquad \sum_{l=1}^{N} a_{jl} a_{j'l} = \delta_{jj'}. \tag{4.5}$$

Exemplarily, we show the results of the diagonalization process for the 20-atomic linear carbon chain and the 270-atomic triangular graphene flake with armchair edges. Their *Jabłonski* energy level diagrams are shown in Figs. 4.1a and 4.1b, respectively. We observe that the chain's energy states are located in the range $|E_j^{\text{chain}}| < 2|t|$, whereas

$|E_j^{\text{triangle}}| < 3|t|$ holds for the triangle. As mentioned above, the energy level diagram of any TB system described by Eq. (4.2) is symmetric with respect to $E = 0$. Hence, this is also the *Fermi* level[1] for electronically neutral structures in TB description that are not doped with additional electrons. Moreover, apart from spin degeneracy, the chain does not exhibit degenerate states, whereas the triangle does for symmetry reasons (see also middle row of Fig. 4.1d).

Figure 4.1c shows the real-space expansion coefficients a_{jl} of the three lowest-energy single-particle states $j = \{1, 2, 3\}$ and the highest-energetic state $j = 20$ of the 20-atomic linear carbon chain. We observe that, in the low- and high-energy regions, the chain behaves similar to a particle in a finite one-dimensional potential well. The fundamental node-less mode $|j = 1\rangle$ contains half a wavelength of the size of the chain, whereas $|2\rangle$ has one node and contains a full wavelength. The highest-energetic mode $|20\rangle$ with $E_{20} = -E_1$ heavily oscillates in sign, but $|a_{1l}| = |a_{20,l}|$ for any fixed l. The latter can be generalized for arbitrary TB structures of size N. We always find

$$E_{N+1-j} = -E_j, \qquad |a_{N+1-j,l}| = |a_{jl}|. \tag{4.6a}$$

In Fig. 4.1d, we show the four lowest-energy eigenstates of the 270-atomic armchair graphene triangle, where we also recognize the similarity to the single-particle wavefunctions of a particle in a potential box of triangular shape.

4.2.1 State Characterization

From their real-space appearance, we can derive many important properties of the energy states in the system. In particular, we are interested in geometrically exceptionally patterned states, and in the question if they participate in optical interaction mechanisms or not. Especially in Ch. 6, when we couple an adatom as impurity to the structure, we want to investigate how the states and their characteristics are modified in the process. To that end, we define scalar measures for the *localization* of a state, its *parity*, and its involvement in *optical absorption*. They are shortly discussed in the following.

Localization

The state localization $\mathcal{L}_j$ of state $|j\rangle$ is a measure for the number of atomic sites l that are considerably involved in the real-space expansion of the state. It is computed according to [A2]

$$\boxed{\mathcal{L}_j = \frac{(1 - p_j)N}{N - 1} \in [0, 1],} \tag{4.7}$$

where p_j is the participation ratio [217–220]

$$p_j = \frac{\left(\sum_{l=1}^{N} |a_{jl}|^2\right)^2}{N \sum_{l=1}^{N} |a_{jl}|^4} \overset{\langle j|j\rangle=1}{=} \left(N \sum_{l=1}^{N} |a_{jl}|^4\right)^{-1}. \tag{4.8}$$

The last equality folds for normalized states only, which we assume throughout the whole thesis. If the state is *fully localized* on a single site l_0, *i.e.* $a_{jl} = \delta_{ll_0}$, then $\mathcal{L}_j = 1$. On the

[1] In the discrete energy landscape of a finite molecular system, the terms *Fermi level*, *Fermi energy*, *valence and conduction bands*, and *band gap* are not well-defined in a strict sense. Instead, one should use terms like *HOMO*, *LUMO*, and *HOMO-LUMO gap* to characterize the occupation of states. However, to keep language simple, we use the expression *Fermi level* even when considering finite structures as follows: If the HOMO is fully occupied, the *Fermi* level is in the middle between the energies of the HOMO and the LUMO. If the HOMO is *not* fully occupied, the *Fermi* energy is identical to the energy of the HOMO.

other hand, $\mathcal{L}_j = 0$ if the state is uniformly distributed across the molecule, *i.e.* $a_{jl} = 1/\sqrt{N}$. Then, we call the state *delocalized*.

Parity

The parity $\mathcal{P}_j$ of state $|j\rangle$ is defined as

$$\mathcal{P}_j = \sum_{l=1}^{N} a_{jl} a_{j,N+1-l}, \tag{4.9}$$

where the labeling of the atoms should reflect the symmetry of the structure, such that $(x_l, y_l) = (-x_{N+1-l}, y_{N+1-l})$ if the structure is axisymmetric with respect to $x = 0$, for instance. The single-particle states of all stand-alone structures without adatom under investigation in this thesis have well-defined parity $\mathcal{P}_j \in \{-1, 1\}$. For ascending energy in structures with an even number of N atoms, the ground state is even, and even and odd parities alternate with $\mathcal{P}_1 = 1$, $\mathcal{P}_2 = -1$, $\mathcal{P}_3 = 1$, ..., $\mathcal{P}_{\mathrm{HOMO}} = -1$, $\mathcal{P}_{\mathrm{LUMO}} = 1$, ..., $\mathcal{P}_N = -1$. For the atomic chain and the graphene triangle, this behavior becomes apparent in Fig. 4.1, for example.

Absorption Activity

As we are particularly interested in the optical properties of the TB structures in the following, we introduce the optical absorption activity $\mathcal{A}_j$ of state $|j\rangle$ according to [A2]

$$\mathcal{A}_j = \sum_{j'=1}^{N} |s_{jj'}|. \tag{4.10}$$

Here, we make use of the oscillator strength

$$s_{jj'} = \left(E_j - E_{j'}\right) |\langle j|e\hat{\mathbf{r}}|j'\rangle|^2 \tag{4.11}$$

of the electronic single-particle transition $|j\rangle \to |j'\rangle$, and the real-space position operator $\hat{\mathbf{r}}$ acts as $\langle l|\hat{\mathbf{r}}|l'\rangle = \mathbf{r}_l \delta_{ll'}$. The quantity $\mathcal{A}_j$ measures if state $|j\rangle$ takes part in the dipolar optical interaction of the structure with electric fields. If $\mathcal{A}_j = 0$, the state population of $|j\rangle$ is unaffected during the optical interaction process, and we call the state optically *inert*. On the other hand, a high absorption activity indicates that $|j\rangle$ is involved in an optically active transition and acts as an electron acceptor or donor state.

Non-Interacting Absorption Cross-Section

For the sake of completeness, we also introduce the absorption cross-section for *non-interacting* electrons here [221],

$$\sigma_{\mathrm{abs}}^{\mathrm{ni}}(\omega) = \sum_{if} s_{if}\, \delta_\varepsilon \left(E_f - E_i - \hbar\omega\right), \tag{4.12}$$

where the oscillator strength of the transition $|i\rangle \to |f\rangle$ is introduced in Eq. (4.11) and $\delta_\varepsilon(x) = 2\varepsilon/(x^2 + \varepsilon^2)$ denotes *Dirac*'s delta distribution broadened to a Lorentzian by

$\varepsilon = 0.05\,\mathrm{eV}$. The summation in Eq. (4.12) runs over all *occupied initial* single-particle states $|i\rangle$ below the *Fermi* energy and *unoccupied final* states $|f\rangle$ above the *Fermi* energy. The non-interacting absorption cross-section is not a property of an individual state, but of the whole energy landscape and its population. Nevertheless, it is introduced here because it can be calculated from the eigenstates and eigenvalues of the structure alone. Calculating the *interacting* absorption cross-section, on the other hand, requires to propagate the system in time after it has been excited by a spectrally broad pulse and will be discussed in detail in Ch. 5.

Having introduced the TB methodology, we discuss in the following the electronic properties of the molecular SSH chains and finite graphene nanoantennas of different shapes and edge types.

4.3 *Su-Schrieffer-Heeger* Chains

Within the past 40 years, the literature on the SSH model has grown extensively [59–71]. The SSH model is capable of modeling a vast variety of properties of linear solid state molecules – both infinite and finite. Among them are the electronic structure, optical properties, and electronic transport characteristics of organic polymers [222], and the onset and formation of topological phases [64, 72] and quasiparticles [59, 73–75]. As it is analytically solvable to a large extent, the SSH model provides useful conceptual insights into the very basic physical principles and mechanisms that play a role in the molecules. Moreover, it constitutes a playground to investigate showcase examples for conducting metallic and insulating molecules. In nature, these are realized by linear polyenes and polyacetylenes, respectively. Whereas the electrons in the former behave as a one-dimensional homogeneous electron gas [121], the latter exhibits electron transport only if doped by additional external electrons to overcome the insulating band gap [76–78].

The three qualitatively different finite model chains in the SSH framework are shortly introduced below.

1. The metallic linear chain consisting of N atoms constitutes a prime example for a species that hosts plasmonic modes. Its atoms are equidistantly spaced and equally strongly coupled to their respective neighboring atoms. The coupling is quantified by the TB hopping parameter t.

2. The insulating dimerized chain, consisting of an *even* number of N atoms, constitutes a prime example for a species that hosts single-particle transitions only, as will be discussed in Ch. 8. As depicted in Fig. 4.2a, neighboring atoms are coupled by strong and weak bonds that alternate, starting with a *strong* bond at the edges. In this way, one can perceive the species as a chain of weakly coupled dimers.

3. The topologically insulating dimerized chain, consisting of an *even* number of N atoms, shares most optical properties with the dimer chain above. As depicted in Fig. 4.2b, neighboring atoms are coupled by strong and weak bonds that alternate, starting with a *weak* bond at the edges. Therefore, one can perceive the species as a chain of weakly coupled dimers, however with two dangling solitary atoms at the edges. These are responsible for near-zero energy states in the spectrum strongly localized at the edges of the chain.

The TB Hamiltonian of the chains reads

$$H_{\mathrm{TB}}^{\mathrm{chains}} = \quad (t+\Delta) \sum_{\text{odd } l=1}^{N-1} \Big(|l\rangle\langle l+1| + |l+1\rangle\langle l| \Big) + (t-\Delta) \sum_{\text{even } l=2}^{N-2} \Big(|l\rangle\langle l+1| + |l+1\rangle\langle l| \Big), \tag{4.13}$$

where we use $\Delta = 0$ for the linear chain, the dimer chain requires $\Delta > 0$, and the topological insulator is realized with $\Delta < 0$.

4.3.1 Energy Spectrum and States

In Fig. 4.2a, we show the energy landscape of the 20-atomic dimerized chain as a function of Δ as defined in Eq. (4.13) for $|\Delta| \leq 0.3|t|$. If $\Delta = 0$, the energy landscape of the linear chain in the optically active region around the *Fermi* energy is a set of almost equally spaced energy states. In that case, the states and their energies are analytically given by [64, A2]

$$|j\rangle = \sum_{l=1}^{N} \sqrt{\frac{2}{N+1}} \sin\left(\frac{jl\pi}{N+1}\right) |l\rangle, \qquad E_j = -2|t| \cos\left(\frac{j\pi}{N+1}\right). \tag{4.14}$$

We observe that with increasing $|\Delta|$, as the linear chain transforms into the dimer chain, a band gap $E_g = E_{\mathrm{LUMO}} - E_{\mathrm{HOMO}}$ opens up in the spectrum. In that way, two sets of closely spaced states below and above $E = 0$ form, reminiscent of the valence and conduction bands in an infinite solid, respectively. This transformation from a conductor to an insulator is also reflected in the real-space expansion of the single-particle states in Figs. 4.2c and 4.2d. Whereas the low-energy states are only mildly modified, especially the optically active states around the HOMO-LUMO gap change their shape considerably.

In Fig. 4.2b, the energy level diagram of the topological insulator is shown. In large part, its spectrum resembles Fig. 4.2a. However, unlike for the dimer chain, the HOMO and LUMO states do not move apart, but they approach each other and almost meet at $E = 0$. Their energies get exponentially close to zero with the chain size and with $|\Delta|$ [67].

4.3.2 State Characteristics

It is interesting to note that the **localization** of *all* states in the linear chain attains exactly the same value, independent of their energies. It can be computed analytically through Eqs. (4.7) and (4.14) to be $\mathcal{L}_j = \frac{1}{3}(1 - \frac{1}{N-1}) \quad \forall j$. For the dimer chain's states, this value is only marginally modified when Δ is varied, which can be seen in Fig. 4.2a. In contrast, the topological insulator's edge states behave more complex, see Fig. 4.2b. We observe that the localization of said states increases with Δ and even reaches 0.86 for $|\Delta/t| = 0.3$. In real space, this translates to high expansion coefficients at the edges of the chain, see $j = 10$ and $j = 11$ in Fig. 4.2e.

The **parity** of state $|j\rangle$ in all the chains is even if j is odd and vice versa, see Figs. 4.2c-e. Therefore, the transition dipole moments $d_{jj'} = |\langle j|e\hat{\mathbf{r}}|j'\rangle|$ of the transitions involving neighboring states, such as the HOMO-LUMO transition, is non-zero. Figure 4.3a shows the matrix elements $\hat{r}_{jj'}$ of the position operator for all three chains. Generally, we observe a checkerboard pattern of alternatingly vanishing and non-vanishing contributions. Moreover, transitions along the diagonal with small $\Delta j = |j - j'|$ attain

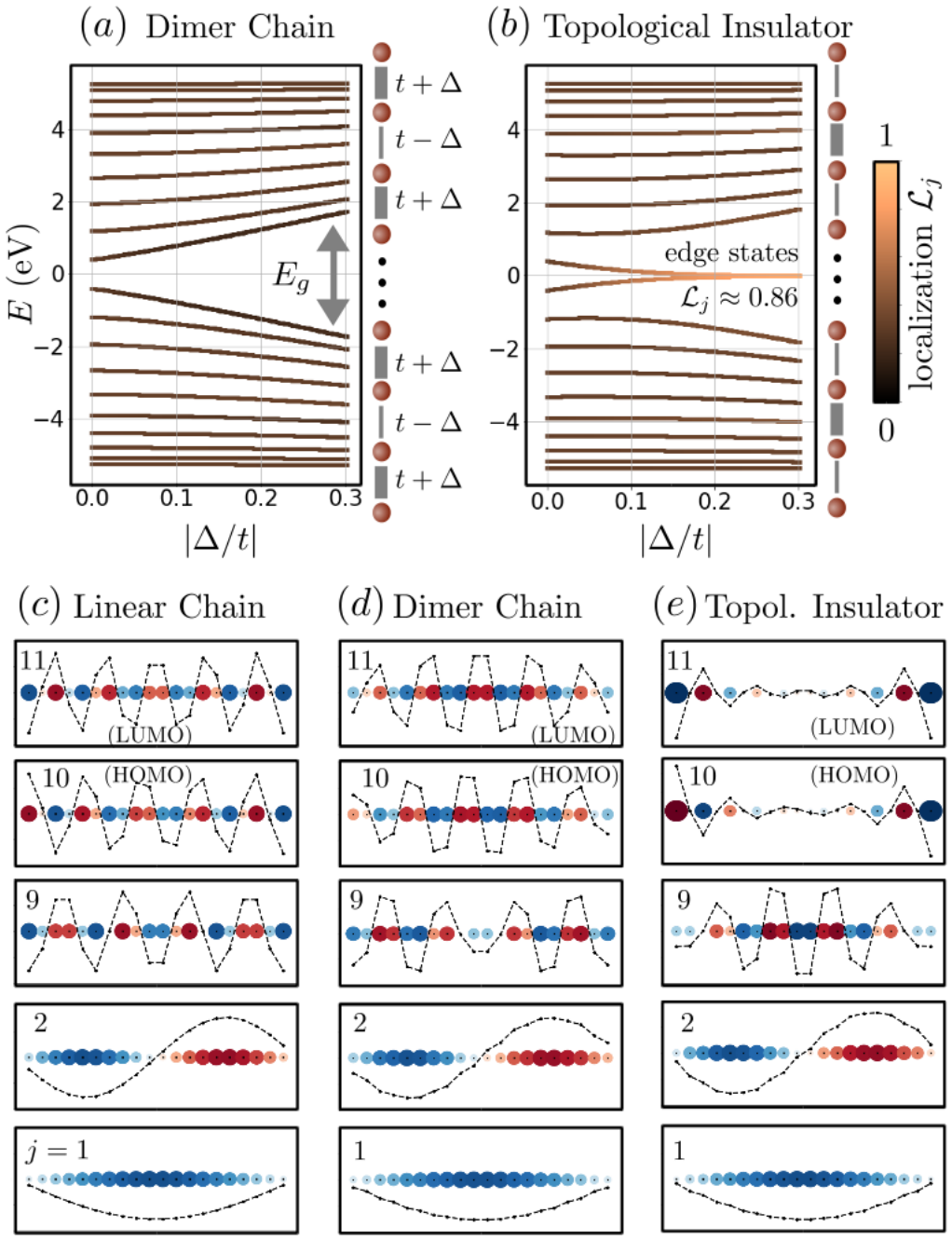

Figure 4.2: Energy level diagrams of the 20-atomic **(a)** dimer chain and **(b)** topological insulator for $|\Delta| \leq 0.3t$. For $\Delta = 0$, the linear chain is reproduced in both cases. The energy E_g indicates the HOMO-LUMO gap in the undoped dimer chain. The line color encodes the state localization $\mathcal{L}_j$, see Eq. (4.7). Single-particle eigenstates for $j \in \{1, 2, 9, 10, 11\}$ of the 20-atomic **(c)** linear chain, **(d)** dimer chain, and **(e)** topological insulator for $|\Delta| = 0.3t$.

the highest values. For the linear chain and the dimer chain, the HOMO-LUMO transition (at the intersection of the black dashed lines) shows the most prominent contribution. The dimer chain and the topological insulator additionally exhibit non-zero values on the anti-diagonal. Moreover, it is noteworthy that the HOMO-LUMO transition between the edge states does *not* play a prominent role in the optical interaction of the topological insulator, as is apparent by the relatively small transition dipole moment for

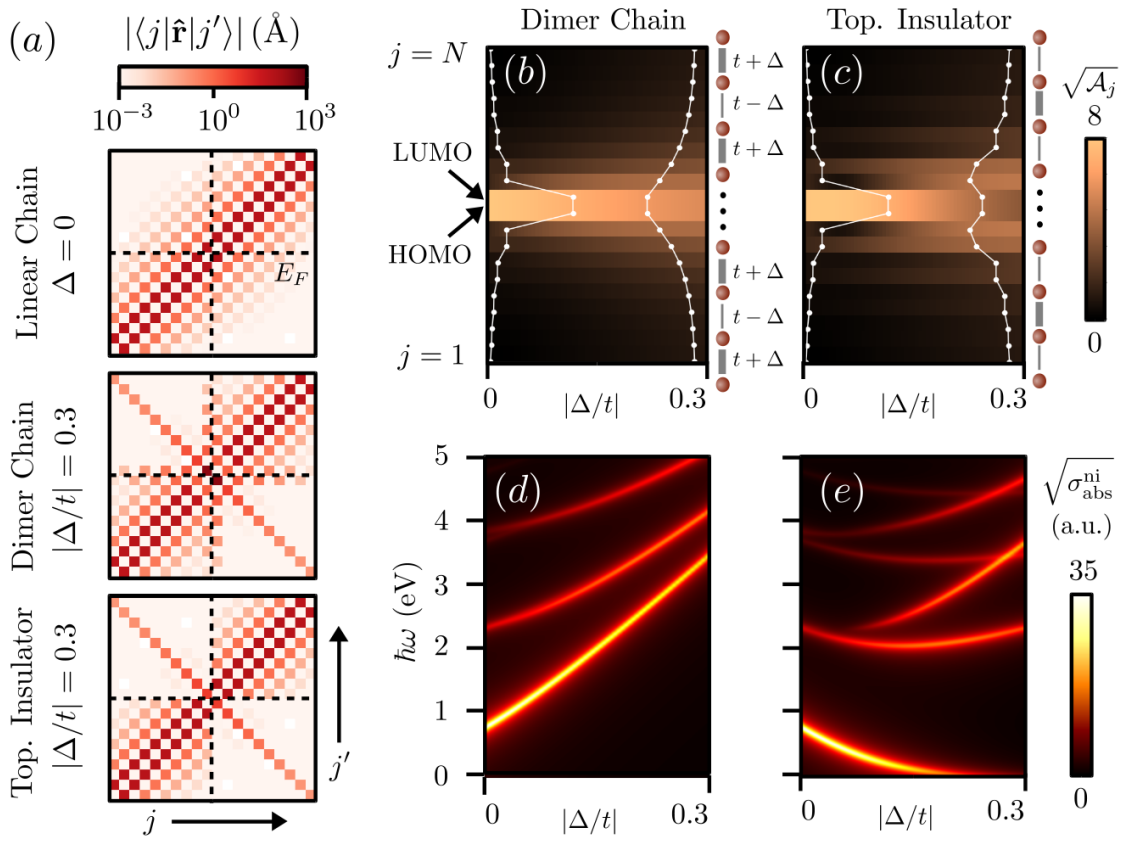

Figure 4.3: **(a)** Matrix elements $|\langle j|\hat{\mathbf{r}}|j'\rangle|$ of the states in the 20-atomic SSH chains. The black dashed lines indicate the *Fermi* energy in undoped chains. Square root of the absorption activity $\sqrt{\mathcal{A}_j}$ for the 20-atomic **(b)** dimer chain and **(c)** topological insulator. The white insets correspond to the absorption activities for $|\Delta/t| = 0$ (linear chain) and 0.3, respectively. Square root of the non-interacting absorption cross-section for the 20-atomic **(d)** dimer chain and **(e)** topological insulator.

$|\Delta/t| = 0.3$ (note the logarithmic color scale). Also, their energy difference exponentially approaches zero, which additionally quenches the transition's oscillator strength, *c.f.* Eq. (4.11). However, as we will see below, the edge states are nevertheless efficiently coupled to the states well above and below $E = 0$, resulting in additional absorption modes in the band gap of the dimer chain that the latter lacks.

The observation of the optical inactivity of the HOMO-LUMO transition in the topological insulator is supported by investigating the **absorption activity** $\mathcal{A}_j$. In Fig. 4.3b, we note that in the course of the transition from the linear ($|\Delta/t| = 0$) to the dimer chain ($|\Delta/t| = 0.3$), the HOMO and LUMO states become less optically active, compensated by the gain of activity of all other states below and above the HOMO and LUMO. The states in the topological insulator behave similarly, see Fig. 4.3c. However, the HOMO and LUMO states are not the most optically active ones because they are not coupled to each other with a high dipole moment like it is the case in the other two chains.

Figure 4.3 shows the non-interacting optical **absorption cross-section** $\sigma^{\mathrm{ni}}_{\mathrm{abs}}(\omega)$ of the (d) dimer chain and (e) topological insulator as a function of $|\Delta/t|$ (the linear chain is obtained for $\Delta = 0$). The opening of the band gap as Δ increases consequently leads to a blue-shift of the fundamental mode in the dimer chain, which originates almost exclu-

sively from the HOMO-LUMO transition [A2]. Likewise, all other modes shift to higher energies, opening up a transparency window in the visible frequency range.

The fundamental mode in the topological insulator, on the other hand, red-shifts, since the edge states that produce the mode approach each other for increasing $|\Delta/t|$. The other modes both red-shift and blue-shift partly, depending on the involvement of the edge states in the formation of the modes. The next higher mode between 2 and $2.4\,\mathrm{eV}$, for example, stemming from the transition $|\mathrm{HOMO}\rangle \rightarrow |\mathrm{LUMO}+2\rangle$, first red-shifts for $0 \leq |\Delta/t| \leq 0.15$ because the HOMO edge state tends toward zero from below faster than the state $|\mathrm{LUMO}+2\rangle$ departs from it (see Fig. 4.2b). Therefore, the transition energy is effectively reduced. After the edge state has reached zero, though, the mode blue-shifts again for $|\Delta/t| > 0.15$, and the topological insulator qualitatively behaves like the dimer chain with an additional set of modes in the band gap of the latter. Also in the *interacting* system, we will see in the following that the optical properties of the dimer chain and the topological insulator differ only marginally. Thus, the topological insulator will not play an important role in the discussion of optical properties of the chains. Only later in Ch. 6, when it comes to the investigation of the hybrid system where a foreign atom is coupled to the edge of the topological insulator, we see significant differences.

4.4 Graphene Nanoantennas

After we have introduced the chain model systems, we move on to the graphene nanoantennas discussed in detail in later chapters. There is a huge body of literature on the electronic and optical properties of finite graphene nanoantennas, including several review articles [51, 223–228] and even textbooks devoted to the topic [50, 143, 229]. This work is not intended to be another comprehensive review of the properties of graphene nanoantennas, but we rather capitalize on their tuning properties for our study of nonlinear effects in Ch. 5 and plasmonics on the nanoscale in Ch. 8. Thus, we discuss below exemplarily the triangular armchair- and zigzag-edged graphene triangles, as well as a rectangle, that hosts both edge types simultaneously.

Armchair Graphene Triangle

In Fig. 4.4a, the energy landscape of a 546-atomic armchair-edged graphene nanotriangle with side length $5.4\,\mathrm{nm}$ in the optically active energy region around $E = 0$ is shown. The system exhibits two sets of closely spaced states below and above $E = 0$, reminiscent of the valence and conduction bands in infinite structures, that are separated by a band gap of $0.8\,\mathrm{eV}$. Therefore, the system electronically behaves like a semiconductor with a small band gap that can easily be overcome by additional doping electrons. The insets show the real-space expansions of selected single-particle eigenstates including the HOMO and LUMO $j = 273$ and 274, respectively. All states in the structure are *bulk* states and extend over a large part of the molecule. Moreover, the remaining symmetry considerations that apply to the dimer chain, also apply to the triangle. In particular, the electronic transition from the HOMO to the LUMO states is dipole-allowed and produces a bright fundamental mode at $\hbar\omega = 0.8\,\mathrm{eV}$ in the associated absorption cross-section.

Zigzag Graphene Triangle

Figure 4.4b shows the energy landscape of the 526-atomic zigzag-edged graphene triangle with side length $5.2\,\mathrm{nm}$, in the optically active energy region around $E = 0$. Here, we see 20 zero-energy states in the band gap, reminiscent of the edge states in the topological insulator chain. Indeed, the real-space insets reveal that all these zero-energy states

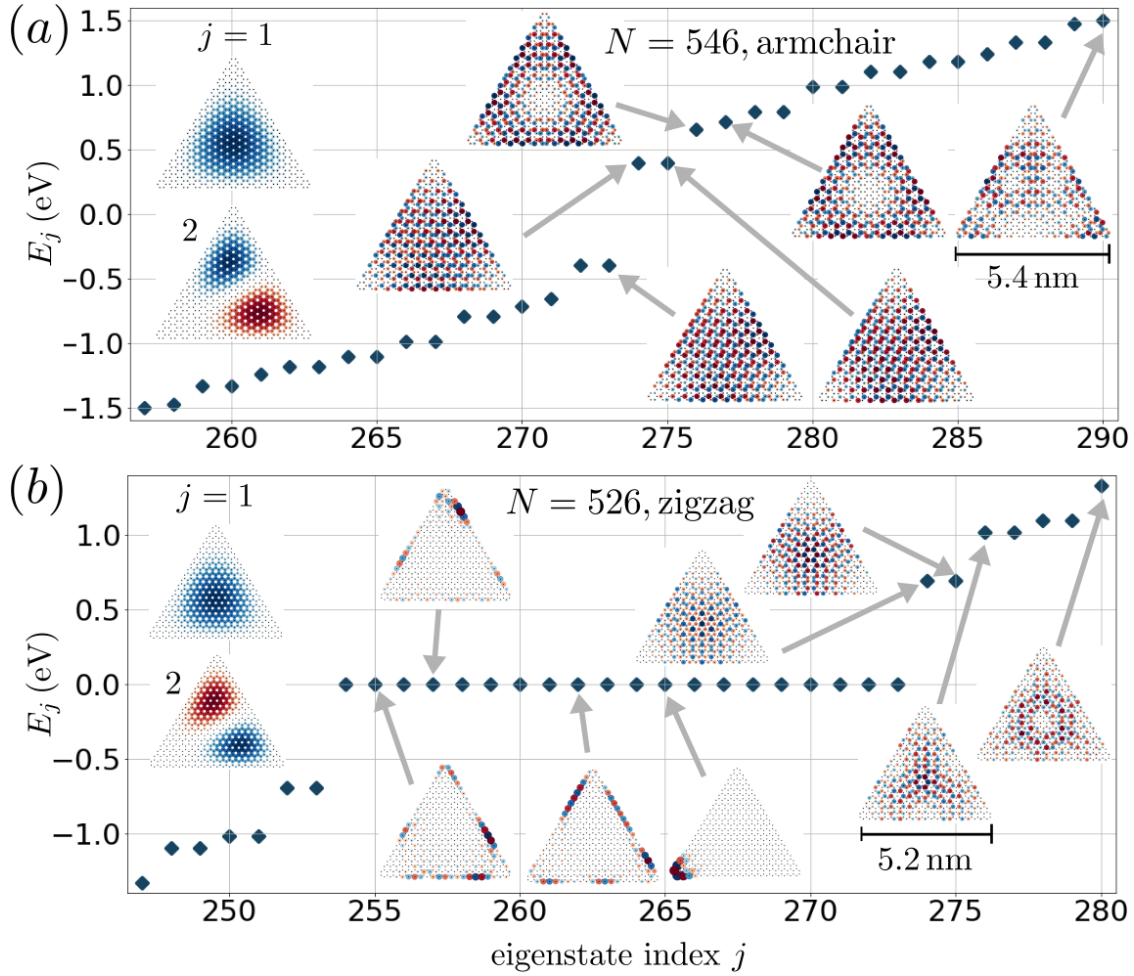

Figure 4.4: Energy landscape of a triangular graphene nanoantenna **(a)** with $N = 546$ atoms, side length $5.4\,\mathrm{nm}$ and armchair edges and **(b)** with $N = 526$ atoms, side length $5.2\,\mathrm{nm}$ and zigzag edges around $E = 0$. The insets show the real-space expansions of selected states for $j = 1$ and 2, as well as in the optically active region around $E = 0$.

are localized at the edges of the triangle, whereas states with $j < 254$ and $j > 273$ are bulk states. Moreover, we note that in the low- and high-energy regions, the single-particle states of the armchair and zigzag triangles look qualitatively the same, see the insets for $j = 1$ and 2. Also, it gets apparent from Fig. 4.4b why zigzag graphene nanoantennas are not suitable candidates as tunable optical nanostructures.[2] In total, the 20 degenerate edge states offer space for 40 electrons, of which only 20 are present in the neutral species. Therefore, it is necessary to dope with 21 additional electrons to change the *Fermi* energy by populating the first non-zero bulk state $j = 274$ and, consequently, to achieve a modification of the absorption cross-section, for example [45]. For that reason, we focus in the following chapters of this thesis on armchair-edged structures only.

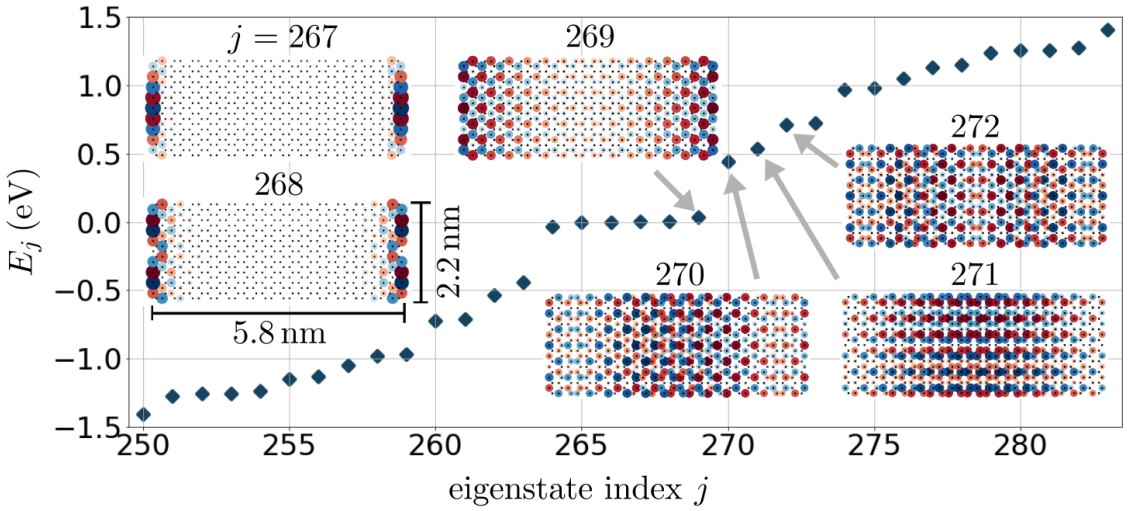

Figure 4.5: Energy landscape of a 532-atomic graphene rectangle with armchair edges on the horizontal edge and zigzag edges on the vertical edges around $E = 0$. The insets show selected states in the optically active region in real space.

Graphene Rectangle

Finally, we present the hybrid-edged 532-atomic rectangular graphene nanoantenna with width $2.2\,\mathrm{nm}$ and length $5.8\,\mathrm{nm}$. The horizontal edges at the top and at the bottom are of armchair type, whereas the left and right vertical terminations exhibit zigzag edges. The structure's energy landscape is shown in Fig. 4.5 and exhibits four zero-energy states ($265 \leq j \leq 268$) and two near-zero states ($j = 264, 269$). It is noteworthy, that the zero-energy states are fully localized at the left and right zigzag edges of the rectangle. Also the near-zero state $j = 269$ exhibits a strong localization toward the edges, whereas the states further away from zero, $j < 264$ and $j > 269$, are bulk states. We conclude that also in structures with both edge types, only the zigzag edges lead to zero-energy edge states.

4.5 Conclusions

In this chapter, we have introduced a TB formalism to determine the electronic structure and single-particle eigenstates of planar carbon-based molecules. Also, we have proposed scalar measures to assess the localization, parity, and absorption activity of said states, that will be of use to engineer the absorption properties of hybrid systems in Ch. 6. We have then extensively discussed the electronic structure of the three *Su-Schrieffer-Heeger* chains as model systems for metallic, insulating, and topologically insulating finite molecular species. In the last section, we have shown that the formalism can also be applied to graphene nanostructures, and that their electronic and optical behavior can be easily deduced from the insights that were obtained from the chains. Furthermore, we have motivated why we will concentrate only on armchair-edged graphene nanoantennas when discussing optical effects in the following.

[2]Zigzag-edged graphene structures offer interesting favorable physical properties in other fields, like spin-polarized edge states in nanoribbons and strong resulting magnetic moments [230–233], for instance. The near-degenerate edge states can furthermore be harnessed in terahertz spectroscopy [185, 234].

In the next chapter, we present an extension of the above formalism that allows to couple the TB structures to electric fields in time-domain and report on an application that shows higher harmonic generation in *Su-Schrieffer-Heeger* chains and graphene nanotriangles.

5 | Optical Properties of Planar Carbon Molecules

5.1 Introduction

In the previous chapter, we have introduced a TB formalism to obtain the electronic structure of planar carbon-based molecules. Both eigenenergies and eigenstates in the single-particle description can be obtained for relatively large structures at low computational cost compared to *ab initio* methods. In 2012, Thongrattanasiri *et al.* first approached the problem to resolve the atomistic structure of graphene in the field of nanoplasmonics within the TB framework [44]. To that end, they applied the random phase approximation (RPA) in frequency domain to the TB electronic structure of graphene antennas and developed the theory further in subsequent works [45, 79–81, 235].

In contrast to that prior work, this chapter is dedicated to the introduction of a *time-domain* simulation method that evolved from the previously mentioned TB-RPA framework. It has initially been developed by Cox and García de Abajo [47] and is superior to the frequency-domain TB-RPA approach in the sense that *nonlinear* optical effects are accessible as well. Hence, after introducing the formalism, we prove the latter by investigating the nonlinear effect of higher harmonic generation in the linear chain, the dimer chain, and a triangular armchair graphene nanoantenna.

5.2 Simulation Method

The simulation method is based on a single-particle density operator description that captures the structure's state and its dynamics in the TB framework. Even though we work in a single-particle description, it is capable of providing the optical properties of *interacting* electrons as well. It does so by taking into account the *Coulomb* interaction in the time propagation of the density operator. From the time-dependent *Schrödinger* equation

$$\mathrm{i}\hbar\frac{\partial}{\partial t}|\Psi(t)\rangle = H(t)|\Psi(t)\rangle \tag{5.1}$$

and its adjoint, we can directly deduce the *Liouville-von Neumann* equation of motion for the density operator $\rho(t) = |\Psi(t)\rangle\langle\Psi(t)|$ that reads

$$\frac{\partial}{\partial t}\rho(t) = -\frac{\mathrm{i}}{\hbar}\left[H(t), \rho(t)\right], \tag{5.2}$$

where $[\cdot,\cdot]$ denotes the commutator, and the Hamiltonian is assumed to be explicitly time-dependent, as it contains a time-varying electric field in our approach. Since Eq. (5.2) is energy-conserving, we need to modify it to take into account dissipative processes in

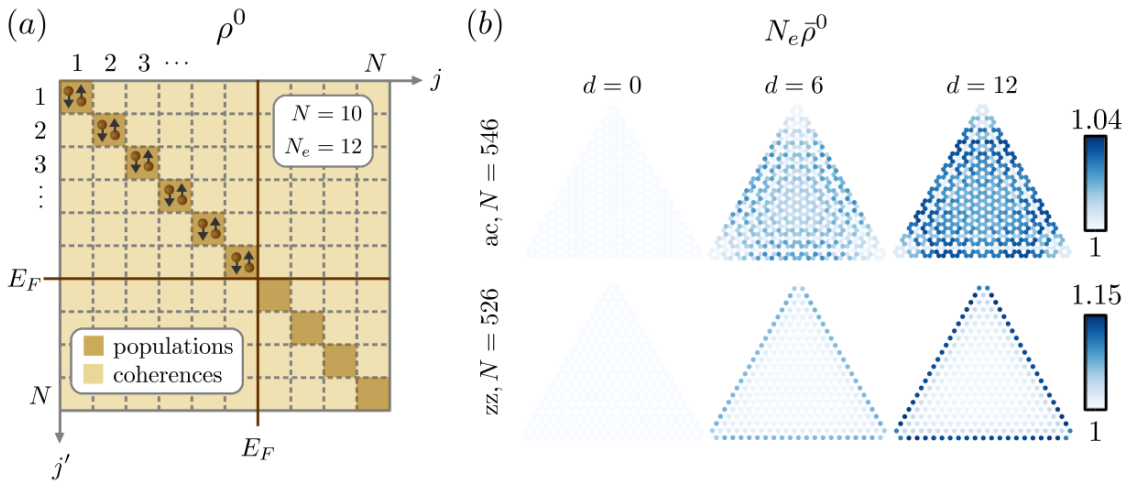

Figure 5.1: (a) Schematic illustration of the matrix elements of the initial density operator in energy basis, $\rho^0_{jj'}$, constructed according to the *aufbau* principle in Eq. (5.4). **(b)** Number of electrons in each p_z orbital at the respective atom in an armchair (top row) and zigzag (bottom row) triangle for different doping levels d in the structure, after the energy-space density matrix has been constructed according to the *aufbau* principle in (a). Note that in the electrically neutral structure ($d = 0$), we have one electron per atomic site in the associated p_z orbital.

the electron dynamics as well. To that end, we add a dissipative term and propagate the density operator according to [47, 236]

$$\frac{\partial}{\partial t}\rho(t) = -\frac{\mathrm{i}}{\hbar}\left[H(t), \rho(t)\right] - \frac{1}{2\tau}\left(\rho(t) - \rho^0\right) \tag{5.3}$$

in our simulations. Here, we adopted a phenomenological relaxation time approximation with an electron scattering time in the order of $\hbar\tau^{-1} \approx 10\,\mathrm{meV}$ [47, 48, 50, 80, 142]. It accounts for all kinds of dissipative processes, such as plasmonic decay through coupling to phononic channels and radiation loss. Moreover, we defined the ground state density operator $\rho^0 := \rho(t = 0)$, which characterizes the system in its equilibrium state at $t = 0$ before any interaction with the external electromagnetic illumination.

5.2.1 Ground State Construction

We follow the notation of the previous chapter and consider a TB Hamiltonian H_{TB} of an N-atomic structure. The N real-space site basis vectors consisting of the carbon p_z orbitals are labeled with $\{|l\rangle\}$ for $1 \leq l \leq N$. Moreover, upon diagonalization of H_{TB}, we find the set of energy eigenstates $\{|j\rangle\}$ with $H_{\mathrm{TB}}|j\rangle = E_j|j\rangle$ and $|j\rangle = \sum_l a_{jl}|l\rangle$, where the expansion coefficients a_{jl} are defined and discussed in Sec. 4.2.

The ground state density operator ρ^0 is constructed in energy space by incoherently filling the diagonal of ρ^0 with π electrons according to the *aufbau* principle, where each state can host two electrons of opposite spin, see Fig. 5.1a. Accordingly, we have

$$\rho^0 = \frac{1}{N_e}\sum_{jj'} f_j(N_e)\delta_{jj'}|j\rangle\langle j'|, \tag{5.4}$$

with the *Fermi-Dirac* distribution $f_j(N_e) = \left(\exp\left(\frac{E_j - E_F(N_e)}{k_\mathrm{B}T}\right) + 1\right)^{-1}$, where E_F is the *Fermi* energy that depends on the number of π electrons N_e in the system, and k_B denotes *Boltzmann*'s constant k_B.[1]

To track the electronic motion across the atoms in the molecule and to obtain the induced charge, we need to convert the density operator to the real-space basis set $\{|l\rangle\}$. Therefore, at any point in time, we can obtain the matrix elements $\bar{\rho}_{ll'}(t)$ in site basis from the energy-space matrix elements $\rho_{jj'}(t)$ and vice versa according to the basis change

$$\bar{\rho}_{ll'}(t) = \sum_{jj'} a_{jl} a_{j'l'} \rho_{jj'}(t) \qquad \text{and} \qquad \rho_{jj'}(t) = \sum_{ll'} a_{jl} a_{j'l'} \bar{\rho}_{ll'}(t), \tag{5.5}$$

with the a_{jl} defined in Eq. (4.4). For instance, the induced charge on atom l at position $\mathbf{r}_l = (x_l, y_l)$ can be determined as $q_l^\mathrm{ind}(t) = -eN_e\left(\bar{\rho}_{ll}(t) - \frac{1}{N}\right)$. The initial state in real space is shown in Fig. 5.1b for an armchair (top row) and zigzag (bottom row) edged graphene nanotriangle for different numbers of additional doping electrons d, such that the total number of electrons in the structure is $N_e = N + d$. Precisely, we show the number $N_e\bar{\rho}_{ll}^0$ of electrons in the p_z orbital of atom l. In the armchair structure, the additional charge is more or less distributed across the whole antenna, whereas in the zigzag structure, the additional doping electrons populate the zero energy edge states and are located at the edges of the triangle.

5.2.2 Coupling to the Electric Field

To study the interaction of the molecule with external electric fields, we couple its Hamiltonian H_TB to the electric potential $\varphi(\mathbf{r}, t)$ it is exposed to,

$$H(t) = H_\mathrm{TB} - e\varphi(\mathbf{r}, t). \tag{5.6}$$

Here, the total electric potential $\varphi(\mathbf{r}, t) = \varphi^\mathrm{ext}(\mathbf{r}, t) + \varphi^\mathrm{ind}(\mathbf{r}, t)$ is the sum of the electric potential of the externally applied field and the potential induced in the structure by a non-uniform charge distribution. The structures under investigation have characteristic length scales much smaller than the wavelength of the external illumination. Therefore, a dipolar coupling scheme in the quasistatic limit as introduced in Sec. 2.7 is justified, and we assume that the electric field is spatially uniform across the structure, $\mathbf{E}(\mathbf{r}, t) = \mathbf{E}(t)$. Hence, the external potential operator is linear in space and diagonal in site basis. It reads

$$\varphi^\mathrm{ext}(\mathbf{r}, t) = -\sum_{ll'} \mathbf{r}_l \cdot \mathbf{E}(t) \delta_{ll'} |l\rangle\langle l'|. \tag{5.7}$$

In classical electrodynamics, the induced potential $\varphi^\mathrm{ind}(\mathbf{r}, t)$ can be obtained from the induced charge density $\rho^\mathrm{ind}(\mathbf{r}, t)$ by [131]

$$\varphi^\mathrm{ind}(\mathbf{r}, t) = \frac{1}{4\pi\varepsilon_0} \int \mathrm{d}^3\mathbf{r}' \frac{\rho^\mathrm{ind}(\mathbf{r}', t)}{|\mathbf{r} - \mathbf{r}'|}. \tag{5.8}$$

[1] At room temperature $T = 300\,\mathrm{K}$, the thermal energy of an electron is $k_\mathrm{B}T \approx 26\,\mathrm{meV}$. On the other hand, the modification of the *Fermi* energies in the structures under investigation in this thesis is readily in the order of several hundreds of meV even when doping with single electrons. Therefore, we do not explicitly study the effect of temperature variation here, since this effect lags behind the effect of doping.

In the site basis of our TB framework, Eq. (5.8) translates to the induced potential operator[2]

$$\varphi^{\mathrm{ind}}(\mathbf{r},t) = -\lambda e N_e \sum_{ll'} \sum_{l''} v_{ll''} \left(\bar{\rho}_{l''l''}(t) - \frac{1}{N} \right) \delta_{ll'} |l\rangle\langle l'|, \tag{5.10}$$

where we used the *Coulomb* interaction matrix v. Its elements $v_{ll'}$ couple the electrons on the atomic sites l and l' *via Coulomb* interaction. For atoms far away from each other, we employ the usual $1/|\mathbf{r}_l - \mathbf{r}_{l'}|$ power law [44] from Eq. (5.8). Elements that couple atoms close to each other have been explicitly calculated by Potasz *et al.* [186]. For a detailed discussion on the computation of the *Coulomb* interaction matrix, see App. B.1. Moreover, motivated by previous work from Bernadotte *et al.* [121], we have introduced a *scaling parameter* $\lambda \in [0,1]$, that can be used to artificially switch the *Coulomb* interaction off and on. By this means, a continuous transition can be created between systems with non-interacting ($\lambda = 0$) and interacting ($\lambda = 1$) electrons. Especially in Ch. 8, where we introduce the energy-based plasmonicity index and discuss the nature of plasmonic modes in small molecules, this feature will be of paramount importance.

5.2.3 Density Operator Evolution

In our simulation framework, the equation of motion for the density operator $\rho(t)$, Eq. (5.3), is implemented in site basis, since the electric potential is diagonal in this case. Plugging in all above-introduced expressions and additionally using $H_{\mathrm{TB},ll'} = -t\delta_{\langle l,l'\rangle}$, where $\delta_{\langle l,l'\rangle} = 1$ if l and l' are nearest neighbors and $\delta_{\langle l,l'\rangle} = 0$ otherwise, we obtain[3]

$$\begin{aligned}
\frac{\partial}{\partial t}\bar{\rho}_{ll'}(t) = &-\frac{\mathrm{i}}{\hbar} t_{\mathrm{TB}} \sum_{l''} \left(\bar{\rho}_{ll''}(t)\delta_{\langle l'',l'\rangle} - \bar{\rho}_{l''l'}(t)\delta_{\langle l,l''\rangle} \right) && \text{TB} \\
&-\frac{\mathrm{i}e}{\hbar} (\mathbf{r}_l - \mathbf{r}_{l'}) \cdot \mathbf{E}(t) \bar{\rho}_{ll'}(t) && \text{external} \\
&-\frac{\mathrm{i}\lambda e^2 N_e}{\hbar} \sum_{l''} (v_{ll''} - v_{l'l''}) \left(\bar{\rho}_{l''l''}(t) - \frac{1}{N} \right) \bar{\rho}_{ll'}(t) && \text{induced} \\
&-\frac{1}{2\tau} \left(\bar{\rho}_{ll'}(t) - \bar{\rho}^0_{ll'} \right). && \text{dissipation}
\end{aligned} \tag{5.11}$$

First, let us emphasize that the first three lines on the right hand side of Eq. (5.11) are purely imaginary and, therefore, free of dissipation (in case ρ is real). The only term that comprises losses is the purely real-valued fourth line. Moreover, from the term proportional to $\bar{\rho}^2$ in the third line, it gets apparent that the time evolution is nonlinear in ρ if and only if electron-electron interaction is taken into account, *i.e.* if $\lambda > 0$.

[2] In the original works where this time-dependent framework has been introduced [47, 237], one finds

$$\varphi^{\mathrm{ind}}(\mathbf{r},t) = -\lambda e N_e \sum_{ll'} \sum_{l''} v_{ll''} \left(\bar{\rho}_{l''l''}(t) - \bar{\rho}^0_{l''l''} \right) \delta_{ll'} |l\rangle\langle l'|, \tag{5.9}$$

instead of Eq. (5.10). There, it is implicitly assumed that the structure does not have a static dipole moment *prior* an excitation with an electric field. However, this assumption ($\bar{\rho}^0 = \mathbb{1}/N$) is strictly true only for undoped structures. Therefore, we modified Eq. (5.9) and use the more general expression in Eq. (5.10) instead.

[3] In literature, the letter t is consistently assigned both to the *TB hopping parameter* and to *time*. We want to stick to this convention as the context always clarifies if the former or latter is meant. However, to not confuse them in Eq. (5.11) where both appear simultaneously for the only time in this thesis, we use t_{TB} as the TB hopping parameter. Time remains t.

From the solutions $\bar{\rho}_{ll'}(t)$ of Eq. (5.11), one can calculate – among others – the following quantities of interest:

1. **Dipole Moment:** The diagonal elements of the density operator in site basis, $\bar{\rho}_{ll}(t)$, reveal the fractions of the total number of π-electrons located in the p_z orbital of atom l at $\mathbf{r}_l$. From that, the induced dipole moment $\mathbf{p}(t)$ can be directly calculated according to

$$\boxed{\mathbf{p}(t) = -eN_e \sum_l \mathbf{r}_l \left(\bar{\rho}_{ll}(t) - \frac{1}{N} \right).} \tag{5.12}$$

2. **Change in Occupation Probability:** The diagonal elements of the density operator in energy basis, $\rho_{jj}(t)$, reveal the fractions of the total number of π-electrons that populate state $|j\rangle$ at time t. In particular, it can be tracked which states participate in the optical interaction if the given share changes in time. Therefore, we compute the change of state population with respect to the ground state ρ^0,

$$\boxed{\Delta P(j,t) = \left(\rho(t) - \rho^0\right)_{jj} = \rho_{jj}(t) - f_j.} \tag{5.13}$$

3. **Coherences:** The off-diagonal elements of the density operator in energy basis, $\rho_{jj'}(t)$ with $j \neq j'$, quantify to what extent the states $|j\rangle$ and $|j'\rangle$ couple and interchange electronic population at time t. In Ch. 8, this information will be used to identify which electronic transitions contribute to which optical modes, and constitutes the basis for the construction of the energy-based plasmonicity index.

From the dipole moment $\mathbf{p}(t)$ in Eq. (5.12), we can compute the polarizability upon *Fourier* transformation, $\alpha_{ij}(\omega) = \tilde{E}_i(\omega)^{-1} \int \mathrm{d}t\, p_j(t) \mathrm{e}^{\mathrm{i}\omega t}$, where $i, j \in \{x, y, z\}$ and $p_j(t)$ is the jth component of the dipole moment that was induced by the ith component of the incident electric field. The interacting absorption cross-section is then obtained through

$$\boxed{\sigma_{\mathrm{abs}}(\omega) = \frac{\omega}{\varepsilon_0 c_0} \operatorname{Im} \left(\sum_{i,j \in \{x,y,z\}} \alpha_{ij}(\omega) \right).} \tag{5.14}$$

Please note that the non-interacting absorption cross-section in Eq. (4.12) and the quantity in Eq. (5.14) coincide if $\lambda = 0$ was chosen for the time propagation Eq. (5.11).

5.2.4 Dependence of Optical Modes on Structure Size

The size dependence of the optical modes both for non-interacting and interacting systems is investigated exemplarily for even-numbered N-atomic linear chains in Fig. 5.2 with $N \in [8, 100]$. To observe the relatively weak higher order modes as well, we show the fourth roots of the absorption cross-sections. For non-interacting electrons (a), we notice considerably more modes at lower energies for a given number N of atoms in the chain as compared to interacting electrons (b). The energies of the modes scale as N^{-1} for all mode orders and both for non-interacting and interacting electrons.[4] In the non-

[4] Please note that for two-dimensional structures like graphene antennas, the energies of the modes in differently sized structures scale as $N^{-1/2}$. This originates from the fact that the length (area) in a one-dimensional (two-dimensional) structure scales with N. Other than that, the qualitative behavior of the size dependence is the same and, therefore, not explicitly discussed for graphene antennas in this thesis.

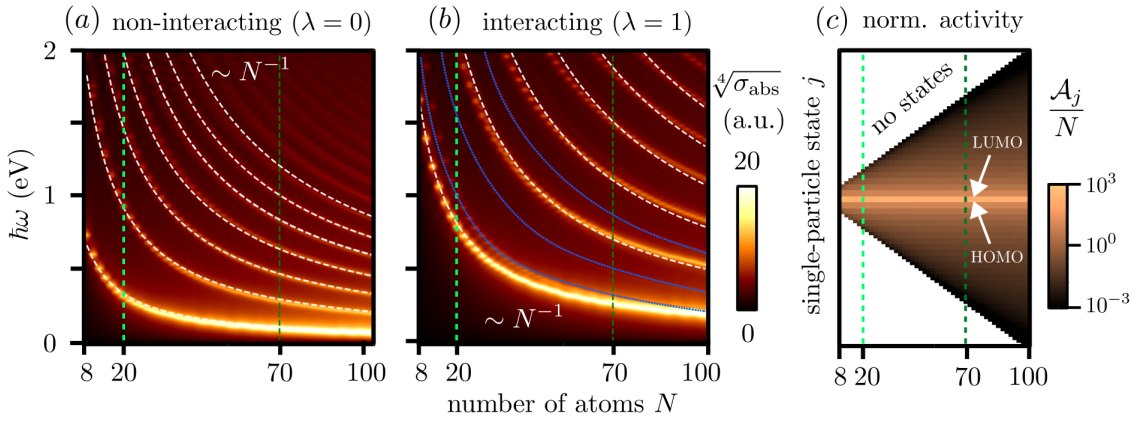

Figure 5.2: Linear absorption cross-sections of the linear polyene chain ($\Delta = 0$) with different sizes for an even number of $N \in [8, 100]$ atoms. We show the results in **(a)** for non-interacting and in **(b)** for interacting electrons. The white dashed lines fall off as $1/N$. **(c)** Normalized absorption activity $\mathcal{A}_j/N$ of the linear chain's states. The light (dark) green dashed lines in all subfigures indicate $N = 20\,(70)$, which is the length of the chains investigated in more detail in this work.

interacting system, we find very flawless mode profiles, descending in intensity with the mode order. It is straightforward to assign the modes to the respective single-particle transitions in the energy landscape of the chain. The brightest low-energy mode corresponds to the HOMO-LUMO transition, whereas the next higher order mode is formed by $|\text{HOMO}\rangle \to |\text{LUMO}+2\rangle$, $|\text{HOMO}-1\rangle \to |\text{LUMO}+1\rangle$, and $|\text{HOMO}-2\rangle \to |\text{LUMO}\rangle$, for symmetry reasons, and so on for increasing mode orders [A2], *c.f.* also Fig. 4.3a for $N = 20$. This assignment of modes to single-particle transitions in the energy landscape is no longer possible in the interacting system. Here, the mode energies are not determined by electronic transition energies, but predominantly by *Coulomb* interaction energy that shifts the modes to the blue. Also, besides the bright prominent modes, marked with white dashed lines in Fig. 5.2b, we additionally observe much fainter ones in between (blue dotted lines).

Figure 5.2c shows the size-normalized absorption activity of the states in the linear chain for several chain lengths. We notice that the length of the chain does not have any impact on which states participate in the optical interaction of the chain. For all lengths, the transition between the HOMO and LUMO states is responsible for the lowest-energy prominent mode. All other states contribute much less to the absorption spectrum (note the logarithmic color scale). We conclude, therefore, that no qualitative differences are expected regarding the optical interaction mechanisms when considering atomic chains with different lengths within the investigated range.

In Ch. 8, we will make extensive use of the simulation framework introduced in this section. On the one hand, we will determine absorption spectra and induced charge dynamics as functions of electron doping and *Coulomb* interaction strength. On the other hand, energy-space state population analysis and coherence dynamics reveal which single-particle transitions intrinsically lead to the formation of optical modes both in the SSH chains and in graphene nanoantennas. To close this chapter, we present simulation results in the next section, where we apply the above-introduced framework to the structures already presented in Ch. 4.

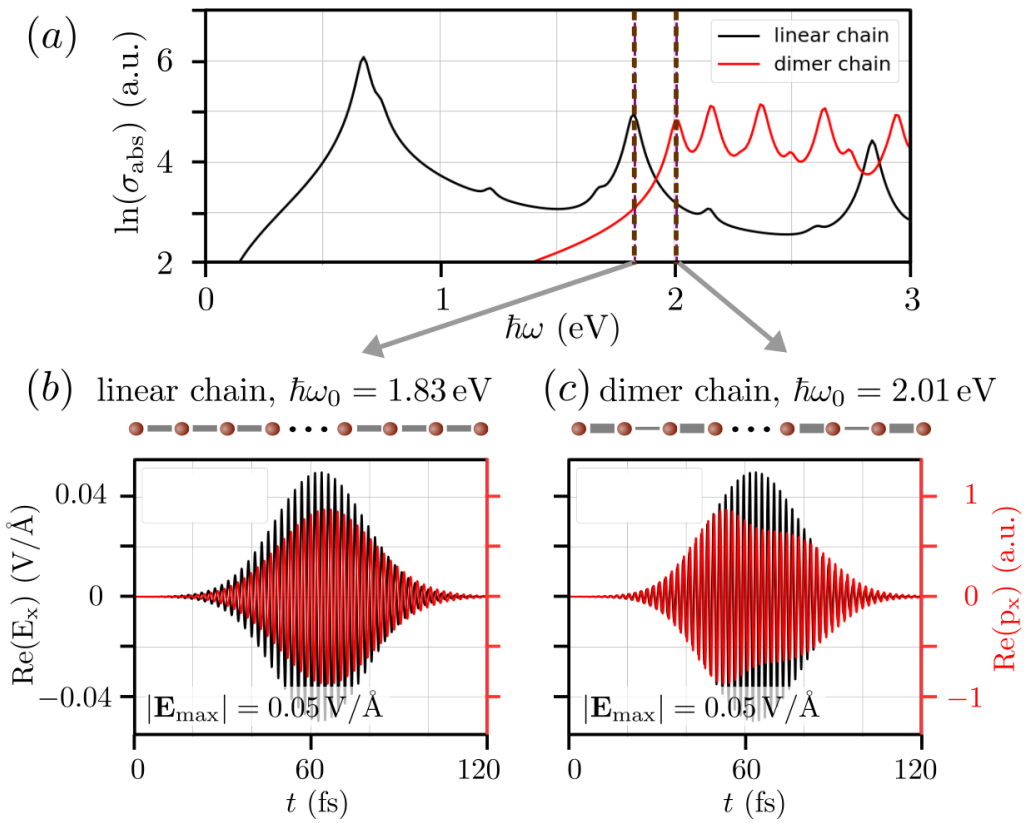

Figure 5.3: **(a)** Logarithms of the interacting absorption cross-sections of the 70-atomic linear (black) and dimer (red) chains with $\Delta = 0.18t$. Vertical dashed lines indicate the resonances at 1.83 and $2.01\,\mathrm{eV}$, investigated in (b) and (c). **(b)** Electric field component (in $\mathrm{V/Å}$) of the excitation pulse along the chain direction with carrier frequency $1.83\,\mathrm{eV}$ (black, left axis) and corresponding induced dipole moment (red, right axis) as a function of time. **(c)** Same as (b), but for the dimer chain, excited with carrier frequency $2.01\,\mathrm{eV}$.

5.3 Higher Harmonic Generation

As introduced in Sec. 2.6, the interaction of high-intensity electric fields with matter can lead to nonlinear interaction mechanisms such as frequency conversion processes. We observe this effect both in the SSH chains and in the graphene nanoantennas and report on it in this section.

5.3.1 *Su-Schrieffer-Heeger* Chains

Figure 5.3a shows the interacting absorption cross-sections of the 70-atomic linear and dimer chains ($\Delta = 0.18t$), provided by Eq. (5.14). We observe two modes of similar energy and oscillator strength in the two species that are investigated in more detail below. In the linear chain, it resides at $1.83\,\mathrm{eV}$ and in the dimer chain at $2.01\,\mathrm{eV}$, indicated by the vertical dashed lines. The same structures are discussed in Fig. 8.4 of Sec. 8.3, but there with an emphasis on the nature of their modes. It is shown there that the investigated mode at $1.83\,\mathrm{eV}$ in the linear chain is *plasmonic*, whereas the mode at $2.01\,\mathrm{eV}$ in the dimer

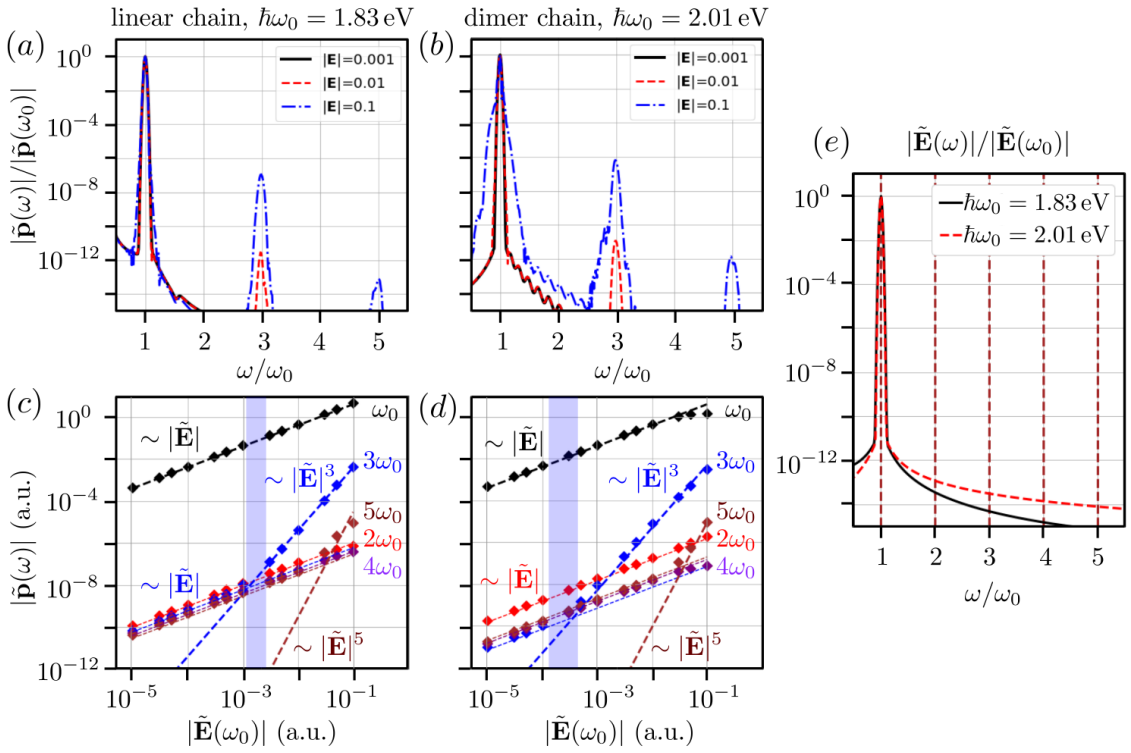

Figure 5.4: Normalized dipole moment frequency spectra induced by the electric field pulses with carrier frequency ω_0 as already highlighted in Figs. 5.3b and 5.3c, respectively. Results for **(a)** the linear chain excited with $\hbar\omega_0 = 1.83\,\mathrm{eV}$ and **(b)** the dimer chain excited with $\hbar\omega_0 = 2.01\,\mathrm{eV}$ for three different electric field amplitudes $|\mathbf{E}_{\mathrm{max}}| = 0.001$ (black), 0.01 (red), and $0.1\,\mathrm{V/Å}$ (blue). Absolute values of $|\tilde{\mathbf{p}}(\omega)|$ evaluated at multiples of the incident carrier frequency ω_0, as a function of the electric field amplitude for the **(c)** linear chain and **(d)** dimer chain. The differently colored markers refer to our simulation results, dashed lines are a guide to the eye for the associated functional dependencies. The blue shaded regions indicate the region where third harmonic generation gets noticeable. **(e)** Normalized spectrum of the *Gaussian* electric excitation pulses.

chain is *single-particle-like*.[5] We want to investigate in this section, if and how the nature of the resonance influences the nonlinear response. Therefore, we study the higher harmonic generation in the emission spectrum.

To that end, we drive the two chains into resonance by illuminating them with a spectrally narrow *Gaussian* pulse of carrier frequency ω_0 polarized along the chain direction in Figs. 5.3b and 5.3c (black lines). Subsequently, we record the induced dipole moment $\mathbf{p}(t)$ (red lines) for various electric field amplitudes.

In Sec. 2.5, we have seen that the emission spectrum of a structure is proportional to the square of the frequency spectrum of the induced dipole moment, $I(\omega) \sim |\tilde{\mathbf{p}}(\omega)|^2$. Thus, we present in Figs. 5.4a and 5.4b the normalized spectra of the induced dipole moment, $|\tilde{\mathbf{p}}(\omega)|/|\tilde{\mathbf{p}}(\omega_0)|$, of the linear chain and the dimer chain, respectively, for three incident maximum field amplitudes $|\mathbf{E}_{\mathrm{max}}| = 0.001$ (black), 0.01 (red), and $0.1\,\mathrm{V/Å}$ (blue). For the

[5] In Ch. 8, we discuss in detail how we define *plasmonic* and *single-particle-like* modes in nanostructures. For reasons of brevity and readability, however, we cannot reproduce the discussion at this point and refer to Chs. 7 and 8 for an extended treatise.

excitation field with the lowest amplitude, we do not see higher harmonic generation in any of the species. In contrast, there is *third* harmonic generation for $|\mathbf{E}| = 0.01\,\mathrm{V/Å}$, and *third* and even *fifth* harmonic generation for the largest amplitude under consideration, $|\mathbf{E}_{\max}| = 0.1\,\mathrm{V/Å}$, in both structures. Moreover, in agreement with the discussion in Sec. 2.6, all nonlinear effects of *even* order vanish, since the chains are symmetric under the transformation $\mathbf{r} \to -\mathbf{r}$.

The latter is also supported by Figs. 5.4c and 5.4d, where we show the relation between the incident electric field amplitude $|\tilde{\mathbf{E}}(\omega_0)|$ and the resulting induced dipole moment $|\tilde{\mathbf{p}}(\omega)|$. Differently colored markers refer to the different frequency components where the dipole moment is evaluated, and the dashed lines serve as a guide to the eye to highlight the functional dependencies. We observe qualitatively the same behavior in both structures. The black lines correspond to the *Fourier* component $|\tilde{\mathbf{p}}(\omega_0)|$ proportional to the incident electric field component at ω_0, $|\tilde{\mathbf{p}}(\omega_0)| \sim |\tilde{\mathbf{E}}(\omega_0)|$. In contrast, the component associated to the third harmonic (blue) grows linearly with the electric field first. However, when the electric field amplitude of the excitation pulse exceeds some critical value in the blue shaded regions, we find $|\tilde{\mathbf{p}}(3\omega_0)| \sim |\tilde{\mathbf{E}}(\omega_0)|^3$. The reason for the linear increase for small excitation amplitudes can be found in Fig. 5.4e, where we show the frequency spectrum of the *Gaussian* excitation pulses. We notice that the tails of the excitation pulses also contain small *Fourier* components at the higher harmonics of ω_0, for numerical reasons. These components *elastically* interact with the chains as well and, hence, are conveyed to the spectrum of the dipole moment. Therefore, the higher order *Fourier* components that grow linearly with the excitation amplitude have *not* been generated in a nonlinear process, but they were already carried by the excitation pulse *prior* the interaction with the structure.[6] In particular, this also explains why even orders exist at all in the spectrum of the centrosymmetric chain molecules in Figs. 5.4c and 5.4d. While – for the above-mentioned reason – the even order components $|\tilde{\mathbf{p}}(2\omega_0)|$ and $|\tilde{\mathbf{p}}(4\omega_0)|$ grow linearly with $|\tilde{\mathbf{E}}(\omega_0)|$ for all excitation field amplitudes, the fifth order nonlinear effect becomes apparent as well and we observe $|\tilde{\mathbf{p}}(5\omega_0)| \sim |\tilde{\mathbf{E}}(\omega_0)|^5$ for strong electric fields both in the linear and dimer chain.

The two investigated absorption modes in Figs. 5.3 and 5.4 were chosen such that they do not differ much in excitation energy nor in oscillator strength. Though, the mode in the linear chain is *plasmonic*, the one in the dimer chain is *single-particle-like*. It is noteworthy here, that despite their different nature, we do not see any qualitative and only mild quantitative differences between the higher harmonic generation characteristics of the two modes. In particular, the parameter β_3 that defines the blue dashed lines in Figs. 5.4c and 5.4d according to $|\tilde{\mathbf{p}}(3\omega_0)| = \beta_3 |\tilde{\mathbf{E}}(\omega_0)|^3$ is equal for both chains. The same statement holds for the fifth order as well. As a result, we conclude that the two modes of different nature are equally well suited for generating higher harmonics.

In literature, we find that "plasmon-assisted higher harmonic generation" [130] and also "plasmon-enhanced nonlinear" effects [238] emerge in nanostructured graphene. Therefore, in the following section, we want to intensify the above investigation by considering the triangular graphene nanoantennas that were proposed for this purpose in literature before. In particular, we make use of the doping degree of freedom and investigate one single structure at two different doping levels and for *resonant* and *off-resonant* illumination. The structure is suitable for such kind of investigation because it simultaneously hosts plasmonic *and* single-particle-like modes, as will be ascertained in Sec. 8.5. Also,

[6] In Fig. 5.4c, for instance, we see that $|\tilde{\mathbf{p}}(2\omega_0)| \sim |\tilde{\mathbf{E}}(\omega_0)|$ for all excitation amplitudes. However, this should not be misinterpreted to mean that $|\tilde{\mathbf{p}}(2\omega_0)|$ is generated in a *nonlinear* process from $|\tilde{\mathbf{E}}(\omega_0)|$. Rather, we need to realize that $|\tilde{\mathbf{E}}(2\omega_0)| \sim |\tilde{\mathbf{E}}(\omega_0)|$ in the excitation pulse and, therefore, $|\tilde{\mathbf{p}}(2\omega_0)|$ is generated in a *linear* process from the *elastic* interaction of the component $|\tilde{\mathbf{E}}(2\omega_0)|$ with the chains.

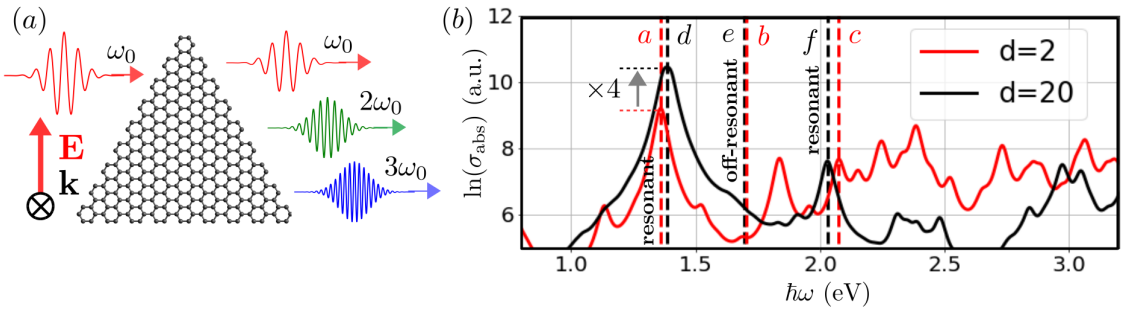

Figure 5.5: (a) Schematic illustration of higher harmonic generation in a 270-atomic armchair graphene triangle, illuminated at ω_0. **(b)** Logarithm of the interacting absorption cross-section of the graphene triangle in (a) for $d = 2$ (red) and $d = 20$ (black) additional doping electrons, probed with vertically polarized light.

when the excitation light is polarized suitably, the symmetry of the triangle allows to access nonlinear effects of *even* order as well.

5.3.2 Triangular Graphene Nanoantenna

In the previous section, we observed that all higher harmonics of even order could not be generated due to the symmetry of the linear chain molecules. Here, we study a 270-atomic triangular graphene nanoantenna with side length $3.7\,\mathrm{nm}$, armchair edges, and $d = 2$ and 20 doping electrons.[7] To break the axial symmetry of the configuration in Fig. 5.5a, we illuminate it with a vertically polarized pulse at three different carrier frequencies for both doping levels. In Fig. 5.5b, the interacting absorption cross-section of the structure in (a) is shown for $d = 2$ (red) and $d = 20$ (black) doping electrons. In the two-fold and 20-fold doped triangles, we choose the modes at (a) 1.36 and (b) $1.39\,\mathrm{eV}$, respectively, that dominate the absorption spectra. In Sec. 8.5, these modes are found to be of single-particle-like ($1.36\,\mathrm{eV}$) and plasmonic ($1.39\,\mathrm{eV}$) nature. Additionally, we simulate the off-resonant response at $1.7\,\mathrm{eV}$ (b and e) for both doping levels. Eventually, enabled by the doping degree of freedom, we can engineer the absorption cross-section of the triangle such that there are again two modes of similar energy and oscillator strength that only differ by their nature. In the two-fold doped triangle, we pick the single-particle-like mode at (c) $2.08\,\mathrm{eV}$ and for $d = 20$, the plasmonic mode at (f) $2.03\,\mathrm{eV}$ is investigated. The inset letters in Fig. 5.5b refer to the labeling in Figs. 5.6 and 5.7 below.

Figure 5.6 shows the normalized spectra of the induced dipole moments, $|\tilde{\mathbf{p}}(\omega)|/|\tilde{\mathbf{p}}(\omega_0)|$, for five maximum electric field amplitudes (legend on the top right, in $\mathrm{V/Å}$). The higher the transparency of the line, the stronger is the incident electric field $|\mathbf{E}|$. In all cases, we consistently observe no higher harmonic generation for the smallest incident electric field amplitude $|\mathbf{E}| = 10^{-7}\,\mathrm{V/Å}$. Also, for the highest incident field amplitude under investigation, $|\mathbf{E}| = 0.1\,\mathrm{V/Å}$, all inspected cases show higher harmonic generation for all presented even and odd higher orders.

To determine the electric field strength where nonlinear effects become noticeable in the spectra of the dipole moments, we analyze them as a function of the incident field amplitude in Fig. 5.7 as well. Like in the previous section, the differently colored markers show our simulation results and dashed lines serve as a guide to the eye highlighting the

[7] The same structure is studied extensively also in Sec. 8.5. See Fig. 8.6 for the energy landscape of the structure and Fig. 8.7 for its non-interacting and interacting absorption cross-sections as a function of doping level d for $0 \leq d \leq 20$.

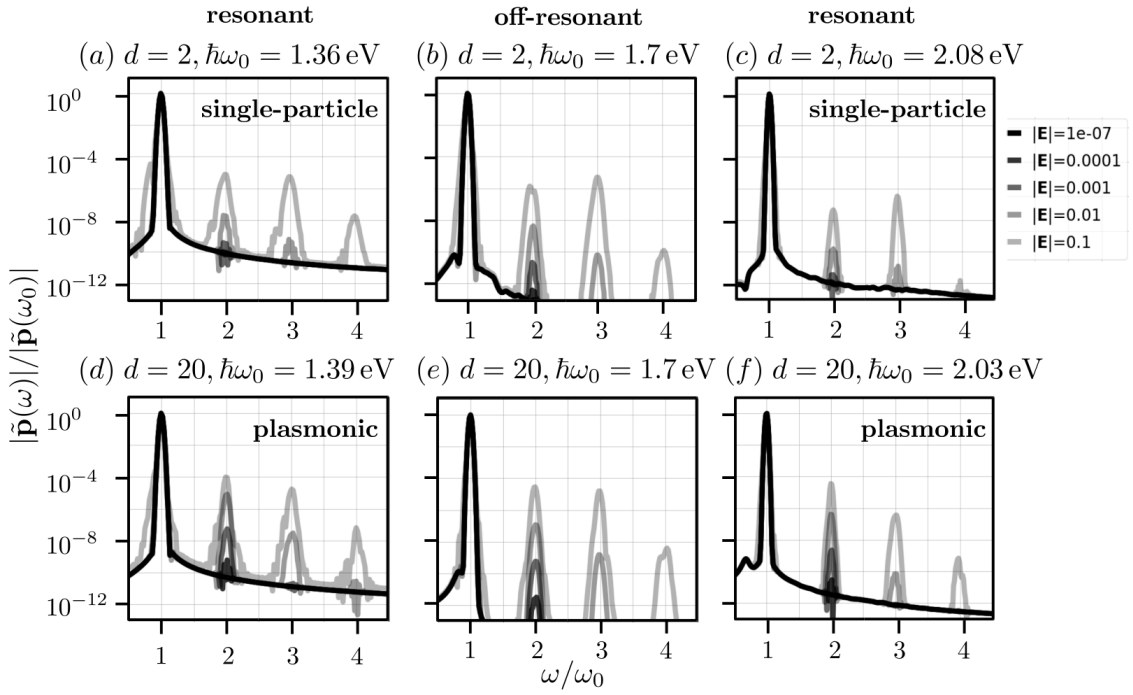

Figure 5.6: (a-c) Normalized dipole moment frequency spectra of the two-fold doped graphene triangle specified in Fig. 5.5, analogously to Figs. 5.4a and 5.4b. **(d-f)** Same as (a-c), but for the 20-fold doped triangle. The incident electric field strength is encoded in the transparency of the lines, see the legend on the top right.

associated functional dependencies. In the top row, we show the shaded regions where nonlinear effects become apparent for the different orders, the bottom row indicates the functional dependencies of the dashed lines.

The direct comparison of the first pair of modes in Figs. 5.6a and 5.6d, in general, reveals no major differences except for a slightly stronger response in all higher orders in the latter case. However, two things can be noted in particular. First, the response at the second harmonic, $|\tilde{\mathbf{p}}(2\omega_0)|$, for the single-particle-like mode at $1.36\,\mathrm{eV}$ is five orders of magnitude smaller as compared to the response at the fundamental frequency $|\tilde{\mathbf{p}}(\omega_0)|$ for $|\mathbf{E}| = 0.1\,\mathrm{V/Å}$. On the other hand, the plasmonic mode at $1.39\,\mathrm{eV}$ shows a stronger second-order response with a difference of only four orders of magnitude. Second, while the second-order and third-order nonlinear effects in the single-particle-like mode are of comparable strength for the highest investigated incident field, the second-order response in the plasmonic mode is stronger than that of the third order.

Figures 5.7a and 5.7d additionally reveal the magnitudes of the higher-order nonlinearity parameters $\beta_n^{(a)}$, that determine the dashed lines and are defined through $|\tilde{\mathbf{p}}(n\omega)| = \beta_n^{(a)}|\tilde{\mathbf{E}}(\omega_0)|^n$ for the nth order in subfigure (a), for instance. All values are tabulated in Tab. C.1 in App. C. To make the parameters of different modes comparable, we compare their parameters at the fundamental frequencies and calculate $\beta_1^{(d)}/\beta_1^{(a)} = 4$. Please note that this is exactly the ratio of the oscillator strengths of modes a and d in the absorption cross-sections in Fig. 5.5b. Thus, we can now make statements independent of the oscillator strengths of the modes. The *adjusted* oscillator strength-independent parameter ratios between the plasmonic and the single-particle-like modes for the higher orders are $\beta_2^{(d)}/\beta_2^{(a)} = 15$, $\beta_3^{(d)}/\beta_3^{(a)} = 3.8$, and $\beta_4^{(d)}/\beta_4^{(a)} = 10.7$. Conclusively, we note that the generation of even harmonics is amplified to a considerably larger extent in the plasmonic

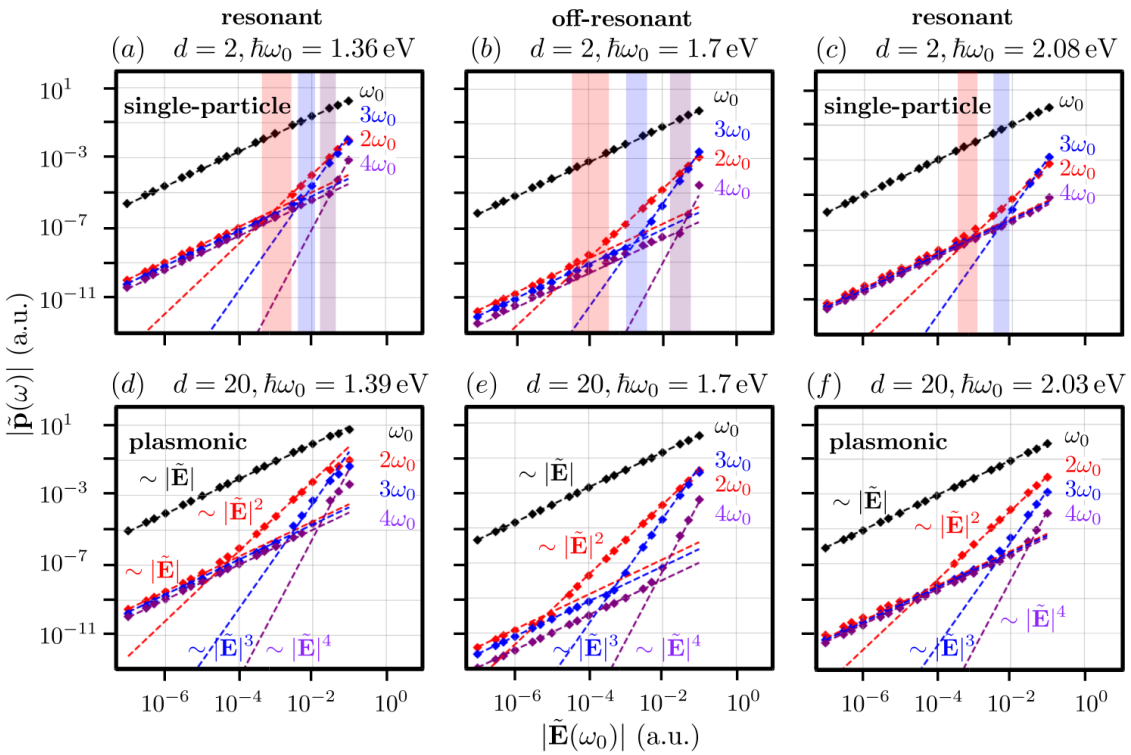

Figure 5.7: (a-c) Absolute values of $|\tilde{\mathbf{p}}(\omega)|$ evaluated at multiples of the incident carrier frequency ω_0, as a function of the maximum electric field amplitude of the incident pulse in the two-fold doped graphene triangle. The shaded regions indicate the region where nonlinear effects become noticeable. **(d-f)** Same as (a-c), but for the 20-fold doped triangle, analogously to Figs. 5.4c and 5.4d.

mode of the heavily doped triangle as compared to the single-particle-like mode in the mildly doped one.

The spectra associated to the off-resonant response in Figs. 5.6b and 5.6e look similar to each other as well. Yet, we see the tendency that the 20-fold doped triangle offers a stronger response in all investigated orders in general as compared to the two-fold doped triangle. Altogether, it is remarkable that the effect of higher harmonic generation in the off-resonant case for all higher orders is of the same strength like in the above-discussed resonant cases (normalized to the response at the fundamental frequency, of course). From Figs. 5.7b and 5.7e, it becomes clear that the induced dipole moment is indeed generally smaller in absolute value in the off-resonant case as compared to the resonant case discussed in the previous paragraph. To compare the modes quantitatively, we calculate $\beta_1^{(e)}/\beta_1^{(b)} = 3.3$, in agreement with the ratios of the absorption cross-sections in Fig. 5.5b. Furthermore, the *adjusted* higher-order parameter ratios are $\beta_2^{(e)}/\beta_2^{(b)} = 4.0$, $\beta_3^{(e)}/\beta_3^{(b)} = 4.5$, and $\beta_4^{(e)}/\beta_4^{(b)} = 6.7$. In conclusion, illuminating the 20-fold doped triangle off-resonantly leads to a stronger higher harmonic generation for all investigated orders as compared to the two-fold doped structure.

Comparing the third pair of modes allows to draw the most interesting conclusions. The absorption strength of the modes and their energy is of similar size, $\beta_1^{(f)}/\beta_1^{(c)} = 0.9$, such that their comparison can indeed be taken as an assessment of what difference the *nature* of the mode makes in the emergence of nonlinear effects. As is shown in Fig. 5.6c, the single-particle-like mode at $2.08\,\mathrm{eV}$ in the two-fold doped triangle exhibits

a dipole *Fourier* component at the second (third) harmonic which is roughly seven (six) orders of magnitude smaller than it is at the fundamental frequency for an incident pulse with maximum amplitude $|\mathbf{E}| = 0.1\,\mathrm{V/Å}$. Moreover, there is barely any fourth-order response. In contrast to that, the plasmonic mode at $2.03\,\mathrm{eV}$ in the 20-fold doped structure in Fig. 5.6f does clearly show fourth harmonic generation. For the third order, we find an adjusted ratio of $\beta_3^{(c)}/\beta_3^{(f)} = 1.1$, which means that the effect of third harmonic generation is of the same strength as compared to the single-particle-like mode. We have $|\tilde{\mathbf{p}}(3\omega_0)|/|\tilde{\mathbf{p}}(\omega_0)| \approx 10^{-6}$ for the highest excitation amplitude both in Figs. 5.6c and 5.6f. The second order effect, however, is substantially larger in the plasmonic case as compared to the single-particle-like mode. The former exhibits a 1000-fold stronger second harmonic generation for $|\mathbf{E}| = 0.1\,\mathrm{V/Å}$, such that we find $|\tilde{\mathbf{p}}(2\omega_0)|/|\tilde{\mathbf{p}}(\omega_0)| \approx 10^{-4}$ instead of 10^{-7}. Also in Figs. 5.7c and 5.7f, this issue is noticeable. While in the former the red and blue dashed lines intersect, we do not see such an intersection in the latter, where $|\tilde{\mathbf{p}}(\omega_0)| > |\tilde{\mathbf{p}}(2\omega_0)| > |\tilde{\mathbf{p}}(3\omega_0)| > |\tilde{\mathbf{p}}(4\omega_0)|$ holds for all presented excitation amplitudes. The adjusted parameter ratio is $\beta_2^{(c)}/\beta_2^{(f)} = 18.5$, rendering the plasmonic mode substantially more efficient for second harmonic generation.

5.4 Conclusions

In this chapter, we have introduced a time-domain simulation framework to determine the electronic dynamics and optical properties of planar carbon molecules when they are exposed to an external electric field. In this approach, electronic motion can be tracked both in real space and in energy space, which makes it feasible to calculate both absorption cross-sections and energy state population dynamics. The nonlinear optical effect of higher harmonic generation was demonstrated to occur in systems with interacting electrons due to a nonlinear term in the time propagation equation of the system's density operator. We find that the effect occurs in the chains for odd orders only and for all orders in the investigated triangular graphene nanoantenna. In the last section, we furthermore studied, how the nonlinear response of single-particle-like and plasmonic modes differ. Our simulation results suggest that the plasmonic nature of the modes is primarily reflected in the even orders of the higher harmonic generation. For single-particle-like modes and off-resonant illumination, there is an excitation field amplitude above which we find stronger third harmonic generation as compared to the second harmonic. On the other hand, in the plasmonic modes under investigation, the higher the order of the harmonic, the weaker is the effect for all presented excitation strengths.

The time-domain TB framework presented in this chapter is easily extendable to hybrid systems that consist of an antenna and an additional adsorbed atom. The latter acts as an impurity in the system and opens up the possibility to tune the absorption cross-section even further – independently from the doping degree of freedom. In the next chapter, we will discuss the theory and implications of this extension. Also, we present simulation results for the electronic structure and optical properties of such hybrid systems, and identify the parameters in the system that are most crucial for tuning and controlling their absorption characteristics.

6 | Optics of Hybrid Systems: Chains and Adatoms

6.1 Introduction

The interaction of optical nanoantennas and nearby located quantum emitters – be it an atom, a molecule, or an artificial quantum dot – is generally described within the *Purcell* formalism [82] with great success. Here, the excited quantum emitter decays from an energetically higher excited state $|e\rangle$ with energy E_e to a lower ground state $|g\rangle$ with energy E_g. In the process, a photon $\hbar\omega = E_e - E_g$ is radiated, where the emission rate of the decay is crucially determined by the photonic environment that the emitter is exposed to. Plasmonic nanocavities [94, 95], photonic crystals [96, 97], and also plasmonic nanoantennas [98, 99], for instance, are suitable candidates to engineer this photonic environment and, consequently, to enhance the spontaneous emission rate by orders of magnitude if the emitter is located nearby.

To capitalize on the locally modified density of states or the enhanced electric field around the plasmonic nanoantenna and, consequently, to engineer its emission rate, it is necessary to bring the emitter into the very close proximity – to distances in the order of nanometers or at most tens of nanometers, depending on the details of the geometry and the wavelengths of interest. At these distances, the macroscopic description of the materials as homogeneous may break down and the atomistic details of the material from which the photonic structure is made needs to be considered. Non-classical corrections to the plasmonic response of the antennas due to their atomic structure and electronic spill-out effects, for instance, were considered in Refs. [239–242]. However, at these short length scales, an additional coupling mechanism starts to play an important role that the above-mentioned *Purcell* description lacks – electron tunneling. Modes that encounter the effect of electronic coupling between the constituents of plasmonic dimer antennas are well-known as charge transfer plasmons (CTP) and have been studied before [100–109]. Besides the CTP, though, the electronic coupling channel between the quantum emitter itself and the antenna deserves a proper investigation as well.

Theory already offers approaches to electronically couple adsorbates to extended 2D graphene from a material physics point of view [110–113]. Here, we focus on the *optical* perspective and extend the discussion to *finite* structures. Following the TB single-particle density matrix approach of the previous chapters, we introduce a framework to include an adsorbed atom (*adatom*) into the TB description of the nanoantenna, and we study the optical properties of the *hybrid* system. In particular, it is our goal to identify system parameters like the coupling position and the coupling strength that influence the electronic structure and optical properties of the nanoantenna the most. Moreover, as recently observed in carbon nanotube quantum dots [243], we will also see that a weakening of the optical selection rules can be achieved in carbon nanoantennas with broken sym-

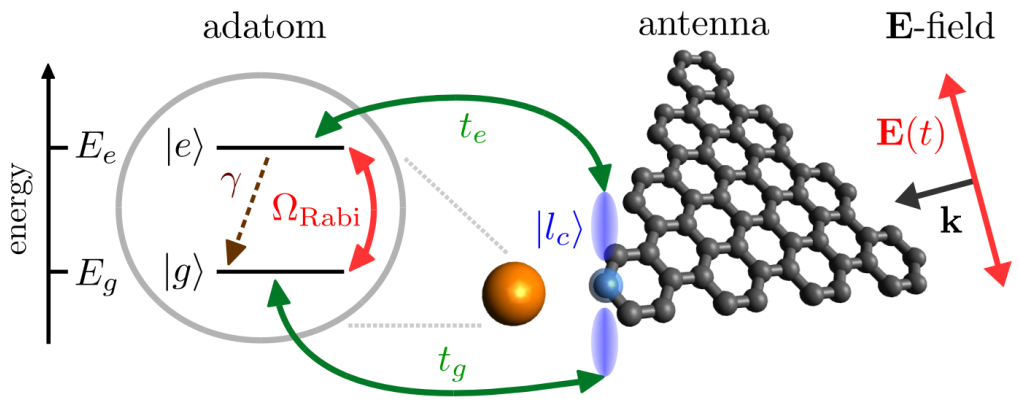

Figure 6.1: Schematic representation of a hybrid system that consists of an adatom coupled to a nanoantenna, as described by the Hamiltonian in Eq. (6.1). The excited state $|e\rangle$ and $|g\rangle$ with energies E_e and E_g, respectively, are coupled with the hopping rates t_e and t_g to the p_z orbital $|l_c\rangle$ of the coupling carbon atom l_c (blue). Additionally, we sketch the *incoherent* spontaneous emission mechanism with rate γ (brown) and the *coherent Rabi* oscillation with frequency Ω_{Rabi} that occurs in two-level systems which are resonantly exchanging energy with an electric field $\mathbf{E}$.

metries. As a consequence, previously forbidden optical transitions become allowed and enrich the absorption spectrum. We discuss the SSH chains to a large extent, since they can be viewed as very basic model systems for both conducting and insulating molecular species. This chapter mostly relies on Refs. [A2, A5].

Adatoms in Carbon Structures

Generally, there are two ways to introduce structural modifications or impurities into the crystal matrix of a carbon nanostructure.

1. **Intrinsic** modifications can be introduced into the carbon lattice by adding additional carbon adatoms [244] or lattice defects [245, 246], *i.e.*, removing lattice atoms from the host material. This situation can be easily accounted for within the TB approach presented above by modifying the geometry of the considered structure.
2. **Extrinsic** modifications can be represented by foreign adatoms of different atomic species [247–249]. Especially transition metal adatoms are well suited to be treated within a TB approach, as they predominantly interact with the carbon nanostructure through their p_z orbitals [250–253]. Thus, their valence electrons may be treated as π-electrons as well, just like in the case of carbon.

The extended *Hückel* model [111, 254] constitutes an approach to couple these foreign adatoms to the matrix of a host material. It is a variation of the *Anderson* impurity model [255, 256] and was successfully applied to couple one-level adatoms to extended 2D graphene before [257–261].

In our approach, however, the adatom is represented by a two-level system to also include spontaneous emission from the excited state $|e\rangle$ to the ground state $|g\rangle$ of the adatom. The configuration is sketched in Fig. 6.1. Also, the model is capable of describing the *Rabi* oscillation mechanism, which is the coherent exchange of energy between a two-level system and the modes of an electromagnetic field. In turn, contrary to the

above-cited works that were predominantly interested in spin-orbit coupling of the adatom with graphene, we continue to treat electrons of opposite spin equally and work with a *nonmagnetic* alteration of the above-mentioned *Hückel* approach.

We discuss the modifications of spontaneous emission and *Rabi* oscillations in hybrid systems in detail for adatoms coupled to triangular graphene antennas in Ref. [A5] and shortly report on it at the end of this chapter. However, this work concentrates on the systematic analysis of the relevance of the system parameters and the impact that the adatom has on the electronic structure and optical properties of the *nanoantenna*.

6.2 Hybrid System Hamiltonian

The TB Hamiltonian of the hybrid structure, that consists of a carbon nanoantenna and an adatom coupled to it reads

$$\begin{aligned} H = t \sum_{\langle l,l' \rangle, l<l'} \big(|l\rangle\langle l'| + |l'\rangle\langle l| \big) \qquad & \text{antenna} \\ + E_e |e\rangle\langle e| + E_g |g\rangle\langle g| \qquad & \text{adatom} \\ + t_e \Big(|l_c\rangle\langle e| + |e\rangle\langle l_c| \Big) + t_g \Big(|l_c\rangle\langle g| + |g\rangle\langle l_c| \Big). \qquad & \text{interaction} \end{aligned} \tag{6.1}$$

Here, the first line is equal to the TB Hamiltonian of the stand-alone nanoantenna in the previous chapters, Eq. (4.2). In the second line, we introduced the ground and excited states of the adatom, $|g\rangle$ and $|e\rangle$, with energies E_g and E_e, respectively. Unless explicitly stated otherwise, we assume $E_e = 0.5\,\mathrm{eV}$ and $E_g = -0.5\,\mathrm{eV}$ which are energies measured relative to the energy landscape of the antenna.

The third line represents the interaction Hamiltonian between the carbon structure and the adatom. It is characterized by two hopping parameters t_e and t_g that quantify the overlap of the excited and ground state orbitals of the adatom with the p_z orbital $|l_c\rangle$ of the coupling atom l_c in the carbon structure. In the below investigation, we vary the adatom coupling strengths t_e and t_g from 0 (uncoupled) to $2t$ (strongly coupled). In DFT simulations it has been found that, on the one hand, the case $t_e, t_g < t$ is realized when metal adatoms are considered [262]. On the other hand, $t_e, t_g > t$ holds true for fluorine, OH groups, and some carbon radicals as adatoms [253, 263].

The above Hamiltonian implicitly assumes that the adatom is coupled in *top configuration* to only one of the atoms (l_c) in the carbon structure. This assumption holds true for covalently functionalized graphene, for instance, and is justified for a whole set of covalently bonded impurity adatoms, such as hydrogen, fluorine, and the hydroxyl group OH, for instance [111, 263].

In our approach, we extend the N_a-atomic TB basis set of the carbon structure by two more states that represent two chemically active orbitals of the adatom, such that $N = N_a + 2$ is the total number of active orbitals and energy eigenstates in the system. Furthermore, we proceed with a joint real-space basis index $\{|\tilde{l}\rangle\} = \{|l\rangle\} \cup \{|g\rangle, |e\rangle\}$, such that l labels the N_a antenna sites only, and $\{|\tilde{l}\rangle\}$ denotes the set of all N elements in the real-space basis set. Like in the above chapters, the set of energy eigenstates $\{|j\rangle\}$ and the eigenenergies of the hybrid system in Eq. (6.1) can be found by solving $H|j\rangle = E_j|j\rangle$.

Also, we may expand the eigenstates into the joint basis according to

$$|j\rangle = \sum_{\tilde{l}=1}^{N} a_{j\tilde{l}}|\tilde{l}\rangle = a_{je}|e\rangle + a_{jg}|g\rangle + \sum_{l=1}^{N_a} a_{jl}|l\rangle. \tag{6.2}$$

6.2.1 State Hybridization and Adatom Population

The state characterization measures for stand-alone antennas introduced in Sec. 4.2.1 can be generalized to the hybrid system in a straightforward manner by replacing l with $\tilde{l}$ in the respective equations. Additionally, for the hybrid system we define two more measures that quantify to what extent the two subsystems are *hybridized*, and to what extent the state is localized on the adatom.

The *state hybridization* of state $|j\rangle$ reads

$$\boxed{h_j = 1 - |\langle j|j^0\rangle| \in [0,1],} \tag{6.3}$$

where $|j^0\rangle$ is an eigenstate of the Hamiltonian Eq. 6.1 for $t_e = t_g = 0$, *i.e.*, of the uncoupled system. In that case, we have $|j\rangle = |j^0\rangle$ and, consequently, $h_j = 0$ as intended. Once the coupling between the adatom and the antenna is turned on, $t_e, t_g > 0$, state $|j^0\rangle$ evolves toward $|j\rangle \neq |j^0\rangle$ and $h_j > 0$. It is necessary to point out here, that the state hybridization depends on the *ordering* of the states in the energy landscape, *i.e.*, on their *index*. Thus, it is crucial to scan the energy landscape for energy level crossings to obtain a correct interpretation of the hybridization. Below, to circumvent this problem, we will not only consider h_j, but also its derivative $\partial h_j/\partial t_{e,g}$ with respect to the coupling strengths t_e, t_g to identify parameter regions where the adatom and the antenna interact with each other the most and, thus, might serve as sweet spots for *tuning* purposes.

The *adatom population* of state $|j\rangle$ reads

$$\boxed{\Pi_j = |a_{jg}|^2 + |a_{je}|^2 \in [0,1],} \tag{6.4}$$

and it denotes the fraction of the wavefunction of state $|j\rangle$ located on the two adatom orbitals.

6.3 *Su-Schrieffer-Heeger* Chains

Like in Ch. 4, we begin by first discussing the SSH chains to get an understanding of the adatom's impact on the electronic and optical properties of TB systems in general. From that, we can generalize the behavior to more complicated structures. The chains under investigation here are obtained from the Hamiltonian in Eq. (4.13) with $N = 70$ and $\Delta = \pm 0.3t$.

6.3.1 Electronic Structure

Figure 6.2 shows the energy landscape of (a-e) the linear chain, (f-j) the dimer chain, and (k-o) the topological insulator in the optically active region around the *Fermi* energy for $|E| \leq 2.5\,\mathrm{eV}$ as a function of the coupling strengths $t_e = t_g$. We couple the adatom successively to three edge atoms ($l_c = 1, 2, 3$) and to two atoms from the bulk ($l_c = 18, 35$)

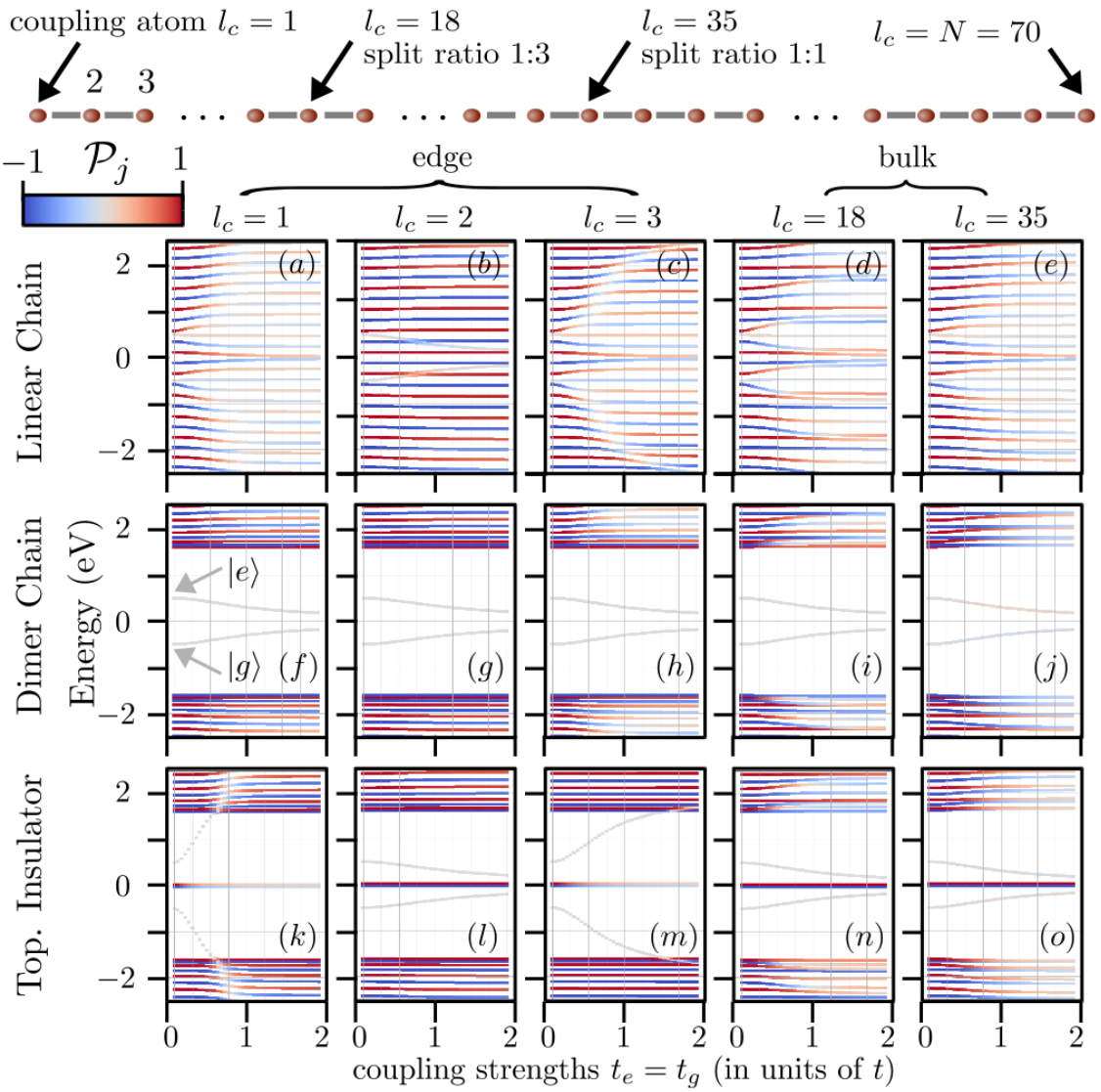

Figure 6.2: Energy landscapes of the hybrid system that consists of an adatom coupled to a 70-atomic (**a**)-(**e**) linear chain, (**f**)-(**j**) dimer chain, and (**k**)-(**o**) topological insulator with $|\Delta| = 0.3t$. The color encodes the parity of the states' wavefunction part that is located on the chain, *i.e.*, $\mathcal{P}_j = \sum_{l=1}^{N_a} a_{jl} a_{j,N_a+1-l}$.

of the chains. The bulk coupling atoms are chosen such that the adatom splits the 70-atomic chain in ratios of nearly 1:3 and 1:1, respectively. The line colors encode the parity of that part of the respective state's wavefunction that is located at the chain sites, $\mathcal{P}_j = \sum_{l=1}^{N_a} a_{jl} a_{j,N_a+1-l}$. It is apparent from the figure that the coupling position plays a crucial role for the electronic structure of the hybrid system. Therefore, in the following we treat edge coupling and bulk coupling separately.

Coupling to Edge Atoms

Let us consider the first three columns of Fig. 6.2 first, where we couple the adatom to the edge atoms $l_c = 1, 2$, and 3. Coupling the adatom to $l_c = 2$ barely leads to any changes in the spectrum of any of the the hybrid systems, as can be seen in Figs. 6.2b, g, and l. In all three subfigures, the states that originate from the chain are hardly affected and neither change their parity nor their energy, no matter how strongly the adatom is

coupled to the chain. This can be explained by investigating the expansion coefficients c_{j2} of the stand-alone chains' states that are energetically close to the adatom's energies. For these states, $c_{j2} \approx 0$ in all three species. See for example the HOMO and LUMO states in Figs. 4.2c-e, which exhibit nearly vanishing expansion coefficients c_{j2} in the 20-atomic chain. The same reasoning applies to the 70-atomic chain as well. Thus, coupling effects between the chain and the adatom are negligible in this configuration. However, in all three cases, the states that stem from the adatom ($|g\rangle$ and $|e\rangle$ for $t_e = t_g = 0$, see Fig. 6.2f) strive toward $0\,\mathrm{eV}$ for increasing coupling strengths. In the case of the linear chain, see Fig. 6.2b, they even cross chain state levels in the process without disturbing them notably.

On the other hand, within one chain species, we observe that the electronic structure exhibits qualitatively the same behavior when we couple the adatom to the chain sites $l_c = 1$ and $l_c = 3$. Indeed, as can be seen in Figs. 4.2c-e, the expansion coefficients c_{j1} and c_{j3} of the relevant states in the stand-alone chains attain comparably high values. Yet, in the dimer chain, they are energetically still rather far away from the adatom's energies which is why also in these configurations we hardly observe any coupling of the adatom with the quasi-continuum states below and above the band gap. Also in the topological insulator case, coupling of the adatom states with the quasi-continuum states practically does not occur. However, as the coupling atoms $l_c = 1, 3$ host the famous edge states of the topological insulator, which are, furthermore, energetically relatively close to the adatom states, we observe strong energy shifts and strong hybridization already for comparably small coupling strengths in Figs. 6.2k and 6.2m. We will see below in Sec. 6.3.4 that, despite the drastic shift of the states' energies in the spectra of these two configurations, their absorption cross-sections are nevertheless hardly affected due to the low optical activity of the involved states.

The most interesting species for the purpose of optical tuning is the linear chain. Here, both for $l_c = 1$ and 3, all states in the investigated energy region are shifted in energy and also change their parity value. Both of these observations are important for the tunability of the optical properties of the chains. Whereas the former is reflected in the absorption cross-section by a shift of already existing modes, the latter relaxes optical selection rules and enables electronic transitions that were previously symmetry-forbidden. For these reasons, we will only discuss the most interesting case of the linear chain in more detail in the following.

Coupling to Bulk Atoms

The right two columns in Fig. 6.2 present the simulation results for coupling the adatom to the bulk atoms $l_c = 18$ and 35, such that the chains are geometrically split in ratios 1:3 and 1:1, respectively. For the dimer chain and the topological insulator, we observe qualitatively the same behavior. As the two near-zero edge states in the topological insulator are located on the edge sites, they do not participate to the bulk coupling here and are left unaffected. Only the quasi-continuum states below and above the band gap participate in both insulating species. Their states both shift in energy and lose their well-defined parity which are beneficial trends for optical tuning purposes. On the other hand, the states which are introduced *via* the adatom tend toward zero for increasing coupling strength just as for $l_c = 2$.

Figures 6.2d and 6.2e show the linear chain's bulk coupling characteristics. With the naked eye, it is hard to distinguish both cases from another and also from the edge coupling case $l_c = 1$ in Fig. 6.2a. However, for $l_c = 18$, we find energy regions in the strong coupling limit where states cluster together, not necessarily with alternating parity, as in

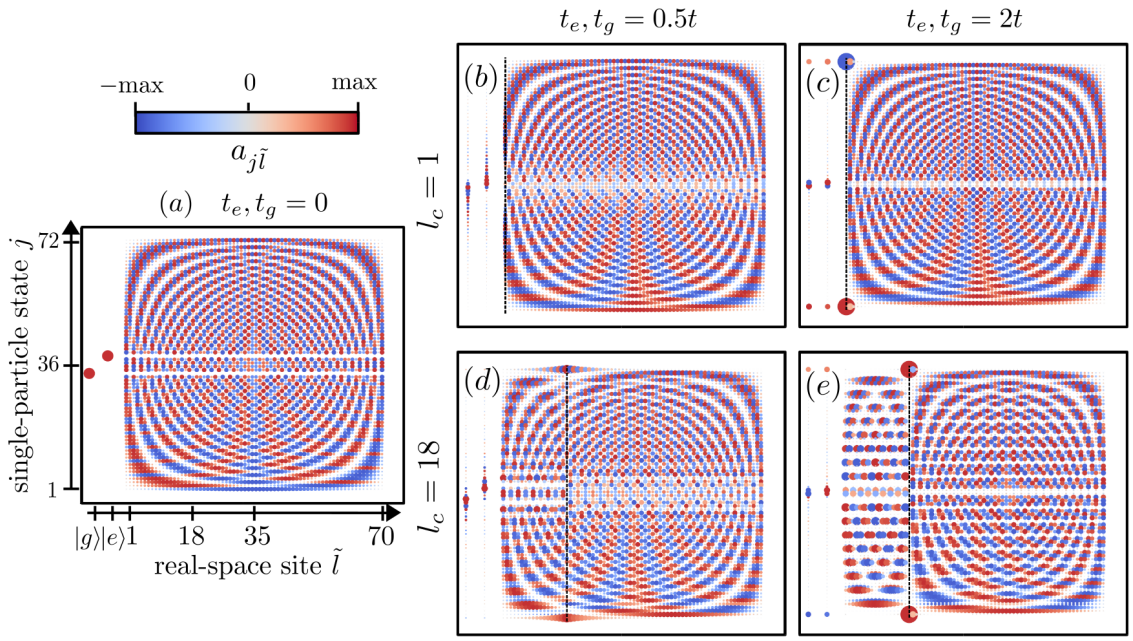

Figure 6.3: Real-space expansion coefficients $a_{j\tilde{l}}$ of the states in the hybrid system that consists of an adatom and a linear chain. In (**a**), we show the decoupled system with $t_e = t_g = 0$. (**b**) and (**c**) present the situation when the adatom is coupled to the edge atom $l_c = 1$ (indicated by the vertical dashed line) with coupling strengths $t_e = t_g = 0.5t$ and $2t$, respectively. (**d**) and (**e**) present the situation when the adatom is coupled to the bulk atom $l_c = 18$ with coupling strengths $t_e = t_g = 0.5t$ and $2t$, respectively.

all other cases before. For $l_c = 35$, however, we obtain almost equally spaced energy states of alternating parity signs both for vanishing and non-zero coupling strengths.

Exemplarily for edge and bulk coupling, Fig. 6.3 shows the real-space expansion coefficients $a_{j\tilde{l}}$ of all energy eigenstates of the hybrid system that consists of the adatom and the linear chain as specified above for $l_c = 1$ (edge) and 18 (bulk). We show the uncoupled system ($t_e = t_g = 0$) in Fig. 6.3a, where the adatom states are fully localized on the adatom orbitals. In contrast, all other states are located on the chain's atoms and exhibit a particle-in-a-box pattern as already discussed in Fig. 4.1c before.

Figures 6.3b and 6.3c show the edge coupling case $l_c = 1$ for relatively small ($t_e = t_g = 0.5t$) and high ($t_e = t_g = 2t$) coupling strengths. In the former situation, we see that the adatom hybridizes with the chain considerably. Many energy eigenstates exhibit population contributions on both the adatom and the chain orbitals simultaneously. In the latter case of high coupling strength, on the contrary, there are only two states in the optically active middle part of the spectrum that comprise the adatom. These states, however, hardly comprise the chain orbitals. Additionally, $a_{j1} \approx 0$ holds for all states except for $j = 1$ and $j = 72$ (see the atomic sites along the vertical dashed line). Therefore, the system effectively turns into a 69-atomic linear chain on the one side, and a solitary carbon atom $l_c = 1$ that the adatom is coupled to, on the other side.

Figures 6.3d and 6.3e refer to the bulk coupling configuration at $l_c = 18$ for the cases of relatively small ($t_e = t_g = 0.5t$) and high ($t_e = t_g = 2t$) coupling strengths. In the former case, we observe hybridization of the adatom with the chain in the optically active region around the *Fermi* energy. Also, the wavefunctions of the highest and lowest single-

particle energy states get attracted by the adatom. In the case of stronger coupling, we observe a similar behavior like in the edge case. The system collapses into its fragments and turns into a short 17-atomic chain, a long 52-atomic chain, and a solitary carbon atomic which is very strongly coupled to the adatom. Interestingly, the two chains of different lengths are electronically effectively decoupled from each other.

6.3.2 Hybrid State Characterizations

To obtain a complete understanding of the coupling configurations that are not explicitly shown in the above-presented figures, we show the state characteristics for the hybrid adatom-linear chain system in Fig. 6.4 and discuss them briefly. In this system, the response of the *coupled* system differs strongest in a non-trivial sense from the states of the *uncoupled* one among all investigated species.

Figures 6.4a-e show the square root of the **absorption activity** $\sqrt{\mathcal{A}_j}$ as a function of the coupling strength $t_e, t_g \in [0, 2t]$ for the five coupling positions already discussed above. It can be stated that for every coupling position, the HOMO and LUMO states dominate the absorption mechanism at small coupling strengths. If coupling is increased, though, the bulk coupling configuration shows more additional contributions from other states below and above the HOMO and LUMO that become relevant, whereas we hardly notice any changes for $l_c = 2$. Only the states HOMO-1 and LUMO+1 for $l_c = 1$ and 3 play a role as well.

The **hybridization** h_j is shown in Figs. 6.4f-j. In all five cases, the adatom states exhibit strong increases in hybridization. For $l_c = 2$, though, this is only an artefact of their state index change. Concerning the states that were introduced into the system by the chain, and that contribute the most to the optical interaction of the hybrid system in total, the discussion can be split into edge and bulk coupling configurations again. In the edge coupling cases, the hybridization remains comparatively small – apart from the faint contributions of the HOMO and LUMO for $l_c = 1, 3$. On the other hand, bulk coupling leads to a broad increase of hybridization for almost all states in the presented range in Figs. 6.4i and 6.4j. The **derivatives of the hybridization** with respect to the coupling strengths in Figures 6.4k-o reveal that the hybridization sets in predominantly for small coupling strengths in all five cases. Moreover, not all states hybridize at the same coupling strength. There is a trend for states further away from the adatom energies to hybridize at higher coupling strengths.

Figures 6.4p-t show the **localization** $\mathcal{L}_j$ of the hybrid system's states. As previously discussed in Sec. 4.3.2, all chain states attain the localization $\mathcal{L}_j = 0.33$ in the uncoupled system. The localization of the states introduced by the adatom, on the other hand, is 1 in the uncoupled structure. In the edge coupling configuration for $l_c = 1$ and 3, increasing the coupling strengths leads to a substantial increase of localization for the HOMO and LUMO, as they are almost exclusively localized on the adatom orbitals, see Fig. 6.3c. In contrast, bulk coupling affects the localization of almost all states as the coupling strength is increased. Our observations are in line with the findings of Fig. 6.3e, where we argued that the chain collapses into two smaller ones for high coupling strengths. In Fig. 6.4t, this translates to the fact that – except for the HOMO and LUMO – all states are either completely localized on the one side of the chain or on the other with respect to the adatom that effectively separates the two sides. Since the two chain fragments have almost equal lengths, their states attain the same localization value again. Figure 6.4s shows this fact in an even more instructive manner. As the chain is split in a ratio of 1:3 in this case, we observe a recurring four-state pattern for high coupling strengths. Three states in a row are localized on the longer part of the chain with a relatively small

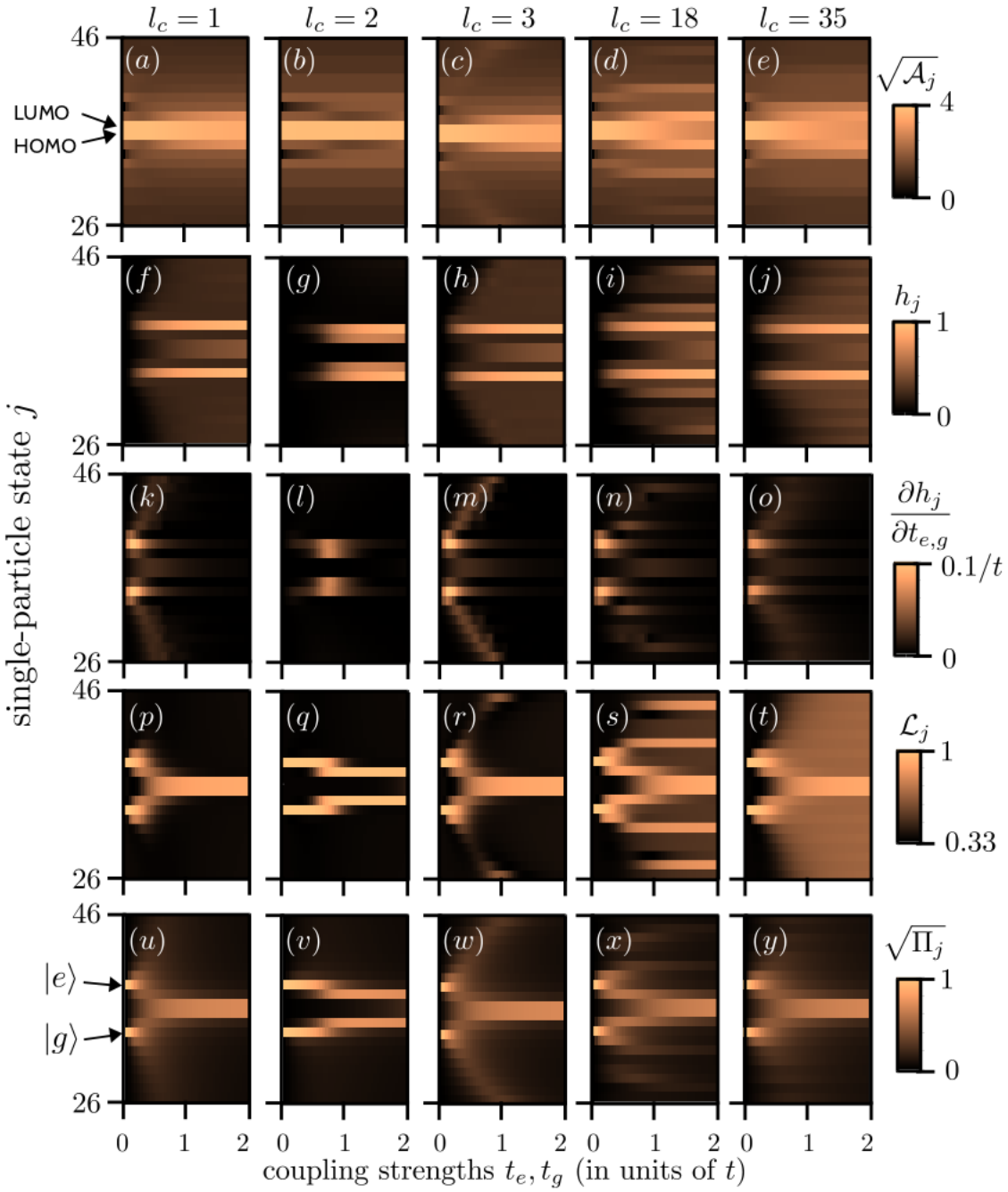

Figure 6.4: (**a**)-(**e**) Square root of the absorption activity $\sqrt{\mathcal{A}_j}$ of the states of the hybrid system consisting of an adatom and the 70-atomic linear carbon chain. We show the states in the region near the *Fermi* energy that is most relevant for optical interaction mechanisms, as a function of adatom coupling strengths t_e, t_g. The adatom is successively coupled to the edge atoms $l_c = 1, 2, 3$ and to the bulk atoms 18 and 35. (**f**)-(**j**) State hybridization h_j of the same hybrid system. (**k**)-(**o**) Derivative of the state hybridization with respect to the adatom coupling strengths $\partial h_j / \partial t_{e,g}$. (**p**)-(**t**) State localization $\mathcal{L}_j$. (**u**)-(**y**) Square root of the adatom population $\sqrt{\Pi_j}$.

localization, followed by one state localized on the shorter part of the chain with a high localization value, see also Fig. 6.3e.

The **adatom population** Π_j of the states in Figs. 6.4u-y reveal that, in the edge coupling case, whenever a state is localized, it is localized in the adatom orbitals (note the similarity of the subfigures in the fourth and fifth rows). On the other hand, when coupling the adatom to the bulk, we observe that localization on chain sites is also possible, especially for higher coupling strengths – supporting the discussion of Fig 6.3e in the previous paragraph.

In this section, we have investigated in detail how the energy landscapes and the state characteristics change upon coupling an adatom to the SSH chains. To that end, we have relied on measures of individual states in the hybrid system. The optical properties, however, emerge as a collective feature involving transitions from one state to others. Therefore, we discuss in the following how the transition dipole moments and, consequently, the oscillator strengths are modified when the adatom is coupled to the chains.

6.3.3 Transition Dipole Moments

Before we finally discuss the absorption cross-sections of the hybrid systems, we first take a look at how the transition dipole moments between the states in the hybrid system are modified. To that end, we show in Fig. 6.5 the transition dipole moments $|\langle j|\hat{\mathbf{r}}|j'\rangle|$ of the hybrid system comprised of an adatom and the linear chain discussed above for the five previously mentioned coupling positions and for different coupling strengths $t_e = t_g = 0.5t$, t, and $2t$. For convenience, at the top of the figure, we repeat the plot of the transition dipole moments of the *uncoupled* linear chain that was already provided in Fig. 4.3a. However, here we additionally introduce two rows and columns for the adatom states $|e\rangle$ and $|g\rangle$.

Let us first discuss the **edge coupling** configurations. Apart from the effects that arise due to the level crossing, the case $l_c = 2$, again, does not exhibit any noteworthy features, as coupling to this atom is negligible for all three coupling strengths (note the logarithmic scale). Coupling to atoms $l_c = 1$ or 3, on the other hand, enables many transitions that are additionally introduced into the the checkerboard pattern along the diagonals, when the coupling is weak and the systems hybridize notably (top row, $t_{e,g} = 0.5t$). For stronger coupling, however (middle and bottom row, $t_{e,g} = t$ and $2t$), the checkerboard patterns of states with well-defined symmetry are restored and, consequently, the associated electronic transitions are symmetry-forbidden again. This is in line with the discussion of Figs. 6.4k and 6.4m, where we saw that notable mixing of the two subsystems to a new hybridized entity occurs predominantly for rather small coupling strengths $t_{e,g} \approx 0.5t$. For larger coupling strengths, this mixing character vanishes, and we find again two separate units of smaller size and states of well-defined parity.

In the **bulk coupling** configuration, we observe a significantly different scheme. Already for the smallest coupling strength under investigation (top row, $t_{e,g} = 0.5t$), many additional strong transitions are enabled by breaking the symmetry of many states in the system. This increased number of optically contributing transitions persists for $t_{e,g} = t$ (middle row), but is reduced for $t_{e,g} = 2t$ (bottom row). We conclude that for small and intermediate coupling strengths, the system still behaves as a hybridized entity with modified optical properties. For higher coupling strengths, however, the chain collapses into its fragments and the resulting absorption characteristics are similar to that of two shorter chains.

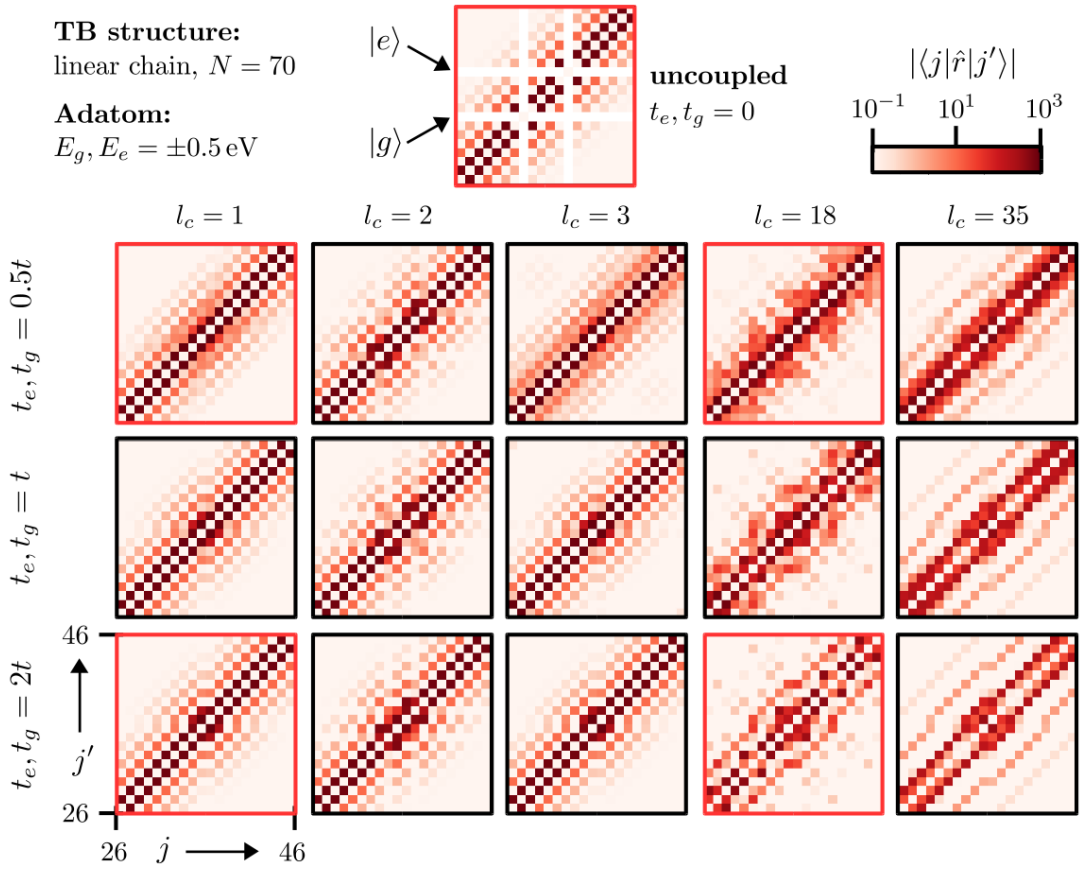

Figure 6.5: Transition dipole elements $|\langle j|\hat{r}|j'\rangle|$ between the states in the hybrid system comprised of an adatom and the linear 70-atomic chain for the edge and bulk coupling positions $l_c = 1, 2, 3$ (three left columns) and $l_c = 18, 35$ (two right columns). The coupling strengths are $t_e = t_g = 0$ (single top figure), $0.5t$ (first row), t (middle row), and $2t$ (bottom row). Red frames indicate the parameter sets discussed in Fig. 6.3.

6.3.4 Absorption Cross-Sections

Non-Interacting Absorption Cross-Sections

Since it is conceptually easier to access and interpret as compared to the system with *interacting* electrons, we first show in Fig. 6.6 the *non-interacting* absorption spectra of all three hybrid adatom–chain systems as a function of adatom coupling strengths for the five coupling positions already discussed above.

We begin with the discussion of the dimer chain (f-j) and the topological insulator (k-o), as they share many features in their spectra. Both absorption spectra are dominated by many closely spaced modes above $3\,\mathrm{eV}$ that belong to electronic transitions from the quasi-continuum of states below the *Fermi* energy to the ones above, see also Fig. 6.2. In infinite chains, one could call them *inter-band* modes made up by transitions from the valence to the conduction band. In the case of the topological insulator, we additionally find a set of closely spaced modes inside the band gap that couple the two edge states to the two quasi-bands even in the uncoupled system. Hence, this effect is intrinsic to the topological insulator and not related to the adatom. A similar set of states is found for non-zero coupling strengths in the dimer chain, too, when the adatom states

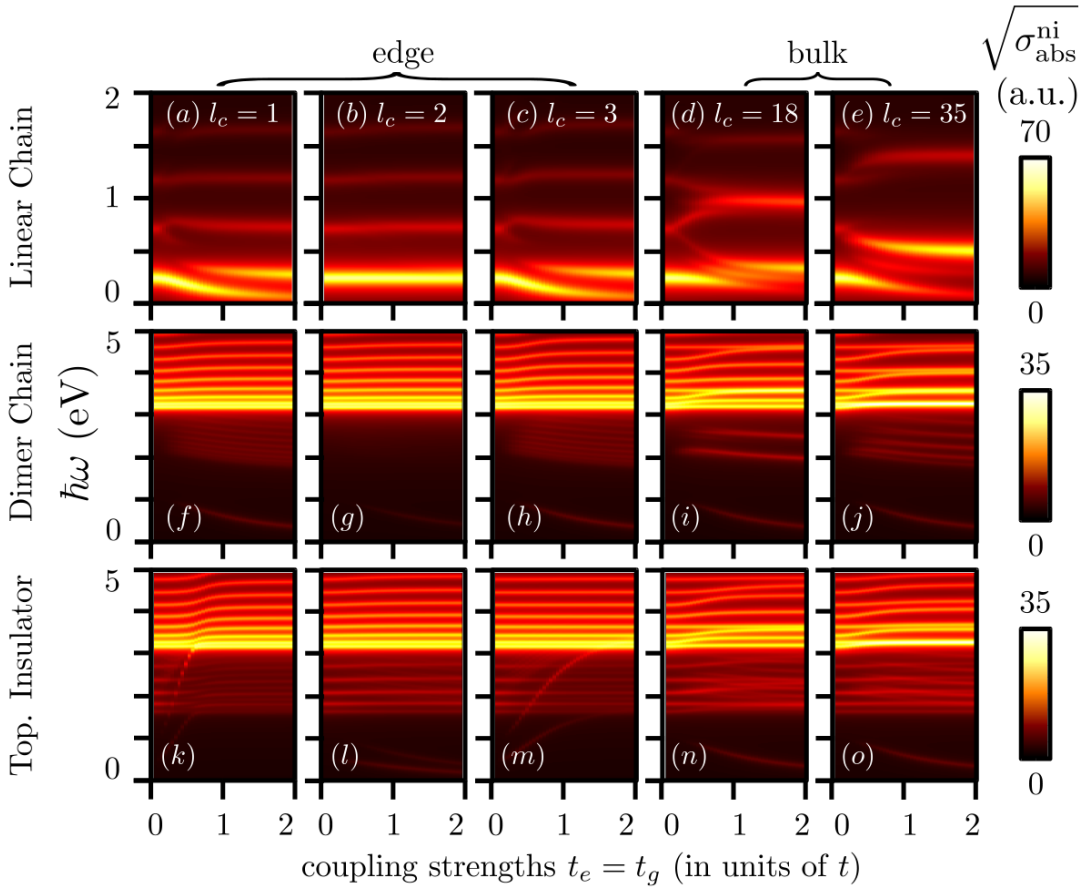

Figure 6.6: Square root of the *non-interacting* absorption cross section for the hybrid chain-adatom systems for the 70-atomic (**a**-**e**) linear chain, (**f**-**j**) dimer chain, and (**k**-**o**) topological insulator, again with $|\Delta/t| = 0.3$, as a function of adatom-chain coupling strengths t_e, t_g. The adatom is successively coupled to the *edge* atoms $l_c = 1$, 2, and 3 in the left columns, and to the *bulk* atoms $l_c = 18$ and 35 in the right columns, such that the chain is roughly split in the ratios 1:3 and 1:1, respectively.

are introduced inside the band gap and serve as mediators between the two quasi-bands. Moreover, also the two states introduced by the adatom couple to each other. In the dimer chain, this translates to a faint red-shifting low-energy mode below $1\,\mathrm{eV}$. In the topological insulator, on the other hand, this is only seen in the bulk coupling configurations in Figs. 6.6n and 6.6o, when the two adatom states energetically approach each other as the coupling strengths are increased, see again Fig. 6.2. In the edge coupling case, however, we observe two strongly blue-shifting modes for $l_c = 1, 3$. They stem from transitions between the parityless states in Figs. 6.2k and 6.2m, which dive into the quasi-continua for coupling strengths around $0.5t$ and $1.5t$, respectively, and from transitions between these states to the edge states. The last noteworthy feature in both species is the slight blue-shift of many quasi-continuum modes in the bulk coupling cases.

The non-interacting absorption cross-section of the linear chain is modified by the adatom in a completely different manner. Rather than introducing new optically active states into an otherwise rather unaffected energy landscape, the adatom completely changes the energy landscape of the linear chain and creates a truly hybridized system. Other than in the previous paragraph, modes that involve predominantly transitions from the

adatom states are not detectable in Figs. 6.6a-e, but all modes stem from the totally hybridized system.

For the edge coupling configurations $l_c = 1$ and 3, for instance, we observe a strong red-shifting mode below $0.5\,\mathrm{eV}$ with energy $0.24\,\mathrm{eV}$ for $t_{e,g} = 0$. It is clearly associated with the transition from the HOMO to the LUMO states at $E = \pm 0.12\,\mathrm{eV}$ in the uncoupled system. As the coupling strengths are increased, the HOMO and LUMO approach each other in Fig. 6.2a and, consequently, the corresponding mode red-shifts. Additionally, another prominent mode emerges for $t_{e,g} > t$ which can be associated to the transitions $|\text{HOMO-1}\rangle \rightleftarrows |\text{HOMO}\rangle$ and $|\text{LUMO}\rangle \rightleftarrows |\text{LUMO+1}\rangle$. Higher order modes are almost unaffected in the edge coupling configuration.

Next, we couple the adatom to the bulk atom $l_c = 18$ of the linear chain. The corresponding non-interacting absorption cross-section in Fig. 6.6d has one prominent mode at $0.24\,\mathrm{eV}$ in the uncoupled structure, which turns into one prominent mode at $0.33\,\mathrm{eV}$ and another pronounced mode at $0.98\,\mathrm{eV}$ for $t_{e,g} = 2t$. The interpretation is supported by considering Fig. 6.3e again. The chain is split into two shorter chains of 18 and 52 atoms, that are effectively decoupled from each other for high adatom coupling strengths. Consequently, the two new modes that emerge can be associated with the HOMO-LUMO transition of these two shorter chains. Indeed, the HOMO and LUMO states of an 18-atomic and 52-atomic linear chain reside at $\pm 0.16\,\mathrm{eV}$ and $\pm 0.49\,\mathrm{eV}$, respectively. Similarly, coupling to the bulk atom $l_c = 35$ effectively creates two shorter 35-atomic chains. The associated HOMO and LUMO states reside at $\pm 0.25\,\mathrm{eV}$ and produce a bright absorption peak around $0.5\,\mathrm{eV}$ in Fig. 6.6e for high adatom coupling strengths.

Interacting Absorption Cross-Sections

To finalize the discussion on the SSH chains, we condense all information of the previous sections and present in Fig. 6.7 the *interacting* absorption cross-section. To determine the induced electric charge in the hybrid system, we need to determine the elements of its *Coulomb* interaction matrix, v^{hyb}. The discussion on how exactly the elements are calculated is moved to App. B.2. Subsequently, the system is propagated in time according to Eq. (5.11) with $\lambda = 1$ after it has been kicked by a spectrally broad electric probing pulse, and the absorption cross-section is found through Eq. (5.14).

By comparing Figs. 6.6 and 6.7, it can be stated that the non-interacting absorption cross sections of the hybrid systems, that contain the dimer chain and the topological insulator, are only mildly modified when we take into account electron-electron interactions. The modes above $3\,\mathrm{eV}$ behave mostly the same. However, we notice that the modes inside the band gap rather blue-shift, while they previously red-shifted in the discussion above. Additionally, the *Coulomb* interaction smears out the heavily shifting modes in Figs. 6.7k and 6.7m that dive into the quasi-continua. Other than that, our results largely overlap with the non-interacting case, which is in agreement with the previous findings, that *Coulomb* interaction may be neglected in stand-alone isolating species like the dimer chain and the topological insulator [A2, 121].

The edge coupling configurations for the linear chain in Figs. 6.7a-c look substantially different as compared to the non-interacting case. First, the prominent low-energy mode has considerably moved to the blue and resides at $0.67\,\mathrm{eV}$ in the uncoupled system. Even when the coupling is increased, the mode remains relatively stable and does not shift considerably. Moreover, the next higher-order mode shifts to much higher energies as well and occurs around $1.8\,\mathrm{eV}$ in the interacting system. In particular, we need to note that the red-shift of the lowest-energetic mode in the non-interacting case is completely destroyed by the *Coulomb* interaction. Coupling to the bulk, on the contrary, offers much

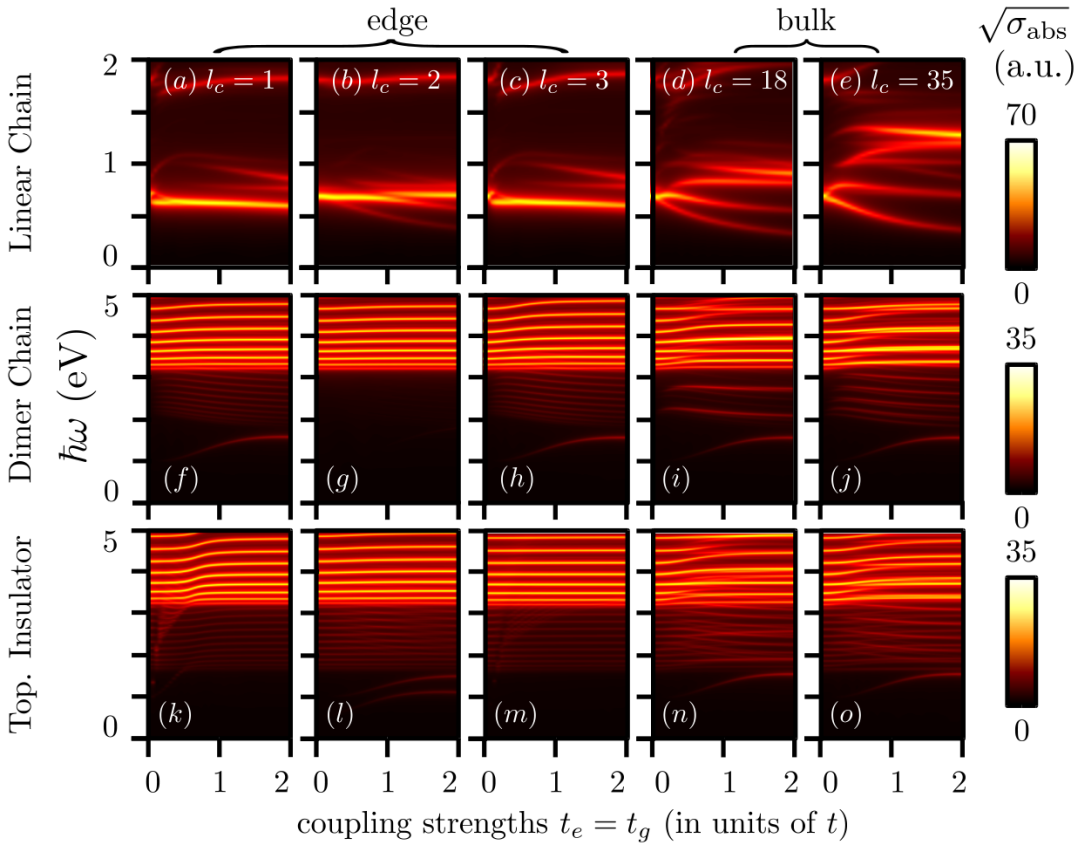

Figure 6.7: Square root of the *interacting* absorption cross section for the hybrid chain-adatom system for the 70-atomic (**a**-**e**) linear chain, (**f**-**j**) dimer chain, and (**k**-**o**) topological insulator. All remaining specifications are equal to the ones in Fig. 6.6.

richer tuning possibilities. For $l_c = 18$, the range between 0.35 and $1\,\mathrm{eV}$ is covered with comparably bright modes, and for $l_c = 35$, it is even possible to reach up to $1.4\,\mathrm{eV}$ for coupling strengths below t.

6.4 Modifications of Quantum Optical Phenomena in Hybrid Systems

The comprehensive discussion of how common quantum optical phenomena are modified by adsorbing an adatom to a nanoantenna in the above-presented manner is far beyond the scope of this thesis. However, to close this chapter, we shortly summarize the main findings of our work in Ref. [A5], where we discuss a hybrid system comprised of a triangular armchair graphene nanoantenna and a two-level system coupled to it. So far, we have focused in this chapter on how the *nanoantenna*'s electronic and optical properties are modified by the presence of the adatom. In Ref. [A5], on the contrary, we change the perspective and focus on how quantum optical phenomena in the *adatom* – such as *Rabi* oscillations and spontaneous emission – are modified upon coupling it to a nanoantenna in a self-consistent manner.

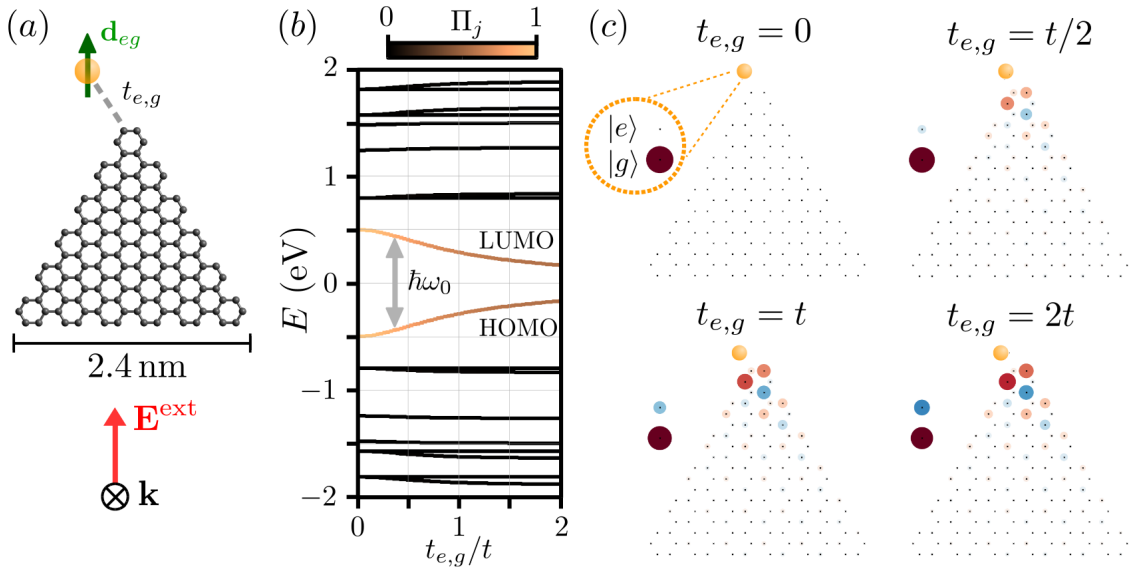

Figure 6.8: (a) A two-level adatom with intrinsic transition dipole moment $\mathbf{d}_{eg}$ is coupled with the coupling strengths $t_{e,g}$ to the top left atom of a 126-atomic armchair triangular graphene nanoantenna. The configuration is illuminated with a vertically polarized plane wave of frequency ω_0, which is determined by the HOMO-LUMO gap in (b). **(b)** Energy level diagram of the hybrid system with $E_{e,g} = \pm 0.5\,\text{eV}$ in (a) in the region $|E| < 2\,\text{eV}$, for coupling strengths in the range $0 \leq t_{e,g} \leq 2t$. The color of the lines indicate the adatom population Π_j of the corresponding state. **(c)** Real-space expansion of the HOMO state for four different coupling strengths.

Rabi Oscillations

To account for the *Rabi* oscillation mechanism in our model, we allow charge transfer between the excited and ground states of the two-level adatom also *via* the *optical* rather than the electronic channel. To that end, we directly couple their intrinsic transition dipole moment $\mathbf{d}_{eg} = e\mathbf{r}_{eg}$ to the total electric field at the position $\mathbf{r}_0$, where the adatom is located. Consequently, the electric potential in Sec. 5.2.2 is augmented and reads

$$\varphi(\mathbf{r},t) = \varphi^{\text{ext}}(\mathbf{r},t) + \varphi^{\text{ind}}(\mathbf{r},t) + \mathbf{r}_{eg}\cdot\mathbf{E}(\mathbf{r}_0,t)\left(|e\rangle\langle g| + |g\rangle\langle e|\right). \tag{6.5}$$

In contrast to the previous chapters, the total electric field $\mathbf{E}(\mathbf{r},t)$ is now dependent on the position. While the external electric field $\mathbf{E}^{\text{ext}}$ is still spatially constant, we now account for the potentially strong inhomogeneous induced electric fields in the vicinity of the nanoantenna, $\mathbf{E}(\mathbf{r},t) = \mathbf{E}^{\text{ext}}(t) + \mathbf{E}^{\text{ind}}(\mathbf{r},t)$. The *Rabi* oscillation frequency between two states $|j\rangle$ and $|j'\rangle$ is then [264, 265]

$$\Omega_{\text{Rabi}} = \frac{1}{\hbar}\sqrt{|\mathbf{E}(\mathbf{r}_0)\cdot\mathbf{d}_{eg}|^2 + \left(E_{j'} - E_j - \hbar\omega_0\right)^2}. \tag{6.6}$$

We study an armchair graphene triangle with 126 atoms and side length $2.4\,\text{nm}$. The adatom with $E_{e,g} = \pm 0.5\,\text{eV}$ and $|\mathbf{d}_{eg}| = 7.5\,\text{D}$ is coupled to the top left atom at the corner of the triangle with $t_e = t_g \leq 2t$, see Fig. 6.8a. The coupled system is exposed to a vertically polarized continuous plane wave illumination. Moreover, the frequency ω_0 of the illumination is chosen to be always resonant with the HOMO-LUMO transition of the system. Please note that this frequency is reduced with $t_{e,g}$ as the HOMO and LUMO states tend

toward zero for increasing coupling strength, like in the above-presented dimer chain system, see Fig. 6.8b.

We observe that the *Rabi* frequency *decreases* whilst the coupling strength between the adatom and the triangle is increased. The reason for this is the relatively large assumed dipole moment of the isolated adatom of $7.5\,\mathrm{D}$ in comparison to the relatively small dipole moments of transitions that occur between states of the isolated graphene nanoantenna, for which we have $d_{jj'} \leq 5\,\mathrm{D}$ [A5]. For $t_{e,g} = 0$, the HOMO and LUMO states are completely localized on the adatom orbitals, as can be seen by the color code in Fig. 6.8b and (for the HOMO) in the top left configuration of Fig. 6.8c. As the coupling is increased, the adatom hybridizes with the nanoantenna more and more. In the process, the HOMO and LUMO states increasingly extend over the nanoantenna as well, as is shown in Fig. 6.8c for different coupling strengths $t_{e,g} \leq 2t$. Thus, the HOMO-LUMO transition dipole moment decreases due to this admixture of the antenna contribution and – according to Eq. (6.6) – so does the *Rabi* frequency.

Spontaneous Emission

The spontaneous decay of an excited system in a cavity, that undergoes a transition from state $|j'\rangle$ with energy $E_{j'}$ to state $|j\rangle$ with energy $E_j < E_{j'}$, accompanied by the emission of a photon $\hbar\omega_{jj'} = E_{j'} - E_j$, can be described within the *Green*'s tensor formalism [266, 267]. In previous works, this approach was not only successfully applied to traditional high-Q cavities, but also to the case of plasmonic nanoantennas as open lossy cavities [268, 269]. The associated decay rate Γ of the excited system is given by [26]

$$\Gamma = \frac{2\omega_{jj'}^2}{\hbar\varepsilon_0 c_0^2}\, \mathbf{d}_{jj'}^{\mathrm{T}} \cdot \mathrm{Im}\, \overleftrightarrow{\mathbf{G}}(\mathbf{r}_0, \mathbf{r}_0, \omega_{jj'}) \cdot \mathbf{d}_{jj'}, \tag{6.7}$$

where $\mathbf{d}_{jj'}$ is the associated transition dipole moment, and $\overleftrightarrow{\mathbf{G}}(\mathbf{r}_0, \mathbf{r}_0, \omega_{jj'})$ denotes the *Green*'s tensor of the configuration including the plasmonic nanoantenna. The total *Green*'s tensor $\overleftrightarrow{\mathbf{G}} = \overleftrightarrow{\mathbf{G}}_{\mathrm{H}} + \overleftrightarrow{\mathbf{G}}_{\mathrm{S}}$ can be decomposed into the *homogeneous* part $\overleftrightarrow{\mathbf{G}}_{\mathrm{H}}$ accounting for the response in free space, and the scattered part $\overleftrightarrow{\mathbf{G}}_{\mathrm{S}}$ quantifying the influence of the nanoantenna [270]. Therefore, also the emission rate can be decomposed into the two parts, $\Gamma = \Gamma_{\mathrm{H}} + \Gamma_{\mathrm{S}}$. According to that, we observe two qualitatively different mechanisms that lead to a modification of the spontaneous emission rate of the HOMO-LUMO transition.

- **Electronic/Chemical Coupling:** The homogeneous component of Eq. (6.7) in the absence of a scatterer (in our case the antenna) is known as the *Weisskopf-Wigner* rate and reads $\Gamma_{\mathrm{H}} = \omega_{jj'}^3 |\mathbf{d}_{jj'}|^2 / 3\pi\varepsilon_0 c_0^3 \hbar$ [271, 272]. Thus, both the transition frequency $\omega_{jj'}$ and the transition dipole moment $\mathbf{d}_{jj'}$ enter the calculation. In Figs. 6.8b and 6.8c, we have seen that both quantities are modified as the adatom and the antenna couple *electronically*. They depend on the coupling strengths $t_{e,g}$, *i.e.*, on the distance of the adatom to the antenna, and are reduced with increasing hybridization. Consequently, also the homogeneous part of the *Green*'s tensor is affected by the electronic tunneling between the adatom and the antenna, and we observe a reduction of the homogeneous part of the spontaneous emission rate.
- **Optical Coupling:** Further alterations of the decay rate stem from the modification of the photonic environment the adatom is exposed to. In particular, the mere presence of the nanoantenna changes the local density of optical states and, in the process, the emission characteristics of the adatom. Our simulation results show a substantially increased spontaneous emission rate as compared to the free space emission rate with $\Gamma_{\mathrm{S}}/\Gamma_{\mathrm{H}} > 10^3$ for distances of a few Ångström [A5].

Conclusively, we can note that for coupling distances below $1\,\mathrm{nm}$ (which belong to interaction strengths in the order of $1\,\mathrm{eV}$), the electronic coupling channel enabled by $t_{e,g} > 0$ leads to a significant modification of the spontaneous emission rate for the HOMO-LUMO transition of the hybrid system. In particular, we find quenching of Γ as compared to the uncoupled case $t_{e,g} = 0$ due to a decrease of both the transition dipole moment and the associated transition frequency.

6.5 Conclusions

In this chapter, we have presented a framework to treat chemically coupled hybrid systems that consist of an optical nanoantenna and an adsorbed atom, modeled as a two-level system. We studied the influence of the system parameters such as coupling position and coupling strength on the electronic structure of the antenna. Furthermore, the tunability of the optical properties of the hybrid system was investigated. In particular, we found that the coupling position is crucial for the way the electronic structure is modified by the presence of the adatom. The metallic linear chain was found to be most attractive for optical tuning purposes in the case of relatively weak bulk coupling. For high coupling strengths, the adatom acts like a potential barrier for the wavefunction of the hybrid system and effectively splits the antenna apart into subsystems. The wavefunction is then located either on one part of the subsystem or the other. The two insulating chains, on the other hand, are affected less by the presence of the adatom, and only the states that were introduced into the band gap by the adatom approach each other for increasing coupling strengths. The model species, whose electronic and optical behavior resembles the armchair graphene triangles the most, is the dimer chain.

In the last section of this chapter, we have shortly reported on our main findings in Ref. [A5]. In particular, we study the modifications of the *Rabi* oscillations and spontaneous emission rate between the HOMO and LUMO states of the hybrid system as a function of the coupling strength, *i.e.* distance between the adatom and the nanoantenna. We find that both the *Rabi* oscillation frequency and the spontaneous emission rate of the transition are suppressed by the electronic coupling channel when $t_{e,g} > 0$.

7 | Quantifying Plasmonicity in Optical Nanostructures: A Literature Review

7.1 Introduction

Many attempts have been made in literature to define and determine what a plasmon is on the nanoscale. For that purpose, a variety of different characteristic features were taken into account [114–116, 118–122, 124, 125, 207, 273–276]. Generally, the object of interest is the electron dynamics in the considered structure upon excitation, be it in real or energy space. However, up to now there is no convincing definition of a plasmon on the nanoscale the scientific community has agreed on. Therefore, we see the need to review and reassess several approaches to characterize plasmons on the nanoscale in this chapter. We also want to raise awareness that all of these approaches only shine light on a certain aspect of what constitutes a plasmon. In particular, the problem has been identified in literature that there coexist definitions of what is a plasmonic response from a classical, a quantum mechanical, and an experimental perspective side by side [119]. While some parts of the definitions and characterization strategies provide consistent results, some also contradict each other.

Since discrete energy states do not exist in a classical framework, the need to distinguish between single-particle-like and plasmonic modes emerged only with the advent of quantum mechanical approaches to model the optical response of nanostructures. Among these methods are the jellium model [196], the configuration interaction method [200, 201], density functional theory (DFT) [80, 114, 118, 121–125, 206–212, 277, 278], the *Bethe-Salpeter* approach [202–204], quantum fluid dynamics [197–199], and the tight binding (TB) approach [46, 47, 185, 187, 279, 280].

Metallic nanoparticles and small molecular atomic clusters are ideal candidates to study the nature of optical modes that they sustain. In many of these systems, we simultaneously observe single-particle-like and plasmonic resonances at the same time:

- *Single-particle-like* modes appear as discrete electronic transitions from an occupied initial state $|i\rangle$ with energy $E_i \leq E_{\mathrm{HOMO}}$ to an unoccupied final state $|f\rangle$ with energy $E_f \geq E_{\mathrm{LUMO}}$ in a given nanoscopic system, see Fig. 7.1a. Consequently, the energy $\hbar\omega_{if}$ of such a transition can be predicted by the energy difference of the involved states in the non-interacting energy level diagram according to $\hbar\omega_{if} = E_f - E_i$. After the system has absorbed a photon with energy $\hbar\omega_{if}$, an electron can be lifted into a higher energetic state accordingly.
- *Plasmonic* modes, on the other hand, are often assumed to emerge as a result of long-range electron-electron interaction, such as *Coulomb* interaction. These mech-

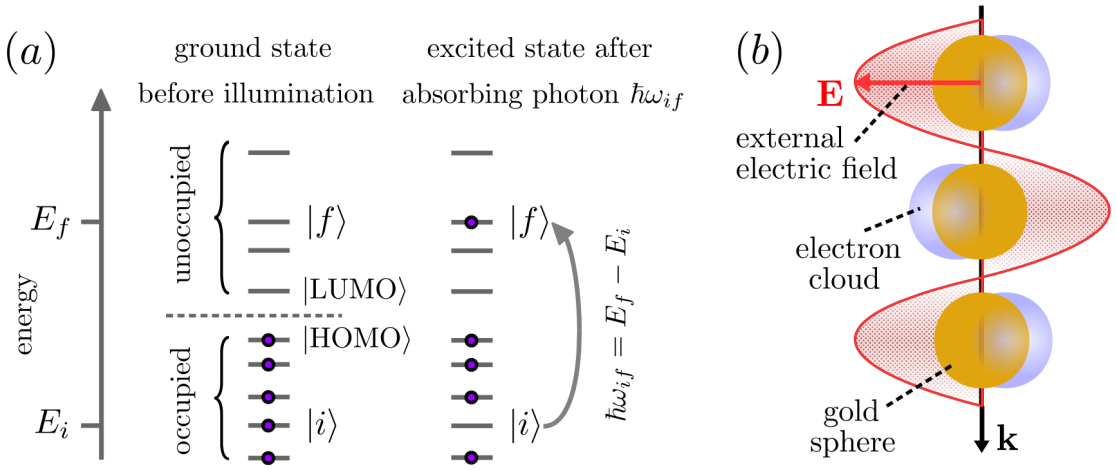

Figure 7.1: (a) Schematic illustration of a single-particle transition of an electron between the states $|i\rangle \rightarrow |f\rangle$ in energy space. **(b)** Real-space graphical illustration of a classical localized dipolar plasmon in a gold sphere as an electric field $\mathbf{E}$ impinges.

anisms couple the involved electrons coherently, such that they move as a collective electron cloud back and forth across the ionic background, *i.e.* the atomic cores of the host material, see Fig. 7.1b. Thus, the associated mode energy may deviate from transition energies that result from energy differences in the non-interacting energy landscape. Rather, *Coulomb* interaction must be taken into account to correctly predict the energy of the mode.

One major issue that comes along with schematic representations of single-particle transitions on the one hand and plasmons on the other hand is already implicitly addressed in Fig. 7.1. Single-particle transitions are predominantly diagrammed in energy space. Conversely, plasmonic modes tend to be graphically schematized in real space in most cases. This practice leads to the situation that many scientists in the field have no clear idea of how a single-particle transition manifests itself in real space. Or, on the contrary, how a plasmon is intrinsically created by electronic motion between states in energy space. This leads to many misleading or even wrong schematic illustrations of these kinds in literature. Therefore, two major objectives of this thesis are to raise awareness for this issue and to clarify which statements about the real-space (energy-space) dynamics of single-particle-like (plasmonic) modes can be made reliably.

Before we introduce our own contribution to the field – the energy-based plasmonicity index (EPI) – in the next chapter, the purpose of this chapter is to provide a broad overview over several approaches that aim to characterize single-particle-like and plasmonic response in nanostructures. To that end, we review the most prominent classical and quantum mechanical concepts of plasmonicity that exist in literature. Moreover, we shine light on computational procedures and metrics that have been developed to decide on *how plasmonic* a given mode is – and discuss what plasmonic exactly means in the respective context.

7.2 Plasmonicity Index and Generalized Plasmonicity Index

From a classical perspective, the smoking gun of a plasmonic resonance is the real-space charge cloud oscillation of mobile electrons relative to the static atomic cores. This oscillation is driven by an externally applied electric irradiation field $\mathbf{E}^{\text{ext}}$ and the resulting

induced electric field $\mathbf{E}^{\mathrm{ind}}$ is experimentally well-observable. The underlying philosophy in this approach of characterizing a plasmon is to trace the electronic motion in *real space* and the induced field generated by this oscillation. Along these lines, Bursi *et al.* [114] proposed the plasmonicity index (PI) in 2016 to determine how plasmonic a mode ξ sustained by a nanostructure is. They introduced the PI according to

$$\mathrm{PI}_\xi = \frac{\int \mathrm{d}^3\mathbf{r}\, |\phi_\xi^{\mathrm{ind}}(\mathbf{r})|^2}{\int \mathrm{d}^3\mathbf{r}\, |\rho_\xi(\mathbf{r})|^2}, \tag{7.1}$$

where $\rho_\xi(\mathbf{r})$ denotes the transition density or the induced charge density of mode ξ in a time-dependent density functional theory (TD-DFT) or classical framework, respectively. Moreover,

$$\phi_\xi^{\mathrm{ind}}(\mathbf{r}) = \frac{1}{4\pi\varepsilon_0} \int \mathrm{d}^3\mathbf{r}' \frac{\rho_\xi(\mathbf{r}')}{|\mathbf{r}-\mathbf{r}'|} \tag{7.2}$$

is the induced potential associated with $\rho_\xi(\mathbf{r})$.

One year later, in 2017, Zhang *et al.* [115] refined the PI by normalizing it with the external potential $\phi^{\mathrm{ext}}(\mathbf{r})$ that is applied to generate the structure's response. This dimensionless measure is called the *generalized plasmonicity index* (GPI),

$$\mathrm{GPI}_\xi = \frac{|\int \mathrm{d}^3\mathbf{r}\, \rho_\xi(\mathbf{r})\phi_\xi^{\mathrm{ind}}(\mathbf{r})|}{|\int \mathrm{d}^3\mathbf{r}\, \rho_\xi(\mathbf{r})\phi^{\mathrm{ext}}(\mathbf{r})|}, \tag{7.3}$$

where $\phi_\xi^{\mathrm{ind}}(\mathbf{r})$ is defined in Eq. (7.2) and the external potential obeys $\mathbf{E}^{\mathrm{ext}}(\mathbf{r}) = -\nabla\phi^{\mathrm{ext}}(\mathbf{r})$. Both measures are based on the induced potential that builds up in the structure as a response to the unequal charge distribution. Therefore, these measures are expected to peak when the transition densities or induced charge densities of the associated modes exhibit a pronounced charge separation and, therefore, induce strong electric fields. Note that both Eqns. (7.1) and (7.3) are evaluated using exclusively real space-based quantities. The GPI is superior to the PI in the sense that it is dimensionless and independent on the absolute value of the external illumination intensity. However, both indices are not normalized to a certain interval. Thus, the (G)PI of, say, the fundamental dipolar mode in a gold Au_{20} chain cannot be directly compared to the (G)PI of the corresponding mode in a sodium Na_{20} chain.

Furthermore, from the two measures one cannot decide if the mode under consideration is only present in the *interacting* system, since it originates from *Coulomb* interaction, or if the mode is present in the associated *non-interacting* system as well and can be related to a single-particle transition in the non-interacting energy level diagram. The real-space induced charge densities of single-particle HOMO-LUMO transitions in polyacene molecules [208] or silver and gold nanowires [276, 281], for example, exhibit large dipole moments and strong charge separation. Also, it has been shown [A2] that the HOMO-LUMO transition in polyene chains features large dipole moments even in the *absence* of *Coulomb* interaction. For that reason, the (G)PI will classify the respective modes as plasmons. Please note that this is by no means a flaw or a fault in construction of these indices. In the sense of the (G)PI, a mode may very well be plasmonic even though it intrinsically origins from a single-particle transition without any contradiction. Only the embodiment of a mode in real space is assessed by the (G)PI, not its origin in energy space.[1]

[1] In fact, the (G)PI can be evaluated with purely classical means. It is neither required to compute energy

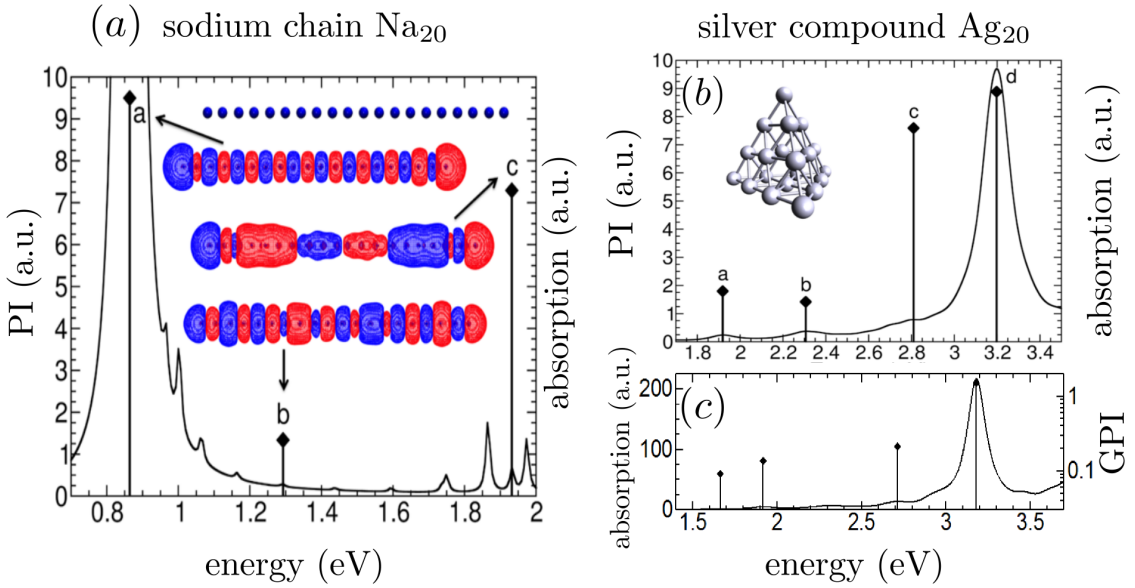

Figure 7.2: (a) Absorption cross-section (solid line) and PIs (diamonds) of the modes in a sodium chain Na_{20}. The insets show the transition densities of the marked modes. **(b)** Absorption cross-section and PIs of four prominent modes in the silver compound Ag_{20}. *Both figures adapted with permission from Ref. [114]. Copyright © 2016 American Chemical Society.* **(c)** Absorption cross-section and GPIs of modes in the same silver species as in (b). Please note the logarithmic scale of the GPI. Also, only the modes around $1.9\,\mathrm{eV}$ and $3.2\,\mathrm{eV}$ are evaluated in both figures and are, therefore, directly comparable. *Adapted with permission from Ref. [115]. Copyright © 2017 American Chemical Society.*

Application: Sodium Chain Na_{20} and Silver Compound Ag_{20}

Figure 7.2(a) shows the absorption spectrum (solid line) and the PIs (diamonds) of three selected modes in the sodium chain Na_{20}. The simulations have been conducted with TD-DFT, and the insets refer to the associated transition densities of the modes. We notice that the PI is not trivially linked to the oscillator strength of the respective mode (neither is the GPI). As expected, the PI is larger for modes that exhibit a prominent charge separation accompanied with a strong dipole moment, since these modes produce the highest induced potentials. In Fig. 7.2b, we see the absorption spectrum and the PI of the silver compound Ag_{20}. The modes c and d around $2.8\,\mathrm{eV}$ and $3.2\,\mathrm{eV}$, respectively, illustrate that two modes of very different absorption can result in similar PIs to assess their plasmonic characters. The absorption spectrum of the same Ag_{20} compound along with its GPI is shown in Fig. 7.2c. In comparison with Fig. 7.2b, we can observe a qualitative correlation of the PI and the GPI values of three directly comparable modes at $1.9\,\mathrm{eV}$, $2.75\,\mathrm{eV}$, and $3.2\,\mathrm{eV}$.[2] Thus, it may be concluded that the PI and the GPI indeed probe the same characteristic feature of a mode and provide consistent classification results.

levels nor the associated states of a nanostructure. Therefore, statements regarding the electron dynamics in energy space in general, and about the involved states in particular, are not possible.

[2]Unfortunately, the mode at $2.3\,\mathrm{eV}$ has not been analyzed in Ref. [115]. Also, we note from direct comparisons of the PI and the GPI of other identical structures, that the absolute value of the oscillator strength of a given mode is much stronger correlated to the GPI than it is to the PI. This observation is also present in the examples given in Figs. 7.2b and 7.2c for the two high-energy modes.

7.3 *Coulomb* Scaling Approach

Crucial for the emergence of modes with collective electronic motion in *classical* systems is the existence of long-range electron-electron interaction. Expressed differently, *Coulomb* interaction is a prerequisite for electron cloud oscillations in real space. In the *quantum* world, however, it is no longer that trivial. In their visionary work [273] on plasmonics in 1952, Pines and Bohm came to the conclusion that charge oscillations may contain single-particle-like *and* collective character at the same time, whereas the latter is only present if long-range electron-electron interaction is taken into account. Their statement already hints to the fact that a collective electronic motion in real space cannot be the sole defining property of a plasmon on the nanoscale any longer, considering that also single-particle transitions reveal themselves in the same way.

Indeed, it has been found that HOMO-LUMO single-particle transitions of polyacene molecules, for instance, appear as electron cloud oscillations in real space [208], reminiscent of classical plasmons. Also, Guerrini *et al.* studied the plasmonic character of optical resonances in J-aggregates based on the GPI [202] in 2019, employing the real space-based plasmonicity concept. In their conclusions section, they state that a "bright excitation in molecular systems, even when coming from a collective mechanism, may well have no relation with plasmons". Fitzgerald *et al.*, on the other hand, write [117] that "a single electron-hole pair separated over a large distance can give a large dipole moment but it does not seem sensible to describe it as plasmonic". Based on these statements, it seems apparent that the concept of a plasmon on the nanoscale is multifaceted and needs further discussion.

Following the above-mentioned interaction energy-based concept of plasmonic modes, Bernadotte *et al.* [121] introduced an electron-electron interaction scaling approach in 2013 to identify plasmons in small molecular compounds that has been generalized to a wide range of simulation frameworks by Krauter *et al.* [122] in 2015. It requires a series of simulations where the electron-electron interaction strength is gradually increased by scaling the *Coulomb* interaction strength[3] with a parameter $\lambda \in [0, 1]$ in each simulation step. Then, the non-interacting simulation ($\lambda = 0$) is compared to the interacting simulations ($0 < \lambda < 1$). Modes that remain spectrally stable are concluded to exist independently of the *Coulomb* interaction and are, therefore, classified as *single-particle-like*. On the other hand, modes that spectrally blue-shift are classified as *plasmonic*, as their energies apparently depend on the *Coulomb* interaction strength.

Application: Sodium Chain Na_{20} and Silver Compound Ag_{20}

In Fig. 7.3, we see a typical set of DFT simulation results of the scaling approach for the two previously discussed species: (a) the sodium chain Na_{20} and (b) the silver compound Ag_{20}. The spectra of the sodium chain exhibit two qualitatively different kinds of states. Small black dots represent states that do not shift considerably with λ. Also, these *single-particle-like* states barely contribute to the absorption spectrum of the structure as can be seen in the middle panel of Fig. 7.3(a). On the other hand, we observe two[4] modes classified as *plasmonic*. They are indicated by red and green color, respectively, and strongly

[3] The computational method of choice in Ref. [121], where the scaling approach has been introduced, is DFT. Here, not only the *Coulomb* interaction has been scaled by the parameter λ, but also the electronic exchange-correlation interaction (XCI). In our TB approach, we assume that its short-ranged nature allows for absorbing the XCI into the hopping parameter t of the model, see Eq. (3.8).

[4] For $0 < \lambda < 0.4$, we can even observe the onset of a second higher-order plasmonic mode. However, since its energy in the fully interacting chain is out of the considered energy window, we do not address it here.

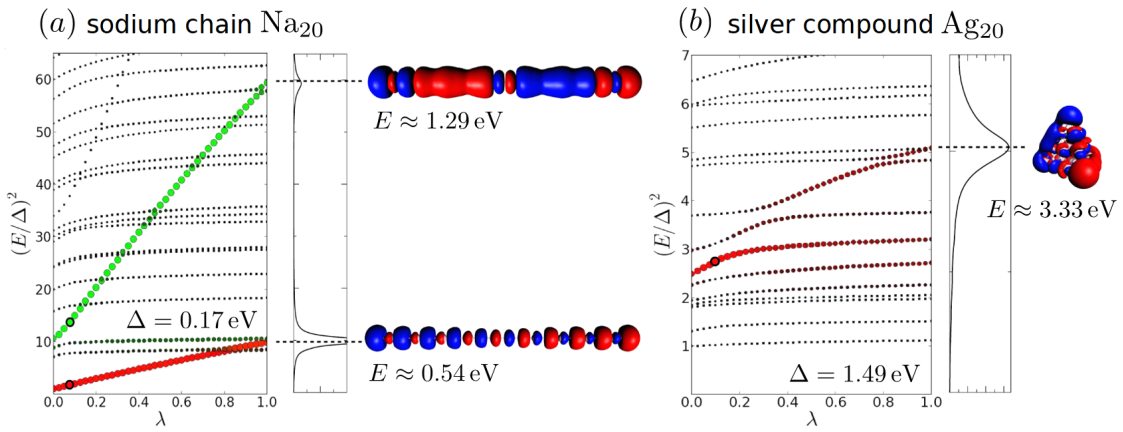

Figure 7.3: (a) Energy spectrum (left) of the sodium chain Na_{20} as a function of the electron-electron interaction scaling parameter λ alongside with its absorption spectrum (middle) and the transition densities (right) of the two prominent longitudinal modes at $0.54\,\mathrm{eV}$ and $1.29\,\mathrm{eV}$. The green and red colors are a guide to the eye to follow the states in the spectrum. In both subfigures, Δ denotes the HOMO-LUMO gap energy of the respective structure. **(b)** Energy spectrum (left) of the silver compound Ag_{20} as a function of the electron-electron interaction scaling parameter λ alongside with its absorption spectrum (middle) and the transition density (right) of the prominent modes at $3.33\,\mathrm{eV}$. *Both figures adapted with permission from Ref. [121]. Copyright © 2013 American Chemical Society.*

blue-shift as λ is increased. Moreover, the absorption spectrum exhibits two strong peaks associated with these modes at $0.54\,\mathrm{eV}$ and $1.29\,\mathrm{eV}$ in the fully interacting chain ($\lambda = 1$). In the right panel, we show the strong structured character of the transition densities of said modes with pronounced charge separation. Whereas the charge pattern of the former reminds one of the fundamental dipolar mode with one node along the chain, the latter resembles the first higher order dipole-active mode with three nodes.

Figure 7.3(b) shows the spectra of the silver compound Ag_{20} for different electron-electron interaction strengths. Apart from various single-particle-like spectrally stable modes, we observe one strongly blue-shifting mode in the energy window $2 < (E/\Delta)^2 < 5$, indicated by the red color. Unlike in the previous case, we see avoided level crossings. This is an indication that the mode strongly hybridizes with other states as it pushes its way through the spectrum. The absorption spectrum exhibits one prominent peak at $3.33\,\mathrm{eV}$ for $\lambda = 1$. Consistent with the investigations regarding the PI and GPI in Sec. 7.2, it is classified plasmonic here as well. Similar to the sodium chain, also the transition density of the plasmonic mode in the Ag_{20} species attracts attention with its strong dipolar embodiment in real space. Further investigations, especially in linear polyene chains, reveal that indeed the classification of resonances according to the scaling method can directly be related to the real-space embodiment of the mode. Real-space transition densities (or induced charge densities) of plasmonic modes exhibit substantially larger dipole moments than their single-particle-like counterparts.

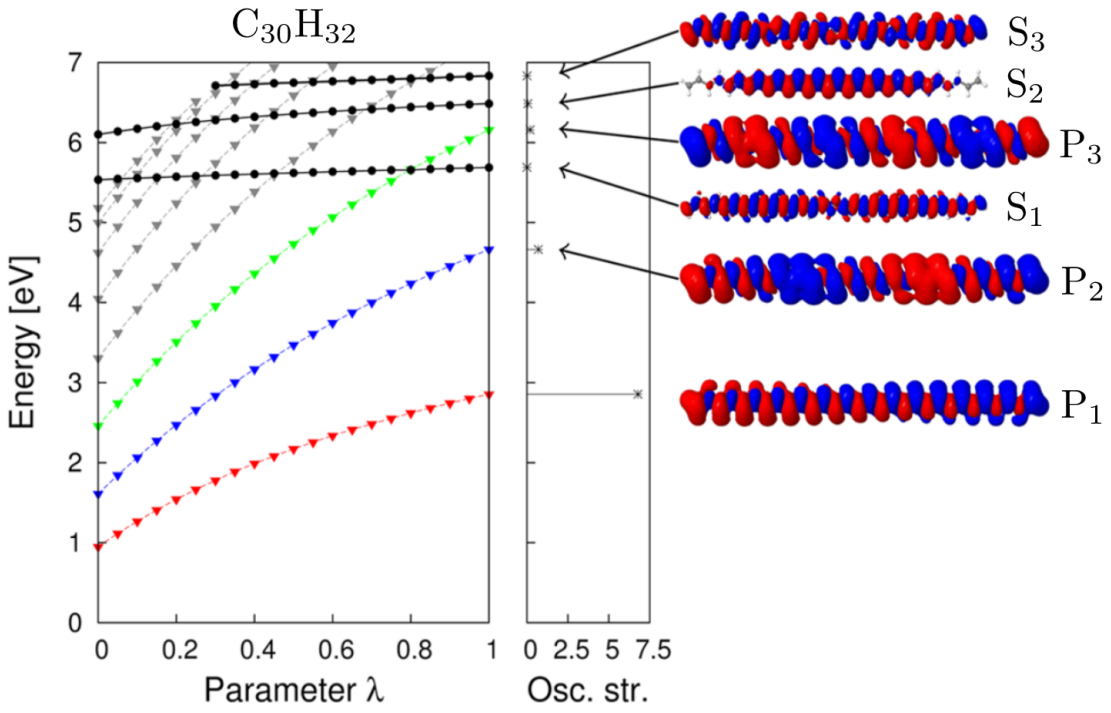

Figure 7.4: Energy spectrum (left) of the carbon-based polyene chain $C_{30}H_{32}$ as a function of the *Coulomb* interaction scaling parameter λ alongside with the oscillator strengths (middle) and the transition densities (right) of the corresponding modes for $\lambda = 1$. *Adapted with permission from Ref. [122]. Copyright © 2015 American Chemical Society.*

Application: Linear Polyene $C_{30}H_{32}$

To elucidate this further, and also to get closer to the carbon-based linear chain species that are treated within the TB framework in this thesis in more detail, we present the scaling approach applied to the linear polyene chain $C_{30}H_{32}$ in Fig. 7.4 [122]. This species hosts both single-particle-like and plasmonic resonances in the same spectral region and is, therefore, of special theoretical interest for the characterization of optical resonances.

For $\lambda = 1$, we observe six modes in the energy range below $7\,\mathrm{eV}$. Based on their scaling behavior, they can be grouped into single-particle-like modes and plasmonic modes, tagged by the letters S and P, respectively. The single-particle-like modes, indicated by black dots in the left panel, remain spectrally relatively stable as the *Coulomb* interaction strength is varied. The associated oscillator strengths are comparatively small and, therefore, the S-modes do not significantly contribute to the absorption spectrum of the chain. Following the atoms along the chains, the signs of the corresponding transition densities change atom by atom. For the modes S_1 and S_2, one can additionally note that the transition densities follow envelopes in the shape of a full wavelength and half a wavelength along the chain, respectively. Furthermore, we note another class of modes that blue-shift with increasing λ and that are indicated by colored triangles in the left panel and the letters P in the right panel of Fig. 7.4. Their associated oscillator strengths and dipoles are considerably higher as compared to the S-modes and, therefore, they dominate the absorption spectrum of the structure. Other than for the S-modes, the transition densities of the P-modes feature the same pronounced charge separation as for the Na_{20}

chain in the previous section. Whereas the notional envelope of the fundamental plasmonic mode P_1 displays one nodal point, the higher order modes P_2 and P_3 show three and five nodes, respectively.

In summary, we note that the scaling approach is based on the electronic interaction energy that is present in the system. The energies of the modes classified as plasmonic by the scaling approach considerably blue-shift with increasing interaction strength. Also, they exhibit a strong dipole moment in real space. The classification results of the (G)PI and the scaling approach can be considered consistent.

7.4 Collectivity Index and Plasmon Index

In real space, plasmonic modes in a finite structure are associated with the collective oscillation of mobile electrons. Naively, one could generalize this concept of a plasmon directly to energy space. Hence, in contrast to the picture of a single-particle transition, plasmonic modes are often imagined as a whole collection of single-particle transitions that perpetually populate and deplete energy states close to the *Fermi* energy or the HOMO-LUMO gap of the system in an oscillatory manner. Along these lines, Yasuike *et al.* proposed in 2011 the collectivity index (CI) [116] to characterize plasmonic modes by quantifying *how many* electron-hole pairs are significantly contributing to a given resonance. Fitzgerald *et al.* then introduced the "Plasmon Index" [117] as the product of the CI with the dipole strength of the respective mode in the absorption spectrum.[5]

By analyzing the CI, it becomes apparent that not all concepts of plasmonicity in literature are compatible with each other. In the following, we will see, for example, that the CI actually classifies the fundamental longitudinal mode in a sodium chain as least plasmonic possible, although it was classified as most plasmonic in the previous approaches.

Application: Sodium Chain Na_{10}

We show the absorption spectrum (red) of the Na_{10} chain in Fig. 7.5a, obtained from linear response density functional theory (LR-DFT). The transition densities of the two most prominent modes are depicted above. The fundamental longitudinal mode (L) slightly below $1\,\mathrm{eV}$ can be associated with the lowest-energy modes of the sodium chain Na_{20} already discussed in Figs. 7.2a and 7.3a. In all previously presented approaches, it is considered the most plasmonic mode in the system. Here, however, we obtain the smallest possible collectivity index value of only 1, while the higher-energy transversal mode (T) has a CI of 4.6, for instance. Also the Plasmon Index of the T-mode is higher than that of the L-mode, as can be seen by the black vertical lines in Fig. 7.5a. Figure 7.5b reveals why this is the case. The CI is a measure of how many electron-hole pairs contribute to the respective resonance. We notice that the L-mode comprises the HOMO-LUMO transition only, indicated by the green arrow. Thus, only one electron-hole pair is involved and, as a result, the CI of the mode is 1. On the other hand, the transversal mode is built up by many single-particle transitions from below the HOMO to well above the LUMO, indicated by the red arrows, resulting in a much higher CI.

In conclusion, it needs to be noted that the CI and the Plasmon Index are not compatible with the concept of a plasmon that the (G)PI and the scaling approach rely on. In

[5] A comprehensive overview of how the CI is explicitly calculated makes it necessary to introduce DFT notation to a large extent. Therefore, and since the interpretation of the CI as the number of involved electron-hole pairs is rather intuitive, we refrain from reproducing computational details here and refer to Refs. [116] and [117].

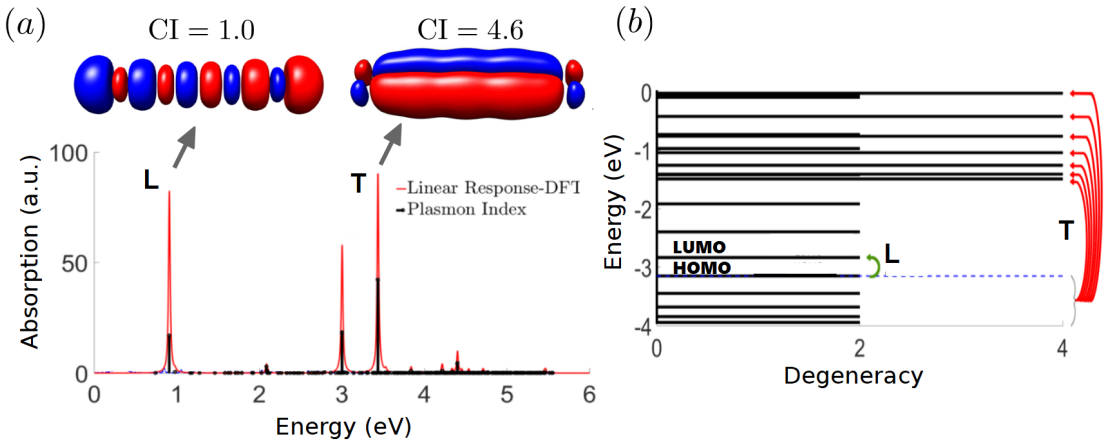

Figure 7.5: (a) Absorption spectrum of the sodium chain Na_{10} obtained from LR-DFT (red solid line) and Plasmon Index (black vertical lines) of the associated absorption modes. Transition densities of the longitudinal (L) and transversal (T) modes are shown together with their collectivity index CI. **(b)** Energy eigenstates of the sodium chain Na_{10} and their degeneracies. The green arrow indicates the HOMO-LUMO transition that produces the longitudinal mode L shown in (a). The set of red arrows indicates that the transversal mode T is built up by many single-particle transitions. *Both figures adapted with permission from Ref. [117]. Copyright © 2017 American Physical Society.*

the sense of the CI and the Plasmon Index, the fundamental longitudinal mode (L) is single-particle-like.[6] The scaling approach and the (G)PI, on the other hand, make a very good argument that it should be considered the most plasmonic mode in the system. To account for this issue, we present an approach in the next section that identifies three quantifiable aspects of plasmonicity at the same time and combines them to a multidimensional characterization approach. In addition, the dichotomy of plasmonic and single-particle-like modes is weakened by grouping optical modes into four categories instead of two.

7.5 Multidimensional Approach: Superatomic Character, Collectivity, and Dipole Additivity

In 2020, Gieseking *et al.* [118] proposed to judge the character of a mode associated to the excited state $|\Psi_e\rangle$ based on three nearly orthogonal characteristic features of a plasmonic response. In the applied TD-DFT framework, the excited state

$$|\Psi_e\rangle = \sum_{i=1}^{N} \lambda_{i,e} |\varphi_i\rangle \tag{7.4}$$

is a linear combination of N single-particle *Kohn-Sham* states $|\varphi_i\rangle$. Its plasmonic character is assessed by computing its superatomic character S_e, its collectivity τ_e, and its dipole additivity d_e, which are defined in the following.

[6] In fact, it could not be more single-particle-like, because it only consists of one single transition in the non-interacting energy landscape.

1. The **superatomic character**

$$S_e = \sum_{i=1}^{N} |\lambda_{i,e}|^2 \delta_{SA,i} \in [0,1] \tag{7.5}$$

of $|\Psi_e\rangle$ indicates whether $|\Psi_e\rangle$ is associated with an excitation of conduction electrons that populate *delocalized* molecular orbitals. Here, $\delta_{SA,i} = 1$ if the single-particle excitation $|\varphi_i\rangle$ is superatomic, *i.e.* if it extends across a large part of the molecule, and $\delta_{SA,i} = 0$ if not. Identifying these superatomic orbitals is not trivial and may involve several strategies. On the one hand, one can identify superatomic orbitals through their delocalized transition densities – either visually or based on the *participation ratio* [282, 283] as a measure for the number of atoms in the molecule that are significantly involved in the orbital. On the other hand, one can project $|\varphi_i\rangle$ onto a wavefunction basis set that is strongly localized around associated atomic potentials (tight binding basis sets, for instance), or apply particle-in-a-box models [284]. For silver clusters, one can in practice judge the superatomic character of an orbital by the amount of $5s$ and $5p$ atomic orbital contributions to $|\varphi_i\rangle$ [118], as these two orbitals mostly form the conduction band in bulk silver.

2. The **collectivity**

$$\tau_e = \left(\sum_{i=1}^{N} |\lambda_{i,e}|^4 \right)^{-1} \in [1,N] \tag{7.6}$$

of $|\Psi_e\rangle$, also called *transition inverse participation ratio* (TIPR) [285], is a measure for the number of single-particle excitations that is involved in $|\Psi_e\rangle$. The collectivity is 1 if only one single-particle excitation contributes with $\lambda_{i,e} = 1$ and it is N if N single-particle excitations contribute with equal weights $|\lambda_{i,e}| = 1/\sqrt{N}$. The collectivity τ_e is equivalent to the CI in the previous section.

3. The **dipole additivity**

$$d_e = \frac{|\sum_{i=1}^{N} \lambda_{i,e} \boldsymbol{\mu}_{gi}|}{\sum_{i=1}^{N} |\lambda_{i,e} \boldsymbol{\mu}_{gi}|} \in [0,1] \tag{7.7}$$

of $|\Psi_e\rangle$ is a measure not only for how collective but also how *coherent* an excited state is. Here, $\boldsymbol{\mu}_{gi}$ is the transition dipole moment between the ground state $|g\rangle$ and $|\varphi_i\rangle$. Intuitively, d_e can be interpreted as a measure for how aligned the dipole moment contributions of different single-particle excitations in $|\Psi_e\rangle$ are. If several contributions cancel out, the numerator stays small. If they line up, the numerator approaches the denominator, where total alignment is assumed, and $d_e \to 1$. Please note that d_e only contains information for states with high collectivity $\tau_e \gg 1$. For $\tau_e = 1$, for instance, d_e always evaluates to 1.

Based on the above three criteria, Gieseking *et al.* present a categorization scheme that includes four kinds of states: Plasmon-like states, collective states, single-particle states, and interband states. Table 7.1 shows an overview of this categorization scheme. A mode is considered *plasmon-like* only if all three characterization indicators attain a large value. The mode's charge oscillation needs to extend across the entire particle, it needs to be comprised of many single-particle transitions, and their transition dipoles need to be

Table 7.1: Gieseking's categorization of plasmon-like, collective, single-particle, and interband states with regard to the criteria superatomic character S_e, collectivity τ_e, and dipole additivity d_e.

	superatomic character S_e	collectivity τ_e	dipole additivity d_e (coherence)
plasmon-like	large	large	large
collective	large	large	small
single-particle	large	small	irrelevant
interband	small	irrelevant	irrelevant

aligned. If the last requirement is not met, the mode is classified as *collective*. *Single-particle* modes have large superatomic character, but small collectivity, and *interband* modes have a small superatomic character.

Application: Icosahedral Ag_{13}^{5+} Cluster

Figure 7.6 shows (a) the absorption spectrum and (b) the analysis of the three presented indicators of an icosahedral Ag_{13}^{5+} cluster for all excited states in the spectral range between $2.5\,\mathrm{eV}$ and $7\,\mathrm{eV}$. In Fig. 7.6b, filled circles indicate a high superatomic character of $S_e > 0.75$, crosses represent values of $S_e < 0.25$. The size of the symbols encodes the collectivity and their color the dipole additivity. We observe only one single plasmon-like mode around $4.2\,\mathrm{eV}$, which at the same time has a large superatomic character, large collectivity, and large dipole additivity. The mode slightly above $3.5\,\mathrm{eV}$ is classified as collective, since its dipole additivity is only small or intermediate. Two modes between $2.5\,\mathrm{eV}$ and $3\,\mathrm{eV}$ are visible with low collectivity and dipole additivity, but large superatomic character. Therefore, they are classified as single-particle modes. All other modes above $4.5\,\mathrm{eV}$ show low superatomic character and are, consequently, classified as interband modes.

In the next section, we review a more thorough analysis of the electron dynamics involved in a mode – not only in real space, but also in energy space. From the treatment of the collectivity τ_e, the CI and the Plasmon Index, we have seen that it is not enough to investigate only the number of involved transitions. Also, Table 7.1 reveals that even modes with large superatomic character and large dipole moment are considered single-particle-like, if they are not collective. This applies to the longitudinal L-modes in the sodium chains (see Fig. 7.5a, for instance), which are classified plasmonic in the (G)PI and scaling approaches.

In conclusion, Gieseking's approach helps to create a clear picture of the multidimensionality of plasmonic response and to provide an overview over relevant characteristic features. Further application examples in silver nanowires and nanorods can be found in Ref. [120]. However, to get an even more comprehensive picture, we now focus on the energy-space electronic motion in *time*.

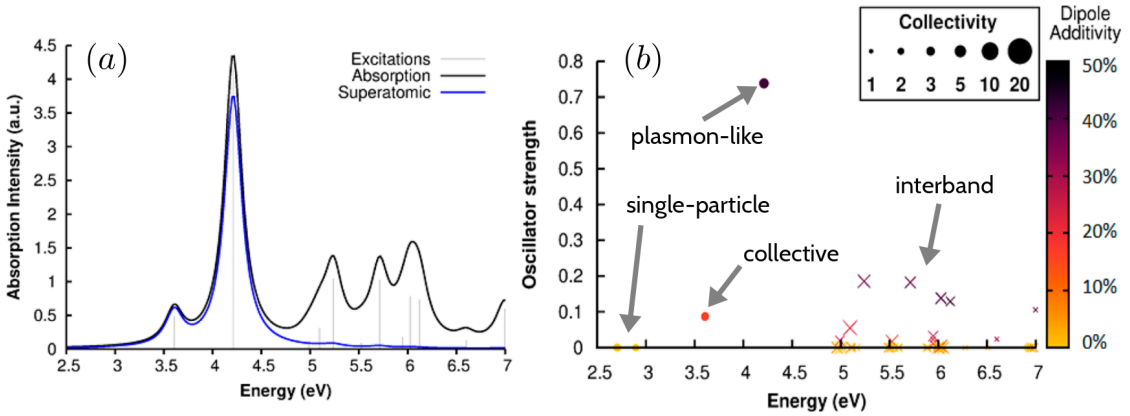

Figure 7.6: (a) Oscillator strengths (light grey sticks) and absorption cross-section (black line) of an icosahedral Ag_{13}^{5+} cluster, obtained with TD-DFT. The blue line is the absorption spectrum taking into account only superatomic excited states. **(b)** Visualization of the oscillator strengths, the superatomic character, the collectivity, and the dipole activity of the excited states in the icosahedral Ag_{13}^{5+} cluster between $2.5\,\mathrm{eV}$ and $7\,\mathrm{eV}$. Filled circles indicate states with $S_e > 0.75$, crosses indicate $S_e < 0.25$. *Both figures adapted with permission from Ref. [118]. Copyright © 2020 American Chemical Society.*

7.6 Sloshing and Inversion Population Dynamics

Quantum mechanically, the electronic properties of nanoparticles can be determined by their single-particle energy level diagram and the associated electronic states. Also, their electronic interaction energy plays a crucial role in the dynamics in the system.[7] State-of-the-art simulation methods allow to track the electronic motion in time – both in real and energy space. Not only can one follow how the electrons move along the atoms through the molecule, but also how they jump back and forth between energy states in the spectrum. Consequently, in addition to real-space electron dynamics and the number of involved transitions, another interesting quantity is investigated in the following: *state population dynamics* in energy space. Before we employ our TB-based method to investigate and *quantify* this aspect with the EPI, we look at prior works where this phenomenon has initially been observed.

Townsend and Bryant investigated the electron dynamics of gold jellium spheres in a TD-DFT framework both in real and energy space [123–125]. They were especially interested in the temporal evolution of the population of each energy eigenstate if the system is subject to an external monochromatic irradiation at different resonant frequencies. In the ground state before the illumination has started $(t = 0)$, the mth energy eigenstate is represented by the single-particle *Kohn-Sham* orbital $|\phi_m(0)\rangle$. As soon as the illumination is turned on, it starts to evolve in time to $|\phi_m(t)\rangle \neq |\phi_m(0)\rangle$. If one continues to express the time-evolved states in the ground state basis, it becomes apparent which energy states couple to each other as time passes. The projection $\langle\phi_m(0)|\phi_n(t)\rangle$, for in-

[7] Please note that the interaction energy may be already included in the definition of the energy states as well, if one employs methods of many-body theory. In that case, the interaction energy contribution is not easily separable from the contribution to the energy landscape that origins from the atomistic and geometric structure of the particle. The TB approach that we employ in this thesis, however, uses single-particle states and incorporates the *Coulomb* interaction in a way that allows us to distinguish the two contributions.

stance, measures to what extent the states $|\phi_m(0)\rangle$ and $|\phi_n(t)\rangle$ overlap after an interaction time t with the electromagnetic fields. In particular, to track the charge exchange of state m with all other states in the system, the change in occupation probability of state m at time t is computed according to

$$\Delta P(m,t) = \sum_n f_n |\langle \phi_n(t) | \phi_m(0) \rangle|^2 - f_m, \tag{7.8}$$

where $0 < f_m < 1$ is the initial occupation of state $|\phi_m\rangle$ with energy E_m at time $t = 0$, following the finite-temperature *Fermi-Dirac* distribution with the smearing temperature $T = 316\,\mathrm{K}$ (or $k_B T \approx 27\,\mathrm{meV}$). Moreover, to observe which pairs of states particularly couple to each other, the square of the projections is analyzed,

$$|\langle \phi_n(t) | \phi_m(0) \rangle|^2. \tag{7.9}$$

From that, one can directly access, how exactly these states interchange population over time. Dependent on the prevalent character of the investigated mode, we observe two different types of population dynamics and charge exchange patterns:

- On the one hand, we observe modes that are predominantly comprised of electronic transitions from states just below the *Fermi* level to states just above the *Fermi* level. The temporal evolution of the change in occupation $\Delta P(m,t)$ for the corresponding states is characterized by an oscillatory *sloshing* behavior. It is said to reflect the electronic movement back and forth from states below the *Fermi* energy to states above. As this process takes place in the vicinity of the *Fermi* level and happens in an oscillatory manner, its existence is attributed to *plasmonic* resonances. Moreover, this kind of resonance is characterized by real-space induced charge oscillations close to the surface of the particles and is, thus, reminiscent of a classical plasmon. The authors state that "[t]he sloshing component corresponds closest to a plasmonic response with the charge near the *Fermi* level involved." [124] and call the associated modes "classical surface plasmons".
- On the other hand, there are modes which are predominantly comprised of *inversion* type transitions. Here, we see a monotonous increase (decrease) of the state population of states above (below) the *Fermi* level in time. The involved states are either steadily populated or depleted such that for all times $\partial_t \Delta P(m,t) > 0$ or $\partial_t \Delta P(m,t) < 0$ holds for a state m above and below the *Fermi* energy, respectively. These transitions may happen from shells deep inside the *Fermi* sea to shells well above the *Fermi* level. The real-space induced charge dynamics of these modes are located mostly in the core of the particles. Therefore, the authors call them "quantum core plasmons". However, they state that "the core resonances [are] more single-particle-like". Therefore, they are associated with modes of less plasmonic character.

Application: Gold Jellium Sphere

Figure 7.7 shows the change in occupation probability $\Delta P(m,t)$ for two prominent resonances of a gold jellium sphere with radius $r = 0.74\,\mathrm{nm}$ and 100 valence electrons, investigated with TD-DFT. In Fig. 7.8, the associated squared projections $|\langle \phi_n(t) | \phi_m(0) \rangle|^2$ are shown. The *Fermi* level of the configuration lies within the $2f$ shell (yellow shaded regions). In Figs. 7.7a and 7.8a, the system is excited on resonance by a monochromatic

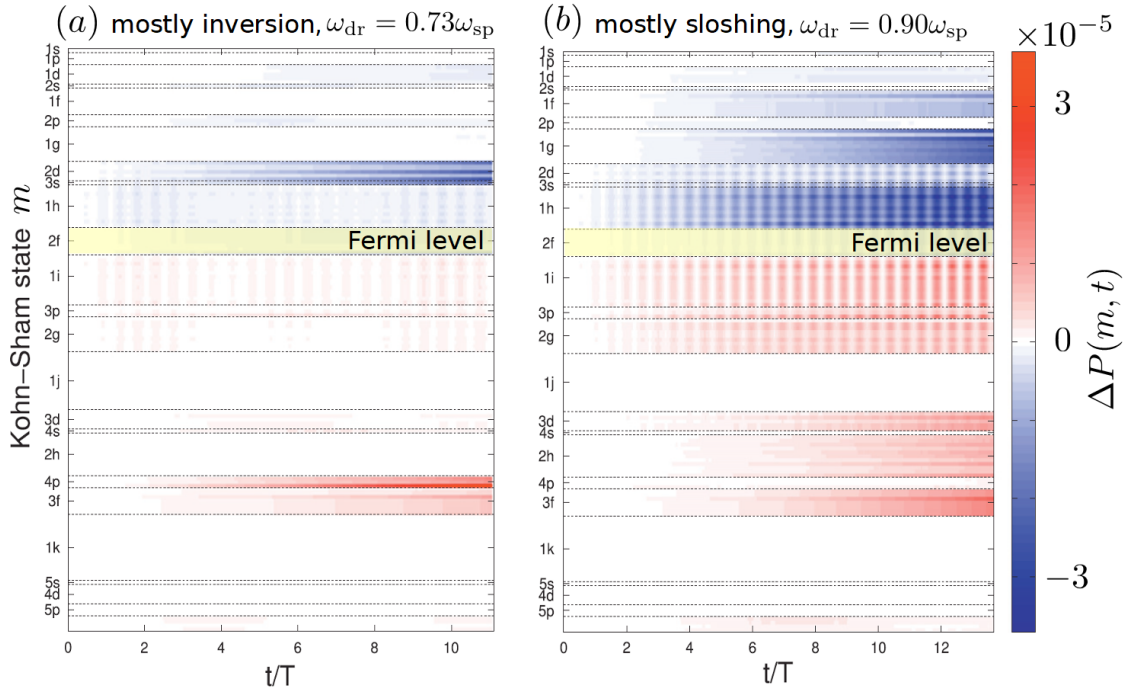

Figure 7.7: Change in occupation probability $\Delta P(m,t)$ for *Kohn-Sham* states m as a function of time t in the gold jellium sphere specified in the text. Time is measured in units of the period $T = 2\pi/\omega_{dr}$ with the driving frequency ω_{dr}, and ω_{sp} denotes the classical surface plasmon resonance frequency of the same sphere. **(a)** "Quantum core plasmon", $\omega_{dr} = 0.73\omega_{sp}$ **(b)** "Classical surface plasmon", $\omega_{dr} = 0.90\omega_{sp}$. *Both figures adapted with permission from Ref. [124]. Copyright © 2010 IOP Publishing.*

field with driving frequency $\omega_{dr} = 0.73\omega_{sp}$, where ω_{sp} is the frequency where the classical surface plasmon of the gold sphere resides. Figures 7.7b and 7.8b show the change in occupation probability and the squared projections of another resonant mode in the absorption spectrum at $\omega_{dr} = 0.90\omega_{sp}$.

In both resonances, sloshing type as well as inversion type dynamics are observed. In Fig. 7.7a, the mode at $0.73\omega_{sp}$ exhibits rather faint oscillating features for states between the $1h$ and $2g$ shells around the *Fermi* level. More marked, states well below and above the *Fermi* level ($2d$, $3s$, and $4p$, $3f$, respectively) gain and lose population in a monotonous, non-oscillatory way. In Fig. 7.8a, the squared projections of the time-evolved states onto the ground state basis are shown. In the high-energy region, mostly the transitions $4p \rightleftarrows 5p$ and $2d \rightleftarrows (4p, 3f)$ are contributing to the mode (marked with black circles). Also, $1d \rightleftarrows 2f$ is faintly involved. Most of these contributions exhibit *inversion* type behavior in the occupation dynamics. From that, it is concluded that the mode is mostly a "quantum core plasmon" and, therefore, predominantly of single-particle-like character.

In contrast to this, Fig. 7.7b shows much richer oscillatory *sloshing* features in the occupation dynamics of states right above and below the *Fermi* level between the $2d$ and $2g$ shells. Additionally, also inversion type dynamics especially in the $1f$, $1g$, $3d$, $2h$, and $3f$ shells are visible. From the projections in Fig. 7.8b it is apparent how the states are coupled in more detail. We see, for instance, that the pairs $1g \rightleftarrows 3f$ and $1f \rightleftarrows 3d$ are related *via* inversion type transitions in Fig. 7.7b. However, the strong oscillatory features translate to the appearance of a whole collection of coupled states in Fig 7.8b that are

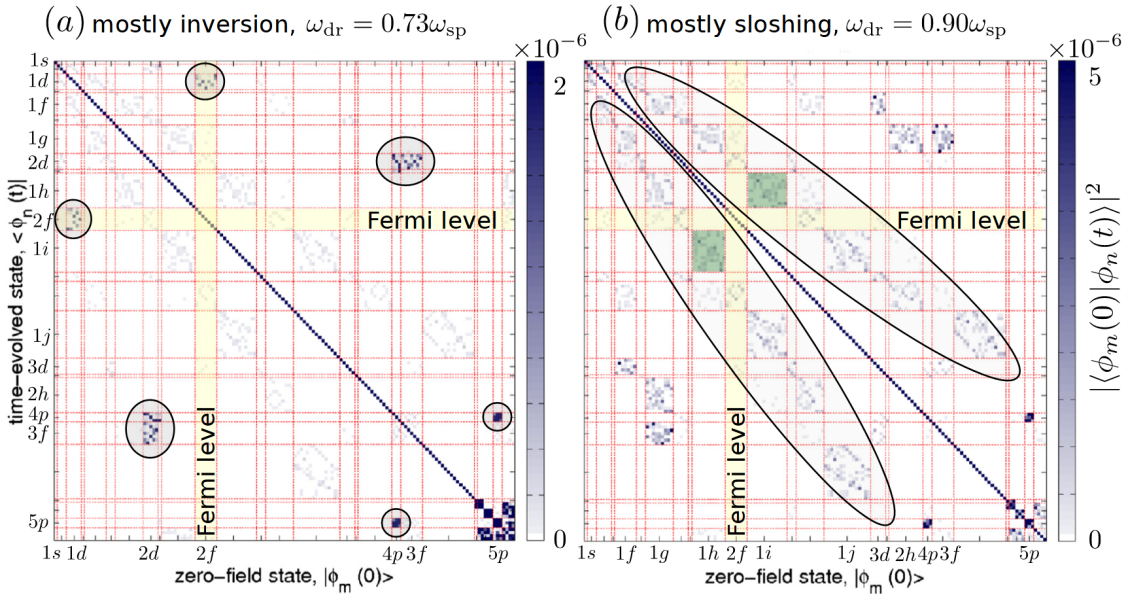

Figure 7.8: Squared projections $|\langle\phi_n(t)|\phi_m(0)\rangle|^2$ of the time-evolved single-particle states $|\phi_n(t)\rangle$ onto the ground states $|\phi_m(0)\rangle$ for an arbitrarily chosen time. The yellow shaded $2f$ orbital is the *Fermi* level in the simulation. Please note the different scale of the color bars. **(a)** "Quantum core plasmon", $\omega_{dr} = 0.73\omega_{sp}$ **(b)** "Classical surface plasmon", $\omega_{dr} = 0.90\omega_{sp}$. *Both figures adapted with permission from Ref. [124]. Copyright © 2010 IOP Publishing.*

arranged along two lines close to the diagonal of the matrix (marked with black ellipses; please also note the different color bars). Exemplarily for a sloshing type state coupling, the $1i \rightleftarrows 1h$ transition is highlighted with green color in Fig. 7.8b. The associated changes in occupation probability $\Delta P(1h,t)$ and $\Delta P(1i,t)$ are heavily oscillating, as can be seen in Fig. 7.7b. In conclusion, the mode is classified as a "classical surface plasmon" of mainly plasmonic character.

In summary, it can be stated that Townsend and Bryant rely on a different concept of a plasmonic response as compared to the above approaches, such that direct comparison is hardly possible. It is based on the energy rather than real space. The analysis shows that there are two fundamentally different ways how single-particle energy states exchange electronic population. Oscillatory *sloshing* type charge exchange occurs close to the *Fermi* level and is reflected by real-space induced charge oscillations close to the surface of the particle. Therefore, it seems natural to associate these transitions to plasmonic modes. However, the real-space induced charge has never entered the considerations as an input.

An evident disadvantage of the present method is that the simulations must be subsequently evaluated by a human being to finally arrive at a classification result. This bears the risk that subjective views influence the outcome and the final classification result depends on the individual. To prevent this, we introduce the energy-based plasmonicity index (EPI) in the next chapter. It is designed to quantitatively capture the *inversion* and *sloshing* type contents of a mode. With the EPI, the plasmonic character of a resonance – following the energy space-based concept of plasmonicity according to Townsend and Bryant – may be judged based on a number between 0 and 1.

7.7 Conclusions

In this chapter, we have introduced several approaches that exist in literature to assess and quantify the nature of a resonance in a nanostructure – all focusing on slightly different aspects of what constitutes a plasmon on the nanoscale. In particular, single-particle-like modes are to be distinguished from plasmonic ones both for theoretical interest and for many practical purposes.

Among these approaches were the real space-based *plasmonicity index (PI)* and *generalized plasmonicity index (GPI)*. These two measures rely on the charge patterns induced in real space and the resulting induced potential that builds up in the nanostructure. The *collectivity index (CI)* indicates how many single-particle transitions are significantly involved in a given mode. Being defined as the product of the CI and the oscillator strength of a mode, the *plasmon index* constitutes a quantity that relies both on the mode's real-space and energy-space characteristics. In a multidimensional classification table, the *superatomic character* of a mode, its *collectivity*, and its *dipole additivity* are determined to group nanooptical resonances into four categories – *plasmon-like*, *collective*, *single-particle*, and *interband*.

Moreover, we introduced two more complex computational procedures to determine the character of a mode based on energy-space characteristics. The *Coulomb scaling approach* proposes to artificially alter the electron-electron interaction strength in a series of simulations gradually and observe the shifting behavior of the modes in the spectrum. An investigation method based on *sloshing* and *inversion* type dynamics of the population of single-particle eigenstates was presented in the last section. The latter is also the basis for the next chapter where we introduce our own contribution to the scientific discussion – the energy-based plasmonicity index (EPI) as an approach to quantify the sloshing and inversion type content of a mode.

8 | The Energy-Based Plasmonicity Index

8.1 Introduction

In the previous chapter, we have given an overview over several approaches that exist in literature to assess the nature of optical modes in nanostructures. With the PI, the GPI, the superatomic character, the dipole additivity, the plasmon index, the CI, and the collectivity, literature provides many quantitative measures for mode characterization with respect to several distinctive features of nanooptical response. Whereas the former four of them rely on real-space charge dynamics, the latter two quantify the number of single-particle energy states involved in the formation of a given mode, and the plasmon index combines both approaches.

Although with the scaling approach, we have a powerful tool at hand to investigate interaction energy-based aspects of modes, there is no quantitative measure relying on the population dynamics of single-particle eigenstates in energy space yet. The EPI is intended to fill that gap and to provide an easy-to-calculate index for the classification process based on the method by Townsend and Bryant. To that end, the EPI measures the content of sloshing and inversion type transitions in a nanooptical mode. The EPI can be readily computed in any wavefunction-based method, such as TD-DFT, for instance. However, in the following, it is introduced based on the notation of the TB framework, which has been discussed in detail in this thesis earlier.

8.2 The EPI in Tight Binding Notation

Instead of the state vector $|\Psi(t)\rangle$, the central quantity within the employed TB simulation method is the density operator $\rho(t) = |\Psi(t)\rangle\langle\Psi(t)|$. Since this is a unique map $|\Psi(t)\rangle \mapsto \rho(t)$, we refer to $\rho(t)$ as 'state' in the following as well. First, we want to recall very briefly the basic relevant properties of the density operator that have been introduced in detail in Sec. 5.1.

Let $\{|j\rangle\}$ be the set of N TB eigenstates of a Hamiltonian H_{TB}, such that $H_{\mathrm{TB}}|j\rangle = E_j|j\rangle$ for $1 \leq j \leq N$. The diagonal elements $\rho_{jj} = \langle j|\rho|j\rangle$ of the matrix representation of the density operator in the basis of the TB eigenstates $|j\rangle$ can be interpreted as the *populations* of the associated eigenstates. Similarly to the approach in Sec. 7.6, these populations are initialized at time $t = 0$ according to $\rho_{jj} = f_j$, where f_j is the *Fermi-Dirac* distribution. Moreover, all off-diagonal elements $\rho_{jj'}$, $j \neq j'$, are zero at $t = 0$. They are called *coherences* and assumed to vanish in the ground state $\rho^0 := \rho(t = 0)$, as they quantify the degree of coherent coupling between states $|j\rangle$ and $|j'\rangle$. Consequently, the density matrix

of the ground state initially reads

$$\rho^0_{jj'} = \rho_{jj'}(t=0) = f_j \delta_{jj'}, \tag{8.1}$$

and it evolves in time according to

$$\frac{\partial}{\partial t}\rho(t) = -\frac{\mathrm{i}}{\hbar}\left[H(t), \rho(t)\right] - \frac{1}{2\tau}\left(\rho(t) - \rho^0\right), \tag{8.2}$$

where $H(t) = H_{\mathrm{TB}} - e\varphi(t)$ is the time-dependent Hamiltonian of a TB structure, which is coupled to a time-dependent electric field *via* its electric potential $\varphi(t)$, see Eqs. (5.7) and (5.10). Moreover, the last term in Eq. (8.2) phenomenologically accounts for all dissipative processes in the structure. As time passes, both the populations and the coherences of $\rho(t)$ change. However, the underlying basis set in which the density operator is expressed does not. It always remains the ground state basis taken at time $t = 0$. Therefore, the matrix element $\rho_{jj'}$ in the TB framework is the direct counterpart of the *Kohn-Sham* state projection $\langle\phi_n(t)|\phi_m(0)\rangle$ of the TD-DFT method in Eq. (7.9) and has the same interpretation. The coherence

$$C_{jj'}(t) = \rho_{jj'}(t) \qquad (j \neq j') \tag{8.3}$$

quantifies to what extent states $|j\rangle$ and $|j'\rangle$ are coupled at time t and how much charge they interchange. In case a single-particle transition $|j\rangle \rightleftarrows |j'\rangle$ occurs, it is indicated by $C_{jj'}(t)$. Moreover, we can track the change in occupation probability just like in the TD-DFT framework. Equation (7.8) can be directly transferred to TB notation and reads (*c.f.* Eq. (5.13))

$$\Delta P(j,t) = [\rho(t) - \rho^0]_{jj} = \rho_{jj}(t) - f_j. \tag{8.4}$$

8.3 Construction of the EPI

To calculate the EPI, we first define two auxiliary density operators, ρ^ω and $\tilde{\rho}^\omega$. The operator

$$\boxed{\rho^\omega_{jj'} := |\rho_{jj'}(t_s \gg 0)|} \tag{8.5}$$

is the density operator of the system after it has been illuminated with a monochromatic laser field at frequency ω for a sufficiently long[1] period of time t_s. Moreover, we define

$$\boxed{\tilde{\rho}^\omega_{jj'} = \frac{\rho^\omega_{jj'}}{||E_j - E_{j'}| - \hbar\omega + \mathrm{i}\epsilon|^2},} \tag{8.6}$$

where ϵ enforces the regularity of the denominator[2] if the incident laser frequency exactly matches the transition frequency, $|E_j - E_{j'}| \approx \hbar\omega$. The operator $\tilde{\rho}^\omega$ is very similar in nature to the non-interacting susceptibility $\chi^0(\omega)$ of the random phase approximation method [45, 121],

$$\chi^0_{ll'}(\omega) = \frac{2e^2}{\hbar}\sum_{jj'}(f_j - f_{j'})\frac{\langle l|j\rangle\langle j|l'\rangle\langle l'|j'\rangle\langle j'|l\rangle}{E_j - E_{j'} - \hbar\omega - \mathrm{i}\hbar/2\tau}. \tag{8.7}$$

[1] In this context, *sufficiently long* means that the system has reached a stationary state, and there exists some $t_s > 0$ such that for all $t > t_s$, we find $\rho(t + T_s) = \rho(t)$ with some period T_s.

[2] Unless otherwise stated, all the simulations in this thesis have been performed with a value of $\epsilon = 0.05\,\mathrm{eV}$, inspired by the universal broadening that is commonly used in DFT to convert a discrete set of oscillator strengths into a continuous absorption spectrum. In the Supplementary Material of Ref. [A1], we showed that the exact value of ϵ has very little influence on the value of the EPI.

Both quantities are designed to feature poles at spectral positions associated with single-particle transitions in the underlying non-interacting system. Please note, however, that unlike $\tilde{\rho}^\omega$, $\chi^0(\omega)$ is a quantity in real space (in the above equation, $|l\rangle$ and $|l'\rangle$ denote real-space orbitals localized around atom l and l' rather than energy eigenstates).

The EPI is then defined as

$$\boxed{\text{EPI}(\omega) = 1 - \langle \tilde{\rho}^\omega, \rho^\omega \rangle \in [0,1],} \tag{8.8}$$

where the scalar product $\langle \cdot, \cdot \rangle$ of $\tilde{\rho}^\omega$ and ρ^ω is calculated through their matrix representations in the ground state basis of H_{TB} as

$$\langle \tilde{\rho}^\omega, \rho^\omega \rangle := \frac{\sum_{jj'} |\tilde{\rho}^\omega_{jj'} \rho^\omega_{jj'}|}{\sqrt{\sum_{jj'} |\tilde{\rho}^\omega_{jj'}|^2} \cdot \sqrt{\sum_{jj'} |\rho^\omega_{jj'}|^2}} \in [0,1]. \tag{8.9}$$

The scalar product in Eq. (8.9) may be interpreted as a measure of similarity of the operators $\tilde{\rho}^\omega$ and ρ^ω. In case the elements of $\tilde{\rho}^\omega$ and ρ^ω are distributed similarly in magnitude, or $\tilde{\rho}^\omega$ and ρ^ω are proportional even, *i.e.* $\tilde{\rho}^\omega = c\rho^\omega$ with a constant $c \in \mathbb{R}$, then we have $\langle \rho^\omega, c\rho^\omega \rangle = 1$. On the other hand, if the elements are disseminated unequally and the overall structure of both operators does not match, then $\langle \tilde{\rho}^\omega, \rho^\omega \rangle \approx 0$. As outlined above, the diagonal elements of the density operator ρ can be interpreted as the electronic populations of the associated energy eigenstates. Therefore, in normalized density operators ($\mathrm{Tr}(\rho) = 1$) their magnitudes are in the order of $1/N$ if the associated states are populated, where N is the dimension of ρ. However, it is the coherences $C_{jj'}(t)$ that determine the coupling characteristics of a given mode. And their absolute values are orders of magnitude smaller usually. Therefore, we deplete the diagonal of ρ^ω before we obtain $\tilde{\rho}^\omega$ in Eq. (8.6), that is, $\rho^\omega \to \rho^\omega - \sum_j \rho^\omega_{jj} |j\rangle\langle j|$. In this way, we ensure that the coherences are the only relevant input for the calculation of the EPI and the populations do not bias the results due to their different order of magnitude.

Single-Particle and Plasmonic Contributions in ρ^ω and $\tilde{\rho}^\omega$

The reasoning behind Eq. (8.8) shall be outlined in the following. Figure 8.1a shows an example of the operator ρ^ω for a linear polyene chain $C_{70}H_{72}$ at resonance for $\hbar\omega = 5.45\,\mathrm{eV}$. This specific mode has been selected as a showcase example since it has an intermediate EPI of 0.48 and, thus, exhibits both kinds of contributions to a similar extent. Just as in Fig. 7.8, its matrix representation is symmetric with respect to the artificially depleted diagonal, $\rho^\omega_{jj'} = \rho^\omega_{j'j}$. The *Fermi* level is indicated by the black dashed lines, and the red shaded area marks the notional region where the energy matching condition $|E_j - E_{j'}| \approx \hbar\omega$ holds for the adjacent coherences $C_{jj'}$. We observe the following two kinds of contributions:

1. In the red shaded region, we notice a number of significantly contributing elements, indicating single-particle transitions that happen in an energy-conserving manner. To highlight this, we exemplarily pick the most prominent coherences $C_{17,42}$ and $C_{29,54}$ and investigate them in more detail. The associated energies of the single-particle eigenstates are $E_{17} = -3.88\,\mathrm{eV}$, $E_{42} = 1.51\,\mathrm{eV}$, $E_{29} = -1.51\,\mathrm{eV}$, and $E_{54} = 3.88\,\mathrm{eV}$. Thus, the energy differences $|E_{42} - E_{17}| = |E_{54} - E_{29}| = 5.39\,\mathrm{eV}$ can be clearly related to the incident laser frequency $\hbar\omega = 5.45\,\mathrm{eV}$. Consequently, this set of coherences is associated to electronic transitions in the system's non-interacting energy landscape and is dominant in single-particle-like modes.

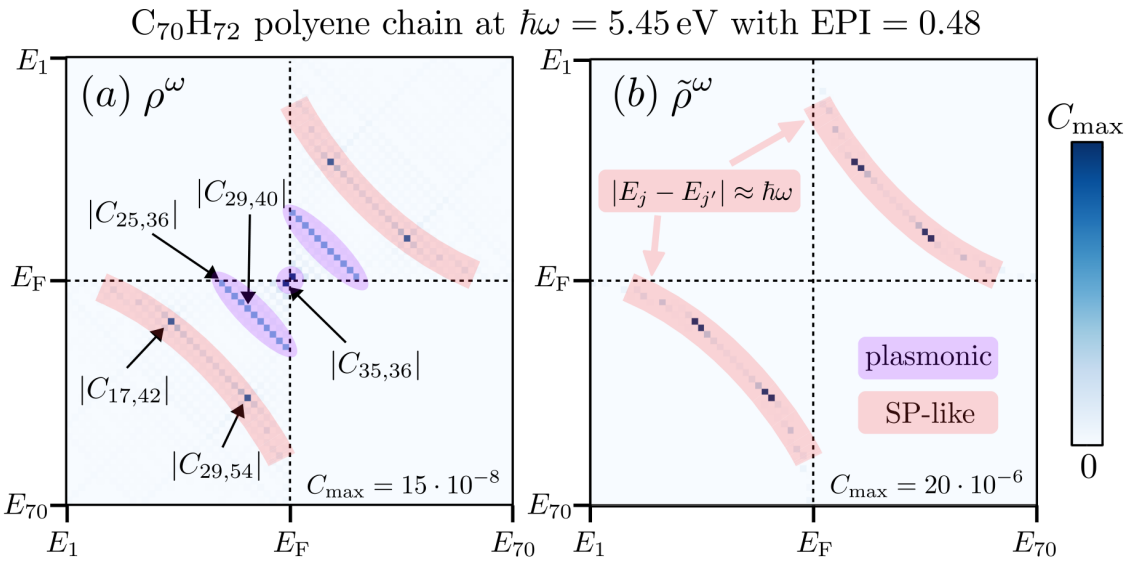

Figure 8.1: Matrix representations of the operators (**a**) ρ^{ω} and (**b**) $\tilde{\rho}^{\omega}$ for the linear polyene chain $C_{70}H_{72}$ illuminated at resonance for $\hbar\omega = 5.45\,\mathrm{eV}$. The red shaded area indicates the notional region where the energy matching condition $|E_j - E_{j'}| \approx \hbar\omega$ holds and contains coherences that are associated to inversion type transitions. The purple shaded area contains coherences of predominantly sloshing type. The hybrid mode has an intermediate EPI of 0.48 and is neither of clearly plasmonic or single-particle-like nature.

2. Close to the *Fermi* energy, connecting the two black dashed lines, we observe another set of non-vanishing coherences (marked with purple). They indicate the coupling of states from closely below the *Fermi* energy to states closely above. Exemplarily, we present the associated energy differences of two prominent representatives of this set of coherences: Both $C_{25,36}$ and $C_{29,40}$ cannot be related to the incident laser frequency, as their associated transition energies are $2.50\,\mathrm{eV}$ and $2.56\,\mathrm{eV}$, respectively. We conclude, therefore, that their existence is due to the electronic interaction energy in the system and a signature of plasmonic response. Also the HOMO-LUMO transition is heavily involved in the presented mode, indicated in the very middle by $C_{35,36}$ with an associated transition energy of $0.24\,\mathrm{eV}$.

The purpose of the defining expression for $\tilde{\rho}^{\omega}$ in Eq. (8.6) is to selectively amplify only those contributions in the matrix ρ^{ω} that are related to inversion type single-particle transitions and to neglect those that are indicative of sloshing plasmonic transitions. In Fig. 8.1b, we show the matrix representation of the associated operator $\tilde{\rho}^{\omega}$. It can be noted that the single-particle-like contributions in the red shaded areas are still present. In contrast, the plasmonic purple contributions around the *Fermi* energy have been considerably suppressed. They do not fall under the energy matching condition $|E_j - E_{j'}| \approx \hbar\omega$ and are not even visible in Fig. 8.1b.

It has become apparent now how Eq. (8.8) judges the character of a mode. In case a mode is foremost single-particle-like and, therefore, ρ^{ω} features predominantly coherences of inversion type (type 1), $\tilde{\rho}^{\omega}$ and ρ^{ω} are nearly proportional as all existing coherences get enhanced. Consequently, $\langle \tilde{\rho}^{\omega}, \rho^{\omega} \rangle \approx 1$ and $\mathrm{EPI}(\omega) \approx 0$. The mode is then classified "single-particle-like". In the other case, if ρ^{ω} features mostly coherences of sloshing type (type 2), they get heavily suppressed through applying Eq. (8.6), and we

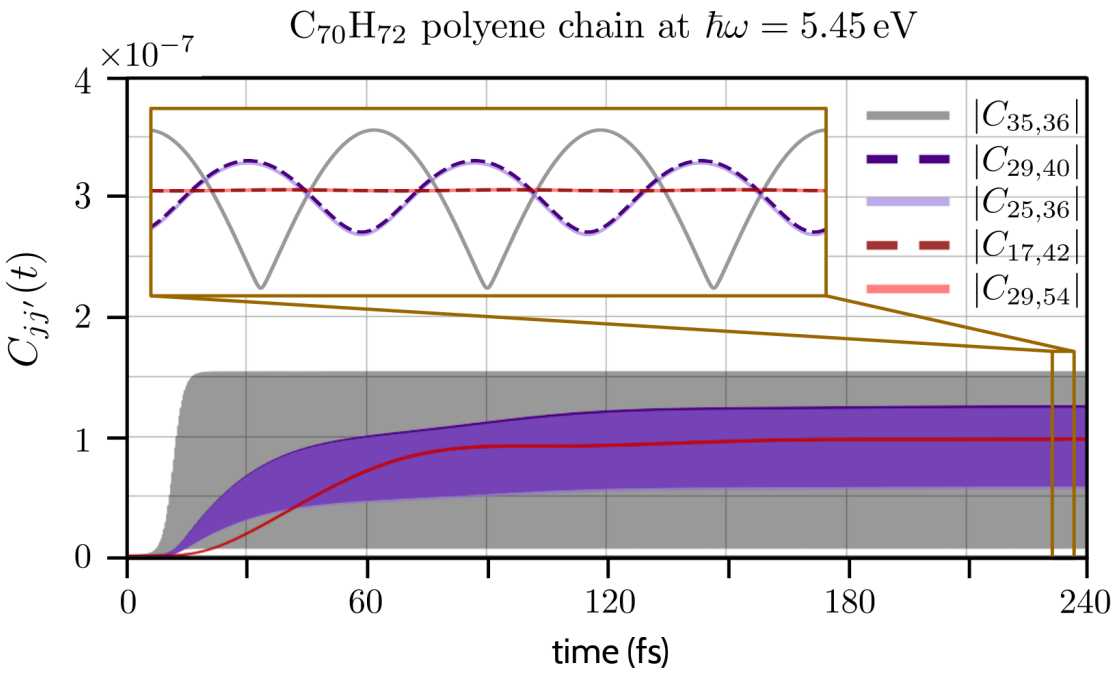

Figure 8.2: Time evolution of the absolute values of the coherences investigated in Fig. 8.1a. The $C_{70}H_{72}$ polyene chain has been illuminated for $240\,\mathrm{fs}$ with a CW illumination of frequency $\hbar\omega = 5.45\,\mathrm{eV}$. The inset shows the dynamics of the coherences in the stationary state.

obtain $\tilde{\rho}^{\omega} \approx \mathbf{0}_{N\times N}$. As a consequence, $\langle \tilde{\rho}^{\omega}, \rho^{\omega} \rangle \approx 0$ and $\mathrm{EPI}(\omega) \approx 1$. Thus, the mode is classified as "plasmonic".

Coherence and Population Dynamics

Not only the arrangement of coherences in the matrix representation of ρ^{ω} is indicative of the physical nature of the associated transition, but also its evolution in time. Thus, in the following, we discuss the temporal evolution of both the coherences $C_{jj'}(t)$ and the changes in occupation probability of the associated states, $\Delta P(j,t)$ and $\Delta P(j',t)$. The reasoning of classifying the involved transitions into two groups is further supported by this analysis, as will become apparent below. Moreover, we prove the above-made statements that coherences in the red (purple) shaded areas in Fig. 8.1 are of inversion (sloshing) type.

In Figs. 8.2 and 8.3, we show the temporal evolution of the coherences investigated in Fig. 8.1a and the respective changes of occupation probability. We show representatives of the inversion type process (red shaded region in Fig. 8.1), the sloshing type process (purple shaded region), and hybrid transitions, as well as the HOMO-LUMO transition, which is also contributing significantly to the mode.

We observe in Fig. 8.2 that the absolute values of the coherences $C_{17,42}(t)$ and $C_{29,54}(t)$ (red lines) – taken from the red shaded region of Fig. 8.1a – steadily increase with time. Moreover, in Fig. 8.3, we note that the associated electron donor state below the *Fermi* energy of the former coherence ($j = 17$) also loses population monotonically, and $\Delta P(17,t)$ does not exhibit any oscillatory features – as expected for inversion type single-particle-like transitions. Accordingly, the acceptor state $j = 42$ *gains* population monotonically, $\Delta P(42,t) = -\Delta P(17,t)$, as E_{42} lies above the *Fermi* energy and is initially unoccupied

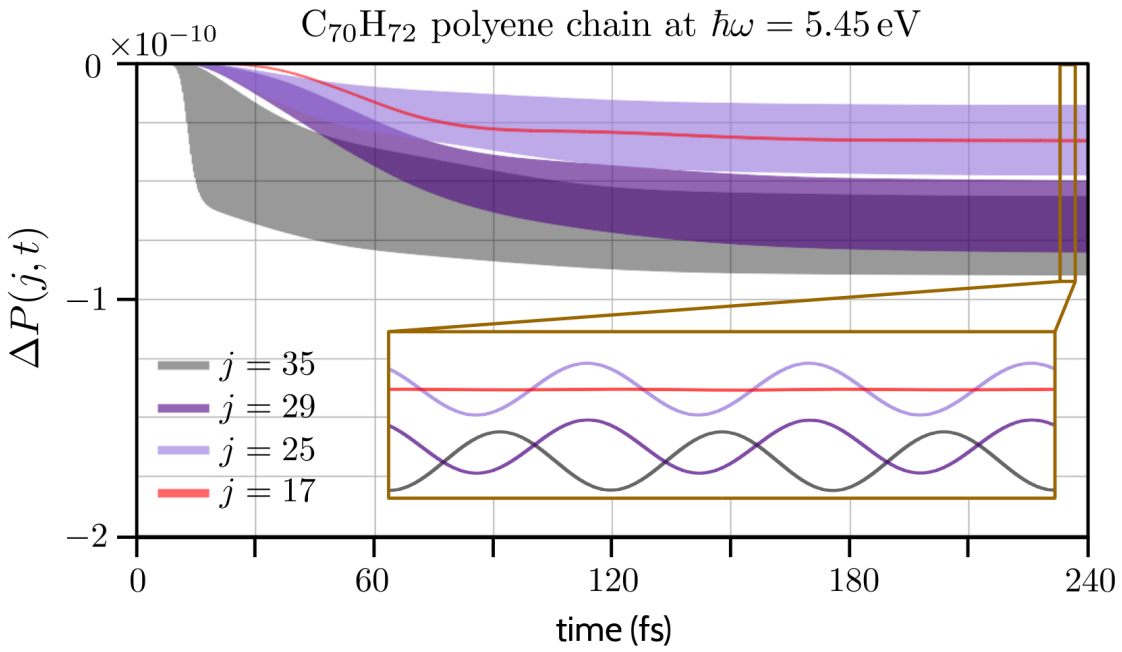

Figure 8.3: Time evolution of the change of population $\Delta P(j,t)$ for four selected states below the *Fermi* level. The states are chosen as representatives of four categories: the HOMO-LUMO transition ($j = 35$), purely sloshing type dynamics ($j = 25$), purely inversion type dynamics ($j = 17$), and a hybrid transition ($j = 29$), where both sloshing and inversion type dynamics are involved in the associated coherences. The inset shows the dynamics of the change of population in the stationary state.

(not shown in the figure). The discussion of the more complicated case of $\Delta P(29,t)$ as a hybrid state is moved to a later stage.

On the contrary, the purple lines in Fig. 8.2 reveal that the absolute values of $C_{25,36}(t)$ and $C_{29,40}(t)$ – both taken from the purple shaded region in Fig. 8.1a – considerably oscillate in time. Also, the associated change in occupation probability of the former coherence, $\Delta P(25,t)$ (light purple line in Fig. 8.3), oscillates in a sloshing type manner – as expected for interaction energy-mediated plasmonic transitions. The coherence associated with the HOMO-LUMO transition, $C_{35,36}(t)$, is also of sloshing type, as apparent from the grey lines in Figs. 8.2 and 8.3.

One may conclude from Fig. 8.1a that the population of state $j = 17$ is transferred exclusively to state $j = 42$ in a pure inversion type process. This leads to an inversion type steady decrease of population of state $j = 17$. On the other hand, states $j = 25$ and $j = 35$ exclusively exchange population in purely sloshing type processes, leading to oscillatory features in the associated time-evolution of their population decrease. State $j = 29$, however, is of hybrid nature. From Fig. 8.1a, we note that it is coupled to both state $j = 40$ and $j = 54$. The former coupling is of sloshing type, the latter one of inversion type. In Fig. 8.3, this is reflected in the fact that the corresponding loss of population is higher as compared to state $j = 25$ but completely in phase with it. The dark purple line may be regarded as the sum of the red and the light purple line. Please note here, that state $j = 35$ also loses comparatively much population as it couples to two other states as well. However, both couplings are of sloshing type in this case.

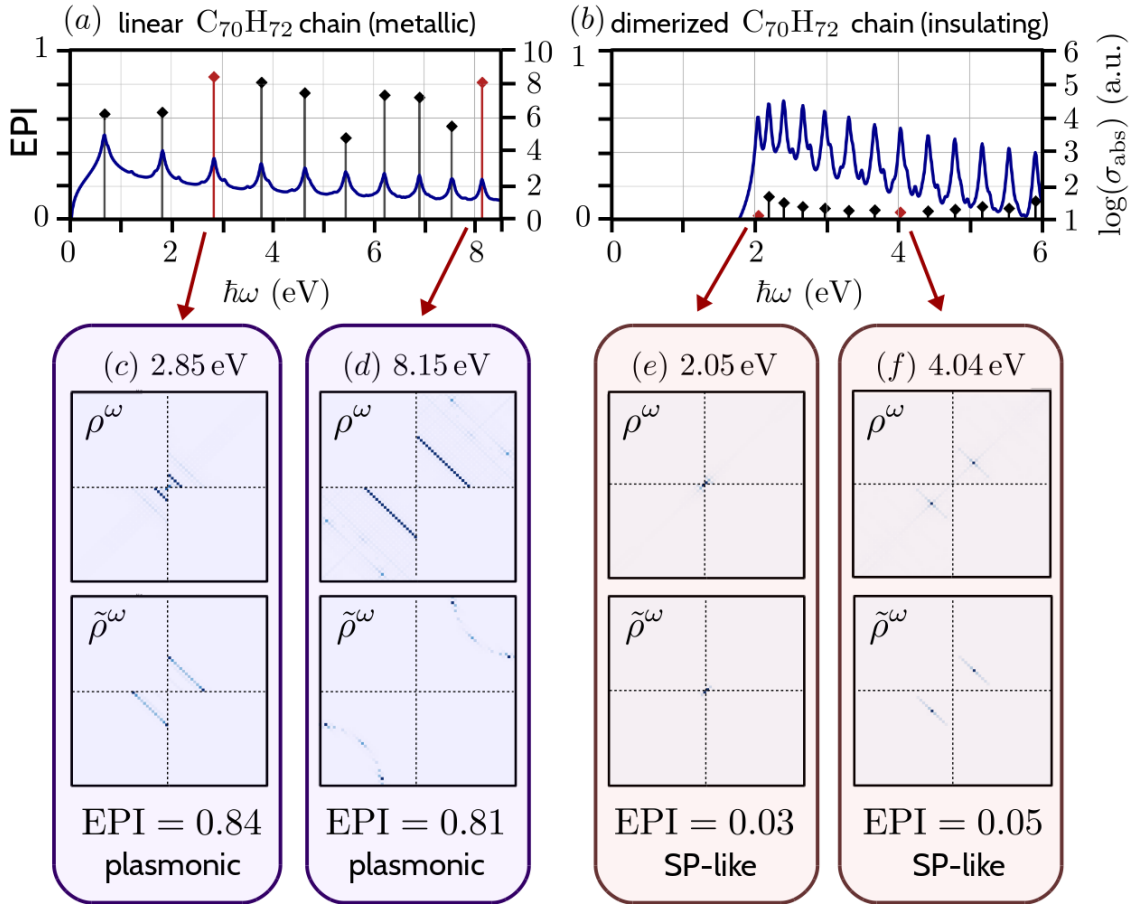

Figure 8.4: Absorption spectra (blue solid lines, right axes) and EPI (vertical lines and diamonds, left axes) of the most pronounced absorption peaks for **(a)** the linear $C_{70}H_{72}$ polyene chain with constant inter-atomic hopping rates $t = 2.66\,\mathrm{eV}$ and **(b)** the dimerized $C_{70}H_{72}$ chain with alternating hopping rates $t \pm \Delta$ with $\Delta = 0.18t$. Matrix representations of ρ^ω and $\tilde{\rho}^\omega$ for the plasmonic modes **(c)** $\hbar\omega = 2.85\,\mathrm{eV}$ and **(d)** $\hbar\omega = 8.15\,\mathrm{eV}$ of the linear chain with high EPI values of 0.84 and 0.81, respectively. Matrix representations of ρ^ω and $\tilde{\rho}^\omega$ for the single-particle-like modes **(e)** $\hbar\omega = 2.85\,\mathrm{eV}$ and **(f)** $\hbar\omega = 8.15\,\mathrm{eV}$ of the insulating dimerized chain with low EPI values of 0.03 and 0.05, respectively.

Limiting Cases: Metallic and Insulating Carbon Chains

The above example shown in Fig. 8.1 is a hybrid resonance leading to an intermediate EPI value of 0.48. To complete the picture, we show additional simulation results of more distinct cases in Fig. 8.4. The top row shows the absorption spectra (blue solid lines) of (a) a linear $C_{70}H_{72}$ polyene chain with constant inter-atomic hopping rates and (b) a dimerized $C_{70}H_{72}$ polyene chain with alternating inter-atomic hopping rates. Being known as a metallic molecule, the former supports many plasmonic modes. The latter is insulating and exhibits a band gap of around $2\,\mathrm{eV}$ for the chosen set of parameters, which prevents intraband electron dynamics and, thus, plasmonic modes from emerging. Along with the absorption spectra, we show the EPI values of the most prominent modes in both species as sticks. From both spectra, we pick the two modes of highest (and lowest) EPI values (marked with red) of the linear and dimer chain, respectively, and present their associated matrix representations of ρ^ω and $\tilde{\rho}^\omega$ in the bottom rows of the figure.

In the case of the linear chain, we present ρ^ω and $\tilde{\rho}^\omega$ for the modes at (c) $\hbar\omega = 2.85\,\mathrm{eV}$ with EPI $= 0.84$ and at (d) $\hbar\omega = 8.15\,\mathrm{eV}$ with EPI $= 0.81$. In both cases, the associated ρ^ω exhibits a typical plasmonic fingerprint, featuring a set of prominent contributions that connect the black dashed *Fermi* energy lines. However, in $\tilde{\rho}^\omega$ we mostly observe the coherences that belong to the energy matching region. Thus, $\tilde{\rho}^\omega$ looks substantially different compared to ρ^ω and the respective matrix overlap $\langle\tilde{\rho}^\omega, \rho^\omega\rangle$ is small, rendering a high EPI value.

As an insulating species, the dimerized chain offers two single-particle-like modes of strikingly small EPI at $\hbar\omega = 2.05\,\mathrm{eV}$ with EPI $= 0.03$ and at $\hbar\omega = 4.04\,\mathrm{eV}$ with EPI $= 0.05$. The matrix representations of their auxiliary density operators are shown in Figs. 8.4e and 8.4f, respectively. For both modes, the matrix representations of ρ^ω and $\tilde{\rho}^\omega$ have a clear single-particle-like fingerprint and look nearly identical, indicating that all contributing coherences $C_{jj'}$ fulfill the condition $E_j - E_{j'} \approx \hbar\omega$. Consequently, the two operators may be regarded as almost proportional and their overlap is close to unity, leading to a small EPI value.

8.4 Validation of the EPI

After we have introduced the reasoning behind the EPI and presented the above showcase examples, we now apply the EPI to more elaborate structures in the following. To further validate the idea of the EPI also by utilizing other simulation methods, we first investigate structures that have already been extensively studied in literature before. Within a TD-DFT scheme, we[3] examine the sodium chain Na_{20} and the silver tetrahedron Ag_{20} [A4] and compare our results to the classification outcomes of the *Coulomb* scaling and the (G)PI approaches outlined above. For a detailed discussion on the calculation of the EPI in linear-response TD-DFT (LR-TD-DFT), see App. A. After this validation, we perform a very detailed EPI analysis of the modes in another carbon-based structure described within a TB formalism: a finite triangular graphene nanoantenna.

8.4.1 Validation 1: Sodium Chain Na_{20}

In Fig. 8.5a, we present the absorption spectrum (black line, left axis) of the sodium chain Na_{20} and the associated EPIs (blue sticks, right axis) for excited states in the spectral region between $0\,\mathrm{eV}$ and $2\,\mathrm{eV}$. The absorption spectrum exhibits two well-separated peaks around $0.6\,\mathrm{eV}$ and $1.5\,\mathrm{eV}$, following almost flawless Gaussian shapes. Related to these two modes, we also see high EPI values. It is apparent that two of the modes with EPIs of above 0.4 (marked with thickened blue lines) are distinctly more plasmonic than all the others that have EPIs of around or less than 0.1. For these two modes, we also plot the transition densities as insets: The fundamental longitudinal mode with one nodal point at around $0.6\,\mathrm{eV}$ and the higher-order mode with three nodes at $1.5\,\mathrm{eV}$. They both exhibit high dipole moments. This is qualitatively consistent with the findings of the (G)PI in Fig. 7.2a and the *Coulomb* scaling approach in Fig. 7.3a. Both of these approaches also label two modes in the same spectral region as plasmonic and the associated transition densities are in qualitative agreement with our findings.

Thus, it may be concluded that these characterization methods agree in classifying the longitudinal modes of the sodium chain Na_{20}. This is easily explained by the fact, that in this molecule, the defining plasmonic features that these methods rely on, overlap. Both plasmonic modes exhibit a large dipole moment of the charge cloud oscillation in

[3] The TD-DFT simulations of the Na_{20} and Ag_{20} species for the validation of the EPI have been performed by my colleague *Christof Holzer*, who is also one of the co-authors of Ref. [A4].

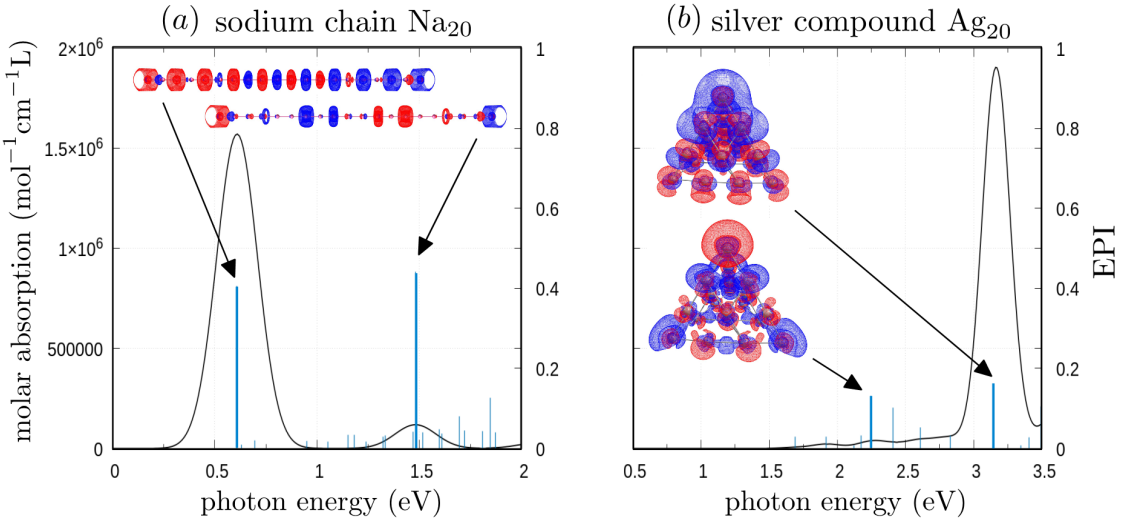

Figure 8.5: Absorption spectra (black line, left axis) and EPIs (blue vertical sticks, right axis) of **(a)** the sodium chain Na_{20} and **(b)** the silver tetrahedron Ag_{20}, obtained with TD-DFT. For the two excited states with the highest EPI values in each case, the associated transition densities (isovalue of 0.0005 atomic units) are plotted as insets. *Both figures adapted with permission from Ref. [A4]. Copyright © 2022 AIP Publishing.*

real space as well as they emerge from *Coulomb* interaction energy, such that they blueshift with increasing *Coulomb* interaction strength. Moreover, the associated dynamics in energy space are of sloshing type.[4]

8.4.2 Validation 2: Silver Tetrahedron Ag_{20}

Figure 8.5b shows the absorption spectrum (black line, left axis) of the silver tetrahedron Ag_{20} and the associated EPIs (blue sticks, right axis) for the excited states in the spectral region between $0.5\,\mathrm{eV}$ and $3.5\,\mathrm{eV}$. The absorption spectrum exhibits one pronounced peak around $3.2\,\mathrm{eV}$ and a broad absorption tail towards lower energies between $1.5\,\mathrm{eV}$ and $2.7\,\mathrm{eV}$, mainly consisting of three much smaller peaks. The two modes with the highest EPI values at $2.25\,\mathrm{eV}$ and $3.2\,\mathrm{eV}$ are highlighted with thickened sticks and the insets show the corresponding transition densities. The high-absorbing mode is classified most plasmonic, in accordance with the PI, the GPI, and the *Coulomb* scaling approach in Figs. 7.2b, 7.2c, and 7.3b, respectively. However, we find two more modes with a relatively high EPI value around $2.25\,\mathrm{eV}$ and $2.4\,\mathrm{eV}$. In the *Coulomb* scaling approach, the same qualitative behavior can be observed around $(E/\Delta)^2 \approx 2.7$ and $(E/\Delta)^2 \approx 3.1$, which translates to $E \approx 2.4\,\mathrm{eV}$ and $E \approx 2.6\,\mathrm{eV}$, respectively. Here, we see two relatively close modes in the broad absorption shoulder that shift moderately with increasing *Coulomb* interaction strength, also indicating moderate plasmonic character. In contrast, the PI and the GPI find only one more plasmonic mode between $2.7\,\mathrm{eV}$ and $2.8\,\mathrm{eV}$ besides the high-absorption peak. Thus, we may conclude that the real space-based PI and GPI deviate from the interaction energy-based scaling method and EPI as there are apparently inversion type single-particle transitions with high dipole moment in the system.

[4]Please note again here that the CI, for instance, and the multidimensional approach classify the longitudinal L-modes as single-particle-like. This is because they take into account the number of involved single-particle transitions. The EPI is independent of this number, but only judges if the transitions happen in an inversion or sloshing type manner.

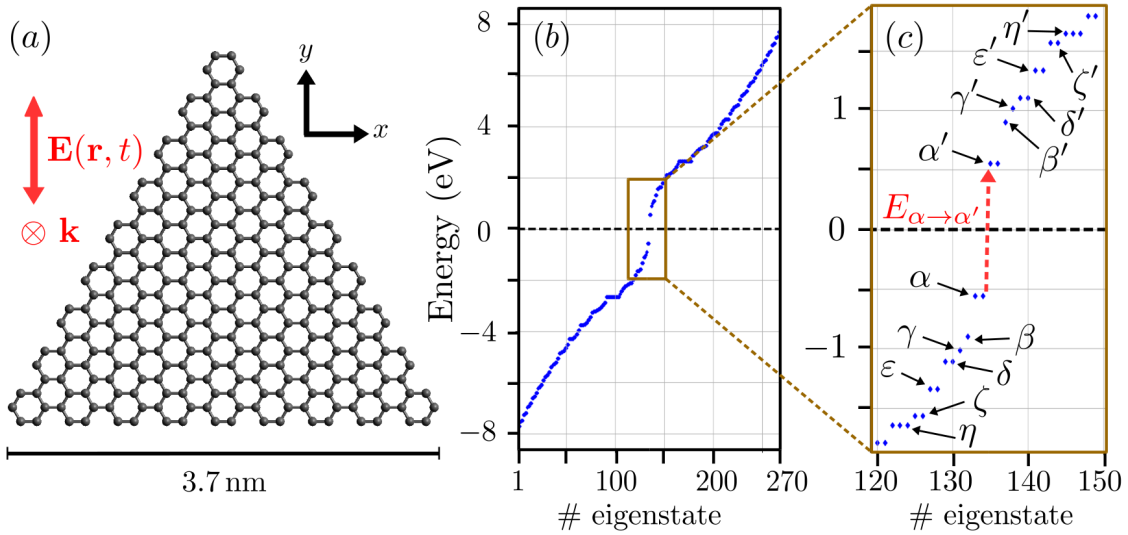

Figure 8.6: (a) Armchair-edged triangular graphene nanoantenna consisting of 270 atoms with side length $3.7\,\mathrm{nm}$. The wave vector of the incident y-polarized electric field is perpendicular to the antenna. **(b)** Full TB energy landscape of the triangle shown in (a). **(c)** Energy landscape of the triangle close to the particle-hole symmetry line $E = 0$, where the optical interaction mostly occurs. We label energy levels below (above) $E = 0$ with (primed) Greek letters. The red dashed arrow indicates the transition energy $E_{\alpha\to\alpha'} = 1.11\,\mathrm{eV}$ between the energy levels α and α'.

After we have validated the performance of the EPI by applying it to two benchmark model systems in a TD-DFT framework in this section, the remainder of this chapter is dedicated to the detailed application of the EPI to a graphene nanoantenna described within the TB formalism.

8.5 Application of the EPI: Graphene Nanotriangle

Through recent progress in the fabrication of nanostructured graphene [37, 38], the interest in investigating the plasmonic response supported by these structures has lately experienced a boost both theoretically [22, 43–49, 80, 237] and experimentally [39–42, 286, 287]. In the following, to get a comprehensive picture, we aim to shed light not only on the EPI of the modes in a graphene nanotriangle but on many aspects of the structure's response to optical excitation at the same time. Among them are the real-space and energy-space electron dynamics, *Coulomb* interaction scaling, and – as we work with graphene – the *doping* degree of freedom. Although it is known already that doping finite graphene antennas with single electrons may evoke previously absent infrared modes [45], we investigate them in more detail. Especially, we study if they are really *plasmonic*, as often claimed. Or, more precisely, we want to work out concerning which aspect one may call them plasmonic or not. The content of this section is based on our work in Ref. [A3].

The structure of interest – a triangular graphene nanoantenna consisting of 270 atoms – is shown in Fig. 8.6a. It has armchair edges and a side length of $3.7\,\mathrm{nm}$. At these small scales, classical methods cannot accurately capture the structure's properties anymore, and quantum mechanical approaches are inevitable [44, 45]. Although the associated TB

Hamiltonian without external electric field can be solved analytically [288], we rely here on the numerical simulation method presented in Sec. 5.1 that is necessary as soon as external irradiation or interacting electrons are taken into account. We consider y-polarized monochromatic plane wave illumination hitting the antenna perpendicularly.

Figure 8.6b shows the non-interacting energy level diagram of the system. We note that the triangle appears to be already large enough that the discrete energy levels follow the characteristics of the continuous band structure of 2D graphene, as shown in Fig. 3.4f. Yet, as a result of the finiteness of the antenna, the continuous bands in 2D graphene discretize, and we observe discrete energy states with a relatively large HOMO-LUMO gap of $1.11\,\mathrm{eV}$ in the undoped antenna. In Fig. 8.6c, we zoom to the energetic region close to the particle-hole symmetry line $E = 0\,\mathrm{eV}$, identical to the *Fermi* level in an undoped structure. In this spectral region, we find the single-particle states primarily involved in optical interaction mechanisms and label their associated energy with (primed) Greek letters below (above) $E = 0\,\mathrm{eV}$. Accordingly, $E_{\alpha\to\alpha'}$ is the transition energy that lifts an electron from energy level α to α'. Please note that we are labeling energy levels rather than energy eigenstates. The $\alpha(\eta)$-level of the antenna, for instance, consists of two (three) degenerate states.

8.5.1 Absorption and the Effect of Doping Charge

Due to the conical shape of the band structure of extended 2D graphene near its Dirac points at the edges of the first *Brillouin* zone and the linearly vanishing density of states at $E = 0$, raising or lowering the charge carrier density by electrostatic gating or optical pumping substantially influences the electronic and the optical properties of the material. Being called a *semi-metal* or a *gap-less semiconductor*, graphene is not conducting in its neutral configuration. Not until the conduction (valence) band is populated with electrons (holes), electric current can be evoked [140], and plasmonic response expected. This practical feature translates to finite graphene nanoantennas as well, as discussed in detail in Sec. 3.4. Here, we investigate how the number of doping electrons affects the absorption characteristics of the nanotriangle.

Non-interacting Absorption

Figure 8.7a shows the absorption cross-section of the above presented triangular graphene nanoantenna for non-interacting electrons in the absence of *Coulomb* interaction as a function of the number of doping electrons. In the undoped ($d = 0$) antenna, the lowest-energy absorption peak is at $1.11\,\mathrm{eV}$, which can readily be attributed to the transition from level α to α' across the HOMO-LUMO gap. Accordingly, the following two prominent modes in the undoped antenna around $2\,\mathrm{eV}$ and $2.15\,\mathrm{eV}$, correspond to the transitions $\delta \to \beta'$ and $\delta \to \delta'$, respectively.[5]

Characteristic for the non-interacting absorption spectrum is the spectral stability of the modes with respect to the doping charge d. As long as a transition is allowed, it always takes place at the same energy. However, doping can change the oscillator strength of a mode or cause it to disappear from the spectrum altogether. For instance, after doping the antenna with $d = 4$ electrons, the α'-level is fully occupied by electrons. Consequently, the transition $\alpha \to \alpha'$ vanishes from the spectrum since the α'-level cannot act as an acceptor state anymore. On the other hand, doping can also give rise to new modes. For example, in the one-fold doped antenna, three new modes appear in the mid-infrared

[5] Whenever the occupation of the energy levels allows it, the inverse transition is also possible for symmetry reasons, *i.e.* if $E_{\delta\to\beta'}$ occurs, then also $E_{\beta\to\delta'}$ does.

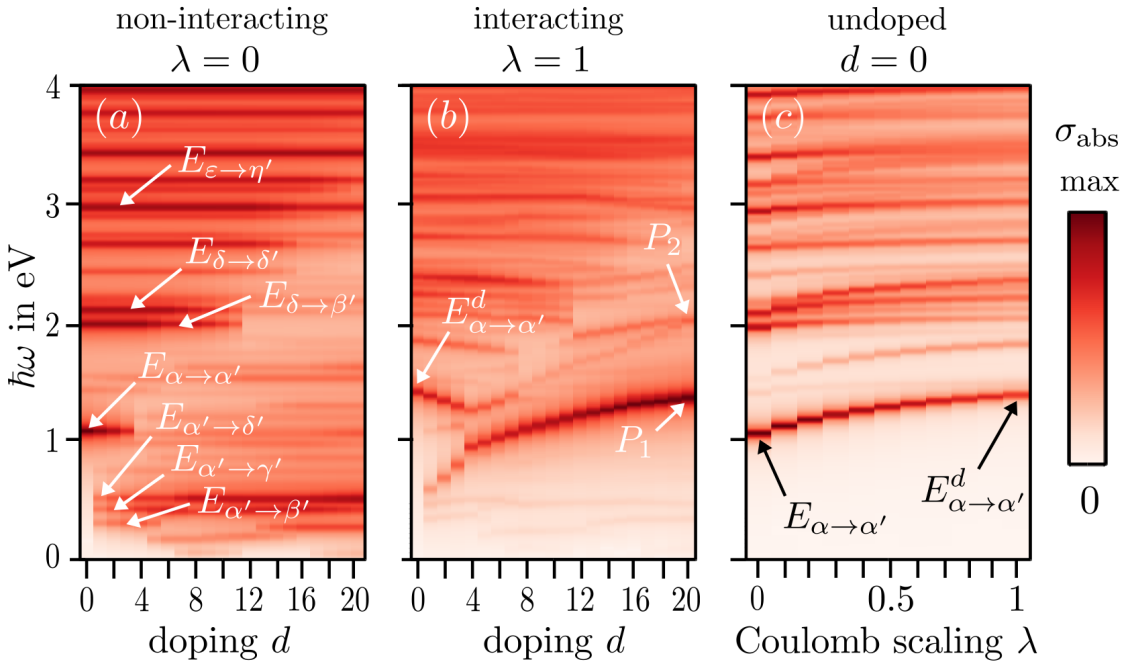

Figure 8.7: (a) Non-interacting $(\lambda = 0)$ and **(b)** interacting $(\lambda = 1)$ absorption cross-sections of the triangle shown in Fig. 8.6a as a function of the doping charge. Arrows indicate prominent absorption peaks that are related to single-particle transitions in the energy level diagram in Fig. 8.6c. The energy $E_{\alpha\to\alpha'}$ reflects the bare transition from level α to α', whereas $E^d_{\alpha\to\alpha'}$ in the interacting case accounts for the transition that is *dressed* by the *Coulomb* interaction energy. **(c)** Absorption cross-section of the undoped $(d = 0)$ structure as a function of the *Coulomb* interaction scaling parameter λ.

region below $0.5\,\text{eV}$. They belong to the transitions $\alpha' \to \beta'$, $\alpha' \to \gamma'$, and $\alpha' \to \delta'$, respectively, where the newly occupied α'-level acts as the electron donor state now.

Interacting Absorption

The interacting absorption cross-section as a function of the doping charge taking into account *Coulomb* interaction is shown in Fig. 8.7b. It substantially differs from its non-interacting counterpart. In the undoped case, we observe again one prominent mode between $1\,\text{eV}$ and $2\,\text{eV}$, which can be mainly attributed to the $\alpha \to \alpha'$ transition. However, it is blue-shifted and resides around $1.4\,\text{eV}$ now. Thus, we conclude that it is considerably *dressed* by *Coulomb* interaction energy that shifts it toward higher energies and call the mode $E^d_{\alpha\to\alpha'}$.

To prove that it is indeed a congeneric mode, we show in Fig. 8.7c the smooth transition from $E_{\alpha\to\alpha'}$ to $E^d_{\alpha\to\alpha'}$ as the *Coulomb* interaction scaling parameter λ is gradually increased from 0 to 1. We observe a substantial blue-shift of the mode and a decrease of its oscillator strength for higher *Coulomb* interaction strengths. Moving to higher doping levels in Fig. 8.7b, two blue-shifting modes appear that build up their intensity as the number of electrons in the system is growing. In anticipation of the results of our later analysis, we name them P_1 and P_2.

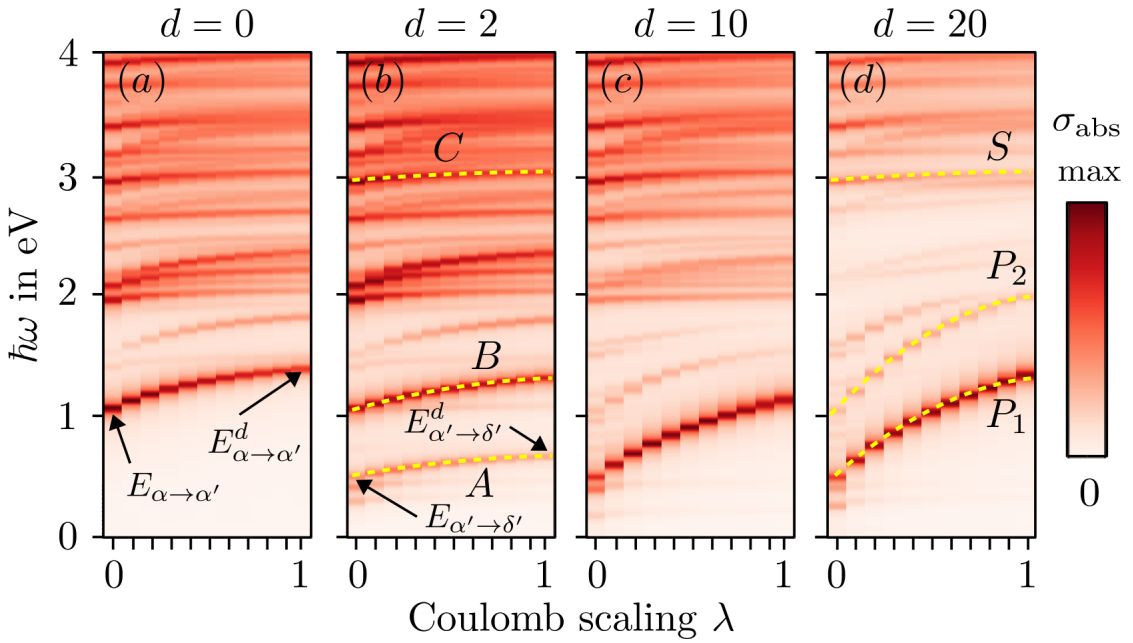

Figure 8.8: Absorption cross-sections of the 270-atomic nanotriangle specified in Fig. 8.6a for **(a)** 0, **(b)** 2, **(c)** 10, and **(d)** 20 doping electrons as a function of *Coulomb* interaction scaling parameter λ. The yellow dashed lines mark modes that are investigated in more detail below for the two-fold (modes A, B, and C) and 20-fold (modes P_1, P_2, and S) doped structures.

Characteristic for the interacting absorption spectrum is the gradual shift of the energies of many modes when single electrons are added or removed from the structure. Since the plasma frequency of classical plasmons depends on the charge carrier density as $\omega_p \propto \sqrt{n}$, they are known to blue-shift with increasing charge carrier density (see also Eq. (2.14)). The modes under consideration here show a more complex behavior. Some of the modes red-shift ($E^d_{\alpha\to\alpha'}$), others blue-shift (P_1 and P_2) with increasing doping d, and still others (mostly above $3\,\mathrm{eV}$) remain spectrally stable, just like in the non-interacting case.

8.5.2 *Coulomb* Scaling Approach

Before we investigate the above-presented modes in real and energy space in more detail, let us focus on the *Coulomb* interaction scaling approach for differently doped triangles before. In Fig. 8.8, we present the absorption cross-sections of (a) an undoped, (b) a two-fold doped, (c) a ten-fold doped, and (d) a 20-fold doped triangular antenna (Figs. 8.7c and 8.8a coincide). Besides the previously mentioned continuous passage from $E_{\alpha\to\alpha'}$ to $E^d_{\alpha\to\alpha'}$ both in Figs. 8.8a and 8.8b (mode B), we note a similar behavior for the low-energy mode A in Fig. 8.8b that is the (dressed) $\alpha' \to \delta'$ transition. But in accordance with the overall analysis in Sec. 7.3, not all modes exhibit the same shifting characteristics. Mode C in Fig. 8.8b, for example, barely changes its spectral position as a function of the *Coulomb* scaling parameter. In the heavily doped species in Figs. 8.8c and 8.8d, we observe both spectrally stable modes (S) and considerably shifting ones (P_1 and P_2). Based on the *Coulomb* scaling approach, only the modes P_1 and P_2 in the heavily doped case $d = 20$ can be considered plasmonic, although the transition here is admittedly very smooth and the classification not obvious. Modes A and B could be called intermediate, and modes C and S could be classified as single-particle-like.

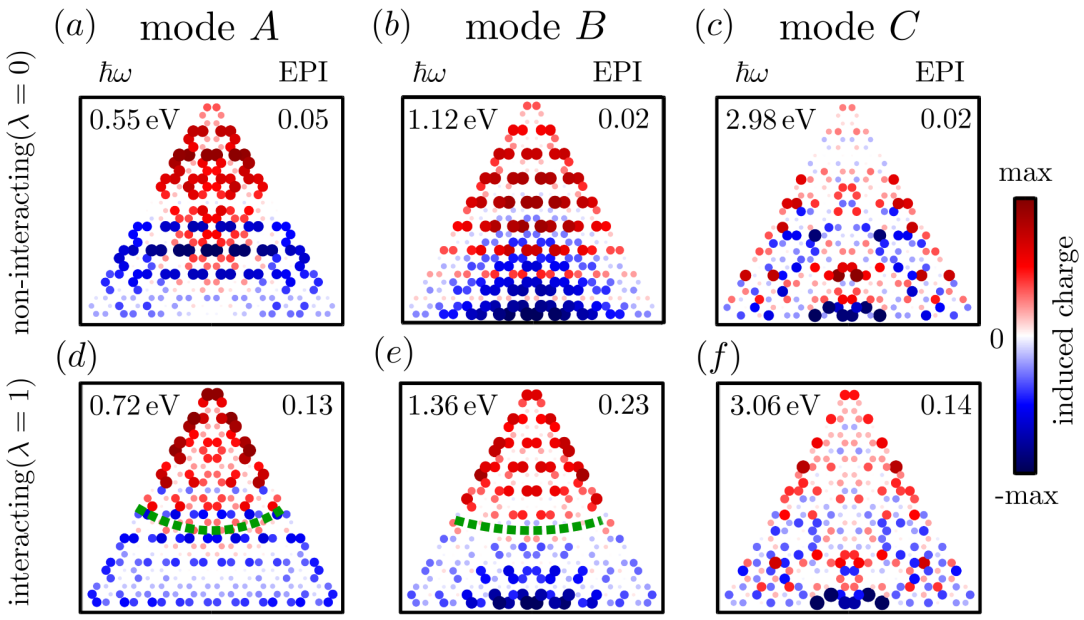

Figure 8.9: Real-space induced charge distribution in the two-fold doped 270-atomic graphene nanotriangle in the non-interacting case for **(a)** mode A, **(b)** mode B, and **(c)** mode C, as labeled in Fig. 8.8b. **(d)**-**(f)** Same as **(a)**-**(c)**, but for interacting electrons. In the top left and top right corners of the subfigures, we show the energy and the EPI of the corresponding modes, respectively. The green dashed lines indicate the nodal line of the charge distribution. The size of the atoms is proportional to the absolute value of the induced charge.

To get an even more complete picture, we thoroughly investigate below the modes A, B, and C in the moderately doped case $d = 2$ (which is similar to the undoped case but additionally supports the mid-infrared mode around $0.5\,\mathrm{eV}$) and the modes P_1, P_2, and S in the heavily doped species with $d = 20$.

8.5.3 Real-Space Dynamics

Classically, plasmonic modes are accompanied by oscillating long-range charge distribution patterns in real space. To judge the real-space characteristics in the present case, we show in Fig. 8.9 the induced charges of modes A, B, and C in the two-fold doped triangle, both for non-interacting (Figs. 8.9a-c) and for interacting electrons (Figs. 8.9d-f).

Moderate Doping: $d = 2$

In the non-interacting case, modes A and B reside at $0.55\,\mathrm{eV}$ and $1.12\,\mathrm{eV}$, respectively, and have exceptionally low EPIs of 0.05 and 0.02, which clearly indicates their single-particle nature. However, their real-space induced charge patterns have palpably dipolar character, and we observe a charge separation, which leads to strong induced potentials and, consequently, to high (G)PI values, as will be shown below. From that, it is apparent that the existence of *Coulomb* interaction in nanostructures is by no means a prerequisite for the emergence of long-range structured dipolar charge oscillation in real space like it is in classical systems.

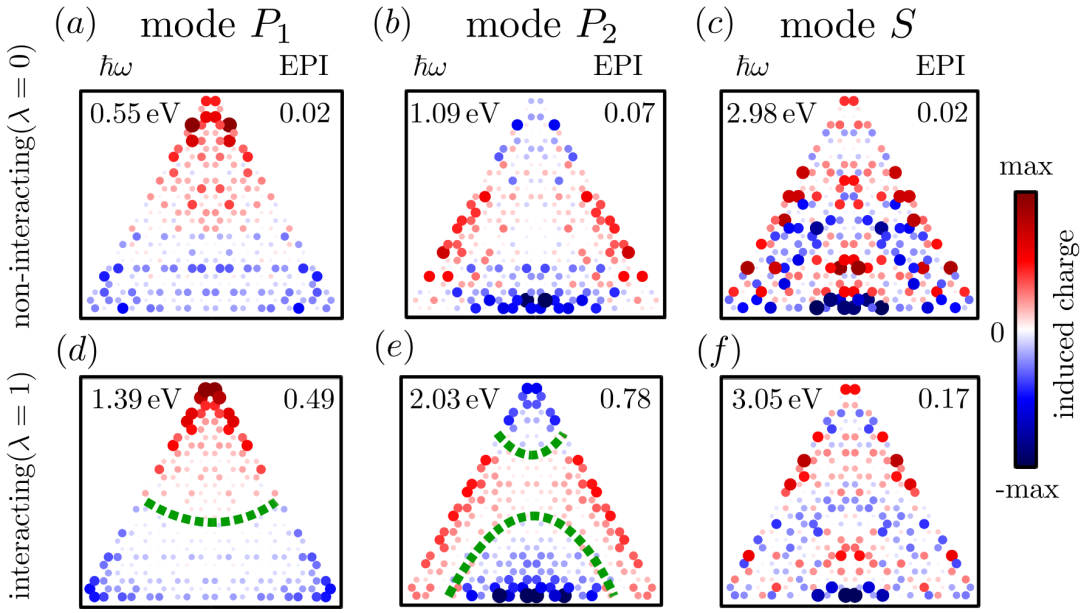

Figure 8.10: Real-space induced charge distribution in the 20-fold doped 270-atomic graphene nanotriangle in the non-interacting case for **(a)** mode P_1, **(b)** mode P_2, and **(c)** mode S, as labeled in Fig. 8.8d. **(d)**-**(f)** Same as **(a)**-**(c)**, but for interacting electrons. In the top left and top right corners of the subfigures, we show the energy and the EPI of the corresponding modes, respectively. The green dashed curves roughly indicate the nodal lines of the charge distribution. The size of the circles is proportional to the absolute value of the induced charge.

In the interacting case, both modes reside at higher energies, $0.72\,\mathrm{eV}$ and $1.36\,\mathrm{eV}$, and also their EPIs attain slightly higher values, 0.13 and 0.23. While in the non-interacting cases, regions of atoms with positive and negative excess charges strongly overlap spatially, the charge patterns in the interacting cases in Figs. 8.9d and 8.9e exhibit a more distinct charge separation along the green dashed nodal lines.

The *Coulomb* scaling approach in Fig. 8.8 reveals that both modes are mildly shifting with λ and are, thus, neither completely single-particle-like nor fully plasmonic. Other than modes A and B, mode C does not shift with *Coulomb* interaction strength and is classified single-particle-like within the *Coulomb* scaling framework. In the non-interacting and the interacting cases, the induced charge patterns look rather jumbled and orderless. The EPIs of 0.02 for $\lambda = 0$ and 0.14 for $\lambda = 1$ classify both modes as single-particle-like – in agreement with the *Coulomb* scaling method.

Heavy Doping: $d = 20$

The heavily doped triangle offers two modes that blue-shift very strongly in the scaling approach in Fig. 8.8d. Moreover, we note that mode C from Fig. 8.8b is retained in the energy region around $3\,\mathrm{eV}$ such that it can be directly compared to mode S in Fig. 8.8d.[6] Figures 8.10c and 8.10f show the induced charge of mode S at $2.98\,\mathrm{eV}$ and $3.05\,\mathrm{eV}$ in the non-interacting and interacting case, respectively. With 0.02 and 0.17, their EPI values are essentially equal to those of mode C, and the associated induced charge patterns are

[6] Modes C and S are mainly associated with the single-particle transition $\varepsilon \to \eta'$ that is still allowed as level η' remains unpopulated even after doping with 20 electrons.

also very similar. Therefore, it can be seen as a prime example of a single-particle-like mode – unaffected by an increased charge carrier density in the system and spectrally stable as the *Coulomb* interaction strength is varied.

Contrary to that, the modes P_1 and P_2 exhibit significantly higher EPIs of 0.49 and 0.78 in the interacting case, respectively. This identifies them as truly plasmonic in the sense of the EPI. Reminiscent of the labeling in Fig. 7.4, we assign P_1 to the fundamental dipolar plasmonic mode with one nodal line and P_2 to the next higher order plasmonic mode with two nodal lines (see the green dashed lines in Figs. 8.10d and 8.10e). Figures 8.10a and 8.10d show the associated induced charge of P_1. It resides at $0.55\,\mathrm{eV}$ for $\lambda = 0$ with an EPI of 0.02 and at $1.39\,\mathrm{eV}$ for $\lambda = 1$ with an EPI of 0.49. Figures 8.10b and 8.10e show the associated induced charge of P_2. It resides at $1.09\,\mathrm{eV}$ for $\lambda = 0$ with an EPI of 0.07 and at $2.03\,\mathrm{eV}$ for $\lambda = 1$ with an EPI of 0.78. Both plasmonic modes have very clean charge separation patterns without any overlapping regions of alternating signs. In general, it can be stated that the presence of *Coulomb* interaction causes a tendency to push the charge toward the edges of the structure. By comparing the upper and lower rows of Figs. 8.9 and 8.10, this can be easily seen.

The comparably low EPI value of the fundamental mode P_1 nicely highlights a shortcoming of the EPI that needs to be discussed here: the *Coulomb* interaction-mediated energy of the mode, $1.39\,\mathrm{eV}$, *accidentally* coincides with the energies of contributing single-particle transitions, $E_{139\to164} = 1.41\,\mathrm{eV}$ and $E_{137\to160} = 1.43\,\mathrm{eV}$, for instance. Although the mentioned transitions only weakly contribute to the mode in total, the expression in Eq. (8.6) causes their contribution to get significantly enhanced in $\tilde{\rho}^{\omega}$ and, therefore, they reduce the EPI of the overall plasmonic mode to an intermediate value.

Moreover, from the close inspection of modes A and B in Fig. 8.7b, we can conclude that the shifting characteristics of a mode as a response to a modification of the charge carrier density in the system cannot be used to unambiguously determine the character of that mode. While mode A (which is the *dressed* single-particle transition $E^d_{\alpha\to\alpha'}$) red-shifts as a function of charge carrier density, mode B (which is $E^d_{\alpha'\to\delta'}$) blue-shifts. This is true, although both modes shift in the *Coulomb* scaling approach in a similar way toward the blue (see Fig. 8.8b), and both modes have a very similar real-space induced charge pattern (see Figs. 8.9d and 8.9e). It can be further highlighted here that the mode P_1 (P_2) in the non-interacting and the interacting case have substantially different EPI values despite their real-space charge distribution is very similar to each other. This emphasizes that the EPI is not based on real-space quantities.

8.5.4 Energy-Space Dynamics

One of the key advantages of the used simulation method is the possibility to access the time-resolved energy space population dynamics. Therefore, we outline in the following how the modes whose real-space characteristics have been studied in the previous section are characterized in energy space. To that end, we investigate the change in population probability $\Delta P(j,t) = \rho_{jj}(t) - \rho^0_{jj}$ of the states $|j\rangle$ (see Eq. (8.4)) for the modes A, B, C, P_1, P_2, and S, both for non-interacting and for interacting electrons.

Moderate Doping: $d = 2$

Figure 8.11 shows the changes in population probability of the two-fold doped triangle as a function of time. We plot the five last optical cycles of the simulation period after the system has reached the stationary state. We show only the states $|j\rangle$ in the range $100 \leq$

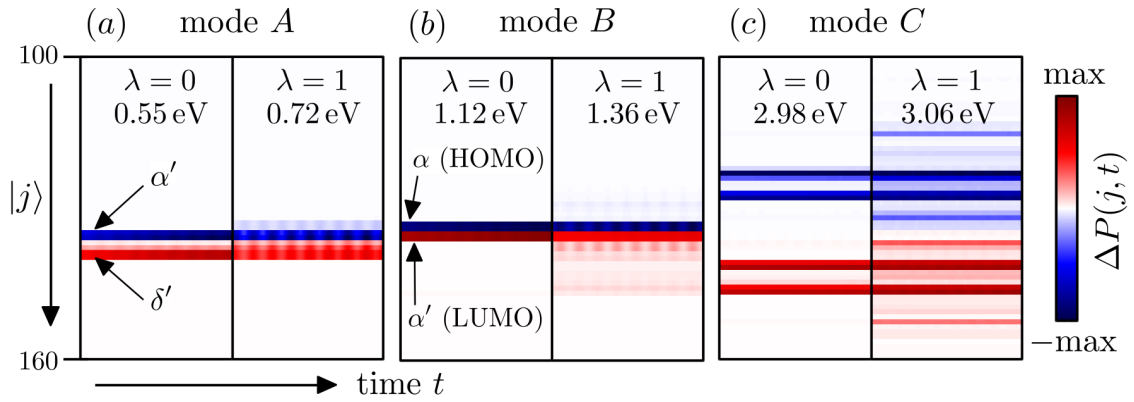

Figure 8.11: Difference in population probability $\Delta P(j,t)$ for the modes **(a)** A with EPIs of 0.05 $(\lambda = 0)$ and 0.13 $(\lambda = 1)$, **(b)** B with EPIs of 0.02 and 0.23, and **(c)** C with EPIs of 0.02 and 0.14 in the two-fold doped graphene nanotriangle. We show the states with $100 \leq j \leq 160$. The left (right) subfigures correspond to non-interacting (interacting) electrons. The time axis is limited to five optical cycles of the stationary state dynamics.

$j \leq 160$, as all the other states do not contribute to the formation of the investigated modes.

Modes A and B in Figs. 8.11a and 8.11b show clean and constant inversion type dynamics of the changes in population in the non-interacting cases ($\lambda = 0$, left subfigures). We see that, indeed, the levels α' and δ' for mode A and α and α' (or HOMO and LUMO) for mode B are defining the mode in energy space as donor and acceptor states, respectively. They interchange population in a monotonic manner, typical of single-particle-like modes. However, in the interacting cases ($\lambda = 1$, right subfigures), a slightly more complex structure becomes apparent. Although the involved states are mostly the same ones, we now also observe sloshing type oscillatory patterns on top. Moreover, especially in mode B, additional states below and above the HOMO and LUMO are weakly activated by the *Coulomb* interaction and contribute by interchanging the population in an oscillatory manner.

The same quantity for mode C is shown in Fig. 8.11c. In contrast to modes A and B, we find exclusively inversion type non-oscillatory contributions, both for the non-interacting and the interacting case. The only difference is that in the interacting case, a whole set of additional transitions occurs, and additional states become enabled. It is emphasized here that despite the two subfigures in Figs. 8.11a and 8.11b differ only slightly from each other, the energies of the associated modes are considerably different from each other. On the other hand, the two subfigures in Fig. 8.11c differ comparably strongly, as many additional pairs of states are engaged in the mode after the *Coulomb* interaction is turned on. Yet, the energies of the associated modes are similar. This illustrates that the energy of a mode is not primarily determined by *how many* or *which* transitions contribute to it, but rather by *how* they contribute to it – in an inversion type or sloshing type manner. The EPI can be seen as a quantification of the share of sloshing type transitions that contribute to the mode.

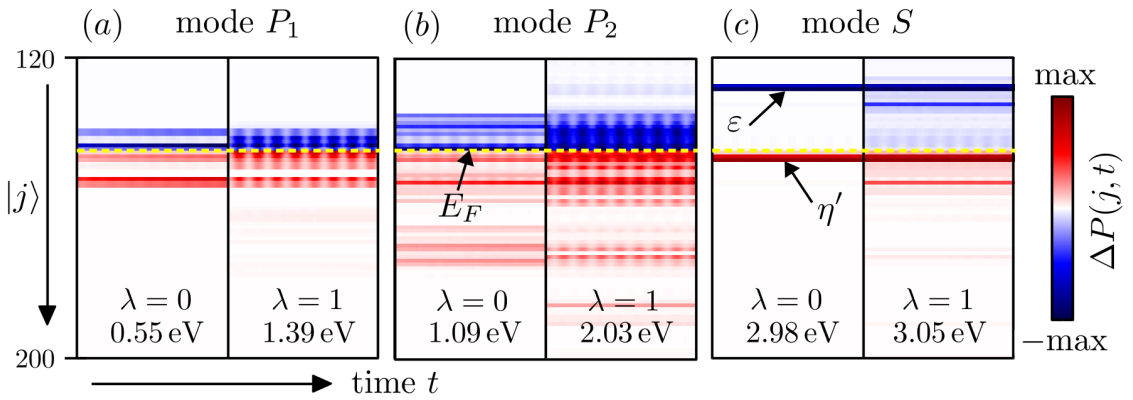

Figure 8.12: Difference in population probability $\Delta P(j,t)$ for the modes **(a)** P_1 with EPIs of 0.02 $(\lambda = 0)$ and 0.49 $(\lambda = 1)$, **(b)** P_2 with EPIs of 0.07 and 0.78, and **(c)** S with EPIs of 0.02 and 0.17 in the 20-fold doped graphene nanotriangle. We show the states with $120 \leq j \leq 200$. The left (right) subfigures correspond to non-interacting (interacting) electrons. The horizontal dashed line represents the *Fermi* energy and the time axis is limited to five optical cycles of the stationary state dynamics.

Heavy Doping: $d = 20$

In Fig. 8.12a, we present the change in population probability of mode P_1 in the heavily doped ($d = 20$) graphene nanotriangle. Whereas only inversion type monotonic transitions are visible in the non-interacting case with an EPI of 0.02, we observe oscillatory features in all of these transitions in the interacting case. It is remarkable here, that only very few additional states are engaged through the onset of electron-electron interaction. The set of active states remains mostly the same, but the nature of the already present transitions is altered from inversion to sloshing type. This alone leads to a massive shift of the mode from $0.55\,\mathrm{eV}$ to $1.39\,\mathrm{eV}$ as *Coulomb* interaction is gradually turned on, as well as to a substantial increase of the associated EPI value from 0.02 to 0.49. The change in population of mode P_2 is depicted in Fig. 8.12b. Similarly to the previous case, we observe a substantial onset of oscillatory behavior when the *Coulomb* interaction is taken into account as compared to the non-interacting simulation. Also, it is highlighted that the set of active states in both plasmonic modes (EPI of 0.78) is strongly located in the vicinity of the *Fermi* energy E_F (see the yellow dashed line in Fig. 8.12b). Please note, that this characteristic feature of a plasmonic mode has been observed by Townsend and Bryant in TD-DFT simulations before already (see Figs. 7.7 and 7.8), and was consistently reproduced in the TB approach here.

The change in population probability of mode S is shown in Fig. 8.12c. In the non-interacting case, we notice the strong contribution of the transitions from level ϵ, which is deep below the *Fermi* energy, to level η' just above E_F (see again Fig. 8.6c for the labeling). This highlights the single-particle character of the mode. Besides another faint additional inversion type transition that arises in the interacting case, the mode practically retains its single-particle energy-space characteristics, as the *Coulomb* interaction is turned on. Also the energy of the mode barely changes in that process.

In conclusion, we can note that in the moderately doped[7] structure, we do not identify plasmons in the sense of the EPI. All three modes (A, B, and C) can be considered predominantly single-particle-like, but moderately dressed by interaction energy. This renders low, but non-negligible EPI values between 0.13 and 0.23. The presence of the modes can be largely attributed to single-particle transitions in the non-interacting energy landscape of the structure in Fig. 8.6c. Only after doping the structure heavily, we find plasmons in the sense of the EPI. In the 20-fold doped structure, for instance, modes P_1 and P_2 yield EPI values of 0.49 and 0.78, respectively. They both show the expected dipolar (multipolar) real-space induced charge and their energies can only be explained by taking into account electron-electron interaction energy considerably. However, mode S (which is closely related to C) retains its single-particle character even after heavy doping. While both for P_1 and P_2, sloshing type transitions appear in the interacting case, mode S remains to be comprised of inversion type transitions mostly.

8.6 The EPI in Differently Sized Structures

The EPI of a mode is dependent on the single-particle eigenenergies of a given system that sustains it and, therefore, also on the method that is in use. The eigenenergies E_j of graphene-based nanoantennas in the TB description always lie in the energetic range $|E_j| \leq 3t$, where $t = 2.66\,\mathrm{eV}$ is the hopping in the TB framework, see Figs. 3.4 and 8.6b. Since the number of energy eigenstates is equal to the number of atoms in the structure, larger antennas provide denser spacing of eigenenergies in the mentioned interval. As *accidental* energy matching events like in mode P_1 are less likely to happen in larger antennas when more states are available in a given energy range, we expect better results for larger antennas.

In Fig. 8.13a, we show the EPIs of the lowest-energy fundamental dipolar modes in triangular nanoantennas of different side lengths in the range $3\,\mathrm{nm} \leq \mathrm{L} \leq 9\,\mathrm{nm}$ with 168 and 1386 atoms, respectively. To keep the modes in the structures as comparable as possible, we fix the *Fermi* energy of the nanoantennas at roughly $E_F \approx 0.75\,\mathrm{eV}$ for every size. This means, that a different number of electrons has been used for doping in each case. As expected, we observe that the EPI of the associated fundamental dipolar mode increases the larger the antenna gets. While in small antennas with a small number of excess doping charge, this fundamental mode is still associated with dressed single-particle-like transitions (see modes A and B in Fig. 8.8b), in the classical limit ($L \geq 10\,\mathrm{nm}$) with many doping electrons, the fundamental mode belongs intrinsically to a sloshing type plasmon (see mode P_1 in Fig. 8.8b), and the EPI approaches 1.

8.7 Direct Comparison of the EPI and GPI

Comparing the EPI to other classification approaches, one may state the following things. The EPI identifies all modes in the undoped and two-fold doped antennas as predominantly single-particle-like. At the utmost, one could call mode B with an EPI of 0.23 in the interacting case *intermediate*. Modes P_1 and P_2 can be regarded as plasmonic, whereas S is single-particle-like. The scaling approach completely agrees with this classification. While in Fig. 8.8b, modes A and C hardly shift with *Coulomb* interaction strength, mode B does to a greater extent. In Fig. 8.8d, mode S is spectrally stable, but P_1 and P_2 shift very strongly. In the multidimensional classification scheme of Tab. 7.1, all modes in the

[7] The same reasoning applies for the completely undoped structure as well. Besides the appearance of the additional low-energy modes in the moderately doped structure, the discussion is along the same lines and the corresponding modes qualitatively equivalent for $d = 0$.

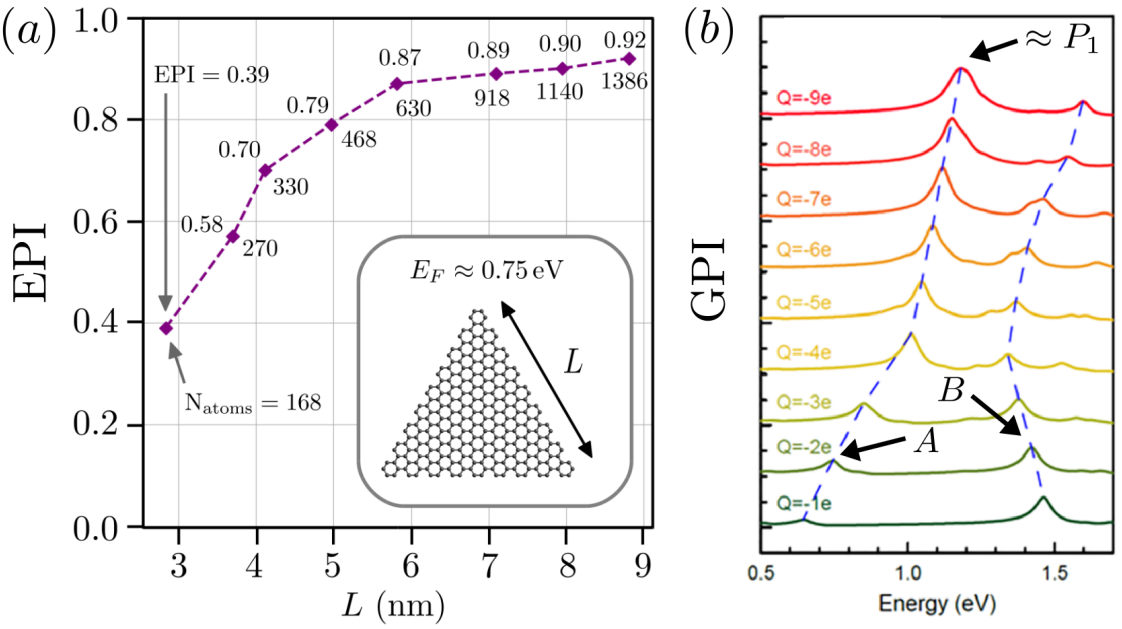

Figure 8.13: **(a)** EPI of the lowest-energy fundamental dipolar mode in graphene nanotriangles of different side lengths L. The *Fermi* energy is kept at a similar level $E_F \approx 0.75\,\mathrm{eV}$, which means that differently sized triangles are doped with a different number of electrons. **(b)** GPI of the two lowest-energy modes in the 270-atomic graphene nanotriangle for different doping levels in the range $1 \leq d \leq 9$. $Q = -2e$ is equivalent to $d = 2$. *Adapted with permission from Ref. [115]. Copyright © 2017 American Chemical Society.*

two-fold doped triangle fall under the category "single-particle", as they mainly consist of one single transition only, $\alpha \rightarrow \alpha'$ or $\alpha' \rightarrow \delta'$. This is also in accordance with the EPI, albeit for different reasons.

On the other hand, however, the GPI is in conflict with the EPI in many cases. As the GPI is not a normalized quantity, a direct comparison of the GPIs of differently doped triangles is cumbersome. In the spectral region evaluated in Ref. [115], modes A and B of the two-fold doped structure have the highest GPI values of the investigated part of the spectrum, 3 and 5.5, respectively (see Fig. 8.13b). Consequently, they are both considered plasmonic in the GPI approach. We furthermore observe that the GPI of the lowest-energy mode increases the stronger the antenna is doped. In the limiting case of $d = 9$, the onset of the plasmonic mode P_1 is visible and accompanied with the largest GPI value attained in the figure. It should be emphasized, however, that the author considers the blue dashed lines in Fig. 8.13b misleading. One should not perceive mode A for $d = 2$ and P_1 for $d = 9$ as the same modes, as it is insinuated by the figure. Whereas the former mode is predominantly single-particle-like and associated with the dressed single-particle transition $\alpha' \rightarrow \delta'$, the spectral position of the latter is predominantly determined by interaction energy and emerges from many single-particle transitions, as has been outlined above.

It needs to be emphasized here, that the GPI and the EPI are based on different concepts of plasmonicity on the nanoscale. Thus, it is neither surprising nor an inconsistency that the classification results do not coincide. The former attains a high value when the mode displays strong charge separation and, consequently, produces a high induced potential in the molecule. The latter attains high values when transitions in the non-interacting

energy landscape of a structure cannot explain the spectral position of a mode, and when it is dominated by sloshing type transitions in energy-space. We want to highlight here, that these characteristics go hand in hand in macroscopic systems, but need to be distinguished in nanoscale systems. Thus, the GPI and the EPI complement each other excellently to get a full comprehensive picture of a mode in a nanostructure.

8.8 Conclusions

In this chapter, we have introduced and applied the EPI as our own contribution to the scientific discussion. First, we outlined in detail how it is computed and interpreted, and then motivated the correspondence to the computational method of Townsend and Bryant. To validate the EPI on simple model systems, we applied it to the metallic linear carbon polyene chain and to the insulating dimerized polyacetylene chain in a TB-based framework, as well as to the sodium chain Na_{20} and to a small silver tetrahedron Ag_{20} in a TD-DFT framework. Finally, we investigated thoroughly the EPI of the optical modes in a 270-atomic doped triangular graphene nanoantenna, which has been studied in literature before in the context of the GPI also. Finally, we discussed the EPI in comparison with other classification methods, such as the GPI.

The EPI constitutes a powerful tool to complement other existing approaches for the classification of modes on the nanoscale using quantum mechanical simulation schemes. The underlying concept of a plasmon is based on electron-electron interaction as the essential mechanism that leads to the formation of the mode. Therefore, the energy of a plasmon in the sense of the EPI is determined by a complex interplay of coherently coupled electrons and cannot be trivially linked to transitions in the non-interacting energy landscape of a given structure. The EPI of a mode lies between 0 (single-particle-like) and 1 (plasmonic). By comparing either Figs. 8.9d and 8.9f with similar EPIs but substantially different real-space charge distributions or Figs. 8.10b and 8.10e with similar real-space charge distributions but substantially different EPIs, it can further be seen that the real-space induced charge is not linked to the EPI of a mode. The EPI is rather determined by the amount of sloshing type single-particle transitions that contribute to the population dynamics in energy space.

9 | Conclusions and Outlook

In the presented work, we developed a time-domain tight binding (TB)-based simulation framework to describe the optical properties of carbon-based nanostructures. It is applicable to stand-alone planar nanoantennas and to hybrid systems that comprise a nanoantenna and a foreign adsorbed atom (adatom) which interacts optically and chemically with the antenna. Our TB framework is computationally much cheaper than common *ab initio* approaches, such as density functional theory (DFT), and can handle molecules with hundreds or even thousands of atoms utilizing a reasonable amount of computational resources. Of course, this speed-up comes with the cost of lower accuracy in general. However, the employed TB approach is very accurate for the nanostructures discussed in this work – especially in the case of graphene, which is one of the most prominent candidates for future tunable optical devices due to its exceptional geometry and band structure.

Capitalizing on this simulation framework, in the first part of the thesis, we investigated **hybrid systems** of adatoms that are chemically coupled to carbon-based antennas. Particularly, we consecutively adopted two different perspectives. First, we studied what impact the coupling parameters of an adatom have on the electronic structure and the optical properties of an antenna. Then, we focused on how the quantum optical phenomena of spontaneous emission and *Rabi* oscillations in the adatom are modified by taking into account both the optical and the chemical interaction channel.

In the second part of the thesis, we discussed the issue of defining and measuring **plasmons in nanoscale systems** beyond the classical realm. Many previous approaches to classify optical modes rely on the associated induced charge or the number of involved single-particle transitions. To complement the body of literature on this issue, we constructed a normalized and dimensionless measure for plasmonicity – the *energy-based plasmonicity index (EPI)* – that relies on the energy-space coherence dynamics in the system's density operator and, hence, neither on real-space characteristics of the modes nor on the number of involved single-particle transitions.

Conclusions

In the first part of the thesis, after we recapitulated the necessary theoretical background on nanoplasmonics in Ch. 2 and the electronic and optical properties of graphene in Ch. 3, we focused on the electronic and optical properties of *finite* carbon structures. Based on the TB method that is widely applied to calculate the band structure of extended 2D graphene, we determined the single-particle eigenenergies and eigenstates of planar carbon nanoantennas in Ch. 4. In particular, we discussed the linear carbon chains of the *Su-Schrieffer-Heeger* (SSH) model, *i.e.* the conducting polyene and insulating polyacetylene molecules, and graphene nanoantennas of different shapes and edge types.

We argued that graphene antennas with armchair edges are more suitable for applications in tunable optics as compared to zigzag-terminated antennas. Moreover, we saw that the armchair graphene triangle under investigation has a similar energetic structure as the dimerized carbon chain, exhibiting a band gap across zero energy and two quasi-continua of states above and below this gap, reminiscent of the conduction and valence bands in infinite structures. Therefore, the conceptually easily accessible chain species can serve as a starting point to understand electronically more complex systems like the graphene antennas. In anticipation of the need to characterize hybrid systems on the basis of their single-particle eigenstates, we introduced scalar measures to quantify their localization, symmetry, hybridization, and their involvement in optical interaction mechanisms.

Chapter 5 concentrated on the time-domain approach to describe the optical properties of planar carbon molecules with electric fields. The presented framework allows to track electronic dynamics both in real and energy space. Especially when focusing on higher harmonic generation, we found that both plasmonic and single-particle-like modes are suitable for producing higher harmonics in the emission spectrum of a structure. Both the conducting linear chain and the isolating dimer chain offered higher harmonic generation of odd higher orders with similar strength. However, in the investigated graphene nanoantenna, it was found that the generation of even-order higher harmonics is supported to a higher degree in the plasmonic modes of the highly doped antenna as compared to the single-particle-like mode of the moderately doped one. On the other hand, odd orders are generated for both kinds of modes to a similar extent.

Hybrid antenna-adatom systems were introduced in Ch. 6, where we extended the formalism from the previous chapters to include also two-level quantum emitters that are optically and chemically coupled to the antenna. We concluded that there are two qualitatively different coupling configurations, *edge* and *bulk* coupling that need to be distinguished. Moreover, in different structures, different coupling strengths are optimal to achieve maximum hybridization and tuning of the absorption cross-section. It was found that, among all investigated configurations, the conducting linear chain offers the highest degree of tunability when the adatom is coupled to a bulk atom of the chain. The adatom effectively splits the chain into two smaller chains in this case. Consequently, instead of exhibiting one prominent low-energy absorption mode that is associated with the long chain, we observe two less intense modes at higher energy that belong to the two smaller chains. The absorption of the insulating dimerized chain species, on the other hand, remained relatively inert for all investigated coupling configurations. Conversely, also quantum optical phenomena routinely discussed in the context of two-level systems are modified. Upon coupling the adatom to the antenna also chemically, the spontaneous emission of the adatom is suppressed as compared to the case when only optical coupling is present. Moreover, we observe a decrease of the *Rabi* oscillation frequency of the HOMO-LUMO transition in the hybrid system as the coupling strength between the adatom and the antenna increases. These results highlight the necessity to also consider electronic tunneling when a quantum emitter is brought close to a nanoantenna at distances in the order of a few Ångström or a nanometer.

To begin the second complex of this thesis, we gave a broad overview of the research field in Ch. 7, assessing different concepts of plasmonicity and presenting measures and characterization approaches that already exist in literature. In particular, strategies to tell apart single-particle-like modes from plasmonic ones are reviewed. They mostly focus on the following three aspects of the modes: the induced charge distribution, the number of involved single-particle-transitions, or the amount of *Coulomb* energy associated with the mode.

In the last chapter, we introduced our own contribution to this discussion – the EPI. First, we motivated the idea of its construction as a quantification of the *sloshing* and *inversion* type dynamics of state populations that were previously found in DFT simulations by Townsend and Bryant. We then validated the EPI by applying it to structures that are routinely discussed in this context – the polyene and polyacetylene chains in a TB framework and the sodium chain Na_{20} and the silver tetrahedron Ag_{20} within a DFT framework. Finally, we applied the EPI to the modes in a graphene antenna that is known to support both single-particle-like and plasmonic modes at the same time, and compared our findings to other classification methods like the generalized plasmonicity index (GPI) and the *Coulomb* scaling approach. We find that the classification results of the EPI and the GPI do not coincide in general, as the latter is based on the real-space induced charge of the mode. We showed that modes with incrementally different induced charge patterns may have substantially different EPI values. Also, hybrid modes tend to resemble plasmonic ones in real space. On the other hand, the *Coulomb* scaling approach of Bernadotte *et al.* is mostly in agreement with our classification outcomes as it also predominantly relies on energy-space considerations and *Coulomb* interaction. A substantial advantage of the EPI over the scaling approach is that only a single simulation is needed to asses the nature of a mode instead of a whole series of simulations with different *Coulomb* interaction strengths. Altogether, we find real-space considerations unreliable to determine a mode's nature as both single-particle-like and plasmonic modes were shown to exhibit very similar induced charge patterns. On the other hand, we see clear signatures of both mode types in the *oscillating sloshing* and *monotonous inversion* dynamics of the state populations in energy space.

Outlook

Future research along similar lines could involve the following topics. The optical properties of the molecules considered in this thesis rely on the regularity of their geometric structure. It was not investigated in this thesis how robust the discussed phenomena are with respect to positional disorder of the antenna atoms. While the natural carbon-carbon atomic distance is rather rigid, the inter-atomic distance in artificially fabricated chains of quantum dots can be readily controlled and tailored. Also, graphene antenna edges often exhibit pentagonal and heptagonal irregularities that disturb the hexagonal structure and, hence, modify the energy landscape. For the sake of simplicity, in this thesis, the behavior of the hybrid systems was investigated under the assumption of particle-hole symmetry of the energy landscape. We also kept the energies of the adatom orbitals fixed and did not capitalize on the doping degree of freedom. Although we briefly discuss asymmetric energy landscapes in Ref. [A5] as well, this discussion can surely be intensified. Graphene is a representative of the so-called *Van der Waals* materials that exhibit *strong in-plane* atomic bonds, but *weak out-of-plane* coupling. Therefore, it is possible to create layered structures combining different *Van der Waals* materials on top of each other. This opens up the route to control and engineer optical properties of low-dimensional materials even further. Hence, developing our hybrid simulation framework further along these lines seems auspicious.

Bibliography

[A1] M. M. Müller, M. Kosik, M. Pelc, G. W. Bryant, A. Ayuela, C. Rockstuhl, and K. Słowik, "Energy-Based Plasmonicity Index to Characterize Optical Resonances in Nanostructures," *The Journal of Physical Chemistry C*, vol. 124, no. 44, pp. 24 331–24 343, 2020.

[A2] M. M. Müller, M. Kosik, M. Pelc, G. W. Bryant, A. Ayuela, C. Rockstuhl, and K. Słowik, "Modification of the optical properties of molecular chains upon coupling to adatoms," *Physical Review B*, vol. 104, no. 23, p. 235 414, 2021.

[A3] M. M. Müller, M. Kosik, M. Pelc, G. W. Bryant, A. Ayuela, C. Rockstuhl, and K. Słowik, "From single-particle-like to interaction-mediated plasmonic resonances in graphene nanoantennas," *The Journal of Applied Physics*, vol. 129, no. 9, p. 093 103, 2021.

[A4] M. M. Müller, N. Perdana, C. Rockstuhl, and C. Holzer, "Modeling and measuring plasmonic excitations in hollow spherical gold nanoparticles," *The Journal of Chemical Physics*, vol. 156, no. 9, p. 094 103, 2022.

[A5] M. Kosik, M. M. Müller, K. Słowik, G. Bryant, A. Ayuela, C. Rockstuhl, and M. Pelc, "Revising quantum optical phenomena in adatoms coupled to graphene nanoantennas," *Nanophotonics*, vol. 11, no. 14, pp. 3281–3298, 2022.

[1] M. I. Stockman, "Nanoplasmonics: The physics behind the applications," *Physics Today*, vol. 64, no. 2, pp. 39–44, 2011.

[2] M. I. Stockman, "Nanoplasmonics: Past, present, and glimpse into future," *Optics Express*, vol. 19, no. 22, pp. 22 029–22 106, 2011.

[3] G. Baffou and R. Quidant, "Nanoplasmonics for chemistry," *Chemical Society Reviews*, vol. 43, no. 11, pp. 3898–3907, 2014.

[4] O. Hess, J. B. Pendry, S. A. Maier, R. F. Oulton, J. M. Hamm, and K. L. Tsakmakidis, "Active nanoplasmonic metamaterials," *Nature Materials*, vol. 11, no. 7, pp. 573–584, 2012.

[5] S. Mühlig, A. Cunningham, J. Dintinger, T. Scharf, T. Bürgi, F. Lederer, and C. Rockstuhl, "Self-assembled plasmonic metamaterials," *Nanophotonics*, vol. 2, no. 3, pp. 211–240, 2013.

[6] A. F. Koenderink, "Plasmon nanoparticle array waveguides for single photon and single plasmon sources," *Nano Letters*, vol. 9, no. 12, pp. 4228–4233, 2009.

[7] Y. Chen, P. Lodahl, and A. F. Koenderink, "Dynamically reconfigurable directionality of plasmon-based single photon sources," *Physical Review B*, vol. 82, no. 8, p. 081 402, 2010.

[8] P. Yu, J. Wu, E. Ashalley, A. Govorov, and Z. Wang, "Dual-band absorber for multispectral plasmon-enhanced infrared photodetection," *Journal of Physics D: Applied Physics*, vol. 49, no. 36, p. 365 101, 2016.

[9] M. L. Brongersma, N. J. Halas, and P. Nordlander, "Plasmon-induced hot carrier science and technology," *Nature Nanotechnology*, vol. 10, no. 1, p. 25, 2015.

[10] J.-T. Kim, Y.-J. Yu, H. Choi, and C.-G. Choi, "Graphene-based plasmonic photodetector for photonic integrated circuits," *Optics Express*, vol. 22, no. 1, pp. 803–808, 2014.

[11] Y. Salamin, P. Ma, B. Baeuerle, A. Emboras, Y. Fedoryshyn, W. Heni, B. Cheng, A. Josten, and J. Leuthold, "100 ghz plasmonic photodetector," *ACS Photonics*, vol. 5, no. 8, pp. 3291–3297, 2018.

[12] S. S. Mousavi, A. Stöhr, and P. Berini, "Plasmonic photodetector with terahertz electrical bandwidth," *Applied Physics Letters*, vol. 104, no. 14, p. 143 112, 2014.

[13] J. Melendez, R. Carr, D. U. Bartholomew, K. Kukanskis, J. Elkind, S. Yee, C. Furlong, and R. Woodbury, "A commercial solution for surface plasmon sensing," *Sensors and Actuators B: Chemical*, vol. 35, no. 1-3, pp. 212–216, 1996.

[14] K. Awazu, C. Rockstuhl, M. Fujimaki, N. Fukuda, J. Tominaga, T. Komatsubara, T. Ikeda, and Y. Ohki, "High sensitivity sensors made of perforated waveguides," *Optics Express*, vol. 15, no. 5, pp. 2592–2597, 2007.

[15] C. Lee, F. Dieleman, J. Lee, C. Rockstuhl, S. A. Maier, and M. Tame, "Quantum plasmonic sensing: beyond the shot-noise and diffraction limit," *ACS Photonics*, vol. 3, no. 6, pp. 992–999, 2016.

[16] A. Boltasseva and H. A. Atwater, "Ultrafast active plasmonics," *Science*, vol. 331, pp. 290–291, 2011.

[17] S. A. Maier, *Plasmonics: Fundamentals and applications*. Springer Science & Business Media, 2007.

[18] S. Zouhdi, A. Sihvola, and A. P. Vinogradov, *Metamaterials and plasmonics: Fundamentals, modelling, applications*. Springer Science & Business Media, 2008.

[19] M. A. Cazalilla, J. S. Dolado, A. Rubio, and P. M. Echenique, "Plasmonic excitations in noble metals: The case of Ag," *Physical Review B*, vol. 61, pp. 8033–8042, 12 Mar. 2000.

[20] M. Pelton, J. Aizpurua, and G. W. Bryant, "Metal-nanoparticle plasmonics," *Laser & Photonics Reviews*, vol. 2, no. 3, pp. 136–159, 2008.

[21] V. Giannini, A. I. Fernández-Domınguez, S. C. Heck, and S. A. Maier, "Plasmonic nanoantennas: fundamentals and their use in controlling the radiative properties of nanoemitters," *Chemical Reviews*, vol. 111, no. 6, pp. 3888–3912, 2011.

[22] F. H. L. Koppens, D. E. Chang, and F. J. García de Abajo, "Graphene plasmonics: a platform for strong light-matter interactions," *Nano Letters*, vol. 11, no. 8, pp. 3370–3377, 2011.

[23] L. R. Hirsch, R. J. Stafford, J. A. Bankson, S. R. Sershen, B. Rivera, R. E. Price, J. D. Hazle, N. J. Halas, and J. L. West, "Nanoshell-mediated near-infrared thermal therapy of tumors under magnetic resonance guidance," *Proceedings of the National Academy of Sciences*, vol. 100, no. 23, pp. 13 549–13 554, 2003.

[24] D. O'Neal, L. R. Hirsch, N. J. Halas, J. Payne, and J. L. West, "Photo-thermal tumor ablation in mice using near infrared-absorbing nanoparticles," *Cancer Letters*, vol. 209, no. 2, pp. 171–176, 2004, issn: 0304-3835.

[25] X. Qian, X.-H. Peng, D. O. Ansari, Q. Yin-Goen, G. Z. Chen, D. M. Shin, L. Yang, A. N. Young, M. D. Wang, and S. Nie, "In vivo tumor targeting and spectroscopic detection with surface-enhanced Raman nanoparticle tags," *Nature Biotechnology*, vol. 26, no. 1, pp. 83–90, 2008.

[26] L. Novotny and B. Hecht, *Principles of nano-optics*. Cambridge University Press, 2012.

[27] S. I. Bozhevolnyi and N. A. Mortensen, "Plasmonics for emerging quantum technologies," *Nanophotonics*, vol. 6, no. 5, pp. 1185–1188, 2017.

[28] G. W. Bryant, E. Waks, and J. R. Krenn, "Plasmonics: The rise of quantum effects," *Optics and Photonics News*, vol. 25, no. 11, pp. 50–53, 2014.

[29] M. S. Tame, K. R. McEnery, Ş. K. Özdemir, J. Lee, S. A. Maier, and M. S. Kim, "Quantum plasmonics," *Nature Physics*, vol. 9, no. 6, pp. 329–340, 2013.
[30] F. Wang and Y. R. Shen, "General properties of local plasmons in metal nanostructures," *Physical Review Letters*, vol. 97, no. 20, p. 206 806, 2006.
[31] M. Wubs and N. A. Mortensen, "Nonlocal response in plasmonic nanostructures," in *Quantum plasmonics*, Springer, 2017, pp. 279–302.
[32] K. S. Novoselov, A. K. Geim, S. V. Morozov, D.-e. Jiang, Y. Zhang, S. V. Dubonos, I. V. Grigorieva, and A. A. Firsov, "Electric field effect in atomically thin carbon films," *Science*, vol. 306, no. 5696, pp. 666–669, 2004.
[33] N. D. Mermin, "Crystalline order in two dimensions," *Physical Review*, vol. 176, no. 1, p. 250, 1968.
[34] D. Robertson, D. Brenner, and C. White, "On the way to fullerenes: Molecular dynamics study of the curling and closure of graphitic ribbons," *The Journal of Physical Chemistry*, vol. 96, no. 15, pp. 6133–6135, 1992.
[35] K. Novoselov, "Nobel lecture: Graphene: Materials in the flatland," *Reviews of Modern Physics*, vol. 83, no. 3, p. 837, 2011.
[36] D. Basov, M. Fogler, and F. García de Abajo, "Polaritons in van der waals materials," *Science*, vol. 354, no. 6309, aag1992, 2016.
[37] T. Yamada, J. Kim, M. Ishihara, and M. Hasegawa, "Low-temperature graphene synthesis using microwave plasma CVD," *Journal of Physics D: Applied Physics*, vol. 46, no. 6, p. 063 001, 2013.
[38] E. Jabari, F. Ahmed, F. Liravi, E. B. Secor, L. Lin, and E. Toyserkani, "2D printing of graphene: A review," *2D Materials*, vol. 6, no. 4, p. 042 004, Aug. 2019.
[39] L. Ju, B. Geng, J. Horng, C. Girit, M. Martin, Z. Hao, H. A. Bechtel, X. Liang, A. Zettl, Y. R. Shen, *et al.*, "Graphene plasmonics for tunable terahertz metamaterials," *Nature Nanotechnology*, vol. 6, no. 10, pp. 630–634, 2011.
[40] J. Chen, M. Badioli, P. Alonso-González, S. Thongrattanasiri, F. Huth, J. Osmond, M. Spasenović, A. Centeno, A. Pesquera, P. Godignon, *et al.*, "Optical nano-imaging of gate-tunable graphene plasmons," *Nature*, vol. 487, no. 7405, pp. 77–81, 2012.
[41] Z. Fei, G. O. Andreev, W. Bao, L. M. Zhang, A. S. McLeod, C. Wang, M. K. Stewart, Z. Zhao, G. Dominguez, M. Thiemens, *et al.*, "Infrared nanoscopy of dirac plasmons at the graphene–sio2 interface," *Nano Letters*, vol. 11, no. 11, pp. 4701–4705, 2011.
[42] A. N. Grigorenko, M. Polini, and K. S. Novoselov, "Graphene plasmonics," *Nature Photonics*, vol. 6, no. 11, p. 749, 2012.
[43] M. Jablan, H. Buljan, and M. Soljačić, "Plasmonics in graphene at infrared frequencies," *Physical Review B*, vol. 80, no. 24, p. 245 435, 2009.
[44] S. Thongrattanasiri, A. Manjavacas, and F. J. García de Abajo, "Quantum finite-size effects in graphene plasmons," *ACS Nano*, vol. 6, no. 2, pp. 1766–1775, 2012.
[45] A. Manjavacas, S. Thongrattanasiri, and F. J. García de Abajo, "Plasmons driven by single electrons in graphene nanoislands," *Nanophotonics*, vol. 2, no. 2, pp. 139–151, 2013.
[46] T. Christensen, W. Wang, A.-P. Jauho, M. Wubs, and N. A. Mortensen, "Classical and quantum plasmonics in graphene nanodisks: Role of edge states," *Physical Review B*, vol. 90, no. 24, p. 241 414, 2014.
[47] J. D. Cox and F. J. García de Abajo, "Electrically tunable nonlinear plasmonics in graphene nanoislands," *Nature Communications*, vol. 5, no. 1, p. 5725, 2014.
[48] R. Yu, J. D. Cox, J. Saavedra, and F. J. García de Abajo, "Analytical modeling of graphene plasmons," *ACS Photonics*, vol. 4, no. 12, pp. 3106–3114, 2017.
[49] García de Abajo, F. J., "Graphene plasmonics: Challenges and opportunities," *ACS Photonics*, vol. 1, no. 3, pp. 135–152, 2014.

[50] P. A. D. Gonçalves and N. M. R. Peres, *An Introduction to graphene plasmonics*. WORLD SCIENTIFIC, 2016.
[51] S. Huang, C. Song, G. Zhang, and H. Yan, "Graphene plasmonics: Physics and potential applications," *Nanophotonics*, vol. 6, no. 6, pp. 1191–1204, 2017.
[52] S.-h. Phark, J. Borme, A. L. Vanegas, M. Corbetta, D. Sander, and J. Kirschner, "Direct observation of electron confinement in epitaxial graphene nanoislands," *ACS Nano*, vol. 5, no. 10, pp. 8162–8166, 2011.
[53] F. Recio, N. Zabala, A. Rivacoba, P. Crespo, A. Ayuela, P. M. Echenique, and A. Hernando, "Optical resonances of colloidal gold nanorods: From seeds to chemically thiolated long nanorods," *The Journal of Physical Chemistry C*, vol. 119, no. 14, pp. 7856–7864, 2015.
[54] P. Wallace, "The band theory of graphite," *Physical Review*, vol. 71, pp. 622–634, 1947.
[55] S. Reich, J. Maultzsch, C. Thomsen, and P. Ordejon, "Tight-binding description of graphene," *Physical Review B*, vol. 66, no. 3, p. 035 412, 2002.
[56] A. Ayuela, L. Chico, and W. Jaskólski, "Electronic band structure of carbon nanotube superlattices from first-principles calculations," *Physical Review B*, vol. 77, p. 085 435, 8 Feb. 2008.
[57] R. Ribeiro, V. M. Pereira, N. Peres, P. Briddon, and A. C. Neto, "Strained graphene: Tight-binding and density functional calculations," *New Journal of Physics*, vol. 11, no. 11, p. 115 002, 2009.
[58] E. Kogan, V. Nazarov, V. Silkin, and M. Kaveh, "Energy bands in graphene: Comparison between the tight-binding model and ab initio calculations," *Physical Review B*, vol. 89, no. 16, p. 165 430, 2014.
[59] W. P. Su, J. R. Schrieffer, and A. J. Heeger, "Solitons in Polyacetylene," *Physical Review Letters*, vol. 42, pp. 1698–1701, 25 Jun. 1979.
[60] S. Kivelson and D. E. Heim, "Hubbard versus Peierls and the Su-Schrieffer-Heeger model of polyacetylene," *Physical Review B*, vol. 26, no. 8, p. 4278, 1982.
[61] E. Fradkin and J. E. Hirsch, "Phase diagram of one-dimensional electron-phonon systems. I. The Su-Schrieffer-Heeger model," *Physical Review B*, vol. 27, no. 3, p. 1680, 1983.
[62] K. Harigaya, "Lattice distortion and energy-level structures in doped C60 and C70 molecules studied with the extended Su-Schrieffer-Heeger model: Polaron excitations and optical absorption," *Physical Review B*, vol. 45, no. 23, p. 13 676, 1992.
[63] P. Quémerais, D. K. Campbell, J.-L. Raimbault, and S. Aubry, "Quantum tunneling effects in the SSH model of electron-phonon interactions," *International Journal of Modern Physics B*, vol. 7, no. 25, pp. 4289–4303, 1993.
[64] M. Atala, M. Aidelsburger, J. T. Barreiro, D. Abanin, T. Kitagawa, E. Demler, and I. Bloch, "Direct measurement of the Zak phase in topological Bloch bands," *Nature Physics*, vol. 9, no. 12, pp. 795–800, 2013, issn: 1745-2481.
[65] Y. Ando, "Topological Insulator Materials," *The Journal of the Physical Society of Japan*, vol. 82, no. 10, p. 102 001, 2013.
[66] E. J. Meier, F. A. An, and B. Gadway, "Observation of the topological soliton state in the Su–Schrieffer–Heeger model," *Nature Communications*, vol. 7, no. 1, p. 13 986, 2016, issn: 2041-1723.
[67] J. K. Asbóth, L. Oroszlány, and A. Pályi, "A Short Course on Topological Insulators," *Lecture Notes in Physics*, vol. 919, p. 166, 2016.
[68] M. Di Liberto, A. Recati, I. Carusotto, and C. Menotti, "Two-body physics in the Su-Schrieffer-Heeger model," *Physical Review A*, vol. 94, p. 062 704, 6 Dec. 2016.

[69] Z. Turker, S. Tombuloglu, and C. Yuce, "PT symmetric Floquet topological phase in SSH model," *Physics Letters A*, vol. 382, no. 30, pp. 2013–2016, 2018, issn: 0375-9601.
[70] S. Lieu, "Topological phases in the non-Hermitian Su-Schrieffer-Heeger model," *Physical Review B*, vol. 97, p. 045 106, 4 Jan. 2018.
[71] C. Yuce and H. Ramezani, "Topological states in a non-Hermitian two-dimensional Su-Schrieffer-Heeger model," *Physical Review A*, vol. 100, p. 032 102, 3 Sep. 2019.
[72] C. Yang, L. Li, and S. Chen, "Dynamical topological invariant after a quantum quench," *Physical Review B*, vol. 97, p. 060 304, 6 Feb. 2018.
[73] A. J. Heeger, S. Kivelson, J. R. Schrieffer, and W.-P. Su, "Solitons in conducting polymers," *Reviews of Modern Physics*, vol. 60, pp. 781–850, 3 Jul. 1988.
[74] S. Nadj-Perge, I. K. Drozdov, J. Li, H. Chen, S. Jeon, J. Seo, A. H. MacDonald, B. A. Bernevig, and A. Yazdani, "Observation of Majorana fermions in ferromagnetic atomic chains on a superconductor," *Science*, vol. 346, no. 6209, pp. 602–607, 2014.
[75] B. E. Feldman, M. T. Randeria, J. Li, S. Jeon, Y. Xie, Z. Wang, I. K. Drozdov, B. A. Bernevig, and A. Yazdani, "High-resolution studies of the Majorana atomic chain platform," *Nature Physics*, vol. 13, no. 3, pp. 286–291, 2017.
[76] Y.-W. Park, A. J. Heeger, M. A. Druy, and A. G. MacDiarmid, "Electrical transport in doped polyacetylene," *The Journal of Chemical Physics*, vol. 73, no. 2, pp. 946–957, 1980.
[77] A. J. Heeger and A. G. Maciarmid, "Transport, magnetic and structural studies of polyacetylene," *Molecular Crystals and Liquid Crystals*, vol. 77, no. 1-4, pp. 1–24, 1981.
[78] N. Basescu, Z.-X. Liu, D. Moses, A. J. Heeger, H. Naarmann, and N. Theophilou, "High electrical conductivity in doped polyacetylene," *Nature*, vol. 327, no. 6121, pp. 403–405, 1987, issn: 1476-4687.
[79] S. Thongrattanasiri and F. J. García de Abajo, "Optical field enhancement by strong plasmon interaction in graphene nanostructures," *Physical Review Letters*, vol. 110, no. 18, p. 187 401, 2013.
[80] A. Manjavacas, F. Marchesin, S. Thongrattanasiri, P. Koval, P. Nordlander, D. Sanchez-Portal, and F. J. García de Abajo, "Tunable molecular plasmons in polycyclic aromatic hydrocarbons," *ACS Nano*, vol. 7, no. 4, pp. 3635–3643, 2013.
[81] S. Thongrattanasiri, A. Manjavacas, P. Nordlander, and F. J. García de Abajo, "Quantum junction plasmons in graphene dimers," *Laser & Photonics Reviews*, vol. 7, no. 2, pp. 297–302, 2013.
[82] E. M. Purcell, H. C. Torrey, and R. V. Pound, "Resonance absorption by nuclear magnetic moments in a solid," *Physical Review*, vol. 69, no. 1-2, p. 37, 1946.
[83] S. Kühn, U. Håkanson, L. Rogobete, and V. Sandoghdar, "Enhancement of single-molecule fluorescence using a gold nanoparticle as an optical nanoantenna," *Physical Review Letters*, vol. 97, no. 1, p. 017 402, 2006.
[84] T. Taminiau, F. Stefani, F. B. Segerink, and N. Van Hulst, "Optical antennas direct single-molecule emission," *Nature Photonics*, vol. 2, no. 4, pp. 234–237, 2008.
[85] M. Schiek, F. Balzer, K. Al-Shamery, J. R. Brewer, A. Lützen, and H.-G. Rubahn, "Organic molecular nanotechnology," *Small*, vol. 4, no. 2, pp. 176–181, 2008.
[86] I. Gryczynski, J. Malicka, W. Jiang, H. Fischer, W. C. Chan, Z. Gryczynski, W. Grudzinski, and J. R. Lakowicz, "Surface-plasmon-coupled emission of quantum dots," *The Journal of Physical Chemistry B*, vol. 109, no. 3, pp. 1088–1093, 2005.
[87] D. E. Chang, A. S. Sørensen, P. R. Hemmer, and M. D. Lukin, "Quantum optics with surface plasmons," *Physical Review Letters*, vol. 97, no. 5, p. 053 002, 2006.

[88] A. Akimov, A. Mukherjee, C. Yu, D. Chang, A. Zibrov, P. Hemmer, H. Park, and M. Lukin, "Generation of single optical plasmons in metallic nanowires coupled to quantum dots," *Nature*, vol. 450, no. 7168, pp. 402–406, 2007.

[89] A. G. Curto, G. Volpe, T. H. Taminiau, M. P. Kreuzer, R. Quidant, and N. F. van Hulst, "Unidirectional emission of a quantum dot coupled to a nanoantenna," *Science*, vol. 329, no. 5994, pp. 930–933, 2010.

[90] N. Manson, J. Harrison, and M. Sellars, "Nitrogen-vacancy center in diamond: Model of the electronic structure and associated dynamics," *Physical Review B*, vol. 74, no. 10, p. 104 303, 2006.

[91] R. Kolesov, B. Grotz, G. Balasubramanian, R. J. Stöhr, A. A. Nicolet, P. R. Hemmer, F. Jelezko, and J. Wrachtrup, "Wave–particle duality of single surface plasmon polaritons," *Nature Physics*, vol. 5, no. 7, pp. 470–474, 2009.

[92] D. Englund, B. Shields, K. Rivoire, F. Hatami, J. Vuckovic, H. Park, and M. D. Lukin, "Deterministic coupling of a single nitrogen vacancy center to a photonic crystal cavity," *Nano Letters*, vol. 10, no. 10, pp. 3922–3926, 2010.

[93] A. Huck, S. Kumar, A. Shakoor, and U. L. Andersen, "Controlled coupling of a single nitrogen-vacancy center to a silver nanowire," *Physical Review Letters*, vol. 106, no. 9, p. 096 801, 2011.

[94] E. J. R. Vesseur, F. J. G. de Abajo, and A. Polman, "Broadband purcell enhancement in plasmonic ring cavities," *Physical Review B*, vol. 82, no. 16, p. 165 419, 2010.

[95] K. J. Russell, T.-L. Liu, S. Cui, and E. L. Hu, "Large spontaneous emission enhancement in plasmonic nanocavities," *Nature Photonics*, vol. 6, no. 7, pp. 459–462, 2012.

[96] D. Englund, D. Fattal, E. Waks, G. Solomon, B. Zhang, T. Nakaoka, Y. Arakawa, Y. Yamamoto, and J. Vučković, "Controlling the spontaneous emission rate of single quantum dots in a two-dimensional photonic crystal," *Physical Review Letters*, vol. 95, no. 1, p. 013 904, 2005.

[97] S. Noda, M. Fujita, and T. Asano, "Spontaneous-emission control by photonic crystals and nanocavities," *Nature Photonics*, vol. 1, no. 8, pp. 449–458, 2007.

[98] G. M. Akselrod, C. Argyropoulos, T. B. Hoang, C. Ciracı, C. Fang, J. Huang, D. R. Smith, and M. H. Mikkelsen, "Probing the mechanisms of large purcell enhancement in plasmonic nanoantennas," *Nature Photonics*, vol. 8, no. 11, pp. 835–840, 2014.

[99] Y. Luo, E. D. Ahmadi, K. Shayan, Y. Ma, K. S. Mistry, C. Zhang, J. Hone, J. L. Blackburn, and S. Strauf, "Purcell-enhanced quantum yield from carbon nanotube excitons coupled to plasmonic nanocavities," *Nature Communications*, vol. 8, no. 1, pp. 1–9, 2017.

[100] T. Atay, J.-H. Song, and A. V. Nurmikko, "Strongly interacting plasmon nanoparticle pairs: From dipole- dipole interaction to conductively coupled regime," *Nano Letters*, vol. 4, no. 9, pp. 1627–1631, 2004.

[101] I. Romero, J. Aizpurua, G. W. Bryant, and F. J. García de Abajo, "Plasmons in nearly touching metallic nanoparticles: Singular response in the limit of touching dimers," *Optics Express*, vol. 14, no. 21, pp. 9988–9999, 2006.

[102] J. B. Lassiter, J. Aizpurua, L. I. Hernandez, D. W. Brandl, I. Romero, S. Lal, J. H. Hafner, P. Nordlander, and N. J. Halas, "Close encounters between two nanoshells," *Nano Letters*, vol. 8, no. 4, pp. 1212–1218, 2008.

[103] M. Schnell, A. Garcıa-Etxarri, A. Huber, K. Crozier, J. Aizpurua, and R. Hillenbrand, "Controlling the near-field oscillations of loaded plasmonic nanoantennas," *Nature Photonics*, vol. 3, no. 5, pp. 287–291, 2009.

[104] J. Zuloaga, E. Prodan, and P. Nordlander, "Quantum description of the plasmon resonances of a nanoparticle dimer," *Nano Letters*, vol. 9, no. 2, pp. 887–891, 2009.

[105] M. Hentschel, D. Dregely, R. Vogelgesang, H. Giessen, and N. Liu, "Plasmonic oligomers: The role of individual particles in collective behavior," *ACS Nano*, vol. 5, no. 3, pp. 2042–2050, 2011.

[106] H. Duan, A. I. Fernández-Domınguez, M. Bosman, S. A. Maier, and J. K. Yang, "Nanoplasmonics: Classical down to the nanometer scale," *Nano Letters*, vol. 12, no. 3, pp. 1683–1689, 2012.

[107] L. Wu, H. Duan, P. Bai, M. Bosman, J. K. Yang, and E. Li, "Fowler–nordheim tunneling induced charge transfer plasmons between nearly touching nanoparticles," *ACS Nano*, vol. 7, no. 1, pp. 707–716, 2013.

[108] F. Wen, Y. Zhang, S. Gottheim, N. S. King, Y. Zhang, P. Nordlander, and N. J. Halas, "Charge transfer plasmons: Optical frequency conductances and tunable infrared resonances," *ACS Nano*, vol. 9, no. 6, pp. 6428–6435, 2015.

[109] S. F. Tan, "Quantum plasmon resonances controlled by molecular tunnel junction," in *Molecular Electronic Control Over Tunneling Charge Transfer Plasmons Modes*, Springer, 2018, pp. 51–67.

[110] A. C. Neto, V. N. Kotov, J. Nilsson, V. M. Pereira, N. M. Peres, and B. Uchoa, "Adatoms in graphene," *Solid State Communications*, vol. 149, no. 27-28, pp. 1094–1100, 2009.

[111] S. Ihnatsenka and G. Kirczenow, "Dirac point resonances due to atoms and molecules adsorbed on graphene and transport gaps and conductance quantization in graphene nanoribbons with covalently bonded adsorbates," *Physical Review B*, vol. 83, p. 245 442, 24 Jun. 2011.

[112] N. A. Pike and D. Stroud, "Tight-binding model for adatoms on graphene: Analytical density of states, spectral function, and induced magnetic moment," *Physical Review B*, vol. 89, p. 115 428, 11 Mar. 2014.

[113] S. Y. Davydov, "Model of adsorption on amorphous graphene," *Semiconductors*, vol. 50, no. 3, pp. 377–383, 2016.

[114] L. Bursi, A. Calzolari, S. Corni, and E. Molinari, "Quantifying the plasmonic character of optical excitations in nanostructures," *ACS Photonics*, vol. 3, no. 4, pp. 520–525, 2016.

[115] R. Zhang, L. Bursi, J. D. Cox, Y. Cui, C. M. Krauter, A. Alabastri, A. Manjavacas, A. Calzolari, S. Corni, E. Molinari, *et al.*, "How to identify plasmons from the optical response of nanostructures," *ACS Nano*, vol. 11, no. 7, pp. 7321–7335, 2017.

[116] T. Yasuike, K. Nobusada, and M. Hayashi, "Collectivity of plasmonic excitations in small sodium clusters with ring and linear structures," *Physical Review A*, vol. 83, p. 013 201, 1 Jan. 2011.

[117] J. M. Fitzgerald, S. Azadi, and V. Giannini, "Quantum plasmonic nanoantennas," *Physical Review B*, vol. 95, p. 235 414, 23 Jun. 2017.

[118] R. L. Gieseking, A. P. Ashwell, M. A. Ratner, and G. C. Schatz, "Analytical approaches to identify plasmon-like excited states in bare and ligand-protected metal nanoclusters," *The Journal of Physical Chemistry C*, vol. 124, no. 5, pp. 3260–3269, 2020.

[119] R. L. Gieseking, "Plasmons: Untangling the classical, experimental, and quantum mechanical definitions," *Materials Horizons*, 2022.

[120] A. D. Dillon and R. L. Gieseking, "Evolution of plasmon-like excited states in silver nanowires and nanorods," *The Journal of Chemical Physics*, 2022.

[121] S. Bernadotte, F. Evers, and C. R. Jacob, "Plasmons in molecules," *The Journal of Physical Chemistry C*, vol. 117, no. 4, pp. 1863–1878, 2013.

[122] C. M. Krauter, S. Bernadotte, C. R. Jacob, M. Pernpointner, and A. Dreuw, "Identification of plasmons in molecules with scaled ab initio approaches," *The Journal of Physical Chemistry C*, vol. 119, no. 43, pp. 24 564–24 573, 2015.

[123] E. Townsend and G. W. Bryant, "Plasmonic Properties of Metallic Nanoparticles: The Effects of Size Quantization," *Nano Letters*, vol. 12, no. 1, pp. 429–434, 2012.
[124] E. Townsend and G. W. Bryant, "Which resonances in small metallic nanoparticles are plasmonic?" *Journal of Optics*, vol. 16, no. 11, p. 114 022, 2014.
[125] E. Townsend, A. Debrecht, and G. W. Bryant, "Approaching the quantum limit for nanoplasmonics," *Journal of Materials Research*, vol. 30, no. 16, pp. 2389–2399, 2015.
[126] J. Takahara, S. Yamagishi, H. Taki, A. Morimoto, and T. Kobayashi, "Guiding of a one-dimensional optical beam with nanometer diameter," *Optic Letters*, vol. 22, no. 7, pp. 475–477, 1997.
[127] D. K. Gramotnev and S. I. Bozhevolnyi, "Plasmonics beyond the diffraction limit," *Nature Photonics*, vol. 4, no. 2, p. 83, 2010.
[128] S. A. Mikhailov, "Theory of the giant plasmon-enhanced second-harmonic generation in graphene and semiconductor two-dimensional electron systems," *Physical Review B*, vol. 84, no. 4, p. 045 432, 2011.
[129] P. Ginzburg, A. Krasavin, Y. Sonnefraud, A. Murphy, R. J. Pollard, S. A. Maier, and A. V. Zayats, "Nonlinearly coupled localized plasmon resonances: Resonant second-harmonic generation," *Physical Review B*, vol. 86, no. 8, p. 085 422, 2012.
[130] J. D. Cox, A. Marini, and F. J. García de Abajo, "Plasmon-assisted high-harmonic generation in graphene," *Nature Communications*, vol. 8, no. 1, pp. 1–7, 2017.
[131] J. D. Jackson, *Classical electrodynamics*. Wiley, 1999.
[132] J. M. McMahon, S. K. Gray, and G. C. Schatz, "Nonlocal optical response of metal nanostructures with arbitrary shape," *Physical Review Letters*, vol. 103, no. 9, p. 097 403, 2009.
[133] N. A. Mortensen, S. Raza, M. Wubs, T. Søndergaard, and S. I. Bozhevolnyi, "A generalized non-local optical response theory for plasmonic nanostructures," *Nature Communications*, vol. 5, no. 1, pp. 1–7, 2014.
[134] H. B. Levine and G. Birnbaum, "Classical theory of collision-induced absorption in rare-gas mixtures," *Physical Review*, vol. 154, no. 1, p. 86, 1967.
[135] A. Babaze, R. Esteban, J. Aizpurua, and A. G. Borisov, "Second-harmonic generation from a quantum emitter coupled to a metallic nanoantenna," *ACS Photonics*, vol. 7, no. 3, pp. 701–713, 2020.
[136] P. Franken, A. E. Hill, C. e. Peters, and G. Weinreich, "Generation of optical harmonics," *Physical Review Letters*, vol. 7, no. 4, p. 118, 1961.
[137] B. E. Saleh and M. C. Teich, *Fundamentals of photonics*. John Wiley & Sons, 2019.
[138] S. Berciaud, L. Cognet, P. Tamarat, and B. Lounis, "Observation of intrinsic size effects in the optical response of individual gold nanoparticles," *Nano Letters*, vol. 5, no. 3, pp. 515–518, 2005.
[139] U. Kreibig and M. Vollmer, *Optical properties of metal clusters*. Springer Science & Business Media, 2013, vol. 25.
[140] A. H. Castro Neto, F. Guinea, N. M. R. Peres, K. S. Novoselov, and A. K. Geim, "The electronic properties of graphene," *Reviews of Modern Physics*, vol. 81, pp. 109–162, 1 Jan. 2009.
[141] M. J. Allen, V. C. Tung, and R. B. Kaner, "Honeycomb carbon: A review of graphene," *Chemical Reviews*, vol. 110, no. 1, pp. 132–145, 2010.
[142] P. A. D. Gonçalves, "Electronic and optical properties of graphene," in *Plasmonics and Light–Matter Interactions in Two-Dimensional Materials and in Metal Nanostructures*, Springer, 2020, pp. 51–70.
[143] A. D. Güçlü, P. Potasz, M. Korkusinski, P. Hawrylak, *et al.*, *Graphene quantum dots*. Springer, 2014.

[144] A. Krishnan, E. Dujardin, M. Treacy, J. Hugdahl, S. Lynum, and T. Ebbesen, "Graphitic cones and the nucleation of curved carbon surfaces," *Nature*, vol. 388, no. 6641, pp. 451–454, 1997.

[145] J. M. Tour, "Scaling up exfoliation," *Nature Materials*, vol. 13, no. 6, pp. 545–546, 2014.

[146] M. Yi and Z. Shen, "A review on mechanical exfoliation for the scalable production of graphene," *The Journal of Materials Chemistry A*, vol. 3, no. 22, pp. 11 700–11 715, 2015.

[147] P. W. Sutter, J.-I. Flege, and E. A. Sutter, "Epitaxial graphene on ruthenium," *Nature Materials*, vol. 7, no. 5, pp. 406–411, 2008.

[148] S. Marchini, S. Günther, and J. Wintterlin, "Scanning tunneling microscopy of graphene on ru (0001)," *Physical Review B*, vol. 76, no. 7, p. 075 429, 2007.

[149] P. Yi, S. Dong-Xia, and G. Hong-Jun, "Formation of graphene on ru (0001) surface," *Chinese Physics*, vol. 16, no. 11, p. 3151, 2007.

[150] J. Coraux, A. T. N 'Diaye, C. Busse, and T. Michely, "Structural coherency of graphene on ir (111)," *Nano Letters*, vol. 8, no. 2, pp. 565–570, 2008.

[151] A. V. De Parga, F. Calleja, B. Borca, M. Passeggi Jr, J. Hinarejos, F. Guinea, and R. Miranda, "Periodically rippled graphene: Growth and spatially resolved electronic structure," *Physical Review Letters*, vol. 100, no. 5, p. 056 807, 2008.

[152] C. Berger, Z. Song, T. Li, X. Li, A. Y. Ogbazghi, R. Feng, Z. Dai, A. N. Marchenkov, E. H. Conrad, P. N. First, *et al.*, "Ultrathin epitaxial graphite: 2d electron gas properties and a route toward graphene-based nanoelectronics," *The Journal of Physical Chemistry B*, vol. 108, no. 52, pp. 19 912–19 916, 2004.

[153] P. N. First, W. A. de Heer, T. Seyller, C. Berger, J. A. Stroscio, and J.-S. Moon, "Epitaxial graphenes on silicon carbide," *MRS Bulletin*, vol. 35, no. 4, pp. 296–305, 2010.

[154] N. Mishra, J. Boeckl, N. Motta, and F. Iacopi, "Graphene growth on silicon carbide: A review," *physica status solidi (a)*, vol. 213, no. 9, pp. 2277–2289, 2016.

[155] W. Yang, G. Chen, Z. Shi, C.-C. Liu, L. Zhang, G. Xie, M. Cheng, D. Wang, R. Yang, D. Shi, *et al.*, "Epitaxial growth of single-domain graphene on hexagonal boron nitride," *Nature Materials*, vol. 12, no. 9, pp. 792–797, 2013.

[156] A. Mehler, N. Néel, E. Voloshina, Y. Dedkov, and J. Kröger, "Second floor of flatland: Epitaxial growth of graphene on hexagonal boron nitride," *Small*, vol. 17, no. 36, p. 2 102 747, 2021.

[157] J. Lin, Z. Peng, Y. Liu, F. Ruiz-Zepeda, R. Ye, E. L. Samuel, M. J. Yacaman, B. I. Yakobson, and J. M. Tour, "Laser-induced porous graphene films from commercial polymers," *Nature Communications*, vol. 5, no. 1, pp. 1–8, 2014.

[158] X. Li, W. Cai, J. An, S. Kim, J. Nah, D. Yang, R. Piner, A. Velamakanni, I. Jung, E. Tutuc, *et al.*, "Large-area synthesis of high-quality and uniform graphene films on copper foils," *Science*, vol. 324, no. 5932, pp. 1312–1314, 2009.

[159] A. Reina, X. Jia, J. Ho, D. Nezich, H. Son, V. Bulovic, M. S. Dresselhaus, and J. Kong, "Large area, few-layer graphene films on arbitrary substrates by chemical vapor deposition," *Nano Letters*, vol. 9, no. 1, pp. 30–35, 2009.

[160] K. S. Kim, Y. Zhao, H. Jang, S. Y. Lee, J. M. Kim, K. S. Kim, J.-H. Ahn, P. Kim, J.-Y. Choi, and B. H. Hong, "Large-scale pattern growth of graphene films for stretchable transparent electrodes," *Nature*, vol. 457, no. 7230, pp. 706–710, 2009.

[161] S. Bae, H. Kim, Y. Lee, X. Xu, J.-S. Park, Y. Zheng, J. Balakrishnan, T. Lei, H. R. Kim, Y. I. Song, *et al.*, "Roll-to-roll production of 30-inch graphene films for transparent electrodes," *Nature Nanotechnology*, vol. 5, no. 8, pp. 574–578, 2010.

[162] Y. Xue, B. Wu, Y. Guo, L. Huang, L. Jiang, J. Chen, D. Geng, Y. Liu, W. Hu, and G. Yu, "Synthesis of large-area, few-layer graphene on iron foil by chemical vapor deposition," *Nano Research*, vol. 4, no. 12, pp. 1208–1214, 2011.

[163] D. V. Kosynkin, A. L. Higginbotham, A. Sinitskii, J. R. Lomeda, A. Dimiev, B. K. Price, and J. M. Tour, "Longitudinal unzipping of carbon nanotubes to form graphene nanoribbons," *Nature*, vol. 458, no. 7240, pp. 872–876, 2009.

[164] L. Tang, X. Li, R. Ji, K. S. Teng, G. Tai, J. Ye, C. Wei, and S. P. Lau, "Bottom-up synthesis of large-scale graphene oxide nanosheets," *The Journal of Materials Chemistry*, vol. 22, no. 12, pp. 5676–5683, 2012.

[165] P. Bøggild, "The war on fake graphene," *Nature*, vol. 562, no. 7728, pp. 502–503, 2018.

[166] L. Lin, H. Peng, and Z. Liu, "Synthesis challenges for graphene industry," *Nature Materials*, vol. 18, no. 6, pp. 520–524, 2019.

[167] A. P. Kauling, A. T. Seefeldt, D. P. Pisoni, R. C. Pradeep, R. Bentini, R. V. Oliveira, K. S. Novoselov, and A. H. Castro Neto, "The worldwide graphene flake production," *Advanced Materials*, vol. 30, no. 44, p. 1 803 784, 2018.

[168] H. Geng, D. Yuan, Z. Yang, Z. Tang, X. Zhang, K. Yang, and Y. Su, "Graphene van der waals heterostructures for high-performance photodetectors," *The Journal of Materials Chemistry C*, vol. 7, no. 36, pp. 11 056–11 067, 2019.

[169] K. S. Novoselov, A. K. Geim, S. V. Morozov, D. Jiang, M. I. Katsnelson, I. Grigorieva, S. Dubonos, and a. Firsov, "Two-dimensional gas of massless dirac fermions in graphene," *Nature*, vol. 438, no. 7065, pp. 197–200, 2005.

[170] M. Katsnelson, K. Novoselov, and A. Geim, "Chiral tunnelling and the klein paradox in graphene," *Nature Physics*, vol. 2, no. 9, pp. 620–625, 2006.

[171] E. Hwang, S. Adam, and S. D. Sarma, "Carrier transport in two-dimensional graphene layers," *Physical Review Letters*, vol. 98, no. 18, p. 186 806, 2007.

[172] A. K. Geim and K. S. Novoselov, "The rise of graphene," in *Nanoscience and technology: a collection of reviews from nature journals*, World Scientific, 2010, pp. 11–19.

[173] F. Liu, Q. Li, R. Wang, J. Xu, J. Hu, W. Li, Y. Guo, Y. Qian, W. Deng, Z. Ullah, *et al.*, "Low resistivity of graphene nanoribbons with zigzag-dominated edge fabricated by hydrogen plasma etching combined with zn/hcl pretreatment," *Applied Physics Letters*, vol. 111, no. 20, p. 203 102, 2017.

[174] M. Katsnelson, "Zitterbewegung, chirality, and minimal conductivity in graphene," *The European Physical Journal B-Condensed Matter and Complex Systems*, vol. 51, no. 2, pp. 157–160, 2006.

[175] F. Liu, P. Ming, and J. Li, "Ab initio calculation of ideal strength and phonon instability of graphene under tension," *Physical Review B*, vol. 76, no. 6, p. 064 120, 2007.

[176] H. Zhao, K. Min, and N. R. Aluru, "Size and chirality dependent elastic properties of graphene nanoribbons under uniaxial tension," *Nano Letters*, vol. 9, no. 8, pp. 3012–3015, 2009.

[177] C. Lee, X. Wei, J. W. Kysar, and J. Hone, "Measurement of the elastic properties and intrinsic strength of monolayer graphene," *Science*, vol. 321, no. 5887, pp. 385–388, 2008.

[178] K. Cao, S. Feng, Y. Han, L. Gao, T. Hue Ly, Z. Xu, and Y. Lu, "Elastic straining of free-standing monolayer graphene," *Nature Communications*, vol. 11, no. 1, pp. 1–7, 2020.

[179] J. S. Bunch, S. S. Verbridge, J. S. Alden, A. M. Van Der Zande, J. M. Parpia, H. G. Craighead, and P. L. McEuen, "Impermeable atomic membranes from graphene sheets," *Nano Letters*, vol. 8, no. 8, pp. 2458–2462, 2008.

[180] V. Berry, "Impermeability of graphene and its applications," *Carbon*, vol. 62, pp. 1–10, 2013.

[181] P. Sun, Q. Yang, W. Kuang, Y. Stebunov, W. Xiong, J. Yu, R. R. Nair, M. Katsnelson, S. Yuan, I. Grigorieva, *et al.*, "Limits on gas impermeability of graphene," *Nature*, vol. 579, no. 7798, pp. 229–232, 2020.

[182] R. R. Nair, P. Blake, A. N. Grigorenko, K. S. Novoselov, T. J. Booth, T. Stauber, N. M. Peres, and A. K. Geim, "Fine structure constant defines visual transparency of graphene," *Science*, vol. 320, no. 5881, pp. 1308–1308, 2008.

[183] J. Akola, H. Heiskanen, and M. Manninen, "Edge-dependent selection rules in magic triangular graphene flakes," *Physical Review B*, vol. 77, no. 19, p. 193 410, 2008.

[184] K. A. Ritter and J. W. Lyding, "The influence of edge structure on the electronic properties of graphene quantum dots and nanoribbons," *Nature Materials*, vol. 8, no. 3, pp. 235–242, 2009.

[185] A. D. Güçlü, P. Potasz, and P. Hawrylak, "Excitonic absorption in gate-controlled graphene quantum dots," *Physical Review B*, vol. 82, no. 15, p. 155 445, 2010.

[186] P. Potasz, A. D. Gü çlü, and P. Hawrylak, "Spin and electronic correlations in gated graphene quantum rings," *Physical Review B*, vol. 82, p. 075 425, 7 Aug. 2010.

[187] P. Potasz, A. D. Güçlü, A. Wójs, and P. Hawrylak, "Electronic properties of gated triangular graphene quantum dots: Magnetism, correlations, and geometrical effects," *Physical Review B*, vol. 85, no. 7, p. 075 431, 2012.

[188] N. M. R. Peres, F. Guinea, and A. H. Castro Neto, "Electronic properties of disordered two-dimensional carbon," *Physical Review B*, vol. 73, p. 125 411, 12 Mar. 2006.

[189] L.A. Falkovsky and A.A. Varlamov, "Space-time dispersion of graphene conductivity," *The European Physical Journal B*, vol. 56, no. 4, pp. 281–284, 2007.

[190] W. Wang, P. Apell, and J. Kinaret, "Edge plasmons in graphene nanostructures," *Physical Review B*, vol. 84, no. 8, p. 085 423, 2011.

[191] P. B. Johnson and R. W. Christy, "Optical constants of the noble metals," *Physical Review B*, vol. 6, pp. 4370–4379, 12 Dec. 1972.

[192] P. G. Etchegoin, E. C. Le Ru, and M. Meyer, "An analytic model for the optical properties of gold," *The Journal of Chemical Physics*, vol. 125, no. 16, p. 164 705, 2006.

[193] R. Sinha-Roy, P. Garcia-Gonzalez, H.-C. Weissker, F. Rabilloud, and A. I. Fernandez-Dominguez, "Classical and ab initio plasmonics meet at sub-nanometric noble metal rods," *ACS Photonics*, vol. 4, no. 6, pp. 1484–1493, 2017.

[194] T. Giovannini, M. Rosa, S. Corni, and C. Cappelli, "A classical picture of subnanometer junctions: An atomistic drude approach to nanoplasmonics," *Nanoscale*, vol. 11, no. 13, pp. 6004–6015, 2019.

[195] T. Giovannini, L. Bonatti, M. Polini, and C. Cappelli, "Graphene plasmonics: Fully atomistic approach for realistic structures," *The Jounal of Physical Chemistry Letters*, vol. 11, no. 18, pp. 7595–7602, 2020.

[196] D. E. Beck, "Self-consistent calculation of the eigenfrequencies for the electronic excitations in small jellium spheres," *Physical Review B*, vol. 35, no. 14, p. 7325, 1987.

[197] P.-G. Reinhard, M. Brack, and O. Genzken, "Random-phase approximation in a local representation," *Physical Review A*, vol. 41, no. 10, p. 5568, 1990.

[198] S. Kümmel, K. Andrae, and P.-G. Reinhard, "Collectivity in the optical response. of small metal clusters," *Applied Physics B*, vol. 73, no. 4, pp. 293–297, 2001.

[199] T. Raitza, H. Reinholz, P. G. Reinhard, G. Röpke, and I. Broda, "Spatially resolved collective excitations of nano-plasmas via molecular dynamics simulations and fluid dynamics," *New Journal of Physics*, vol. 14, no. 11, p. 115 016, 2012.

[200] E. B. Guidez and C. M. Aikens, "Quantum mechanical origin of the plasmon: From molecular systems to nanoparticles," *Nanoscale*, vol. 6, no. 20, pp. 11 512–11 527, 2014.

[201] E. B. Guidez and C. M. Aikens, "Plasmon resonance analysis with configuration interaction," *Physical Chemistry Chemical Physics*, vol. 16, no. 29, pp. 15 501–15 509, 2014.

[202] M. Guerrini, A. Calzolari, D. Varsano, and S. Corni, "Quantifying the plasmonic character of optical excitations in a molecular j-aggregate," *Journal of Chemical Theory and Computation*, vol. 15, no. 5, pp. 3197–3203, 2019.

[203] C. Liu, J. Kloppenburg, Y. Yao, X. Ren, H. Appel, Y. Kanai, and V. Blum, "All-electron ab initio bethe-salpeter equation approach to neutral excitations in molecules with numeric atom-centered orbitals," *The Journal of Chemical Physics*, vol. 152, no. 4, p. 044 105, 2020.

[204] X. Blase and C. Attaccalite, "Charge-transfer excitations in molecular donor- acceptor complexes within the many-body bethe-salpeter approach," *Applied Physics Letters*, vol. 99, no. 17, p. 171 909, 2011.

[205] W. Ekardt, "Size-dependent photoabsorption and photoemission of small metal particles," *Physical Review B*, vol. 31, no. 10, p. 6360, 1985.

[206] M. J. Puska, R. M. Nieminen, and M. Manninen, "Electronic polarizability of small metal spheres," *Physical Review B*, vol. 31, no. 6, p. 3486, 1985.

[207] G. M. Piccini, R. W. A. Havenith, R. Broer, and M. Stener, "Gold nanowires: A time-dependent density functional assessment of plasmonic behavior," *The Journal of Physical Chemistry C*, vol. 117, no. 33, pp. 17 196–17 204, 2013.

[208] L. Bursi, A. Calzolari, S. Corni, and E. Molinari, "Light-induced field enhancement in nanoscale systems from first-principles: The case of polyacenes," *ACS Photonics*, vol. 1, no. 10, pp. 1049–1058, 2014.

[209] T. Noguchi, T. Shimamoto, and K. Watanabe, "Photoabsorption spectra of graphitic nanostructures by time-dependent density-functional theory," *e-Journal of Surface Science and Nanotechnology*, vol. 3, pp. 439–443, 2005.

[210] J. Yan, Z. Yuan, and S. Gao, "End and Central Plasmon Resonances in Linear Atomic Chains," *Physical Review Letters*, vol. 98, p. 216 602, 21 May 2007.

[211] J. Yan and S. Gao, "Plasmon resonances in linear atomic chains: free-electron behavior and anisotropic screening of d electrons," *Physical Review B*, vol. 78, no. 23, p. 235 413, 2008.

[212] M. Kuisma, A. Sakko, T. P. Rossi, A. H. Larsen, J. Enkovaara, L. Lehtovaara, and T. T. Rantala, "Localized surface plasmon resonance in silver nanoparticles: Atomistic first-principles time-dependent density-functional theory calculations," *Physical Review B*, vol. 91, no. 11, p. 115 431, 2015.

[213] J. Hobson and W. Nierenberg, "The statistics of a two-dimensional, hexagonal net," *Physical Review*, vol. 89, no. 3, p. 662, 1953.

[214] M. S. Tang, C. Z. Wang, C. T. Chan, and K. M. Ho, "Environment-dependent tight-binding potential model," *Physical Review B*, vol. 53, pp. 979–982, 3 Jan. 1996.

[215] J. N. B. Rodrigues, P. A. D. Gon çalves, N. F. G. Rodrigues, R. M. Ribeiro, J. M. B. Lopes dos Santos, and N. M. R. Peres, "Zigzag graphene nanoribbon edge reconstruction with stone-wales defects," *Physical Review B*, vol. 84, p. 155 435, 15 Oct. 2011.

[216] M. Pelc, L. Chico, A. Ayuela, and W. Jaskólski, "Grain boundaries with octagonal defects in graphene nanoribbons and nanotubes," *Physical Review B*, vol. 87, p. 165 427, 16 Apr. 2013.
[217] J. R. Bell and P. Dean, "Atomic vibrations in vitreous silica," *Discussions of the Faraday Society*, vol. 50, no. 0, pp. 55–61, 1970.
[218] J. R. Bell, "The dynamics of disordered lattices," *Reports on Progress in Physics*, vol. 35, no. 3, pp. 1315–1409, 1972.
[219] M. Wimmer, A. R. Akhmerov, and F. Guinea, "Robustness of edge states in graphene quantum dots," *Physical Review B*, vol. 82, p. 045 409, 4 Jul. 2010.
[220] C. A. Downing and L. Martín-Moreno, "Polaritonic Tamm states induced by cavity photons," *Nanophotonics*, vol. 10, no. 1, pp. 513–521, 2021.
[221] T. Yamamoto, T. Noguchi, and K. Watanabe, "Edge-state signature in optical absorption of nanographenes: Tight-binding method and time-dependent density functional theory calculations," *Physical Review B*, vol. 74, p. 121 409, 12 Sep. 2006.
[222] A. J. Heeger, "Nobel Lecture: Semiconducting and metallic polymers: The fourth generation of polymeric materials," *Reviews of Modern Physics*, vol. 73, pp. 681–700, 3 Sep. 2001.
[223] M. Bacon, S. J. Bradley, and T. Nann, "Graphene quantum dots," *Particle & Particle Systems Characterization*, vol. 31, no. 4, pp. 415–428, 2014.
[224] X. Li, M. Rui, J. Song, Z. Shen, and H. Zeng, "Carbon and graphene quantum dots for optoelectronic and energy devices: A review," *Advanced Functional Materials*, vol. 25, no. 31, pp. 4929–4947, 2015.
[225] S. Y. Lim, W. Shen, and Z. Gao, "Carbon quantum dots and their applications," *Chemical Society Reviews*, vol. 44, no. 1, pp. 362–381, 2015.
[226] W. Chen, G. Lv, W. Hu, D. Li, S. Chen, and Z. Dai, "Synthesis and applications of graphene quantum dots: A review," *Nanotechnology Reviews*, vol. 7, no. 2, pp. 157–185, 2018.
[227] P. Tian, L. Tang, K. Teng, and S. Lau, "Graphene quantum dots from chemistry to applications," *Materials Today Chemistry*, vol. 10, pp. 221–258, 2018.
[228] Z. Ullah, G. Witjaksono, I. Nawi, N. Tansu, M. Irfan Khattak, and M. Junaid, "A review on the development of tunable graphene nanoantennas for terahertz optoelectronic and plasmonic applications," *Sensors*, vol. 20, no. 5, p. 1401, 2020.
[229] R. Jelinek, "Carbon quantum dots," *Carbon quantum dots. Springer International Publishing, Cham*, pp. 29–46, 2017.
[230] Y.-W. Son, M. L. Cohen, and S. G. Louie, "Energy gaps in graphene nanoribbons," *Physical Review Letters*, vol. 97, no. 21, p. 216 803, 2006.
[231] L. Pisani, J. Chan, B. Montanari, and N. Harrison, "Electronic structure and magnetic properties of graphitic ribbons," *Physical Review B*, vol. 75, no. 6, p. 064 418, 2007.
[232] C. Tao, L. Jiao, O. V. Yazyev, Y.-C. Chen, J. Feng, X. Zhang, R. B. Capaz, J. M. Tour, A. Zettl, S. G. Louie, *et al.*, "Spatially resolving edge states of chiral graphene nanoribbons," *Nature Physics*, vol. 7, no. 8, pp. 616–620, 2011.
[233] O. V. Yazyev, R. B. Capaz, and S. G. Louie, "Theory of magnetic edge states in chiral graphene nanoribbons," *Physical Review B*, vol. 84, no. 11, p. 115 406, 2011.
[234] A. Güçlü and P. Hawrylak, "Optical control of magnetization and spin blockade in graphene quantum dots," *Physical Review B*, vol. 87, no. 3, p. 035 425, 2013.
[235] I. Silveiro, J. M. P. Ortega, and F. J. García de Abajo, "Quantum nonlocal effects in individual and interacting graphene nanoribbons," *Light: Science & Applications*, vol. 4, no. 1, e241–e241, 2015.
[236] N. D. Mermin, "Lindhard dielectric function in the relaxation-time approximation," *Physical Review B*, vol. 1, no. 5, p. 2362, 1970.

[237] J. D. Cox and F. J. García de Abajo, "Nonlinear graphene nanoplasmonics," *Accounts of Chemical Research*, vol. 52, no. 9, pp. 2536–2547, 2019.
[238] J. D. Cox and F. J. García de Abajo, "Plasmon-enhanced nonlinear wave mixing in nanostructured graphene," *ACS Photonics*, vol. 2, no. 2, pp. 306–312, 2015.
[239] P. Zhang, J. Feist, A. Rubio, P. Garcıa-González, and F. Garcıa-Vidal, "Ab initio nanoplasmonics: The impact of atomic structure," *Physical Review B*, vol. 90, no. 16, p. 161 407, 2014.
[240] H.-C. Weissker and X. López-Lozano, "Surface plasmons in quantum-sized noble-metal clusters: Tddft quantum calculations and the classical picture of charge oscillations," *Physical Chemistry Chemical Physics*, vol. 17, no. 42, pp. 28 379–28 386, 2015.
[241] T. Christensen, W. Yan, A.-P. Jauho, M. Soljačić, and N. A. Mortensen, "Quantum corrections in nanoplasmonics: Shape, scale, and material," *Physical Review Letters*, vol. 118, no. 15, p. 157 402, 2017.
[242] P. Gonçalves, T. Christensen, N. Rivera, A.-P. Jauho, N. A. Mortensen, and M. Soljačić, "Plasmon–emitter interactions at the nanoscale," *Nature Communications*, vol. 11, no. 1, pp. 1–13, 2020.
[243] G. Buchs, M. Marganska, J. W. González, K. Eimre, C. A. Pignedoli, D. Passerone, A. Ayuela, O. Gröning, and D. Bercioux, "Metallic carbon nanotube quantum dots with broken symmetries as a platform for tunable terahertz detection," *Applied Physics Reviews*, vol. 8, no. 2, p. 021 406, 2021.
[244] P. O. Lehtinen, A. S. Foster, A. Ayuela, A. Krasheninnikov, K. Nordlund, and R. M. Nieminen, "Magnetic Properties and Diffusion of Adatoms on a Graphene Sheet," *Physical Review Letters*, vol. 91, p. 017 202, 1 Jun. 2003.
[245] T. G. Pedersen, C. Flindt, J. Pedersen, N. A. Mortensen, A.-P. Jauho, and K. Pedersen, "Graphene Antidot Lattices: Designed Defects and Spin Qubits," *Physical Review Letters*, vol. 100, no. 13, p. 136 804, 2008.
[246] J. A. Fürst, J. G. Pedersen, C. Flindt, N. A. Mortensen, M. Brandbyge, T. G. Pedersen, and A.-P. Jauho, "Electronic properties of graphene antidot lattices," *New Journal of Physics*, vol. 11, no. 9, p. 095 020, 2009.
[247] K. T. Chan, J. B. Neaton, and M. L. Cohen, "First-principles study of metal adatom adsorption on graphene," *Physical Review B*, vol. 77, no. 23, p. 235 430, 2008.
[248] A. Ishii, M. Yamamoto, H. Asano, and K. Fujiwara, "DFT calculation for adatom adsorption on graphene sheet as a prototype of carbon nanotube functionalization," *Journal of Physics: Conference Series*, vol. 100, no. 5, p. 052 087, 2008.
[249] Y. Sanchez-Paisal, D. Sanchez-Portal, and A. Ayuela, "Ab *initio* calculations of zirconium adsorption and diffusion on graphene," *Physical Review B*, vol. 80, no. 4, p. 045 428, 2009.
[250] T. Alonso-Lanza, A. Ayuela, and F. Aguilera-Granja, "Substitutional 4d and 5d impurities in graphene," *Physical Chemistry Chemical Physics*, vol. 18, no. 31, pp. 21 913–21 920, 2016.
[251] T. Alonso-Lanza, A. Mañanes, and A. Ayuela, "Interaction of Cobalt Atoms, Dimers, and Co4 Clusters with Circumcoronene: A Theoretical Study," *The Journal of Physical Chemistry C*, vol. 121, no. 34, pp. 18 900–18 908, 2017.
[252] B. Uchoa, V. N. Kotov, N. M. R. Peres, and A. H. C. Neto, "Localized Magnetic States in Graphene," *Physical Review Letters*, vol. 101, no. 2, p. 026 805, 2008.
[253] E. J. G. Santos, D. Sánchez-Portal, and A. Ayuela, "Magnetism of substitutional Co impurities in graphene: Realization of single π vacancies," *Physical Review B*, vol. 81, no. 12, p. 125 433, 2010.
[254] J. H. Ammeter, H. B. Buergi, J. C. Thibeault, and R. Hoffmann, "Counterintuitive Orbital Mixing in Semiempirical and ab Initio Molecular Orbital Calculations,"

The Journal of the American Chemical Society, vol. 100, no. 12, pp. 3686–3692, 1978, issn: 0002-7863.

[255] P. W. Anderson, "Localized Magnetic States in Metals," *Physical Reviews*, vol. 124, pp. 41–53, 1 Oct. 1961.

[256] R. Sollie and P. Schlottmann, "A simple theory of the Kondo hole," *The Journal of Applied Physics*, vol. 69, no. 8, pp. 5478–5480, 1991.

[257] M. Gmitra, D. Kochan, and J. Fabian, "Spin-Orbit Coupling in Hydrogenated Graphene," *Physical Review Letters*, vol. 110, p. 246 602, 24 Jun. 2013.

[258] S. Irmer, T. Frank, S. Putz, M. Gmitra, D. Kochan, and J. Fabian, "Spin-orbit coupling in fluorinated graphene," *Physical Review B*, vol. 91, p. 115 141, 11 Mar. 2015.

[259] K. Zollner, T. Frank, S. Irmer, M. Gmitra, D. Kochan, and J. Fabian, "Spin-orbit coupling in methyl functionalized graphene," *Physical Review B*, vol. 93, p. 045 423, 4 Jan. 2016.

[260] T. Frank, S. Irmer, M. Gmitra, D. Kochan, and J. Fabian, "Copper adatoms on graphene: Theory of orbital and spin-orbital effects," *Physical Review B*, vol. 95, p. 035 402, 3 Jan. 2017.

[261] S. Irmer, D. Kochan, J. Lee, and J. Fabian, "Resonant scattering due to adatoms in graphene: Top, bridge, and hollow positions," *Physical Review B*, vol. 97, p. 075 417, 7 Feb. 2018.

[262] K. Nakada and A. Ishii, *DFT calculation for adatom adsorption on graphene*. Intech, 2011.

[263] E. J. G. Santos, A. Ayuela, and D. Sánchez-Portal, "Universal magnetic properties of sp3-type defects in covalently functionalized graphene," *New Journal of Physics*, vol. 14, no. 4, p. 043 022, 2012.

[264] A. M. Fox, M. Fox, *et al.*, *Quantum optics: an introduction*. Oxford University Press, 2006, vol. 15.

[265] W. Vogel and D.-G. Welsch, *Quantum optics*. John Wiley & Sons, 2006.

[266] S. Scheel, L. Knöll, and D.-G. Welsch, "Spontaneous decay of an excited atom in an absorbing dielectric," *Physical Review A*, vol. 60, no. 5, p. 4094, 1999.

[267] R. Loudon, *The quantum theory of light*. OUP Oxford, 2000.

[268] D. Dzsotjan, A. S. Sørensen, and M. Fleischhauer, "Quantum emitters coupled to surface plasmons of a nanowire: A green's function approach," *Physical Review B*, vol. 82, no. 7, p. 075 427, 2010.

[269] M. Kosik, O. Burlayenko, C. Rockstuhl, I. Fernandez-Corbaton, and K. Słowik, "Interaction of atomic systems with quantum vacuum beyond electric dipole approximation," *Scientific Reports*, vol. 10, no. 1, pp. 1–12, 2020.

[270] W. L. Barnes, S. A. Horsley, and W. L. Vos, "Classical antennas, quantum emitters, and densities of optical states," *Journal of Optics*, vol. 22, no. 7, p. 073 501, 2020.

[271] S. Haroche and J.-M. Raimond, *Exploring the quantum: atoms, cavities, and photons*. Oxford University Press, 2006.

[272] D. A. Steck, "Quantum and atom optics," *available online at http://steck.us/teaching, accessed on 01 June 2022*, 2007.

[273] D. Pines and D. Bohm, "A collective description of electron interactions: II. Collective vs individual particle aspects of the interactions," *Physical Review*, vol. 85, no. 2, p. 338, 1952.

[274] P. K. Jain, "Plasmon-in-a-box: on the physical nature of few-carrier plasmon resonances," *The Journal of Physical Chemistry Letters*, vol. 5, no. 18, pp. 3112–3119, 2014.

[275] H. Zhang, V. Kulkarni, E. Prodan, P. Nordlander, and A. O. Govorov, "Theory of quantum plasmon resonances in doped semiconductor nanocrystals," *The Journal of Physical Chemistry C*, vol. 118, no. 29, pp. 16 035–16 042, 2014.

[276] R. L. Gieseking, "Third-order nonlinear optical properties of ag nanoclusters: Connecting molecule-like and nanoparticle-like behavior," *Chemistry of Materials*, vol. 31, no. 17, pp. 6850–6859, 2019.

[277] W. Ekardt and Z. Penzar, "Collective excitations in open-shell metal clusters: The time-dependent local-density approximation applied to the self-consistent spheroidal jellium particle," *Physical Review B*, vol. 43, no. 2, p. 1322, 1991.

[278] S. Malola, L. Lehtovaara, J. Enkovaara, and H. Hakkinen, "Birth of the localized surface plasmon resonance in monolayer-protected gold nanoclusters," *ACS Nano*, vol. 7, no. 11, pp. 10 263–10 270, 2013.

[279] M. Ezawa, "Metallic graphene nanodisks: Electronic and magnetic properties," *Physical Review B*, vol. 76, no. 24, p. 245 415, 2007.

[280] W. Jaskólski, A. Ayuela, M. Pelc, H. Santos, and L. Chico, "Edge states and flat bands in graphene nanoribbons with arbitrary geometries," *Physical Review B*, vol. 83, no. 23, p. 235 424, 2011.

[281] E. B. Guidez and C. M. Aikens, "Theoretical analysis of the optical excitation spectra of silver and gold nanowires," *Nanoscale*, vol. 4, no. 14, pp. 4190–4198, 2012.

[282] Y. Song, R. Wortis, and W. A. Atkinson, "Dynamical mean field study of the two-dimensional disordered hubbard model," *Physical Review B*, vol. 77, p. 054 202, 5 Feb. 2008.

[283] N. C. Murphy, R. Wortis, and W. A. Atkinson, "Generalized inverse participation ratio as a possible measure of localization for interacting systems," *Physical Review B*, vol. 83, p. 184 206, 18 May 2011.

[284] M. J. Alhilaly, M. S. Bootharaju, C. P. Joshi, T. M. Besong, A.-H. Emwas, R. Juarez-Mosqueda, S. Kaappa, S. Malola, K. Adil, A. Shkurenko, *et al.*, "[ag67 (sphme2) 32 (pph3) 8] 3+: Synthesis, total structure, and optical properties of a large box-shaped silver nanocluster," *The Journal of the American Chemical Society*, vol. 138, no. 44, pp. 14 727–14 732, 2016.

[285] D. Casanova, J. M. Matxain, and J. M. Ugalde, "Plasmonic resonances in the al13– cluster: Quantification and origin of exciton collectivity," *The Journal of Physical Chemistry C*, vol. 120, no. 23, pp. 12 742–12 750, 2016.

[286] Z. Fei, A. Rodin, G. O. Andreev, W. Bao, A. McLeod, M. Wagner, L. Zhang, Z. Zhao, M. Thiemens, G. Dominguez, *et al.*, "Gate-tuning of graphene plasmons revealed by infrared nano-imaging," *Nature*, vol. 487, no. 7405, pp. 82–85, 2012.

[287] D. Kundys, B. Van Duppen, O. P. Marshall, F. Rodriguez, I. Torre, A. Tomadin, M. Polini, and A. N. Grigorenko, "Nonlinear light mixing by graphene plasmons," *Nano Letters*, vol. 18, no. 1, pp. 282–287, 2018.

[288] A. V. Rozhkov and F. Nori, "Exact wave functions for an electron on a graphene triangular quantum dot," *Physical Review B*, vol. 81, p. 155 401, 15 Apr. 2010.

[289] M. E. Casida, "Time-Dependent Density Functional Response Theory for Molecules," in *Recent Advances in Density Functional Methods*, pp. 155–192.

[290] R. Bauernschmitt and R. Ahlrichs, "Treatment of electronic excitations within the adiabatic approximation of time dependent density functional theory," *Chemical Physics Letters*, vol. 256, no. 4, pp. 454–464, 1996, issn: 0009-2614.

[291] R. E. Stratmann, G. E. Scuseria, and M. J. Frisch, "An efficient implementation of time-dependent density-functional theory for the calculation of excitation energies of large molecules," *The Journal of Chemical Physics*, vol. 109, no. 19, pp. 8218–8224, 1998.

[292] F. Furche and R. Ahlrichs, "Adiabatic time-dependent density functional methods for excited state properties," *The Journal of Chemical Physics*, vol. 117, no. 16, pp. 7433–7447, 2002.

[293] W. A. Harrison, “The Physics of Solid State Chemistry, in Festkörperprobleme 17,” in, Springer, 1977, pp. 135–155.

Appendices

A | The EPI in LR-TD-DFT

In linear-response time-dependent density functional theory (LR-TD-DFT), as we applied it in Ref. [A4], the energy eigenstates of a given system are defined by the eigenvalue problem [289–291]

$$\begin{pmatrix} A & B \\ B^* & A^* \end{pmatrix} \begin{pmatrix} X \\ Y \end{pmatrix} = \hbar\omega \begin{pmatrix} 1 & 0 \\ 0 & -1 \end{pmatrix} \begin{pmatrix} X \\ Y \end{pmatrix} \tag{A.1}$$

with the orbital rotation matrices

$$A_{ia,jb} = (E_i - E_a)\delta_{ij}\delta_{ab} + (ai|jb) + f^{\mathrm{XC}}_{ai,bj}, \tag{A.2}$$

$$B_{ia,jb} = (ai|bj) + f^{\mathrm{XC}}_{ai,bj}. \tag{A.3}$$

Here, E_i denotes the energy of the single-particle *Kohn-Sham* eigenstate φ_i and

$$(ai|bj) = \int \mathrm{d}^3\mathbf{r} \int \mathrm{d}^3\mathbf{r}' \varphi_a(\mathbf{r})\varphi_i(\mathbf{r}) \frac{1}{|\mathbf{r} - \mathbf{r}'|} \varphi_b(\mathbf{r}')\varphi_j(\mathbf{r}') \tag{A.4}$$

is a *Coulomb* interaction integral. The exchange-correlation kernel reads

$$f^{\mathrm{XC}}_{ai,bj} = \frac{\partial^2 E^{\mathrm{XC}}}{\partial D_{ai} \partial D_{bj}}, \tag{A.5}$$

where E^{XC} is the exchange-correlation energy within the adiabatic approximation [292].

From the solutions of Eq. (A.1), one can directly compute quantities like the oscillator strengths and dipole moments of excitations. Moreover, the EPI is accessible *via* the transition density in the *Kohn-Sham* molecular orbital basis,

$$\rho^{\omega}_{ai} = X_{ia,\omega} + Y_{ia,\omega}. \tag{A.6}$$

From that, one can obtain the auxiliary density operator in analogy to Eq. (8.6),

$$\tilde{\rho}^{\omega}_{ai} = \frac{|\rho^{\omega}_{ai}|}{||E_a - E_i| - \hbar\omega + \mathrm{i}\varepsilon|^2}, \tag{A.7}$$

and finally arrives at the EPI

$$\mathrm{EPI}(\omega) = 1 - \langle \tilde{\rho}^{\omega}_{ai}, \rho^{\omega}_{ai} \rangle. \tag{A.8}$$

B | *Coulomb* Interaction Matrix

B.1 Stand-Alone Antenna

The elements of the *Coulomb* interaction matrix v are defined in a two-fold way.

1. For elements that relate carbon atoms which are far away from each other, the inverse distance $1/r$ power law is employed [44] according to

$$v_{ll'} = \frac{E_h a_0}{|\mathbf{r}_l - \mathbf{r}_{l'}|}, \tag{B.1}$$

   where $E_h = 27.21\,\mathrm{eV}$ is the *Hartree* energy and $a_0 = 0.53\,\text{Å}$ is the *Bohr* radius.

2. For elements in v, that relate close atoms, the same strategy cannot be applied as divergences would appear for the diagonal elements v_{ll}. Thus, explicitly calculated values for the on-site, nearest neighbor, and next-to-nearest neighbor terms $v_{\mathrm{os}} = 16.52\,\mathrm{eV}$, $v_{\mathrm{nn}} = 8.64\,\mathrm{eV}$, and $v_{\mathrm{nnn}} = 5.33\,\mathrm{eV}$, respectively, are used. They have been determined analytically by Potasz *et al.* [186] by taking into account the spatial extent of the p_z orbitals in graphene through

$$v_{ll'} = \int \mathrm{d}^3\mathbf{r} \int \mathrm{d}^3\tilde{\mathbf{r}}\ \psi_l(\mathbf{r})\psi_{l'}(\tilde{\mathbf{r}})\frac{1}{|\mathbf{r} - \tilde{\mathbf{r}}|}\psi_{l'}(\tilde{\mathbf{r}})\psi_l(\mathbf{r}) \tag{B.2}$$

   directly from the real-valued carbon Slater p_z orbitals

$$\psi_l(\mathbf{r}) = \sqrt{\frac{\xi^5}{32\pi}} z_l \exp\left(\frac{-\xi \mathbf{r}_l}{2}\right) \tag{B.3}$$

   with $\xi = 3.14$ in graphene. The values are taken from Table I in Ref. [186].

B.2 Hybrid System

We construct the extended *Coulomb* interaction matrix of the hybrid system v^{hyb} based on the interaction matrix of the stand-alone antenna v. For the intra-antenna terms, we have

$$v^{\mathrm{hyb}}_{ll'} = v_{ll'} \qquad \text{for } l, l' \in [1, N_a]. \tag{B.4}$$

For the sake of simplicity, the elements of v^{hyb} that relate orbitals within the adatom are set to the on-site value v_{os}, as if all of them were p_z orbitals in graphene, such that $v^{\mathrm{hyb}}_{gg} = v^{\mathrm{hyb}}_{ee} = v^{\mathrm{hyb}}_{eg} = v^{\mathrm{hyb}}_{ge} = v_{\mathrm{os}}$.

Elements that relate orbitals of the adatom with orbitals of the antenna have to meet the constraint that they vanish for vanishing coupling strength, *i.e.* if the adatom is infinitely

far away from the antenna. We assume

$$v_{el_c}^{\mathrm{hyb}} = v_{l_c e}^{\mathrm{hyb}} = v_{\mathrm{nn}} \cdot \frac{a_{cc}}{d} \sqrt{\left| \frac{t_e}{t} \right|}, \tag{B.5a}$$

$$v_{gl_c}^{\mathrm{hyb}} = v_{l_c g}^{\mathrm{hyb}} = v_{\mathrm{nn}} \cdot \frac{a_{cc}}{d} \sqrt{\left| \frac{t_g}{t} \right|}, \tag{B.5b}$$

for the elements that couple adatom orbitals to the coupling atom orbital $|l_c\rangle$, and

$$v_{el}^{\mathrm{hyb}} = v_{le}^{\mathrm{hyb}} = v_{ll_c} \cdot \frac{a_{cc}}{d + a_{cc}} \sqrt{\left| \frac{t_e}{t} \right|}, \tag{B.6a}$$

$$v_{gl}^{\mathrm{hyb}} = v_{lg}^{\mathrm{hyb}} = v_{ll_c} \cdot \frac{a_{cc}}{d + a_{cc}} \sqrt{\left| \frac{t_g}{t} \right|}, \tag{B.6b}$$

for all other antenna orbitals, where d is the distance of the coupling atom l_c in the antenna to the adatom, and $a_{\mathrm{cc}} = 1.42\,\text{Å}$ is the carbon-carbon distance in the antenna. The elements v_{ll_c} are intra-antenna elements and can be calculated through Eq. (B.4). Moreover, the coupling strengths t_e, t_g can be determined from the distance d according to [293]

$$t_{e,g} = t \left(\frac{a_{cc}}{d} \right)^2. \tag{B.7}$$

C | Nonlinear Parameters for Higher Harmonic Generation

Table C.1 presents the full set of nonlinear parameters $\beta_n^{d,E}$ for the nth higher harmonic of the mode at energy $E = \hbar\omega_0$ in the 270-atomic graphene armchair triangle with doping d discussed in Sec. 5.3.2. They relate the incident electric field component $|\tilde{\mathbf{E}}(\omega_0)|$ and the induced dipole moment component $|\tilde{\mathbf{p}}(n\omega_0)|$ according to

$$|\tilde{\mathbf{p}}(n\omega_0)| = \beta_n^{d,E} |\tilde{\mathbf{E}}(\omega_0)|^n. \tag{C.1}$$

Table C.1: Nonlinear parameters $\beta_n^{d,E}$ for the nth higher harmonic of the mode at energy $E = \hbar\omega_0$ with doping d. (n.a. indicates that it was not possible to determine the value reliably due to the lack of data points in Figs. 5.7c and 5.7f.)

	d	2	20	2	20	2	20
n	E	1.36 eV	1.39 eV	1.7 eV	1.7 eV	2.08 eV	2.03 eV
1		20	80	6	20	10	9
2		1	60	0.15	2	0.06	1
3		20	300	2	30	1.5	1.5
4		7	300	0.09	2	n.a.	n.a.

Acknowledgements

This dissertation is written in the plural first person form *"we"*. This is not just for semantic or linguistic reasons, but really gets to the heart of its very literal meaning. In science, one person alone cannot achieve anything. And so I was lucky enough to work with many wonderful people from all over the world in the past four years – primarily from Poland, Spain, the United States, and Germany. To all of them, and to many more, I am deeply indebted which I try to express in the following.

First and foremost, I want to sincerely thank **Carsten Rockstuhl**, my doctoral supervisor, for offering me this *hot topic* to graduate on. Also, for his excellent guidance through this venture of the past four years – both as a scientist and as a person. In particular, for entrusting me with a perfect balance of giving me free rein when possible, and whistling me back when necessary and appropriate. And for always finding a spare time slot in his calendar when I asked for it.

Second, I would like to thank **Ralph Krupke** for agreeing to review my doctoral thesis as the second referee.

Furthermore, I owe my invaluable gratitude to the fabulous **Benasque Graphene Squad**. *"Dziękuję bardzo!"* to …
Karolina Słowik for her supervision and support. For letting me use her private coffee machine during my countless stays at the *Uniwersytet Mikołaja Kopernika* in marvelous Toruń, and for being always available for online discussions when I happened to be out of town for whatever reason. Also, for making me aware of the conferences in Benasque and, of course, for introducing me to the secrets of the hellfire place.
Miriam Kosik, for her passionate work on our joint project, for not leaving me behind but for always forcing me to look into more and more advanced programming frameworks to develop my skills, and for innumerable bilateral scientific and nonscientific discussions. For showing me Gdańsk, Warszawa, and the hidden parts of Toruń's beauty (Przepompownia pub, PERS, and eNeRDe, for instance). And finally, for being not only a colleague but also a friend.

I am very grateful to my remaining co-authors, to **Andrés Ayuela**, **Marta Pelc**, and **Garnett Bryant** for their invaluable expertise and contributions to our project, and to **Christof Holzer** and **Nanda Perdana** for their DFT and T-matrix calculations that found their way into our joint publication.

I thankfully acknowledge the support of the **Karlsruhe House of Young Scientists (KHYS)**, which granted me financial support within the Research Travel Grant (RTG) during my research stay in Donostia.

Additionally, I would like to thank ...

- **Javier Aizpurua** and **Ruben Esteban**, for their kindest hospitality at the *Centro de Física de Materiales (CFM)* in Donostia, and for their valuable time they spent introducing me to the physics of open quantum systems. *Muchas gracias* and *eskerrik asko!*
- **Andreas Poenicke**, for keeping our IT infrastructure in such a great condition that even people like me can use it reasonably. And for keeping calm despite me exceeding my quota another time.
- **Evmarie Schwartz** and **Hannah Belli**, for professionally enduring all the accounting problems related to my business trips, and for solving them ultimately.
- the *Proper People* (**Xavi, Taavi**, and **Yannick**) and the *Cheaters* (**Lina** and **Marjan**), for a memorable bike trip to Avignon.
- **Marvin Schulz**, for countless coffees and beers we had during fruitful discussions on mathematical aspects of my work that I could not cope with alone.
- **Lina, Isi**, and **Alex**, for making me wake up early in the morning in the writing phase, and for letting me use their coffee machine when ours was out of order.
- my (former) office mates **Stefan**, **Fernando**, **Joshua**, **Katharina**, **Taavi**, **Benedikt**, **Daniel**, **Patrick**, **Dominik**, **Mitchell**, **Lukas**, **Theodosios**, and **Xuchen**, for stimulating discussions, for keeping me entertained all the time, and for leaving me alone when they realized I wanted it in the writing phase.
- all remaining members, current and past, of my **research group at TFP**, for the outstanding atmosphere in the group, and for all the off-duty activities that are way too numerous to write them down here.
- the **ESN Bilbao-San Sebastián** and all **Erasmus students** I met in Donostia, for their benignity to admit me as one of their kind, for organized pub crawls, hikes, chess sessions, cookouts, house parties, city trips, and sidrería evenings, and for all other experiences that made my stay in Donostia an unforgettable adventure.
- my **friends** and **family** from Karlsruhe, Rastatt, and Plittersdorf, for many pleasant distractions from work during birthday parties, city trips, hiking tours, or skat nights.
- my **parents**, for their unconditional support not only during my time as a PhD student, but all the time since the very day I was born. And for their perpetual encouragement, that goes far beyond what I could have wished for, and that has enabled me to pursue my interests and dreams during my entire life.
- **Lara**, for being by my side throughout my whole academic career, and even before that. For keeping my spirits up always, but especially in the writing phase. And, above all, for her love, without which I would be much less.

Selbstständigkeitserklärung

Eidesstattliche Versicherung gemäß § 13 Absatz 2 Ziffer 3 der Promotionsordnung des Karlsruher Instituts für Technologie (KIT) für die KIT-Fakultät für Physik:

1. Bei der eingereichten Dissertation zu dem Thema
"electronic and photonic excitations in graphene nanostructures and hybrid systems"
handelt es sich um meine eigenständig erbrachte Leistung.

2. Ich habe nur die angegebenen Quellen und Hilfsmittel benutzt und mich keiner unzulässigen Hilfe Dritter bedient. Insbesondere habe ich wörtlich oder sinngemäß aus anderen Werken übernommene Inhalte als solche kenntlich gemacht.

3. Die Arbeit oder Teile davon habe ich wie folgt/ bislang nicht[1] an einer Hochschule des In- oder Auslands als Bestandteil einer Prüfungs- oder Qualifikationsleistung vorgelegt.

Titel der Arbeit: Electronic and photonic excitations in graphene nanostructures and hybrid systems
Hochschule und Jahr: KIT-Fakultät für Physik 2022
Art der Prüfungs- oder Qualifikationsleistung: Dissertation

4. Die Richtigkeit der vorstehenden Erklärungen bestätige ich.

5. Die Bedeutung der eidesstattlichen Versicherung und die strafrechtlichen Folgen einer unrichtigen oder unvollständigen eidesstattlichen Versicherung sind mir bekannt.

Ich versichere an Eides statt, dass ich nach bestem Wissen die reine Wahrheit erklärt und nichts verschwiegen habe.

Ort und Datum Unterschrift

[1] Nicht Zutreffendes streichen. Bei Bejahung sind anzugeben: der Titel der andernorts vorgelegten Arbeit, die Hochschule, das Jahr der Vorlage und die Art der Prüfungs- oder Qualifikationsleistung.